

SILESIAAN UNIVERSITY OF TECHNOLOGY

FACULTY OF CHEMISTRY

**New poly(3-hexylthiophene)-based materials  
for gas sensors and photovoltaic applications  
- design and synthesis**

**Kinga Kępska**

**Doctoral thesis**

prepared under supervision of:

**Prof. dr hab. inż. Mieczysław Łapkowski, corresponding PAS member**

(supervisor)

**Dr hab. inż. Agnieszka Stolarczyk, prof. PŚ**

(assistant supervisor)

at the Department of Physical Chemistry and Technology of Polymers

**Gliwice 2024**

*With sincere thanks to:*

*my family - for their patience, understanding and motivation,*

*my supervisors - for their guidance and advice,*

*work colleagues - for inspiration, broadening of horizons and hours of fruitful discussions.*

## Table of contents

<b>I.</b>	<b>ABSTRACT IN ENGLISH .....</b>	<b>5</b>
<b>II.</b>	<b>ABSTRACT IN POLISH (STRESZCZENIE PO POLSKU) .....</b>	<b>6</b>
<b>III.</b>	<b>GLOSSARY .....</b>	<b>7</b>
<b>IV.</b>	<b>INTRODUCTION .....</b>	<b>11</b>
<b>V.</b>	<b>AIM OF THE WORK .....</b>	<b>13</b>
<b>VI.</b>	<b>LITERATURE REVIEW .....</b>	<b>14</b>
<b>1</b>	<b>BAND THEORY AND CONDUCTING POLYMERS.....</b>	<b>14</b>
1.1	POLYTHIOPHENE – STRUCTURE AND PROPERTIES .....	16
<b>2</b>	<b>POLY(3-ALKYLTHIOPHENES) - PROCESSABLE DERIVATIVES OF POLYTHIOPHENE .....</b>	<b>18</b>
2.1	REGIOREGULARITY OF POLY(3-ALKYLTHIOPHENES) .....	19
2.2	MECHANISM OF GRIM SYNTHESIS OF POLY(3-ALKYLTHIOPHENES).....	27
2.3	PURIFICATION AND FRACTIONATION OF P3ATs.....	30
2.4	END GROUP FUNCTIONALISATION OF POLY(3-ALKYLTHIOPHENE)S .....	31
<b>3</b>	<b>COPOLYMERS FOR ELECTRONIC APPLICATIONS .....</b>	<b>32</b>
3.1	GRAFT COPOLYMERS.....	33
3.2	POLYSILOXANES .....	35
3.3	HYDROSILYLATION.....	37
3.4	COPOLYMERS BEARING REGIOREGULAR POLY(3-HEXYLTHIOPHENE) SEGMENT.....	39
<b>4</b>	<b>CHARACTERISATION OF POLYMERS .....</b>	<b>43</b>
4.1	DETERMINATION OF MOLECULAR WEIGHT OF POLYMERS.....	44
4.2	NMR SPECTROSCOPY OF POLY(3-HEXYLTHIOPHENES) .....	46
4.3	NMR SPECTROSCOPY OF POLYSILOXANES.....	49
4.4	IR SPECTROSCOPY .....	49
<b>5</b>	<b>CHOSEN APPLICATIONS OF ORGANIC SEMICONDUCTORS .....</b>	<b>52</b>
5.1	GAS SENSORS .....	52
5.2	ORGANIC SOLAR CELLS .....	55
5.2.1	<i>BHI solar cells.....</i>	<i>56</i>
5.2.2	<i>Additives improving performance of solar cells .....</i>	<i>61</i>
<b>VII.</b>	<b>EXPERIMENTAL PART .....</b>	<b>65</b>
<b>6</b>	<b>MATERIALS, METHODS AND EQUIPMENT .....</b>	<b>65</b>
6.1	SYNTHESES OF POLY(3-HEXYLTHIOPHENE)S .....	65

6.2	SYNTHESES OF GRAFT COPOLYMERS .....	67
6.3	MOLECULAR CHARACTERISATION OF POLYMERS AND COPOLYMERS .....	71
6.4	FABRICATION AND TESTING OF GAS SENSORS .....	72
6.5	FABRICATION AND TESTING OF PHOTOVOLTAIC DEVICES .....	73
<b>VIII.</b>	<b>RESULTS AND DISCUSSION.....</b>	<b>76</b>
<b>7</b>	<b>STRUCTURAL ANALYSIS OF POLYMERS AND COPOLYMERS.....</b>	<b>76</b>
7.1	POLY(3-HEXYLTHIOPHENE), POLYSILOXANES AND POLY(ETHYLENE GLYCOL).....	76
7.2	GRAFT COPOLYMERS.....	87
7.3	SUMMARY OF THE COPOLYMERS COMPOSITION.....	95
7.4	SPECTROELECTROCHEMICAL CHARACTERISTICS .....	97
<b>8</b>	<b>APPLICATION OF OBTAINED COPOLYMERS.....</b>	<b>97</b>
8.1	GAS SENSORS .....	97
8.2	PHOTOVOLTAIC DEVICES .....	106
<b>IX.</b>	<b>SUMMARY AND CONCLUSIONS .....</b>	<b>117</b>
<b>X.</b>	<b>SUPPLEMENT .....</b>	<b>120</b>
<b>XI.</b>	<b>LIST OF FIGURES.....</b>	<b>156</b>
<b>XII.</b>	<b>LIST OF TABLES .....</b>	<b>159</b>
<b>XIII.</b>	<b>BIBLIOGRAPHY.....</b>	<b>161</b>

## I. Abstract in English

The primary objective of this work was design and synthesis of novel class of graft copolymers bearing conjugated polymer followed by molecular characterisation of obtained materials. The subsidiary aim was to preliminary recognise application possibilities of the obtained materials as nitrogen dioxide sensors and in photovoltaic devices.

Copolymer architectures were based on the incorporation into the macromolecule the following segments: poly(3-hexylthiophene) as a model electron-donor conjugated polymer in the field of emerging organic photovoltaics and polysiloxane backbone as inert, flexible, thermally and environmentally stable scaffold for graft copolymers. Series of materials with different co-grafted moieties (such as nonpolar alkyl or polar poly(ethylene glycol)) were employed to tune the morphology and optoelectronic properties of the resulting materials. The structure of parent poly(3-hexylthiophene) and the copolymers was thoroughly evaluated by NMR and FT-IR techniques, additionally supported by molecular weight analysis.

Copolymers bearing co-grafted polyether and alkyl side chains were tested as low-temperature gas sensors for detection of nitrogen dioxide. Copolymers demonstrated higher responses to test gas than pristine poly(3-hexylthiophene). It was demonstrated that especially presence of poly(ethylene glycol) segments improved sensitivity of the sensors. Although dynamics of sensor regeneration at room temperature was slow, it was improved by elevating operating temperature to 50-100°C and irradiation of the working sensor with ultraviolet light.

Copolymers: bearing only poly(3-hexylthiophene)-grafts and the ones bearing co-grafted alkyl chains were tested as bulk heterojunction solar cells with fullerene acceptor. Solar cells based on polysiloxane grafted with poly(3-hexylthiophene) and hexyl chains copolymer demonstrated power conversion efficiencies comparable with poly(3-hexylthiophene)-based device. Moreover, copolymer-based solar cells demonstrated higher thermal stability upon prolonged annealing and slightly higher stability upon storing in inert atmosphere compared to poly(3-hexylthiophene)-based devices.

In conclusion, obtained copolymers proved to be promising candidates for the further development of such molecular architectures to fine tune the properties by modifying the structure on the molecular level to obtain materials tailored for highly selective gas sensors and organic solar cells applications.

## II. Abstract in polish (streszczenie po polsku)

Głównym celem pracy było zaprojektowanie i synteza nowej klasy kopolimerów szczepionych zawierających polimer skoniugowany, a następnie charakterystyka molekularna otrzymanych materiałów. Celem pobocznym było wstępne rozpoznanie możliwości zastosowania otrzymanych materiałów jako czujników dwutlenku azotu oraz w urządzeniach fotowoltaicznych.

Architekturę kopolimerów oparto na wbudowaniu do makrocząsteczki następujących segmentów: poli(3-heksylofenu) jako modelowego sprzężonego polimeru elektrondonorowego w obszarze fotowoltaiki organicznej oraz szkieletu polisiloksanowego jako obojętnego, elastycznego, stabilnego termicznie i środowiskowo rusztowania dla kopolimerów szczepionych. W celu dostosowania morfologii i właściwości optoelektronicznych otrzymanych materiałów zsyntezowano serię materiałów z różnymi ko-szczepionymi grupami (takimi jak niepolarny alkil lub polarny poli(glikol etylenowy)). Struktura macierzystego poli(3-heksylofenu) i kopolimerów została dokładnie zbadana technikami NMR i FT-IR, dodatkowo wspartymi analizą masy cząsteczkowej.

Kopolimery zawierające ko-szczepione polieterowe i alkilowe łańcuchy boczne zostały przetestowane jako niskotemperaturowe sensory gazów do wykrywania dwutlenku azotu. Kopolimery wykazywały wyższą odpowiedź na badany gaz niż czysty poli(3-heksylofenu). Wykazano, że szczególnie obecność segmentów poli(glikolu etylenowego) poprawiła czułość sensorów. Chociaż dynamika regeneracji sensorów w temperaturze pokojowej była wolna, została ona poprawiona przez podniesienie temperatury roboczej do 50-100°C i naświetlanie działającego czujnika światłem ultrafioletowym.

Kopolimery szczepione zawierające tylko poli(3-heksylofenu) oraz kopolimery zawierające ko-szczepione łańcuchy alkilowe zostały przetestowane jako ogniwa słoneczne o budowie heterozłącza z akceptorem fulerenowym. Ogniwa słoneczne oparte na polisiloksanie szczepionym poli(3-heksylofenu) i łańcuchami heksylowymi osiągnęły sprawność porównywalną z urządzeniami opartymi na poli(3-heksylofenu). Co więcej, ogniwa słoneczne oparte na kopolimerach wykazały wyższą stabilność termiczną przy długotrwałym wygrzewaniu i nieco wyższą trwałość podczas przechowywania w atmosferze obojętnej w porównaniu do urządzeń opartych na poli(3-heksylofenu).

Podsumowując, otrzymane kopolimery okazały się obiecującymi związkami do dalszego rozwoju takich architektur molekularnych z możliwością precyzyjnego regulowania właściwości poprzez modyfikację struktury na poziomie molekularnym w celu uzyskania materiałów dostosowanych do zastosowań w wysoce selektywnych czujnikach gazu i organicznych ogniwach słonecznych.

### III. Glossary

#### List of abbreviations

2D – two-dimensional

AFM – atomic force microscopy

asym – asymmetric

a.u. – arbitrary unit

br – broad

CB - chlorobenzene

CDCl<sub>3</sub> – deuterated chloroform

COSY (<sup>1</sup>H-<sup>1</sup>H COSY) - correlation spectroscopy

d – doublet

dd - doublet of doublets

dq – doublet of quartets

δ – chemical shift in NMR spectra, expressed in ppm downfield TMS signal *or* deformation vibration in IR spectra

DCTB – *trans*-2-[3-(4-*tert*-butylphenyl)-2-methyl-2-propenylidene]malononitrile

DHAP – direct heteroarylation polymerization

D<sub>M</sub> – dispersity

DMF – dimethylformamid

E – energy

E<sub>g</sub> – band gap

EQE – external quantum efficiency

FC – chloroform fraction

FF – fill factor

FH – hexane fraction

FT-IR – Fourier transform infrared (spectroscopy)

GPC – gel permeation chromatography

GRIM – Grignard metathesis (polymerization)

HH – head-to-head

HT – head-to-tail

HOMO – highest occupied molecular orbital

HPLC – high-performance liquid chromatography

HSQC – heteronuclear single quantum correlation (spectroscopy)

IDT – interdigital transducer

ITO – indium tin oxide

$J_{sc}$  – short circuit current density [ $\text{mA}/\text{cm}^2$ ]

KCTP – Kumada catalyst transfer polycondensation

LDA – lithium diisopropylamide

LUMO – lowest unoccupied molecular orbital

m – multiplet (in NMR) *or* medium intensity (in IR)

MALDI-TOF MS – matrix-assisted laser desorption/ionization time of flight mass spectrometry

MDS RID – multi-detector suite refractive index detector

$M_n$  – number average molecular weight

$M_w$  – weight average molecular weight

$\text{Ni}(\text{dppp})\text{Cl}_2$  – dichloro[1,3-bis(diphenylphosphino)propane]nickel(II)

NMR – nuclear magnetic resonance (spectroscopy)

NOE – nuclear Overhauser effect

NR – nonregular

OSC – organic solar cell

P – power

P3AT – poly(3-alkylthiophene)

P3HT – poly(3-hexylthiophene)

PCBM ( $\text{PC}_{61}\text{BM}$ ) – phenyl- $\text{C}_{61}$ -butyric acid methyl ester

PCE – power conversion efficiency

PDMS – poly(dimethylsiloxane)

PEDOT – poly(3,4-ethylenedioxythiophene)

PEG – poly(ethylene glycol)

PEGMA – poly(ethylene glycol) methyl ether methacrylate

PMHS – poly(methylhydrosiloxane)

ppb – part per billion

ppm – part per milion

$\text{PPh}_3$  – triphenylphosphine

PSS – poly(styrene sulfonate)

PTDD - platinum(0)-1,1,3,3-tetramethyl-1,3-divinyldisiloxane (Karstedt catalyst)

RMS – root mean square

RN - regiorandom

rpm – revolution per minute

RR – regioregular



$\rho$  – rocking vibration

s – singlet (in NMR) *or* strong intensity (in IR)

sym – symmetric

SEC – size exclusion chromatography

t – triplet

Th - thiophene

THF – tetrahydrofuran

TMS – tetramethylsilane (NMR standard)

TT - tail-to-tail

UV - ultraviolet

UV-Vis – (spectroscopy or spectrophotometry) in ultraviolet and visible region

UATR – universal attenuated total reflectance

$V_{OC}$  – open circuit voltage [V]

VWD – variable wavelength detector

w – weak intensity

## List of polymers and copolymers synthesised and used as precursors

- NR P3HT – nonregular poly(3-hexylthiophene)
- RR P3HT – regioregular poly(3-hexylthiophene)
- P3HTvin – vinyl terminated regioregular poly(3-hexylthiophene)
- PMHS-S – poly(methylhydrosiloxane), short, average Mn 390 g/mol
- PMHS-L – poly(methylhydrosiloxane), long, average Mn 1700-3200 g/mol
- P(DMS-*co*-MHS) - poly(dimethylsiloxane-*co*-methylhydrosiloxane), medium, average Mn 950 g/mol
- PEGMA - poly(ethylene glycol) methyl ether methacrylate, average Mn 500
- PMHS-*g*-P3HT - poly(methylhydrosiloxane)-*graft*-poly(3-hexylthiophene), components: PMHS-S, P3HT FC
- PMHS-*g*-(P3HT/PEG) 1 - poly(methylhydrosiloxane)-*graft*-[poly(3-hexylthiophene); (poly(ethylene glycol) methyl ether methacrylate)], components: PMHS-S, P3HT FH
- PMHS-*g*-(P3HT;PEG) 2 - poly(methylhydrosiloxane)-*graft*-[poly(3-hexylthiophene); (poly(ethylene glycol) methyl ether methacrylate)], components: PMHS-S, P3HT FC
- PMHS-*g*-(P3HT;PEG) 3 - poly(methylhydrosiloxane)-*graft*-[poly(3-hexylthiophene); (poly(ethylene glycol) methyl ether methacrylate)], components: PMHS-L, P3HT FC
- PMHS-*g*-(P3HT/hex) 1 - poly(methylhydrosiloxane)-*graft*-[poly(3-hexylthiophene); hexene], components: PMHS-S, P3HT FC, hexene
- PMHS-*g*-(P3HT/hex) 2 - poly(methylhydrosiloxane)-*graft*-[poly(3-hexylthiophene); hexene], components: PMHS-L, P3HT FC, hexene
- PDMS-*co*-MHS-*g*-P3HT - poly(dimethylsiloxane-*co*-methylhydrosiloxane)-*graft*-poly(3-hexylthiophene), components: PDMS-*co*-MHS, P3HT FC
- P(DMS-*co*-MHS)-*g*-(P3HT;PEG) 1 - poly(dimethylsiloxane-*co*-methylhydrosiloxane)-*graft*-[poly(3-hexylthiophene); (poly(ethylene glycol) methyl ether methacrylate)], components: PDMS-*co*-MHS, P3HT FH, PEGMA
- P(DMS-*co*-MHS)-*g*-(P3HT;PEG) 2 - poly(dimethylsiloxane-*co*-methylhydrosiloxane)-*graft*-[poly(3-hexylthiophene); (poly(ethylene glycol) methyl ether methacrylate)], components: PDMS-*co*-MHS, P3HT FC, PEGMA
- P(DMS-*co*-MHS)-*g*-(P3HT;dodec) 1 - poly(dimethylsiloxane-*co*-methylhydrosiloxane)-*graft*-[poly(3-hexylthiophene); dodecene], components: PDMS-*co*-MHS, P3HT FH, dodecene
- P(DMS-*co*-MHS)-*g*-(P3HT;dodec) 2 - poly(dimethylsiloxane-*co*-methylhydrosiloxane)-*graft*-[poly(3-hexylthiophene); dodecene], components: PDMS-*co*-MHS, P3HT FC, dodecene

#### IV. Introduction

20<sup>th</sup> and succeeding 21<sup>st</sup> century are highly dependent on synthetic polymers as organic polymer-derived plastics became more omnipresent and versatile than many other materials, such as metals, wood, glass or ceramics. Whereas term “plastics” usually implies electrically insulating synthetic polymers, the field of electrically conducting polymers has rapidly developed in last five decades. Milestone that in the 1970s changed thinking of organic polymeric materials as insulators was the synthesis of polyacetylene in the form of a silvery-coloured, lustrous film (*trans*-polyacetylene) [1,2], whose conductivity increased seven orders of magnitude when *p*-doped (oxidised) with iodine vapours [3,4]. That significant discovery triggered extensive research in the new field of conducting polymers, which may achieve conductivities comparable to metallic conductors, like copper or silver, and stimulated the development of modern organic electronics (Fig. IV.1 depicts number of papers referring to “conducting polymer” or “conductive polymer” topics in Web of Science database, showing increasing interest in these topics). It also resulted in the Nobel Prize in Chemistry awarded to the pioneers: H. Shirakawa, A. MacDiarmid and A.J. Heeger in 2000.

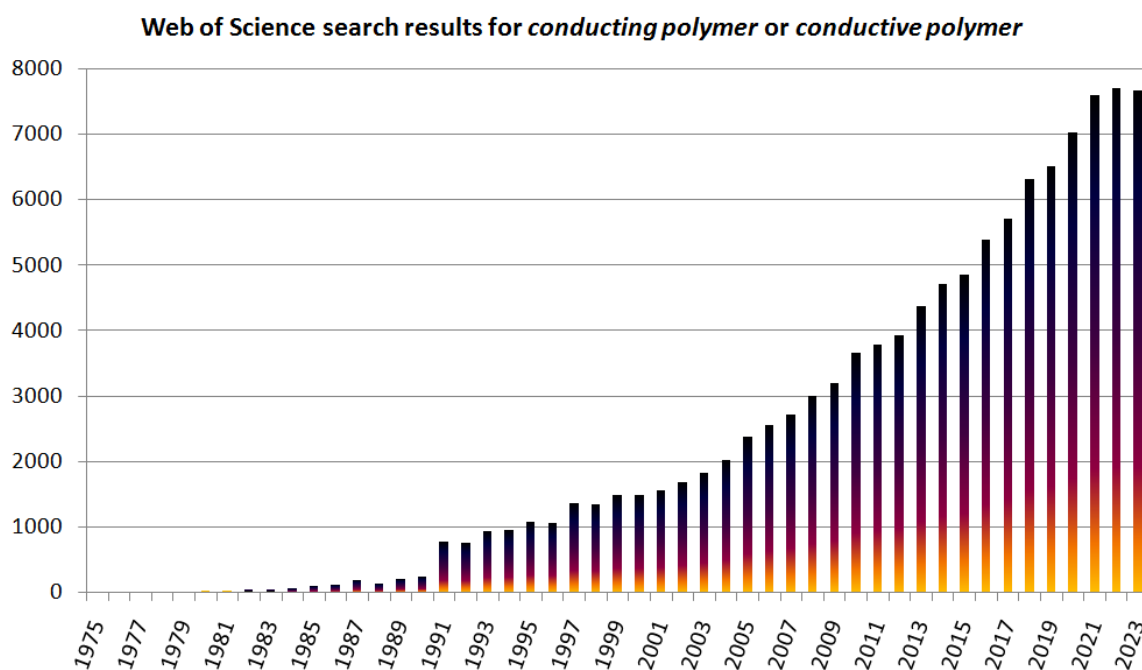


Fig. IV.1 Number of Web of Science records by year for query “conducting polymer” or “conductive polymer”, acquired online 17.05.2024

The perspective to produce cheap, printable, flexible electronics fuelled imagination and efforts of both academic researchers and industrial companies to design and explore new

materials. Conducting polymers – combining the electronic properties of semiconductors with many of the desirable attributes of polymers, including low production costs, possibility of solution processing and mechanical flexibility – have revolutionized modern science, technology and everyday life. They can successfully replace heavy and stiff metallic conductors and inorganic semiconductors in such application areas as: electronic circuits, light emission, clean energy production and bioelectronics [5]. They can be applied in such technologies as: antistatic and anti-corrosion coatings [6,7], batteries [8,9], supercapacitors [10,11], electrochromic devices [12,13], organic photovoltaic devices (OPVs) (organic solar cells (OSCs)) [14,15], organic thin film transistors (OTFTs) [16], organic light-emitting diodes (OLEDs) [17–19], sensors (including gas sensors [20] and biosensors [21,22]), electronic memories [23,24] and smart textiles [25].

Fast development of abovementioned fields forms foundations for pursue for novel tailor-made materials for organic electronics in basic scientific research, as well as in areas of industrial research and development (R&D) and implementation of new technologies. Copolymers are graceful candidates for that purpose, since their complex formulation allow to incorporate different components with versatile characteristics in one macromolecule and provide homogenous composition of the material. Moreover, careful design of copolymers allows for tailoring properties of the final structure [26].

## V. Aim of the work

The primary objective of this work was design and synthesis of novel class of graft copolymers bearing conjugated polymer (regioregular poly(3-hexylthiophene) - P3HT) chains attached to polysiloxane backbone, followed by molecular characterisation of obtained materials.

The subsidiary aim was to preliminary recognise the possibilities of application of the obtained materials as chemoresistive NO<sub>2</sub> sensors and in photovoltaic devices.

Within the framework of the above-formulated objectives the following specific issues had to be addressed:

- planning the structure of tailor-made graft copolymers,
- recognition of the optimal synthetic pathway to connect conjugated polymer chains to polysiloxane backbone,
- choice of the most convenient route to synthesise regioregular P3HT functionalised with proper terminal groups allowing for further coupling with polysiloxane moiety,
- molecular characterisation of obtained copolymers,
- recognition how the molecular structure and composition of copolymers affects performance of conjugated polymer (P3HT) in NO<sub>2</sub> sensors,
- fabrication and testing of photovoltaic devices (bulk heterojunction solar cells) and evaluation of the results.

Regioregular P3HT was pre-selected as a benchmark electron-donor conjugated polymer in field of emerging organic photovoltaics. Polysiloxane backbone was pre-selected as a scaffold for the graft copolymers. Conventional bulk heterojunction solar cell architecture with fullerene acceptor was chosen for investigation of structure-property relationship with respect to photovoltaics.

## VI. Literature review

### 1 Band theory and conducting polymers

In solid state physics the electronic band structure defines the range of energy levels allowed to be populated by electrons and forbidden energy levels. In neutral state electrons occupy valence band – for electric conduction electrons have to be transferred to conduction band. According to the band theory, there are three main types of materials, classified based on width of band gap ( $E_g$ ) between valence band and conduction band: insulators, semiconductors and metallic conductors (Fig. 1.1). In metals valence band and conduction band overlap, therefore electrons can move freely in crystalline lattice which allows for electronic conduction of metals. In semiconductors and insulators valence band and conduction band are separated by band gap.

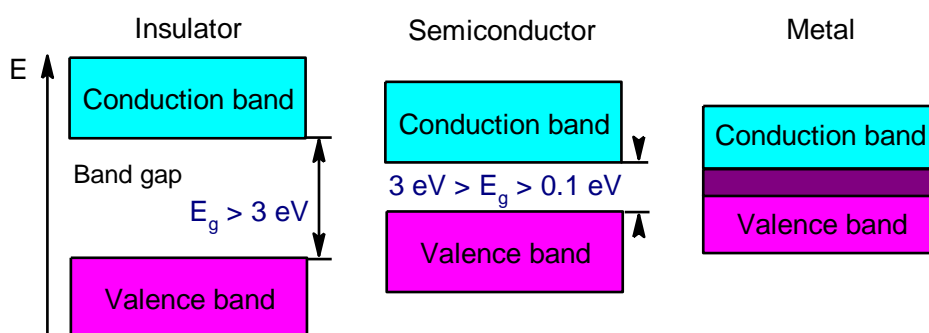


Fig. 1.1 Diagram of energy levels in metals, semiconductors and insulators

The width of the band gap is a key factor determining the distribution of electrons between the valence and conduction bands in semiconducting materials. The charge carriers (negative electrons and positive holes) present in the conduction band give rise to intrinsic conductivity, and the narrower the band gap, the higher the conductivity of the semiconductor.

According to IUPAC Gold Book, interactive version of IUPAC Compendium of Chemical Terminology<sup>1</sup>, *conducting polymer* is “polymeric material that exhibits bulk electric conductivity”, whereas *intrinsically conducting polymer* is defined as “*electrically conducting polymer* composed of macromolecules having fully conjugated sequences of double bonds along the chains”. In other words, intrinsically conducting polymers are

<sup>1</sup><https://goldbook.iupac.org/>; accessed online 04.05.2024

macromolecules that manifest enhanced electric conductivity resulting from the movement of delocalized electrons through conjugated systems. They consist of organic semiconducting materials capable of carrying electric charges (negative electrons or positive holes) in their non-neutral redox states (upon doping). Conducting polymers are generated by oxidation or reduction of conjugated polymers (comprising  $\pi$ -conjugated system along the polymer chain). Examples of the most important conjugated polymers are depicted in Fig. 1.2. In terms of electric conductivity, conducting polymers are classified as semiconductors or as isolators.

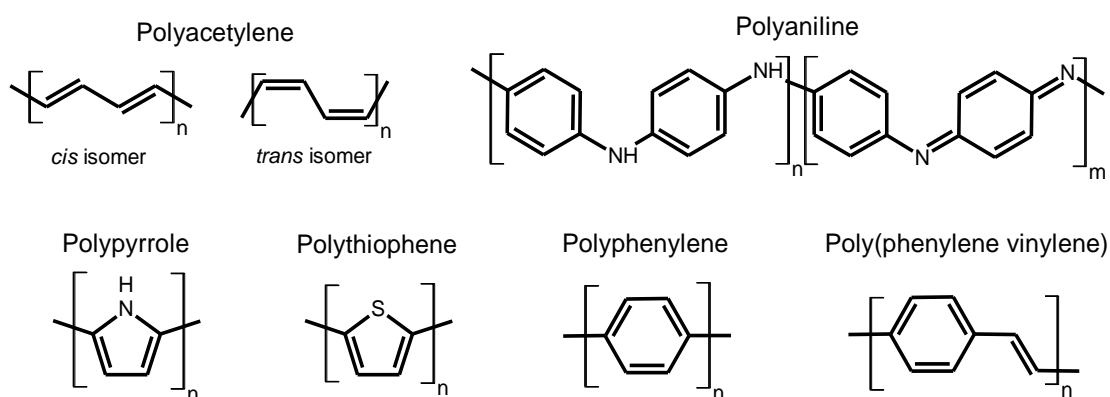


Fig. 1.2 Examples of the most common conjugated polymers

Synthesis and doping of polyacetylene to conductive form was the major breakthrough in the field of conducting polymers, but it didn't gain much commercial interest because of its instability against air and moisture. In the following late 1970s and 1980s particular attention among the conducting polymers was paid to polyaniline, polypyrrole and polythiophene. The latter two can be synthesised electrochemically directly in the doped form as films on the electrode, are stable in air, and achieve conductivities of about  $10^2$  S/cm [27,28]. However, electrochemical synthesis results in quite irregular structure, with defects (connections different than 2,5 couplings between repeating units – Fig. 1.3) reaching up to 1/3 of all linkages in polypyrrole [29], which is undesirable factor, corrupting straight alignment of polymer chains, promoting branching and crosslinking, and resulting in structural disorder, polymer chain twisting and decrease in conjugation length. Application of chemical synthesis methods based on catalyst-coupling resulted in better control of the manner in which monomers connect, higher polymer chains regularity and increase in conjugation length along the polymer backbone [30].

Among conjugated polymers polythiophene-based materials have attracted a lot of attention. Parent thiophene, as well as its numerous derivatives (such as 3-alkylthiophenes,

3-alkoxythiophenes and many others), are very convenient building blocks for transition metal catalysed cross-coupling polymerization resulting in regular, well defined oligo- or macromolecule, they can be also post-functionalised in many ways. The ease of modification creates potential for tuning electronic properties of the material over a wide range. Polythiophenes are stable, both in neutral and doped, conducting state. They feature exceptional electronic, optical, charge transport, redox, and self-assembling characteristics, as well as unique arrangement and stacking properties on solid surfaces and in the bulk, which make them interesting candidates for applications in organic electronics [31].

The structure of the conducting polymer plays a key role in determination of physical properties. The control of the regularity and order of the polymer structure leads to remarkable improvement in the electronic and photonic properties [32], which in turn leads to the conclusion that the properties of the conducting polymer can be designed at the synthetic step. An effective design strategy assumes the control of both microscopic and macroscopic properties in the solid phase, as both of these parameters affect the electronic structure of the material, determining its optical and electrical properties.

Conductive polymers with conjugated, unsubstituted backbone resulting in highly ordered structure are usually infusible and insoluble and thus intractable [33]. In fact, early belief was that substitution of the backbone with side groups promoting solubility would disrupt the solid-state packing and coplanarity of conjugated systems. Fortunately, it turned out not to be true for some conjugated polymers with specific pending groups (such as poly(3-alkylthiophenes)), and opened new possibilities for design and synthesis of solution-processable conducting polymers.

### **1.1 Polythiophene - structure and properties**

Polythiophene (PT) is conducting polymer composed of thiophene (sulphur aromatic heterocycle) units, described by  $(C_4H_2S)_n$  formula. Usually PT term refers to poly(thiophene-2,5-diyl) with monomer units linked through 2 and 5 positions, and polythiophenes (PTs) term refers to group of polymers including parent polythiophene and its derivatives substituted in 3, or 3 and 4 position of the thiophene ring. Polythiophene is infusible and insoluble in common solvents black powder [28].

Polythiophene and its derivatives can be synthesised electrochemically and chemically. Chemical synthesis methods, especially those based on catalytic coupling, allow to obtain



polythiophene with regular 2,5 ( $\alpha$ ) couplings between thiophene units, while electrochemical polymerization may result in mixture of 2,5 ( $\alpha$ ) and 2,4 ( $\beta$ ) couplings –disturbing the structural regularity of the polymer backbone and disrupting the  $\pi$ -conjugation along the chain (Fig. 1.3) [32].

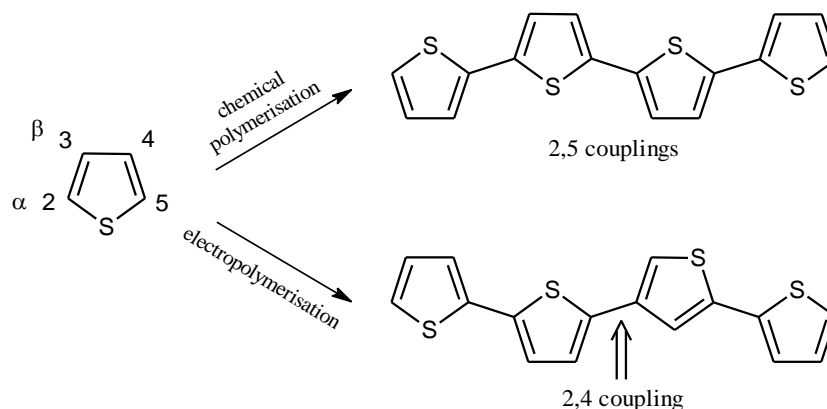


Fig. 1.3 Types of thiophene rings couplings in polythiophene

Regular, defined, 2,5-coupled polythiophene was chemically synthesized for the first time by coupling thiophene Grignard compounds on transition metal catalysts in 1980 (Fig. 1.4). T. Yamamoto et al. used Ni complex with 2,2'-bipyridine [30], whereas J. Lin et al. used Ni complex with acetylacetonate [34]. In general Ni-based catalysts turned out to be the most efficient in synthesis of polythiophene. Polythiophene gained interest because it exhibits high thermal and environmental stability and quite high conductivity when doped with iodine (0,1 S/cm and 6 S/cm for polythiophene annealed in 900°C for 5-15 min), however, due to strong interactions between the polymer chains ( $\pi$ -stacking), it is insoluble and thus difficult to process [34].

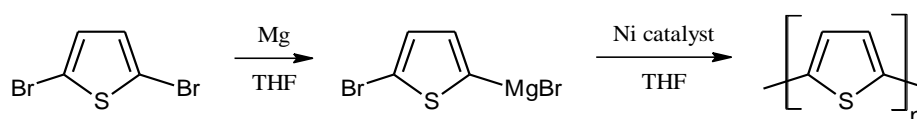


Fig. 1.4 Scheme of synthetic route of Ni-catalysed polymerization of 2,5-dibromothiophene; Ni catalyst: Ni(bpy)Cl<sub>2</sub> [30] or Ni(acac)<sub>2</sub> [34]

There are distinct differences in optical and electric properties between polythiophenes containing only 2,5 couplings (poly(thiophene-2,5-diyl)) and only 2,4 couplings (poly(thiophene-2,4-diyl)) [35]. Electric conductivity of neutral poly(thiophene-2,4-diyl) ( $5 \cdot 10^{-13}$  S/cm) is a little bit lower than the conductivity of neutral poly(thiophene-2,5-diyl) ( $5 \cdot 10^{-11}$  S/cm); upon doping with I<sub>2</sub> conductivity of poly(thiophene-2,5-diyl) increases 9

orders of magnitude (to  $4 \cdot 10^{-2}$  S/cm), whereas conductivity of poly(thiophene-2,4-diyl) changes just slightly (to  $7 \cdot 10^{-11}$  S/cm). Next, poly(thiophene-2,5-diyl) shows bathochromic shift of  $\pi$ - $\pi^*$  absorption band in UV-Vis range (410 nm) compared to poly(thiophene-2,4-diyl) (280 nm) and thiophene (230 nm). Also, exposed to UV light (356 or 253.7 nm) poly(thiophene-2,5-diyl) fluoresces a green colour, but poly(thiophene-2,4-diyl) shows no fluorescence. All above observations suggest that  $\pi$ -electrons in poly(thiophene-2,5-diyl) are extensively delocalised, but in poly(thiophene-2,4-diyl) are not – due to the existence of resonance structures in the former and lack of such structures in the latter as shown in Fig. 1.5. Indeed, 2,4 couplings disrupt delocalisation of  $\pi$ -electrons along polythiophene backbone, as can be seen from changes in UV-Vis spectra and  $I_2$  absorption characteristics for series of oligothiophenes with various ratio of 2,5 and 2,4 couplings [36]. Decreasing content of 2,4 couplings causes bathochromic shift of  $\lambda_{\max}$  (narrowing the optical band gap) and facilitates absorption of iodine vapours implying increasing  $\pi$ -conjugation length with increasing 2,5 couplings content. On the other hand, increasing content of 2,5 couplings promotes structural ordering and lowers solubility of the material.

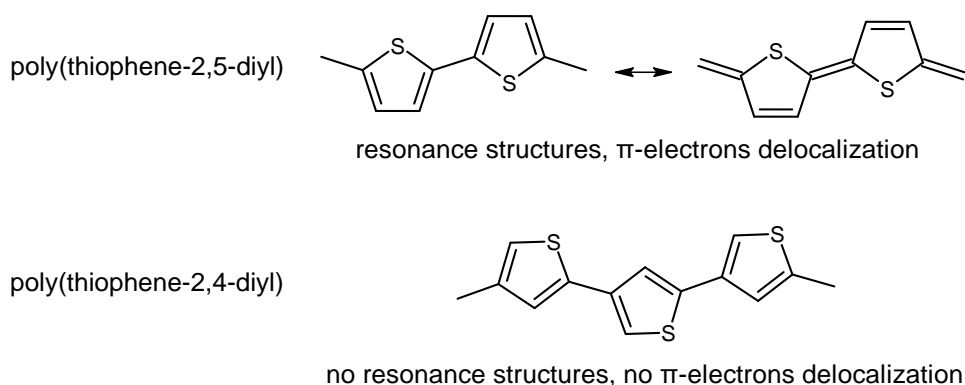


Fig. 1.5 Structural difference between poly(thiophene-2,5-diyl) and poly(thiophene-2,4-diyl)

## 2 Poly(3-alkylthiophenes) - processable derivatives of polythiophene

The main interest in the commercial use of conductive polymers is low-cost devices production using solution processing of film-forming polymers.

The solution to the problem of processability of polythiophene was introduction to the structure alkyl chains as side groups promoting solubility in organic solvents and enabling the processing of polythiophene alkyl derivatives from solution. First, during the studies on optimization of obtaining polythiophene by T. Yamamoto, it was figured out that poly(3-methylthiophene) synthesised from 3-methyl-2,5-dibromothiophene on Ni catalyst yielded

higher molecular weight ( $M_n$  determined by vapor pressure osmometry: 2,300 vs. 1,370) and was more soluble in  $\text{CHCl}_3$  than parent polythiophene [37]. Later, set of polyalkylthiophenes with *n*-alkyl chains in the 3-position (methyl, ethyl, *n*-butyl and *n*-octyl groups) were synthesized by R.L. Elsenbaumer et al. in 1986 [38,39] using Grignard compounds obtained from 2,5-diiodo-3-alkylthiophenes as monomers and polymerized on a nickel catalyst ( $\text{Ni}(\text{dppp})\text{Cl}_2$ ), as done by M. Kobayashi for polythiophene [40]. The molecular weights of products, determined by end group analysis, were about 2,500. Poly(3-alkylthiophenes) (P3ATs) with alkyl substituents consisting of 4 or more carbon atoms (butyl group and longer) in undoped form are well soluble in solvents such as tetrahydrofuran (THF), 2-methyltetrahydrofuran (2MTHF), nitromethane, nitropropane, dimethylformamide (DMF), toluene, xylene, dichloromethane (DCM), anisole, nitrobenzene, benzonitrile, and the solubility increases with increasing length of an alkyl substituent [38,39].

## 2.1 Regioregularity of poly(3-alkylthiophenes)

The introduction of a substituent at the 3 position of the thiophene ring causes asymmetry of the monomer, and during polymerization the asymmetric monomers can link together in 3 ways to give 3 regioisomeric dyads: the 2,5 link is a head-to-tail type coupling (HT), the 2,2 link is a head-to-head type coupling (HH), and the 5,5 link is a tail-to-tail type coupling (TT). Going further, attaching one more monomer molecule to the dyad gives a triad, occurring in one of the 4 possible configurations, etc. The structure of dyads and triads are shown in Fig. 2.1. P3ATs synthesized by methods that do not provide regioisomeric control contain units coupled in all possible ways [41]. Head-to-tail linkage of the monomers

is desirable because it provides planar structure of the polythiophene backbone, as opposed to head-to-head connections (considered as a structure defect). HH defects cause out-of-plane twisting of adjacent thiophene rings in polymer backbone due to the steric hindrance created by alkyl side groups in HT-HH couplings (Fig. 2.2) and the disruption of the  $\pi$ -conjugation along the polymer backbone. High regioregularity of P3AT ensures planar arrangement of the polymeric chains which leads to the self-organization of the P3AT in three dimensions and hence to the formation of conductivity pathways along the polymer chains as well as intermolecular ones, leading to a highly conductive material [42].

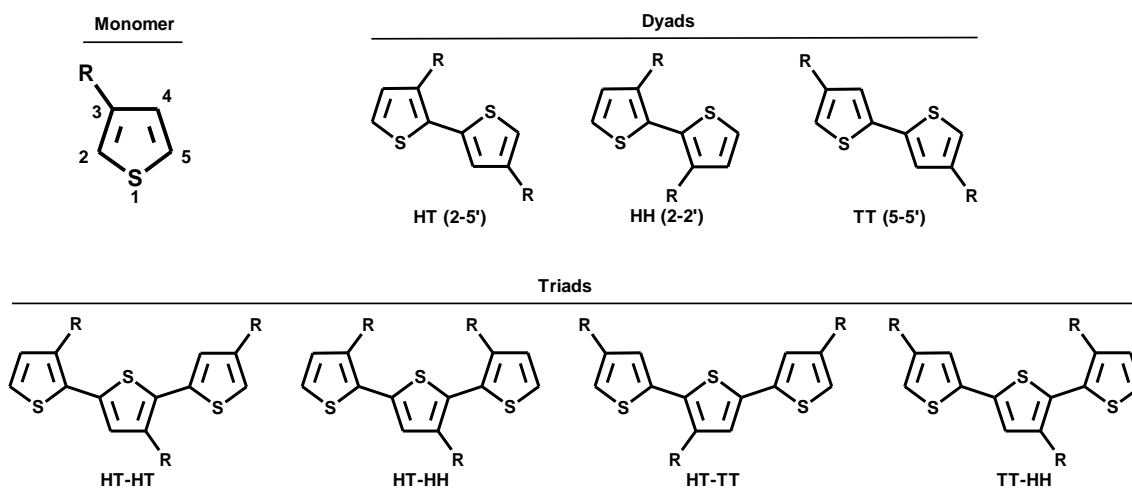


Fig. 2.1 Numbering of atoms in the thiophene ring and the configurations of the regioisomeric couplings of the thiophene rings: dyads: 2,5 - head-to-tail (HT); 2,2 - head-to-head (HH); 5,5 - tail-to-tail (TT) and triads resulting from the combination of two dyads

Degree of regioregularity of P3ATs is usually expressed as percentage of HT connections statistically occurring in polymer chain, e.g. 80% HT-P3AT indicates that 8 out of 10 linkages between thiophene rings are head-to-tail connections, whereas the remaining 2 are different types (head-to-head or tail-to-tail). P3ATs with high HT content (95-100%) are denoted as regioregular (RR), while P3ATs with lower HT content are denoted as regioirregular or nonregular (NR) P3ATs. P3ATs with random couplings are denoted as regiorandom (RN). Most polymerization protocols involving 3-substituted thiophene derivatives, even the ones not ensuring high regiocontrol (such as oxidative polymerization), favour HT couplings between the monomers during polymerization process, due to the steric

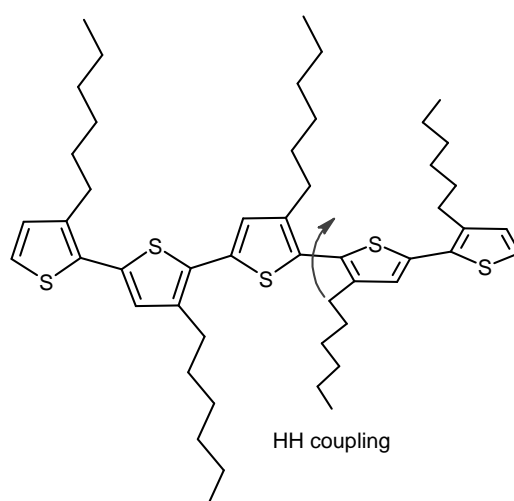


Fig. 2.2 Out-of-plane deformation of the P3HT chain due to the structure defect (HH connection)

hindrance of the substituents in HH couplings. This results in at least 50-80% of regioregularity in “irregular” P3ATs [43], typically 60-88% in P3ATs synthesised by oxidative coupling methods [44]. For high regioregularities (at least 95%, preferably >98-99%, ensuring high coplanarity of thiophene rings and desirable electronic properties, charge mobilities and conductivities) application of regioselective catalytic procedures is required.

Among P3ATs, poly(3-hexylthiophene) (P3HT) has become model species – with linear hydrocarbon side chain made of six carbon atoms granting good solubility in common solvents, self-assembling properties in thin films and relatively inexpensive production.

Two important factors contribute to conductivity of the material: the number of charge carriers (negative electrons or positive holes) and carrier mobility (how easy and fast carriers can move through the material). In conducting polymers number of charge carriers is relatively high, higher than in inorganic semiconductors, but charge transport is limited by the most difficult intermolecular hopping process. Since solution processing of conjugated polymers into thin layers promotes self-organisation of macromolecules into complex microstructures, it results in films in which ordered microcrystalline domains are incorporated in an amorphous matrix. Charge transport in conducting polymer lattice is restricted by crossing disordered matrix, which is well illustrated by the following example: carrier mobility in NR P3HT is 4 orders of magnitude lower ( $10^{-5} \text{ cm}^2 \text{ V}^{-1} \text{ s}^{-1}$ ) than in RRr P3HT ( $0.1 \text{ cm}^2 \text{ V}^{-1} \text{ s}^{-1}$ ) [45]. To achieve high conductivity, carrier mobility has to be improved by elimination of structure defects. Defect-free structure promotes high order and orientation of polymer chains.

Controlling the self-organization and electronic properties of molecular and macromolecular systems on surfaces is among the most challenging quests of organic electronics. It is a crucial need to determine the precise relationship between structural organization at molecular scale and electronic properties. P3HT self-organises into lamellar structures with two-dimensional conjugated sheets composed of folded by interchain stacking polymer chains [46–48] (Fig. 2.3). Degree of crystallinity and charge transport in P3HT films increase with increasing molecular weight [49]. Molecular weight and degree of regioregularity influence orientation of crystallographic planes with respect to substrate: P3HT of regioregularity > 91% and low molecular weight tends to stack with (100) axis perpendicular to substrate and (010) axis in plane of the substrate, whereas P3HT of lower regioregularity (81%) and very high molecular weight tends to stack with (010) axis normal to substrate and (100) axis in plane of the film upon deposition by spin coating [45].

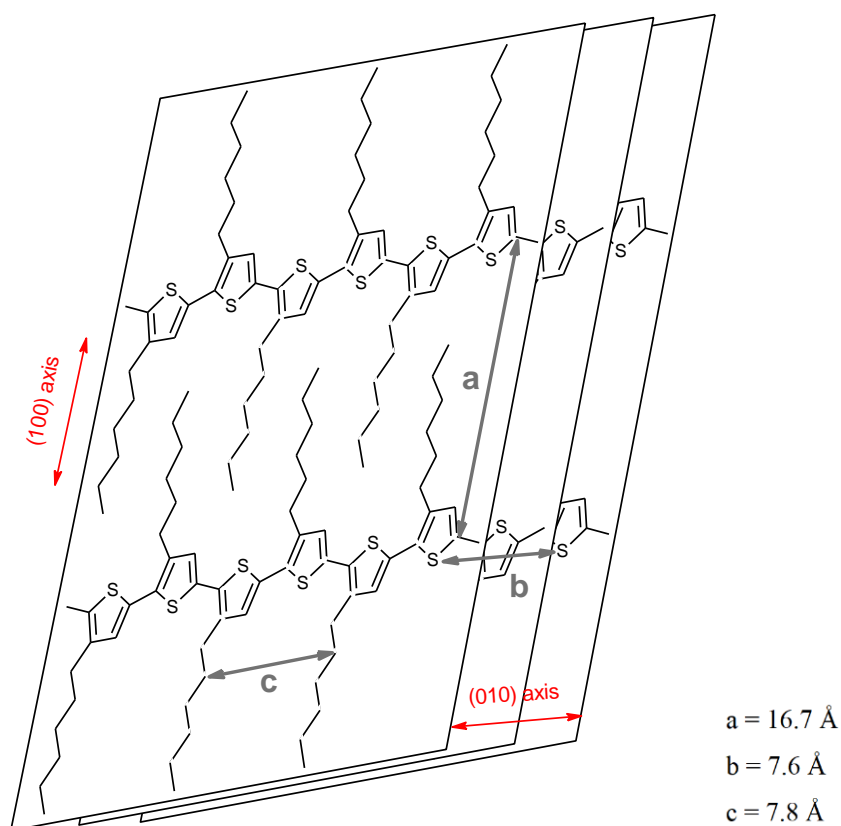


Fig. 2.3 Crystal structure of P3HT

Since mid 1980s protocols for obtaining poly(3-alkylthiophene)s via chemical synthesis are under constant development, mainly focused on obtaining P3ATs with high degree of regioregularity. Hereby literature survey of synthetic pathways leading to P3ATs with HT couplings content exceeding 95% is presented. Synthetic routes can be roughly divided into two groups: based on treatment with oxidizing agents and based on catalytic coupling with transition metals complexes.

Synthetic paths for highly regioregular P3ATs are based on transition metals catalysed cross coupling, including numerous protocols using Ni or Pd catalysts, submitted in Tab. 2.1. First successful syntheses of regioregular P3ATs (content of HT couplings exceeding 90%) were reported in 1992 independently by two research groups. R.D. McCullough's group developed methodology based on Kumada coupling of organomagnesium compound. It involved selective lithiation of 2-bromo-3-alkylthiophene in 5 position of thiophene ring with lithium diisopropylamide (LDA), generated *in situ* from diisopropylamine in reaction with *n*-butyllithium, in low temperatures (-78 to -40°C, requiring use of cooling bath, e.g. dry ice/acetone), followed by transmetalation with magnesium bromide diethyl etherate (MgBr<sub>2</sub>·Et<sub>2</sub>O) and *in situ* polymerization of resulting 2-bromo-5-bromomagnesium-3-alkylthiophene with Ni(dppp)Cl<sub>2</sub> catalyst to give poly(3-dodecylthiophene) with

regioregularity of 91% [50], later improved to 98-99% for poly(3-hexylthiophene) [51]. Regioregularity was provided mostly by regiospecific lithiation and transmetalation to Grignard species. In the same year Chen and Rieke reported method based on Negishi coupling of organozinc species [55]. Treatment of 2,5-dibromo-3-alkylthiophenes with reactive Rieke zinc ( $Zn^*$ ) yielded a mixture of two isomers: 2-bromo-5-bromozincio-3-alkylthiophene and 2-bromozincio-5-bromo-3-alkylthiophene in 90:10 molar ratio for reaction conducted for 1 h in room temperature, and up to 98:2 molar ratio for reaction conducted for 4 h in  $-78^\circ C$ . Alternatively, 2-bromo-5-iodo-3-alkylthiophene was used as monomer, which resulted in exclusive formation of 2-bromo-5-iodozincio-3-alkylthiophene. Subsequent *in situ* polymerization of obtained mixture in all cases resulted in PATs with  $\geq 98.5\%$  HT couplings content [56].

Another procedure for obtaining regioregular P3ATs involved Stille coupling of organotin compound. Starting monomer was 2-iodo-3-hexylthiophene, which was lithiated with LDA and transformed to 2-iodo-3-hexyl-5-tri-*n*-butylstannylthiophene. Obtained organotin derivative, after isolation, was polymerized in the presence of  $Pd(PPh_3)_4$  catalyst to give telechelic P3HT with tri-*n*-butylstannyl end group able to further polymerize or be used in synthesis of block copolymers [57]. Method based on Suzuki coupling polymerization of thienylboronic esters catalysed with palladium catalyst in the presence of various bases was also developed [58,59]. It involved lithiation of 2-halo-3-hexylthiophene in 5 position in the initial step as well. Polymerization in conditions adapted from synthesis of poly(*p*-phenylene), in the presence of CsF and crown ether in THF solution, afforded P3ATs with regioregularities reaching  $>99\%$  [60].

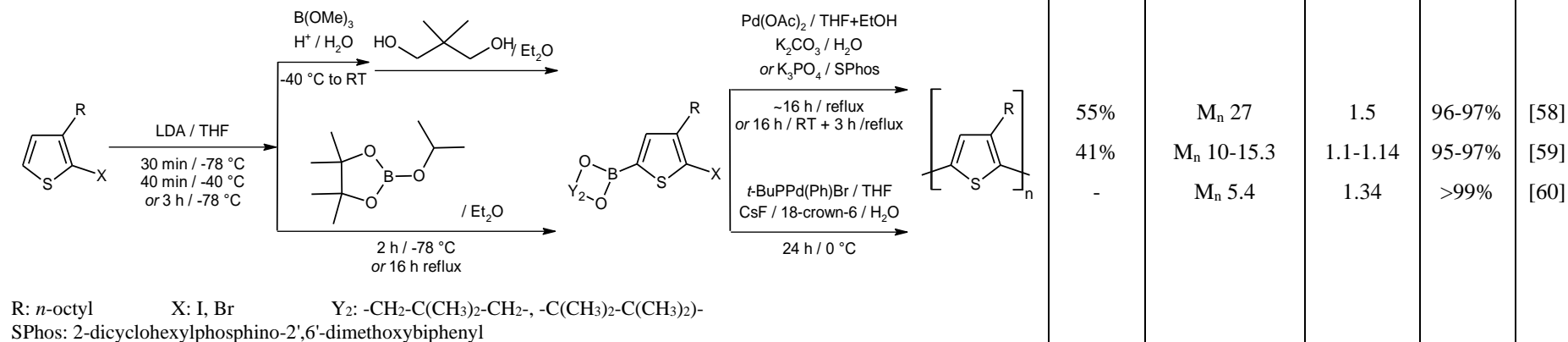
In 1999 R.D. McCullough's group developed improved protocol for synthesis of regioregular P3ATs, named Grignard metathesis method (GRIM), in which 2,5-dibromo-3-alkylthiophenes as starting monomers are transformed into Grignard species and *in situ* polymerized with  $Ni(dppp)Cl_2$  catalyst to yield  $\geq 99\%$  HT P3ATs [61]. Initial step involves exchange of one bromine atom for halomagnesium (Grignard) group in metathesis reaction with 1 equivalent of  $R'MgX$  compound, where  $R'$  can be alkyl or vinyl group, and X can be Br or Cl. Temperature range for metathesis can be from as low as  $-40^\circ C$ , through room temperature, to solvent (THF) reflux – typically reflux is applied to ensure fast exchange rate. In all cases (regardless of metathesis temperature or Grignard reagent employed) distribution of regiochemical isomers obtained was about 85:15, favouring formation of sterically less crowded 2-halomagnesium-5-bromo-3-alkylthiophene derivative. High regioregularity rates

Tab. 2.1 Synthetic routes to regioregular poly(3-alkylthiophenes)

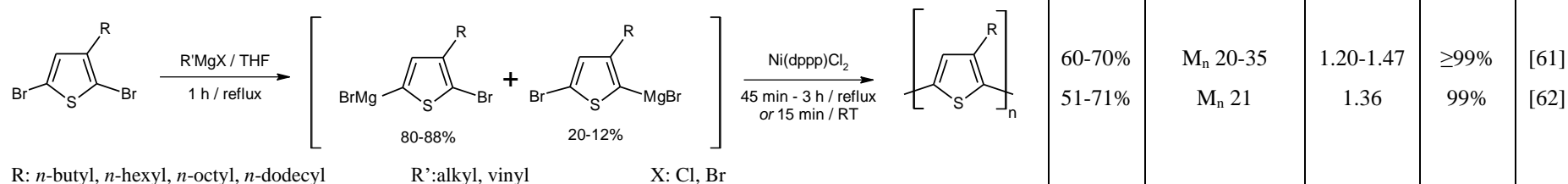
Method	Yield	Molecular weight · 10 <sup>-3</sup>	$\bar{M}_n$	HT content	Ref.
<b>Kumada coupling (McCullough method)</b>					
<p>R: <i>n</i>-butyl, <i>n</i>-hexyl, <i>n</i>-octyl, <i>n</i>-dodecyl</p>	20-69%	$M_w$ 11.6	-	91%	[50]
	33-69%	$M_w$ 10	1.6	93-98%	[51]
	33-69%	$M_w$ 9.2	1.6	93-96%	[52]
	44-69%	$M_n$ 21-40	1.4-1.5	93-99%	[53]
	37%	$M_n$ 16.8-17.9	1.23-1.28	>98%	[54]
<b>Negishi coupling (Rieke method)</b>					
<p>X: Br, I R: <i>n</i>-butyl, <i>n</i>-hexyl, <i>n</i>-octyl, <i>n</i>-decyl, <i>n</i>-dodecyl, <i>n</i>-tetradecyl</p>	-	$M_w$ 15	-	98.5%	[55]
	67-82%	$M_n$ 25.5-34.65	1.13-1.48	98.5%	[56]
<b>Stille coupling</b>					
<p>R: <i>n</i>-hexyl Solvent for polymerization: toluene, CH<sub>2</sub>ClCH<sub>2</sub>Cl</p>	50-54%	$M_n$ 11.5-16.1	1.22-1.44	>96%	[57]



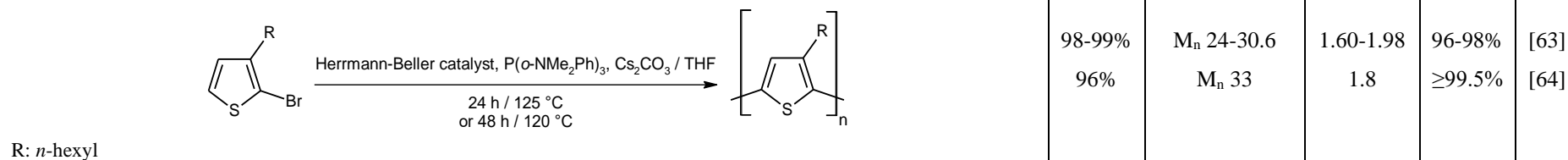
## Suzuki coupling



## Kumada coupling (GRIM method)



## Direct (hetero)arylation polymerization (DHAP)



are then ensured by catalyst selectivity in polymerization step. Polymerization temperature may be also varied – initially THF reflux temperature was applied, but later work showed that polymerization carried out at room temperature resulted in better uniformity of end group types [62].

Recently emerging technique is direct (hetero)arylation polymerization (DHAP, sometimes also abbreviated DARP – direct arylation polymerization), based on formation of C-C bonds between heteroarenes and heteroaryl halides by means of Heck-like coupling. Its use for synthesis of poly(3-alkylthiophene) was reported for the first time in 1999 by M. Lemaire's group. Starting monomer was 2-iodo-3-octylthiophene which was polymerized in one step reaction with catalytic amounts of palladium(II) acetate ( $\text{Pd}(\text{OAc})_2$ ), equimolar quantity of tetra-*n*-butylammonium bromide (*n*- $\text{Bu}_4\text{NBr}$ ) and excess of  $\text{K}_2\text{CO}_3$  (base) in DMF at  $80^\circ\text{C}$  (48 h) [65]. Obtained product had rather low molecular weight (degree of polymerization = 15), but protocol seemed promising. It was later advanced by Ozawa's group: use of Herrmann-Beller catalyst precursor (*trans*-di( $\mu$ -acetato)bis[*o*-(di-*o*-tolylphosphino)benzyl]dipalladium(II)), tris(*o*-*N,N*-dimethylaniline)-phosphine ( $\text{P}(\text{o-NMe}_2\text{Ph})_3$ ) as a ligand,  $\text{Cs}_2\text{CO}_3$  as a base, and reaction conducted in overheated THF ( $125^\circ\text{C}$ ) for 24 h resulted in 98% HT P3HT ( $M_n$  30.6 kDa,  $D_M$  1.6) [63].

In summary, most of the abovementioned methods have some advantages and drawbacks over the others. Rieke method doesn't require lithiation step, is one-pot protocol, provides relatively high yields compared to other early developed methodologies and high regioselectivities of forming organozinc species, but demands cryogenic conditions or 2-bromo-5-iodo-3-hexylthiophene starting monomer, which requires extra step of synthesis. Also, requires preparation of fresh  $\text{Zn}^*$  catalyst via alkali metal reduction of zinc halides or purchase of quite expensive commercially available reagent. Stille and Suzuki coupling are superior methods when it comes to the synthesis of polythiophene derivatives with reactive functional groups hindering polymerization based on reactive organozinc or organomagnesium species (such as hydroxyl or carbonyl groups). On the other hand, both of them proceed via lithiation initial step, which requires cryogenic conditions and both require isolation and purification of intermediate compounds – organotin or organoboron species, respectively. Additionally, Stille method uses and generates as byproduct stoichiometric amount of highly-toxic organotin compound. DHAP seems attractive since it is one step reaction with very high yields and regioregularity, and is eco-friendly (no toxic byproducts, minimum amount of waste), but it requires quite sophisticated catalytic system and long

reaction times in superheated solvent. GRIM method seems advantageous for lab scale synthesis, since it is one pot protocol, all steps are conducted at mild conditions (room temperature or THF reflux), it uses commercially available, affordable Grignard reagents and relatively cheap catalyst. Regioregularities of obtained P3ATs are very high, dispersities relatively low and polymerization times are short, compared to other methods. For GRIM, as well as for Rieke method, starting materials are 2,5-dibromo- derivatives of thiophene, which are easy to synthesise and purify (as highest boiling fraction in post-reaction mixture). Alternatively, they can be purchased as commercially available and not expensive. Moreover, GRIM protocol allows for very convenient *in situ* end group functionalisation, which is important for preparation of end-capped P3ATs able to be attached to other macromolecules to obtain copolymers.

Taking into account considerations outlined above, GRIM method was chosen for synthesis of regioregular poly(3-hexylthiophene) in this work, as it seems the most versatile and adaptable technique [66]. Poly(3-hexylthiophene), thoroughly investigated and well established conducting polymer benchmark, easily synthesised from commercially available monomer 2,5-dibromo-3-hexylthiophene, much cheaper than others with homologous alkyl side chain, was chosen as a model P3AT in this work.

## 2.2 Mechanism of GRIM synthesis of poly(3-alkylthiophenes)

In general, catalytic cycle of transition-metal-catalysed cross-coupling reactions involves three steps: I. oxidative addition of a low-valent transition metal complex (catalyst) to the electrophilic centre of the molecule, II. reaction of the resultant organometallic complex with nucleophile (such as metalated organic compound) generating diorganometallic complex (with two carbon centres) – transmetalation, III. reductive elimination of the product bearing newly formed C-C bond and regeneration of the catalyst [67].

At the beginning of the study on nickel-catalysed polymerization of poly-3-alkylthiophenes it was assumed that it proceeds via step-growth mechanism, as typical polycondensation reaction, especially that early synthesized P3ATs had high dispersities and uncontrolled molecular weights. In 2004 two groups: T. Yokozawa's [68] and R.D. McCullough's [69] published results suggesting that Ni(dppp)Cl<sub>2</sub>-catalysed Kumada coupling polymerization of 2-bromo-5-chloromagnesio-3-hexylthiophene or 2-bromo-5-

chlorozincio-3-hexylthiophene proceeds according to chain-growth manner. Both groups reported that  $M_n$  of the polymer increased in linear fashion with the conversion of the monomer, high monomer conversions were achieved fast (reaching 90% in 2 hours at room temperature),  $M_n$  could be predicted based on the molar ratio of monomer to  $\text{Ni}(\text{dppp})\text{Cl}_2$  in the feed composition, and that constant (1.2-1.4)  $M_w/M_n$  ratio is maintained during the polymerization.

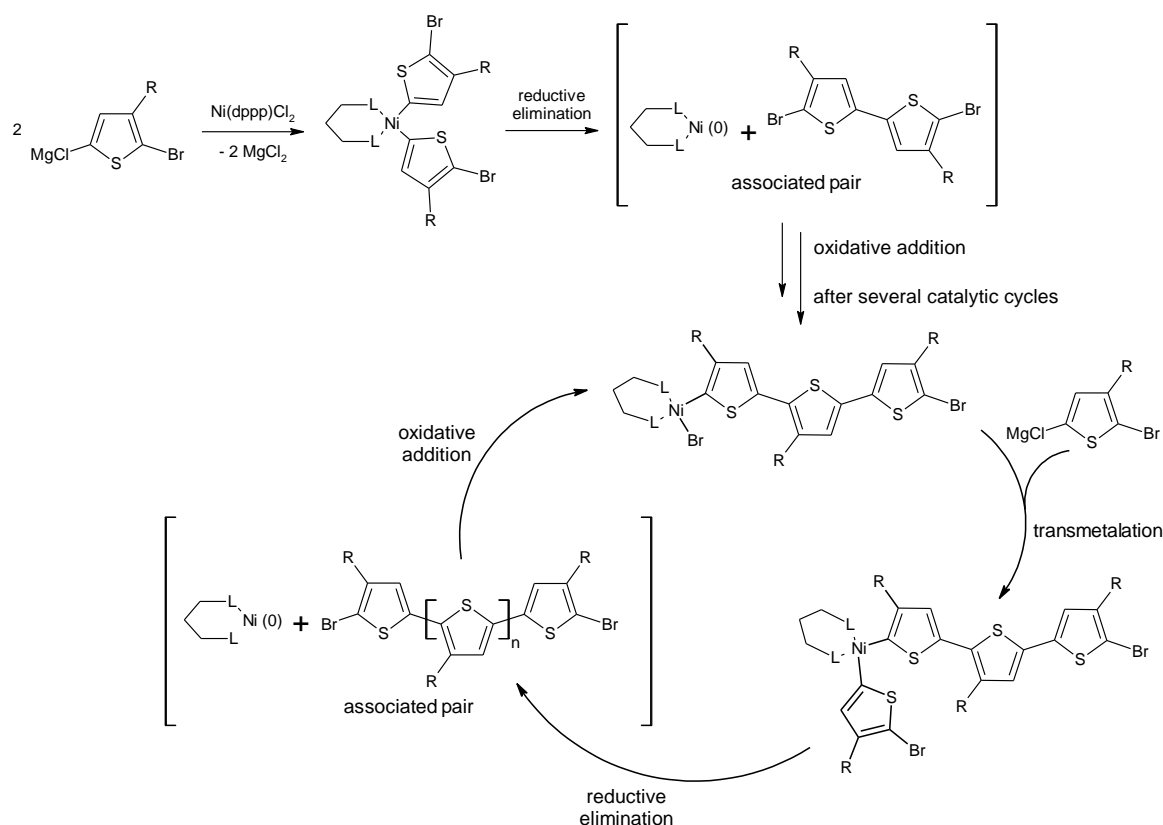


Fig. 2.4 Mechanism of Grignard Metathesis (GRIM) polymerization proposed by McCullough [69,70]; L:  $\text{PPh}_3$ , R: n-hexyl

R.D. McCullough proposed mechanism of catalytic cycle (Fig. 2.4) based on the assumption that  $\text{Ni}(0)$  complex forms nondiffusive  $\pi$ -complex with growing chain end [69,70]. According to this mechanism catalytic process follows the steps:

1. Initial reaction of 2 equivalents of 2-bromo-5-chloromagnesium-3-hexylthiophene (or 2-bromo-5-chlorozincio-3-hexylthiophene) generates bis(organo)nickel compound;
2. 5,5'-dibromothiényl (TT-coupled dimer) and  $\text{Ni}(0)$  complex are generated in reductive elimination step and the nickel complex forms associated pair with the dimer.  $\text{Ni}(\text{dppp})$  coordinates to thiophene ring in  $\eta^2$  or  $\eta^4$  manner [31];

3. Dimer undergoes fast oxidative addition to Ni(0) complex generating new organonickel compound;
4. Organomagnesium or organozinc monomer is bonded to catalyst's centre in the transmetalation step;
5. Reductive elimination with formation of associated pair of Ni(0)-2-bromopolythiophene and fast oxidative addition of the catalyst is repeated;
6. Polymer chain growth proceeds by insertion of one monomer molecule at a time and Ni(dppp) complex remains attached to the macromolecule as an end group.

In 2005 T. Yokozawa proposed mechanism of chain-growth GRIM polymerization called *catalyst transfer polycondensation* (later commonly named *Kumada catalyst transfer polycondensation*, KCTP, as proposed by A. Kiriy [71]), depicted in Fig. 2.5.

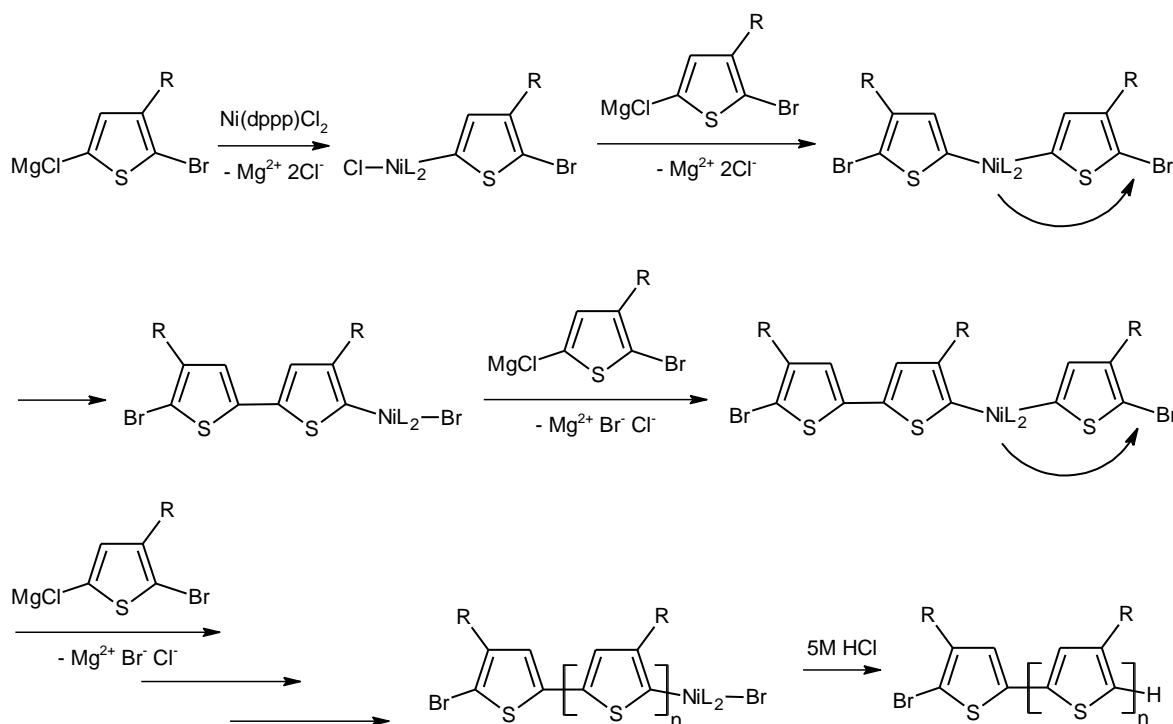


Fig. 2.5 Mechanism of Kumada catalyst transfer polycondensation (KCTP) proposed by Yokozawa [68];  $\text{NiL}_2$ : Ni(dppp), R: *n*-hexyl

In the first step of proposed mechanism transmetalation occurs, resulting in nickel complex bound to two thiophene units. Second step involves coupling between thiophene units followed by intramolecular transfer of Ni(0) complex across the thiophene to the terminal C-Br bond. Catalytic cycle continues with consecutive transmetalation and transfer of the catalyst to the terminal C-Br bond. Polymerization yields macromolecules with

uniform H/Br end groups after hydrolysis of terminal Ni(II) complex, which suggests that Ni catalyst does not detach from propagating polymer chain end during the process.

It was reported that nickel complex can diffuse from chain to chain during the course of polymerization reaction. However, that phenomenon only affects end groups composition, resulting in loss of chain end uniformity, but does not affect molecular weight control determined by catalyst to monomer ratio [72].

High regioregularities of P3AT synthesised by GRIM/KCTP method (>98%) are achieved, much higher than expected based on ratio of 5-chloromagnesio- to 2-chloromagnesio- Grignard derivatives of 3-alkylthiophene (about 85:15) in the initial mixture of monomers. It results from two factors: 1) steric hindrance posed by alkyl chains blocking formation of HH connections between alkylthiophene rings, and 2) stabilization of the growing Ni(II) catalyst-capped chain end by alkyl chains in *ortho* position, promoting oxidative addition of the catalyst to Br terminal adjacent to alkyl chain [73].

Regardless of differences in the details of proposed mechanisms, Ni-mediated GRIM/KCTP polymerization of poly(3-alkylthiophene)s should be qualified as condensative chain polymerization and Ni(dppp)Cl<sub>2</sub> act as initiator rather than a catalyst in the process, limiting polymerization to one end of the macromolecule. One TT defect is incorporated at the one end of every P3AT chain in case of both mechanisms.

GRIM/KCTP method is quasi-living reaction, with active chain end maintained throughout the procedure, as has been shown by the experiments with sequential addition of monomer feed in late stages of the polymerization resulting in the extension of polymer chain length [68] or obtaining poly(3-hexylthiophene)-*block*-poly-(3-dodecylthiophene) diblock copolymer [70].

### 2.3 Purification and fractionation of P3ATs

Crude PATs isolated by quenching reaction mixture in methanol contain impurities: byproduct inorganic salts, catalyst residues (salts, ligands), unreacted monomer and low molecular weight oligomers. Presence of such components, even in very small amounts can impair electronic and optical characteristics of P3ATs and performance of fabricated devices [74,75], so ensuring high purity of compounds for electronic and optoelectronic applications is a crucial demand.

Precipitation from solution in good solvent into methanol removes some impurities but is not enough to obtain suitable for electronic applications levels of purity. Sequential Soxhlet extraction provides facile method for purification and rough fractionation of P3ATs. Solubility of P3ATs in common organic solvents increase in the following sequence: acetone < hexane < dichloromethane < tetrahydrofuran < chloroform [76]. Commonly used procedure involves precipitation of crude polymer in methanol, filtration and sequential Soxhlet extraction with methanol (to remove inorganic salts and monomer), hexane (to remove catalyst and oligomers) and chloroform (to collect purified, soluble polymer) [61].

## 2.4 End group functionalisation of poly(3-alkylthiophene)s

In case of poly(3-alkylthiophenes) synthesised by McCullough, Rieke and GRIM methods, starting from most commonly used 2-bromo- or 2,5-dibromo-3-alkylthiophene monomers, there are three possible end group compositions: bromine atom at one end and hydrogen atom at the other end of polymer chain (denoted as Br/H termination), hydrogen atoms at both ends (H/H), and bromine atoms at both ends (Br/Br). According to the literature, Br/H end group composition prevails (reaching >95% for optimised reaction conditions) for GRIM and McCullough protocols, but H/H and Br/Br-terminated polymer chains are also present, as indicated by MALDI-TOF MS (matrix-assisted laser desorption/ionization time of flight mass spectrometry) analysis [70,77,78].

From the point of view of future modifications of the polymer and implementation of conducting polymers in more complex architectures it is desired to synthesise P3ATs bearing reactive end groups, capable of further polymerization or coupling with another polymeric segments, opening possibilities to obtain more sophisticated polymeric architectures, such as block or graft copolymers, or grafting P3ATs molecules onto surfaces. Chain termini functionalisation by attaching specific electroactive end groups may also extend the range of applications of parent conducting polymer [54,79]. Such possibility was explored for the first time by R.A.J. Janssen. He reported successful synthesis of P3HT terminated at one end with trimethylsilyl group in two approaches: by using Grignard agent, 5-trimethylsilyl-2-thienylmagnesium bromide, 1) for *in-situ* end-capping at the last step of the quasi-living polymerization; 2) for postpolymerization functionalisation by the reaction with Grignard species [79].

There are reports on postpolymerization modifications of H/Br-terminated, as well as H/H-terminated (obtained via debromination with Grignard agents) P3ATs. P3ATs mono- and bis-terminated with –CN, –NH<sub>2</sub>, –OH and –CHO groups were obtained, ready to be further modified in order to become building blocks in various copolymers [54,80]. However, this approach is multistep, and requires isolation and purification of the intermediate products.

On the other hand, one-pot protocol allowing *in situ* end groups modifications is usually the most convenient as time and resources saving. GRIM metathesis protocol with its quasi-living character enables obtaining P3ATs with variety of end groups by addition of end-capping Grignard reagents in one-pot reaction. P3ATs monocapped with vinyl, allyl, ethynyl and 4-aminophenyl groups as well as dicapped with phenyl, tolyl, benzyl, 4-hydroxyphenyl, 4-formylphenyl, methyl and butyl were reported (amine, phenol and aldehyde groups were introduced in protected form and deprotected after end-capping). Only functionalisation with bulky *t*-butyl group failed due to the steric hindrance reason [81,82]. *In situ* end group modification provides useful tool for unhindered, single-step synthesis of polymeric segments with tailor-made end groups suitable for further incorporation into copolymers. The only limitations are bulkiness of the moiety being incorporated as end group and tolerance for Grignard reagent, but in the latter case additional postpolymerization functionalisation/deprotection of end group step can be employed, as PATs are chemically robust, especially against reducing agents, such as 9-borabicyclo[3.3.1]nonane (9-BBN) [83] or LiAlH<sub>4</sub> [54].

### 3 Copolymers for electronic applications

Homopolymers are macromolecules derived from one monomer, whereas copolymers are macromolecules which are obtained by copolymerization of more than one species of monomer, and as such contain more than one type of repeating unit. Copolymers can have either random, statistical distribution of building units in the macromolecule or the components can be arranged in ordered, predictable manner, following distinguishable patterns. The latter include alternating, block and graft copolymers. (Fig. 3.1) [84].

Copolymers allow to combine properties of the components into one material with optimized characteristics, especially in case of block and graft copolymers, bearing significantly large segments of the individual constituents.



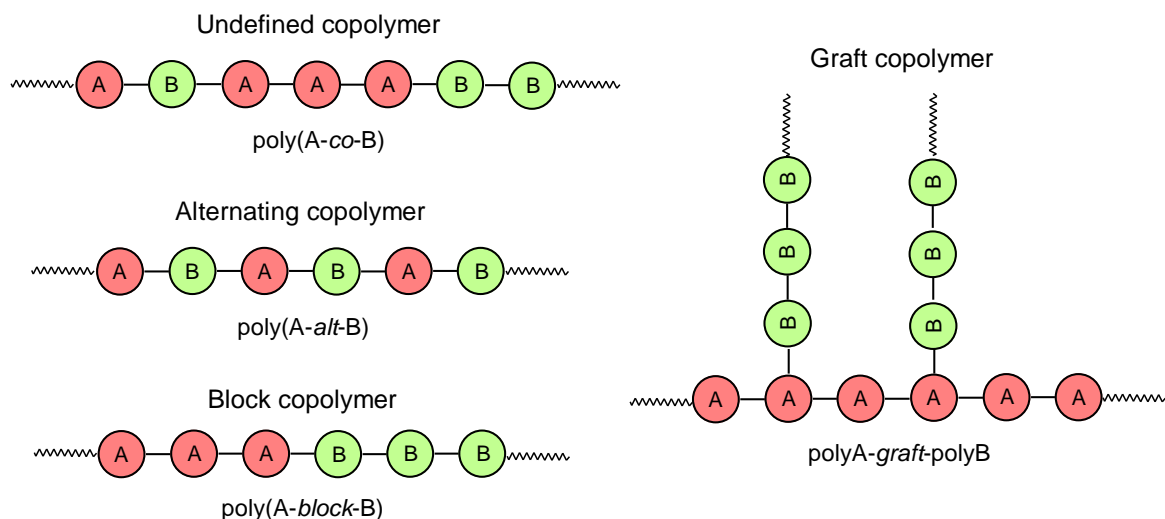


Fig. 3.1 Architectures of chosen copolymer macromolecules and their nomenclature

### 3.1 Graft copolymers

In graft copolymers individual building blocks are connected in nonlinear fashion. One block is the backbone (main chain), to which side chains, comprising building units structurally different from the backbone, are attached. Side chains usually are randomly distributed along the backbone.

In general, there are three synthetic approaches to obtain graft copolymers:

- “Grafting to” (also called “grafting onto”) procedure involves a reaction of a backbone chain bearing functional groups X statistically distributed along the macromolecule with side chains bearing reactive end group Y, capable of coupling with group X (Fig. 3.2 a);
- In “grafting from” method reactive sites, present or generated on the polymer backbone, initiate the polymerization of the monomer which will form side chains of the graft copolymer (Fig. 3.2 b);
- “Grafting through” (also denoted as macromonomer method) utilizes macromonomers, which are oligomeric or polymeric chains ended with group able to polymerize. Macromonomers, constituting future side chains, polymerize alongside with the monomer which forms backbone of the graft copolymer (Fig. 3.2 c).

A special type of regular, well-defined graft copolymers are macromolecules obtained by homopolymerization of macromonomers, without addition of second monomer, where every repeating unit bears side chain. That results in closely packed, stiff structure with bottlebrush conformation [85].

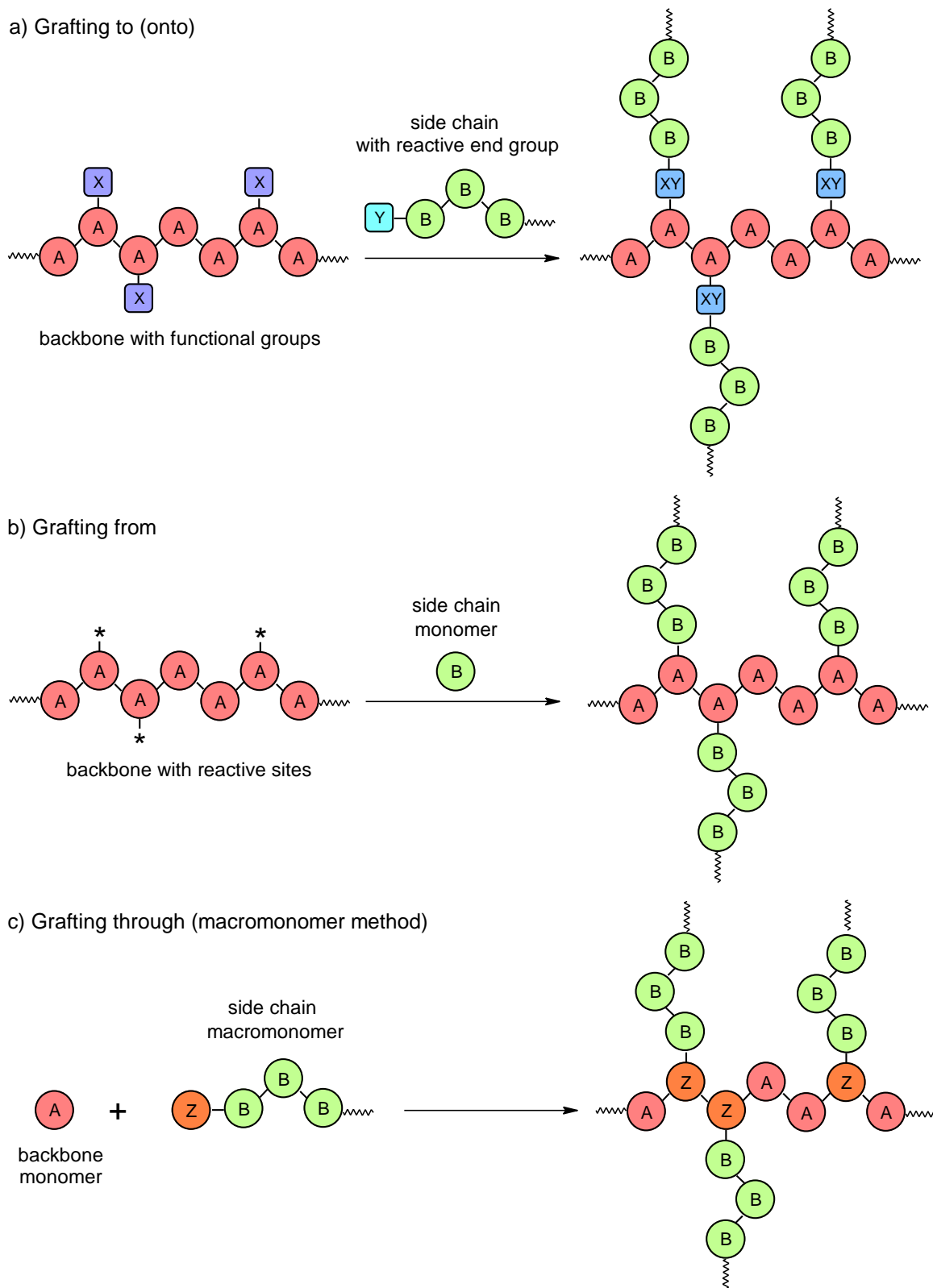


Fig. 3.2 General approaches to the synthesis of graft copolymers

Design resulting in graft copolymers is utilized to modify properties of the parent segment in case to implement unique mechanical, thermal, dilute solution, melt properties and morphology. Graft copolymers are used as compatibilizing agent to improve mixing

properties of polymers forming immiscible blends. For example, nanoparticles made of graft copolymers able to form micelles can be applied as drug carriers for controlled drug delivery systems and for wastewater treatment [85].

### 3.2 Polysiloxanes

Organosilicon compounds are characterised by the presence of carbon-silicon bonds in the structure, which makes them organic-inorganic hybrid material. Among the organosilicon polymers polysiloxanes (silicones) (schematic structure depicted in Fig. 3.3 a) pose the largest and the most widely explored group.

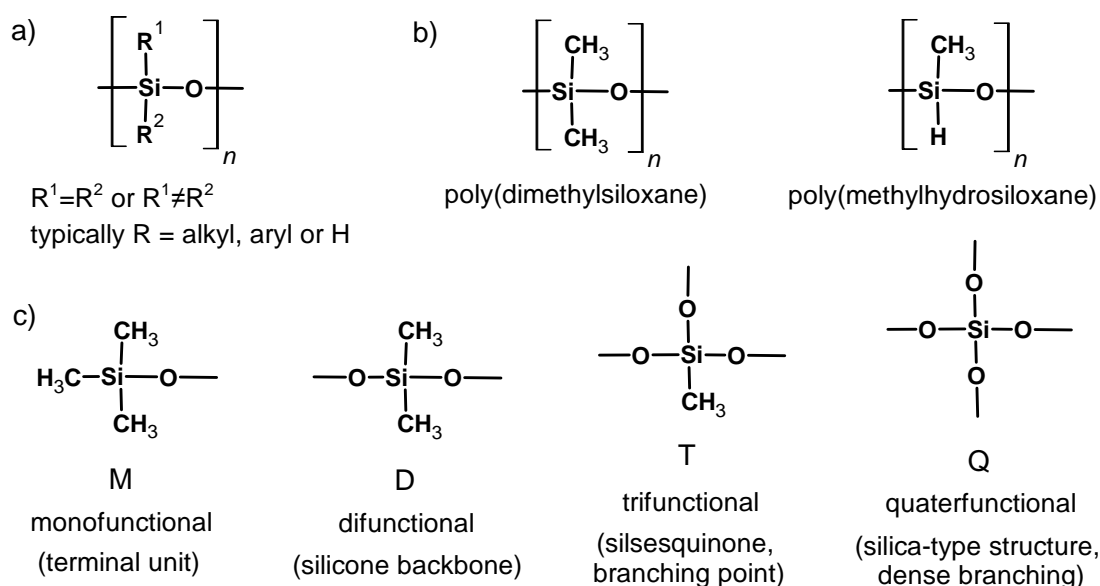


Fig. 3.3 Schematic structure of polysiloxane (a); polysiloxanes: poly(dimethylsiloxane) and poly(methylhydrosiloxane) (b); structural units distinguished based on functionality (c)

Polysiloxane backbones are made of alternating silicon and oxygen atoms connected via Si-O bonds, setting flexible and thermally stable backbone, with various organic moieties attached, usually alkyl (typically methyl) or aryl (typically phenyl) groups, or hydrogen, introducing hydrocarbon-like character [86]. Structural units in polysiloxanes can be described by denoting number of oxygen atoms attached to the addressed silicon atom (monofunctional – M; difunctional – D; trifunctional – T; and quaterfunctional – Q, see Fig. 3.3 c). When this notation is used  $R^1=R^2$ =methyl, unless specified otherwise. Monofunctional units are trimethylsilyl chain end-groups or protecting groups. Difunctional groups contribute to backbone of linear polysiloxanes (silicone fluids, liquid for low molecular weights, or solid for high molecular weights). In silicone elastomers additional trifunctional groups (branching

points) are present besides difunctional units. Quaterfunctional units may occur in highly crosslinked silicone resins or create a core for 3D architectures such as star polymers.

Polysiloxanes in which  $R^1=R^2=CH_3$  (poly(dimethylsiloxanes), PDMS) demonstrate a range of industrially desired properties such as greater flexibility at low temperature and stability at high temperature, greater resistance to UV radiation and weather conditions than organic polymers, and besides that feature: low viscosity, distinctive surface-active behaviour, including low surface tension and high spreading power, inertness, hydrophobicity, as well as low temperature dependence of their physical properties, good damping behaviour, antifriction, lubricity and physiological inertness. The most important industrial silicones are representatives of linear poly(dimethylsiloxanes) (Fig. 3.3 b). Unique flexibility of poly(dimethylsiloxane) chains results from abnormally high angles of  $143^\circ$  in Si-O-Si bonds, which lowers rotational barrier around the Si-O bond (Fig. 3.4) [86]. Polysiloxanes feature low glass transition temperatures and melting points, weak intramolecular interactions and high chain mobility. These properties predispose them to use in production of rubbers and elastomers upon vulcanisation (curing) and reinforcement with silica. Curing via hydrosilylation – addition of C=C (vinyl group) to Si-H bond in the presence of platinum catalyst is often employed.

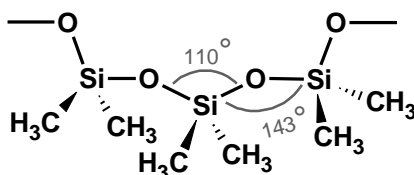


Fig. 3.4 Structural parameters of PDMS chain

Poly(methylhydrosiloxane) (Fig. 3.3 b), bearing reactive Si-H bonds may be used to obtain hyperbranched or densely crosslinked structures, and provides suitable backbone for graft and comb-like copolymers with various organic moieties: low molecular weight compounds, as well as oligomers and polymers [87]. It is also applied in organic synthesis as mild reducing agent [88].

Silicones find a wide range of industrial applications. Silicone fluids are applied as heat-transfer media in heating circuits, refrigerants in cryostats and freeze dryers, lubricants in electric motors and machine bearings, release agents in the processing of plastics and rubbers, additives in water-repellent polishes, waterproofing agents for textiles, protective coatings for construction materials, antifoams, antifatulent agents in medicine and

veterinary, dielectric coolants for transformers and rectifiers, power transmission fluids in viscous and fan couplings, hydraulic and damping fluids in shock absorbers and vibration insulation systems, embedding compounds for glass-fiber cables, absorbents for organic vapours of low water solubility, paint additives and additives for preparations of cosmetics. Silicone rubbers and elastomers are applied as wire insulation, anti-adhesive paper coatings and release liners, water-repellent textile coatings, various industrial, automotive, aviation and home-use seals and gaskets, encapsulation of modules in electronics, flexible casting forms, implants and membranes in medicine, and controlled drug release matrices. Silicone resins are applied as paint binders, impregnates for wall protection, and insulating varnishes for protection of electronic components from moisture and dust [89].

### 3.3 Hydrosilylation

Hydrosilylation (also called catalytic hydrosilylation) is one of the fundamental methods of synthesizing organosilicon compounds on laboratory and industrial scale. It involves addition of organic and inorganic silanes to double or triple bonds, most frequently in accordance with anti-Markovnikov rule. Most commonly, carbon-carbon and carbon-heteroatom bonds (carbon-oxygen, carbon-nitrogen), as well as heteroatom-heteroatom bonds (nitrogen-nitrogen, nitrogen-oxygen) react with Si-H bond, as shown in Fig. 3.5 [90].

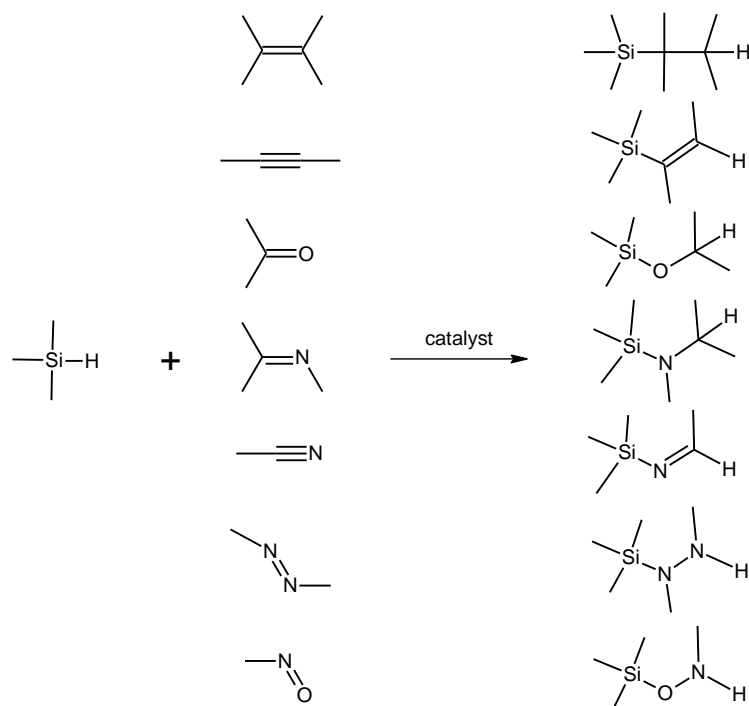


Fig. 3.5 Addition of silanes to double bonds

Hydrosilylation of unsaturated compounds can proceed either through the mechanism of homolytic addition in the presence of free radical initiators, or through heterolytic mechanism, catalysed by transition metal complexes, nucleophilic-electrophilic catalysts, or metals and supported metals [91]. Important moment in the history which fuelled development of this procedure for a wide scale was usage by J.L. Speier hexachloroplatinic acid as a very efficient homogeneous catalyst for hydrosilylation [92]. In 1973 B.D. Karstedt developed catalyst based on Pt(0) complexes containing vinyl-siloxane ligand, which exhibited better solubility in polysiloxane reaction system and much higher activity than Speier catalyst [93]. The most significant species among those complexes is denoted plainly as Karstedt catalyst (platinum(0)-1,1,3,3-tetramethyl-1,3-divinyldisiloxane complex, structure shown in Fig. 3.6), and represents the most versatile and universal catalyst for industrial hydrosilylation processes. Reaction is fast and takes place in mild conditions.

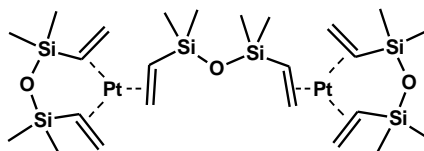


Fig. 3.6 Schematic structure of Karstedt catalyst

Hydrosilylation of olefins is a pivotal catalytic reaction used in the industrial production of organosilicon compounds, such as silanes and silicones coupled with organic segments. Furthermore, catalytic hydrosilylation is applied for crosslinking of silicone polymers to produce silicone-based elastomers and release coatings, as well as for the coupling silanes and silicones to organic polymers resulting in polysiloxane copolymers and silane-modified polymers, which may be applied as adhesive and sealing materials [94].

Transition metal-catalysed hydrosilylation of olefins is usually explained by Chalk-Harrod mechanism. It includes three basic steps: 1) oxidative addition of silane ( $R_3SiH$ ) to a metal-alkene complex, 2) migratory insertion of alkene into the M-H bond, and 3) reductive elimination with formation of Si-C bond to yield organosilane compound. Alternatively, modified Chalk-Harrod mechanism was also proposed (both mechanisms, with  $Pt^0$ - $Pt^{II}$  complex system as a catalyst, are shown in Fig. 3.7). Detailed theoretical investigation on the transition states and intermediates involved in both variants of mechanism concluded that  $Pt^0$ -catalysed hydrosilylation of ethylene proceeds via Chalk-Harrod mechanism [95], and this interpretation prevails in subject matter literature [91,94].

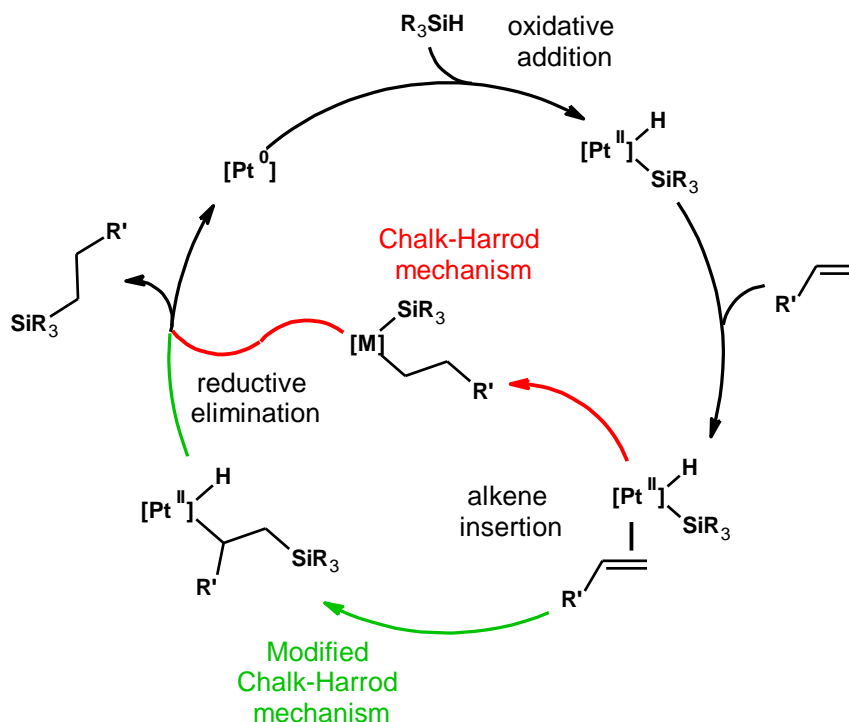


Fig. 3.7 Chalk-Harrod and modified Chalk-Harrod mechanism of platinum-catalysed hydrosilylation

As a result of hydrosilylation reaction between Si-H and C=C bonds two isomeric products are possible:  $\beta$ -adduct and  $\alpha$ -adduct (Fig. 3.8). Hydrosilylation of alkenes catalysed by transition metal catalysts might be also accompanied by side-reactions such as isomerization or dehydrogenative silylation. However,  $\beta$ -adducts are the major products in hydrosilylation reactions [87], especially when siloxanes are silylating agents in systems catalysed by platinum catalysts [96–98].

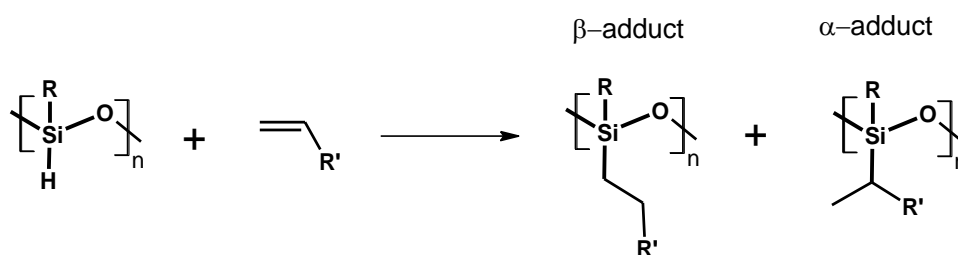


Fig. 3.8 Formation of  $\alpha$ - and  $\beta$ -adducts in hydrosilylation

### 3.4 Copolymers bearing regioregular poly(3-hexylthiophene) segment

In case of poly(3-hexylthiophene), like many other conducting polymer, the goal of copolymerization is to improve mechanical and processing properties, promote film forming

abilities, and to extent optoelectronic properties of the parent conjugated segment [80,99]. Moreover, RR P3HT features poor adhesion to metal electrode compared to high molecular weight NR P3HT [100], hence copolymerization with suitable segments may also target improvement of the adhesion to metal and other surfaces.

Synthesis of many block copolymers bearing regioregular P3HT and diversity of other blocks was reported in literature. In particular living polymerization techniques are readily implemented for this task, such as living anionic polymerization, ring opening cationic polymerization, atom transfer radical polymerization (ATRP), ring-opening metathesis polymerization (ROMP), reversible addition-fragmentation chain-transfer polymerization (RAFT) or nitroxide-mediated radical polymerization (NMP), as they allow to obtain well defined blocks of controlled length. Tab. 3.1 presents selection of diblock and triblock copolymers containing P3HT segment reported in the literature. To fabricate those copolymers either P3HT macroinitiator was end-functionalized by means of *in situ* protocol prior to copolymerization, or copolymerization itself was carried out *in situ*, in environment of GRIM polymerization.

Tab. 3.1 Selection of block copolymers containing RR P3HT segment

Copolymer	Block(s) attached to P3HT	Method used to attach polymer blocks*	Ref.
P3HT- <i>b</i> -PMA	Poly(methyl acrylate)	ATRP	[83]
P3HT- <i>b</i> - <i>Pt</i> BA	Poly( <i>t</i> -butyl acrylate)	ATRP	[83]
P3HT- <i>b</i> -PE	Polyethylene	ROMP	[108]
P3HT- <i>b</i> -PS	Polystyrene	ATRP	[101]
P3HT- <i>b</i> -PS	Polystyrene	RAFT	[102]
P3HT- <i>b</i> -PI	Polyisoprene	NMP	[102]
P3HT- <i>b</i> -PMMA	Poly(methyl methacrylate)	ATRP	[103]
P3HT- <i>b</i> - <i>Pt</i> BuMA	Poly( <i>t</i> -butyl methacrylate)	ATRP	[103]
P3HT- <i>b</i> -PIBMA	Poly(isobornyl methacrylate)	ATRP	[103]
P3HT- <i>b</i> -P2VP	Poly(2-vinyl pyridine)	Living anionic polymerization	[104]
P3HT- <i>b</i> -PAA	Poly(acrylic acid)	ATRP	[105]
PMMA- <i>b</i> -P3HT- <i>b</i> -PMMA	Poly(methyl methacrylate)	Living anionic polymerization	[106]
P3HT- <i>b</i> -THF	Poly(tetrahydrofuran)	Ring-opening cationic polymerization	[109]
P3HT- <i>b</i> -PEOXA	Poly(2-ethyl-2-oxazoline)	Ring-opening cationic polymerization	[110]



P3HT- <i>b</i> -PDMAEMA	Poly[2-(dimethylamino)ethyl methacrylate]	ATRP	[111]
P3HT- <i>b</i> -PEO	Poly(ethylene oxide)	“Click” reaction	[112]
P3HT- <i>b</i> -PPI	Poly(phenylisocyanide) [poly( <i>n</i> -decyl-4-isocyanobenzoate)]	GRIM	[113]
P3HT- <i>b</i> -P3EHT	Poly[3-(2-ethylhexyl)thiophene]	GRIM	[114]
P3HT- <i>b</i> -P3(TEG)T	Poly[3-(triethylene glycol)thiophene]	GRIM	[115]
P3HT- <i>b</i> -PDMS	Poly(dimethylsiloxane)	Living anionic polymerization	[107]
P3HT- <i>b</i> -PDMS	Poly(dimethylsiloxane)	Hydrosilylation	[98]

\* explanation of abbreviations: ATRP - atom transfer radical polymerization ROMP - ring-opening metathesis polymerization, RAFT - reversible addition-fragmentation chain-transfer polymerization, nitroxide-mediated radical polymerization (NMP), GRIM – Grignard metathesis polymerization

P3HT-*b*-PMA and P3HT-*b*-*Pt*BA block copolymers were found soluble in many solvents and formed solid films with very dense, uniform morphology, correlated well with the high conductivities of P3HT-*b*-PMA, comprising up to 52% of PMA, not much lower than parent P3HT [83]. On the other hand, attachment of polystyrene, polyisoprene and methacrylate blocks to P3HT resulted in substantial decrease of the conductivity, but allowed to maintain the nanowire morphology of parent P3HT in drop-casted films [101–103]. P3HT-*b*-P2VP diblock copolymers exhibited microphase separation and self-assembly into structures depending on the volume of PVP segment: spheres or disordered micelles for 14% weight fraction of P3HT, hexagonal close-packed cylinders for 25% wt P3HT, lamellae for 41% wt P3HT, nanofibers for 70% wt P3HT [104]. Amphiphilic diblock P3HT-*b*-PAA copolymer (72% mol P3HT) turned out to be soluble in wider range of solvents than individual segments and maintained nanofibrillar morphology of parent P3HT [105]. PMMA-*b*-P3HT-*b*-PMMA coil–rod–coil triblock copolymer featured similar UV-Vis characteristics as P3HT and organised into nanofibrils upon drop casting [106]. P3HT-*b*-PDMS rod-coil diblock copolymer (P3HT:PDMS block ratio 1:11) self-assembled into cylindrical micelles with a crystalline P3HT core in mixed solvent solutions [107].

More complicated architectures bearing P3HT segments, such as amphiphilic 21-arm, starlike diblock copolymers with poly(acrylic acid)-*block*-poly(3-hexylthiophene) (PAA-*b*-P3HT) arms attached to  $\beta$ -cyclodextrin ( $\beta$ -CD) core were also obtained [116].

A few reports on the topic of graft copolymers bearing RR P3HT side chains can be found in literature. Obtained structures, as well as their potential applications in fields of organic electronics or improved properties are summarized in Tab. 3.2.

Tab. 3.2 Graft copolymers bearing P3HT side chains reported in literature

Obtained graft copolymer	Potential application or achieved improvement	Ref.
Polythiophene- <i>graft</i> -poly(3-hexylthiophene) PT- <i>g</i> -P3HT  Poly{[(N,N'-Bis(2-decyltetradecyl)-2,6-dibromonaphthalene-1,4,5,8-bis(dicarboximide))- <i>co</i> -polythiophene]- <i>graft</i> -poly(3-hexylthiophene) PNDIT- <i>g</i> -P3HT	OFET devices	[123]
Polystyrene- <i>graft</i> -poly(3-hexylthiophene) PS- <i>g</i> -P3HT	Potential applications in optical sensors and solar cells	[117,118]
Poly(norbornene)- <i>graft</i> -poly(3-hexylthiophene) PNB- <i>g</i> -P3HT	Photovoltaic devices; Strong aggregation upon drying; End-on-end linearly assembled fiber morphologies upon annealing	[119–121]
Poly(phenylenethynylene)- <i>graft</i> -poly(3-hexylthiophene) PPE- <i>g</i> -P3HT	Chiral self-assembly	[124]
Poly[N-9'-heptadecanyl-2,7-carbazole- <i>alt</i> -5,5-(4',7'-di-2-thienyl-2',1',3'-benzothiadiazole)]- <i>graft</i> -poly(3-hexylthiophene) PCDTBT- <i>g</i> -P3HT	All-conjugated donor-acceptor graft copolymer	[125]
Polynorbornene- <i>g</i> -[(poly(3-hexylthiophene); poly(D,L-lactide)] bottlebrush copolymer PNB- <i>g</i> -(P3HT;PLA)	Control of P3HT aggregation behaviour, nanoporous P3HT thin films after etching PLA	[126]
Poly(methyl methacrylate- <i>ran</i> -3-(maleimido)propyl methacrylate)- <i>graft</i> -poly(3-hexylthiophene) P(MMA- <i>ran</i> -MPMA)- <i>g</i> -P3HT	Rod-coil copolymer with conjugated segment for potential optoelectronics applications	[122]

Synthesis of polystyrene-*graft*-poly(3-hexylthiophene) (PS-*g*-P3HT) brushes of narrow molecular weight distribution (PDI <1.2) composed of rod-like P3HT side chains densely grafted onto a hydrophobic coil-like PS backbone was reported with high grafting efficiency (>96%). Backbone, poly(4-(chloromethyl)styrene), was synthesised via RAFT polymerisation, then chlorine atoms were converted into azide groups, which were coupled with ethynyl terminated RR P3HT (synthesised via GRIM method) by click reaction. PS-*g*-P3HT brushes self-assembled at the air/water interface into circular domain arrays composed of the P3HT nanofibers [117]. Crystallization and aggregation of PS-*g*-P3HT brushes into lamellar structures, similar to the linear P3HTs, and excellent thermal stability of the brushes in thin films was reported as well [118].

Series of PNB-*g*-P3HT molecular bottlebrushes with RR P3HT side chains (of various molecular mass) were obtained via grafting through approach by controlled ROMP polymerisation of exo-norbornenyl-functionalized P3HT macromonomers [119,120]. Copolymer bearing side chains of 12-repeating units length exhibited very strong physical aggregation upon drying during recovery, attributed to significant increase in the number of  $\pi$ - $\pi$  interactions between P3HT side chains due to the densely grafted bottlebrush architecture [119]. It was also demonstrated that PNB-*g*-P3HT bottlebrushes can form end-on-end linearly assembled fiber morphologies upon thermal annealing [121]. Grafting P3HT on PMMA backbone resulted in slight decrease of crystallinity in comparison with parent P3HT which may indicate that degree of aggregation was reduced [122].

Taking it next step further, series of brush copolymers comprising RR P3HT and amorphous poly(D,L-lactide) (PLA) side chains grafted on poly(norbornene) backbone were synthesized via ring-opening metathesis polymerization (ROMP) of norbornenyl-functionalized P3HT and PLA macromonomers. The relative volume fraction of P3HT and PLA side chains in the brush copolymers determined thermal properties and crystallinity. Solution self-assembly in a mixed solvent selective for PLA resulted in the formation of non-persistent nanofibrils and spheres for brush random copolymer, but the brush block copolymers formed highly persistent nanofibrils [126].

In summary, implementation of non-conjugated segment to conducting polymer molecule, such as P3HT, can improve the mechanical properties and processability of obtained copolymer with respect to the parent conducting species without severe impairment of optoelectronic characteristics. Copolymerization, especially leading to grafted molecules also forces miscibility of used fragments, improving interpenetration and homogeneity of obtained materials compared to polymer blends.

#### **4 Characterisation of polymers**

Polymers are described in means of their structure and degree of polymerization reflecting average size of the macromolecule. For copolymers information about ratio of individual constitutional units and their distribution in the copolymer macromolecule is also required for full characterisation. Different spectroscopic or chromatographic techniques may be applied to determine molecular weight, presence of particular functional groups or fashion in which constitutional units are connected.

#### 4.1 Determination of molecular weight of polymers

As polymers, unlike low-molecular weight compounds, are not species made of uniform, well defined molecules, but are a mixture of macromolecules of particular kind featuring different architectures (e.g. linear or branched) and sizes (various chain lengths). Mechanical properties, processing behaviour and morphology of a polymer depend on molecular weight, molecular weight distribution and shape of macromolecules present in the polymer matrix, therefore it is important to estimate (and control) molecular composition of polymers. Indicators, such as average molar mass and dispersity, are employed to describe polymer samples [84].

Number average molar mass,  $M_n$ , is expressed as arithmetic mean of molar mass of all molecules comprising the sample:

$$M_n = \sum_i x_i M_i = \frac{\sum_i N_i M_i}{\sum_i N_i} = \frac{m}{\sum_i N_i}$$

(where:  $x_i$  – molar fraction of molecules with molar mass  $M_i$ ,  $N_i$  – number of molecules  $i$  present in the sample,  $m$  – mass of the sample)

Weight average molar mass,  $M_w$ , is expressed as weighted average of molar mass of all molecules comprising the sample:

$$M_w = \sum_i w_i M_i = \frac{\sum_i N_i M_i^2}{\sum_i N_i M_i}$$

(where:  $w_i$  – mass fraction of molecules with molar mass  $M_i$ ,  $N_i$  – number of molecules  $i$  present in the sample,  $M_i$  – molar mass of the molecule  $i$ )

It depends not only on the number of molecules in the polymer, but also on the mass of each macromolecule.

Dispersity ( $\mathcal{D}_M$ ) is a measure of the distribution of molar mass (heterogeneity) in polymer sample and is calculated as a ratio of weight average molar mass to number average molar mass:

$$\mathcal{D}_M = \frac{M_w}{M_n}$$

It takes values equal to 1 (for exceptional case of uniform, monodisperse polymer) or greater (for polydisperse polymers). The higher the value, the broader spread of molecular weights in the polymer sample. Molar mass units are g/mol or kg/mol - g/mol is

recommended since then the numerical values of the molar mass are equal to the relative molecular mass (commonly denoted as molecular weight in polymer chemistry) of the macromolecule [127].

Technique most widely used for determination of polymer molecular weight in lab practice is gel permeation chromatography (GPC), in which macromolecules are separated according to their sizes on the chromatography column. Relative molecular mass of the investigated polymer is determined by measuring elution time (eluent volume) of polymer solution flowing through the column and comparison with calibration values obtained for the set of standards with well-defined molar mass (usually polystyrene). It allows for estimation of number and weight average molecular weight.

Another method commonly used to determine molecular weight of polymers is matrix-assisted laser desorption-ionization time of flight mass spectrometry (MALDI-TOF), in which polymer sample is mixed with matrix facilitating desorption of macromolecules from the probe surface and their ionization with avoidance of fragmentation under UV laser pulse. Molecular cations are then analyzed by means of time of flight mass spectrometry. It is a direct method for determination of polymer molecular mass which allows for detailed evaluation of molecular weight distribution and provides information about end group composition, but is not suitable for characterisation of samples with high dispersities, as it tends to underestimate representation of higher molecular weight fractions in mass spectrum, and therefore leads to lowering obtained average molecular weight [128].

Nuclear magnetic resonance spectroscopy of protons ( $^1\text{H}$  NMR) can be also applied to determine number average molar mass based on end group analysis. It is however restricted to analysis of polymers with relatively low molecular weights, bearing quantifiable end group giving strong, well resolved signal on NMR spectrum, not overlapping with other signals, allowing for reliable integration. It was applied by D.S. Seferos group to estimate molecular weight of *o*-tolyl terminated P3HT by comparison of integrals of *o*-tolyl  $\text{CH}_3$  protons and thiophene aromatic protons. For  $M_n$  range 6.5-23 kg/mol (39-138 repeating units) linear correlation was observed between values obtained by NMR and GPC techniques (GPC overestimated  $M_n$  by a factor of 1.3 compared to NMR). For higher molecular weight nonlinear relationship was noted [129]. Integrals ratio of main peak of  $\alpha\text{-CH}_2$  protons in alkyl side chain at about 2.8 ppm and terminal  $\alpha\text{-CH}_2$  protons peaks at about 2.6-2.5 ppm was also applied to estimate P3HT chain lengths, resulting in  $M_n$  corresponding to values obtained by MALDI-TOF MS [130].

In case of P3HT determination of molecular weight by GPC has a major drawback – correlation of hydrodynamic radius of rod-like P3HT molecules with hydrodynamic radius of reference coil-like polystyrene molecules tends to overestimate number average molecular weight of the former:

- by the factor of 1.8-2.0 for absolute  $M_n$  range between 2,300 and 10,100 in comparison with ebulliometry (method for determination of absolute  $M_n$  based on measuring changes of solvent boiling point) [131];
- by the factor of 1.2-1.5 for acetone and hexane fractions, and by the factor of 1.5-2.3 for methylene chloride, tetrahydrofuran and chloroform fractions in comparison with MALDI-TOF [77].

What is more, light scattering characterisation of THF and  $\text{CHCl}_3$  solutions of regioregular poly(3-dodecylthiophene) shows that it tends to form metastable aggregates, even in elevated temperatures (up to 65 °C) [132], which may cause overestimation of  $M_n$  by GPC. Nevertheless GPC is an useful method for estimating dispersity of P3HT samples and for tracking changes of molecular weight and dispersity in copolymerization reactions.

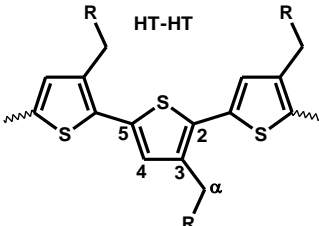
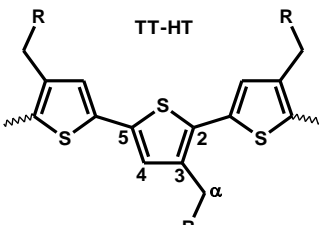
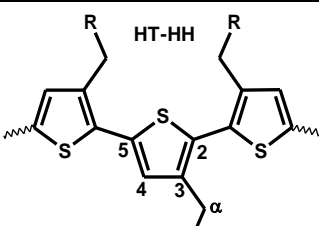
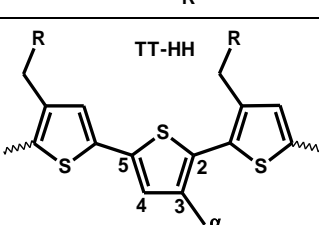
## 4.2 NMR spectroscopy of poly(3-hexylthiophenes)

Nuclear magnetic resonance (NMR) spectroscopy offers simple and viable tool for structure determination and analysis of end groups in P3ATs. Analysis of  $^1\text{H}$  NMR and  $^{13}\text{C}$  NMR spectra provides useful qualitative information about presence or absence of regiodefects in P3AT chain, additionally comparisons of integrals in  $^1\text{H}$  NMR spectrum allows for quantitative estimation of degree of regioregularity. Areas of interest in  $^1\text{H}$  NMR spectrum are: signals of aromatic protons around 6.9-7.1 ppm and signals of  $\alpha$ -methylene protons around 2.5-2.8 ppm.

Different configurations of atoms in regioisomeric triads create different chemical and magnetic surroundings, which affects chemical shifts of aromatic protons and carbons, as well as protons and carbons of methylene group in alkyl chain directly attached to thiophene ring ( $\alpha\text{-CH}_2$ ). Regiorandom P3ATs exhibits four distinct peaks in aromatic region (6.9-7.1 ppm) of  $^1\text{H}$  NMR spectrum and sixteen different peaks in aromatic region (125-145 ppm) of  $^{13}\text{C}$  NMR spectrum, whereas regioregular P3ATs feature single aromatic peak at 6.98 ppm in  $^1\text{H}$  NMR spectrum and four aromatic peaks in  $^{13}\text{C}$  NMR spectrum [55,56].

S. Holdcroft assigned four signals of aromatic protons as follows: HT-HT 6.98 ppm, HT-TT 7.00 ppm, HH-HT 7.02 ppm and HH-TT 7.05 ppm based on the assumption that HT configuration promotes coplanarity of the backbone and shielding of aromatic proton, for TT configuration shielding effect is weaker, and for HH configuration the weakest, due to the forcing thiophene rings out of coplanarity, therefore HT protons should occur at the highest field, and HH protons should occur at the lowest field [133]. Those assignments turned out to be correct, as confirmed by analysis of heteronuclear correlation spectra of model regioisomeric triads (3-hexylthiophene trimers) [134] and nonregular P3HT [134,135]. These correlations provide also information about individual  $^{13}\text{C}$  NMR shifts, as shown in Tab. 4.1.

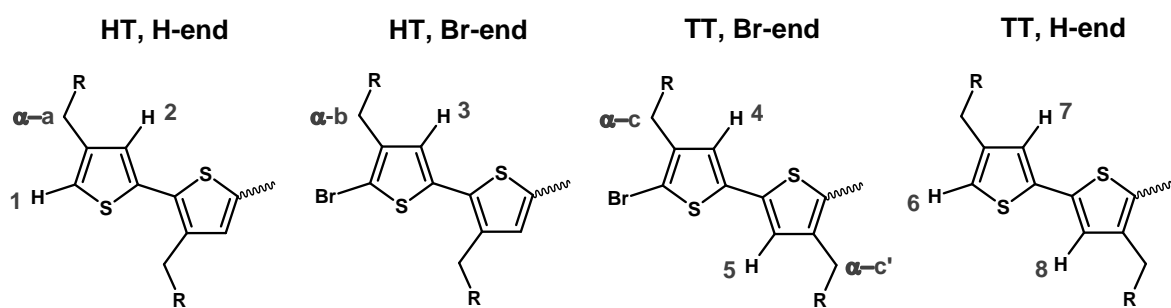
Tab. 4.1 Assignments of signals of aromatic protons and carbons in main chains of poly(3-alkylthiophene)s

Regioisomer	$^1\text{H}$ NMR shifts [ppm]	$^{13}\text{C}$ NMR shifts [ppm]				Notes	Ref.
	H-4	C-2	C-3	C-4	C-5		
 HT-HT	6.92	130.7	139.5	128.6	133.9	Trimer	[134]
	6.98	130.5	139.9	128.7	133.8	NR P3HT	
	6.98	130.7	139.9	128.6	133.9	NR P3HT	[135]
 TT-HT	6.96	129.8	139.9	126.2	135.2	Trimer	[134]
	7.00	-	-	-	-	NR P3HT	
	7.00	-	140.4	126.5	135.0	NR P3HT	[135]
 HT-HH	6.98	128.6	142.6	127.3	135.9	Trimer	[134]
	7.03	-	-	-	-	NR P3HT	
	7.02	-	142.8	127.1	135.7	NR P3HT	[135]
 TT-HH	7.00	127.5	143.1	124.9	137.3	Trimer	[134]
	7.05	-	-	-	-	NR P3HT	
	7.05	-	143.6	125.0	137.0	NR P3HT	[135]

$\alpha$ -methylene protons and carbons are less sensitive to regioisomeric differences. In  $^1\text{H}$  NMR spectrum two overlapping groups of signals are present around 2.5-2.8 ppm. Again, from the comparison of spectra of regioregular and regiorandom P3ATs it can be concluded that broad overlapping signal around 2.80 ppm contribute to HT couplings and broad overlapping signal around 2.58 ppm contribute to HH couplings [55,56]. Similar assignment has been proposed based on 2D-NMR spectroscopy of model regioisomeric P3HT triads (trimers) [136]. Further study involving investigation of nonregular poly(3-decylthiophene) with selective nuclear Overhauser effect spectroscopy (NOESY) showed homonuclear correlations of the following signals: 2.79 with 6.79, 2.77 with 7.00, 2.57 with 7.02, and 2.54 with 7.05 ppm [137], confirming the assignment.

$^1\text{H}$  NMR spectroscopy can be also applied to end groups analysis, provided that polymer chains are not too long, so that peaks originating from characteristic features of end groups are observable.  $^1\text{H}$  NMR characteristics of protons in P3ATs' end groups relevant in GRIM/KCTP polymerization, reported in literature, are summarized in Tab. 4.2.

Tab. 4.2  $^1\text{H}$  NMR chemical shifts, multiplicities and coupling constants of aromatic and  $\alpha$ -CH<sub>2</sub> protons in different end groups resulting from GRIM/KCTP polymerization protocol

												Type	Ref.
$\delta$ [ppm], multiplicity, J [Hz]													
H-1	H-2	H-3	H-4	H-5	H-6	H-7	H-8	$\alpha$ -a	$\alpha$ -b	$\alpha$ -c	$\alpha$ -c'		
6.90, s	-	-	-	-	6.80, s	-	-	-	-	-	-	Polymer	[133]
6.91, s	-	-	-	-	-	-	-	-	-	-	-	Polymer	[56]
6.90, d, $^4J$ 1.2	7.00, d, $^4J$ 1.2	6.82, s	-	-	-	-	-	2.7-2.8	2.5-2.7	-	-	Polymer	[76]
6.898, d, $^4J$ 1.5	6.970, d, $^4J$ 1.5	-	-	-	-	-	-	-	-	-	-	Hexamer	[138]
6.90	6.97	6.83	-	-	-	-	-	2.62	2.58	-	-	Polymer	[139]
6.90	-	6.84	6.86	6.93	6.80	-	-	-	-	2.56	2.77	Polymer	[140]
6.87	6.96	-	-	-	6.76	7.00	6.96	-	-	-	-	Trimer	[134]



### 4.3 NMR spectroscopy of polysiloxanes

In  $^1\text{H}$  NMR spectrum Si-CH<sub>3</sub> protons of polysiloxanes give signals in high field region of 0.05-0.25 ppm, slightly downfield from TMS peak. Signal of Si-CH<sub>3</sub> protons in polydimethylsiloxane occur at 0.066 ppm [141]. In case of polymethylhydrosiloxanes terminated with trimethylsilyl units, three signals at  $^1\text{H}$  NMR spectrum are observed: peak of -Si(CH<sub>3</sub>)<sub>3</sub> terminal groups at 0.15 ppm, peak of CH<sub>3</sub> protons in -Si(H)CH<sub>3</sub>- units at 0.24 ppm and peak of silane (Si-H) protons at 4.75 ppm [142].

In poly(dimethylsiloxane-*co*-methylhydrosiloxane) two sets of signals in 0.1-0.2 ppm region occur: signals at higher field are ascribed to -Si(CH<sub>3</sub>)<sub>2</sub>- segment (D) due to the shielding effect of methyl moieties, and signals at lower are ascribed to -Si(H)CH<sub>3</sub>- segment (D<sup>H</sup>). Detailed analysis of series of such copolymers with different ratio of dimethylsiloxane to methylhydrosiloxane units indicates occurrence of triad effect (dimethylsiloxane-methylhydrosiloxane triads are depicted in Fig. 4.1) – neighbouring units influence chemical shifts of Si-H and Si-CH<sub>3</sub> protons. Six peaks are observed in high field region of  $^1\text{H}$  NMR spectrum, assigned to two groups of Si-CH<sub>3</sub> signals: 1) -Si(CH<sub>3</sub>)<sub>2</sub>-: 0.092-0.095 (DDD), 0.116-0.120 (DDD<sup>H</sup>), 0.143-0.145 (D<sup>H</sup>DD<sup>H</sup>), and 2) -Si(H)CH<sub>3</sub>-: 0.165-0.175 (DD<sup>H</sup>D), 0.190-0.195 (DD<sup>H</sup>D<sup>H</sup>), 0.215-0.220 (D<sup>H</sup>D<sup>H</sup>D<sup>H</sup>), accompanied with group of 3 signals of Si-H protons at about 4.7 ppm: 4.64-4.698 (DD<sup>H</sup>D), 4.713-4.715 (DD<sup>H</sup>D<sup>H</sup>) and 4.731-4.735 (D<sup>H</sup>D<sup>H</sup>D<sup>H</sup>) [143,144].

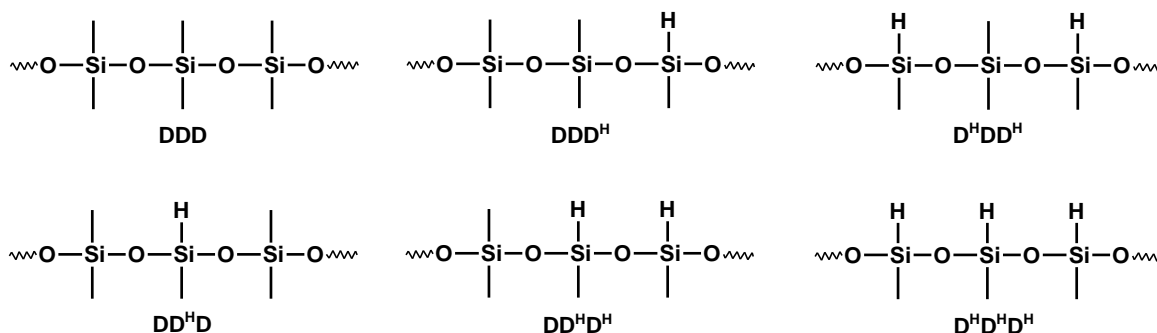


Fig. 4.1 Dimethylsiloxane-methylhydrosiloxane compositional triads and their designation

### 4.4 IR spectroscopy

Infrared (IR) spectroscopy is a spectroscopic technique for study of organic compounds structure, operating on wavelengths between 2.5 and 15  $\mu\text{m}$  (wavenumbers between 4000 and 670  $\text{cm}^{-1}$ ), whose energy matches vibrational-rotational transitions in organic molecules.

IR radiation causes stretching (changes in bonds length) and bending (changes of the angle between bonds corresponding to scissoring, rocking, wagging, and twisting deformations) of chemical bonds in molecules [145]. Functional groups, as well as other characteristic groups of atoms absorb IR radiation in a narrow frequency region, regardless of the structure of the rest of the molecule. This allows the identification of functional groups and other elements of the molecule structure. IR spectrum can be divided into two regions to facilitate the interpretation: group frequency region ( $3700\text{-}1500\text{ cm}^{-1}$ ), which allows for determination of functional groups present in the analyzed molecule, and fingerprint region ( $1300\text{-}700\text{ cm}^{-1}$ ), in which bands of skeletal vibrations characteristic for investigated molecule appear, useful for resolving the structure by comparison with IR spectra of known compounds [146].

Characteristic IR absorption bands of P3HT are as follows: aromatic C-H stretching vibrations at  $3057\text{-}3053\text{ cm}^{-1}$ , aliphatic C-H stretching vibrations as series of three bands at  $2959\text{-}2954$ ,  $2930\text{-}2925$  and  $2858\text{-}2854\text{ cm}^{-1}$ , ring stretching vibrations at  $1516\text{-}1510$  and  $1464\text{-}1454\text{ cm}^{-1}$  (characteristic for 2,5-disubstituted-3-hexylthiophene), methyl group deformation at  $1377\text{ cm}^{-1}$ , C-H out-of-plane deformation vibrations in thiophene ring at  $827\text{-}820\text{ cm}^{-1}$  [56,147]. The last one is particularly interesting, as it can be used as a probe for estimating regioregularity of P3HT. Regioregular P3HT gives rise to C-H out-of-plane deformation band at  $820\text{ cm}^{-1}$ , whereas regiorandom at  $827\text{ cm}^{-1}$ . IR absorption bands typical for regioregular P3HT are collected in Tab. 4.3.

Tab. 4.3 Characteristic infrared absorption bands of regioregular P3HT

Group	IR absorption band	Reference
aromatic C-H (stretching)	$3055\text{ cm}^{-1}$	[56]
aliphatic C-H (stretching)	$2954\text{ cm}^{-1}$ $2925\text{ cm}^{-1}$ $2856\text{ cm}^{-1}$	
thiophene ring (stretching)	$1510\text{ cm}^{-1}$ $1454\text{ cm}^{-1}$	
-CH <sub>3</sub> (deformation)	$1377\text{ cm}^{-1}$	
C-H in thiophene ring (out-of-plane deformation)	$820\text{ cm}^{-1}$	
-CH <sub>3</sub> (rocking)	$725\text{ cm}^{-1}$	

In the infrared spectra of organosilicon compounds characteristic, strong infrared absorption band of Si-O-Si asymmetric stretching vibrations is observed in  $1000\text{-}1100\text{ cm}^{-1}$  region. In hexamethyldisiloxane this band occurs at  $1054\text{ cm}^{-1}$  [148], and with increase in

length of siloxane chain it splits due to the coupling between adjacent chain segments and broadens gradually to emerge as strong broad band with maxima at 1087-1085 and 1024-1022  $\text{cm}^{-1}$  in case of poly(dimethylsiloxane) [149,150]. Another infrared band characteristic for PDMS are: asymmetric and symmetric C-H stretching of Si-CH<sub>3</sub> group at, respectively, 2965 (strong) and 2905  $\text{cm}^{-1}$  (weak), asymmetric and symmetric C-H bending of Si-CH<sub>3</sub> at, respectively, 1411-1400 (medium-weak) and 1260  $\text{cm}^{-1}$  (very strong), rocking vibrations of methyl group and C-Si-C stretching vibrations in 865-700  $\text{cm}^{-1}$  region (medium-weak) with peaks at 864, 842, 802, 740 and 704  $\text{cm}^{-1}$  [149].

Comparative analysis of IR spectra for series of linear (from hexamethyldisiloxane to octadecamethyloctasiloxane), cyclic (from hexamethylcyclotrisiloxane to hexadecamethylcyclooctasiloxane), and branched [3-trimethylsiloxyheptamethyltrisiloxane and 3,3-dit(trimethylsiloxy)hexamethyltrisiloxane] siloxanes were published [148,151]. Accordingly, bands at 845-842 and 759-755  $\text{cm}^{-1}$ , present in spectra of branched and linear trimethylsilyl terminated methylsiloxanes, but absent in spectra of cyclic methylsiloxanes, decreasing in intensity with increasing chain length of linear compounds are attributed to Si-(CH<sub>3</sub>)<sub>3</sub> groups. Bands at about 800 and about 700  $\text{cm}^{-1}$ , present in open chain and cyclic oligosiloxanes, increasing in intensity with increasing chain length of linear compounds are attributed to Si-(CH<sub>3</sub>)<sub>2</sub> groups. Number of CH<sub>3</sub> moieties attached to Si atom determines band pattern of methyl rocking vibrations present in 850-750  $\text{cm}^{-1}$  region: Si-CH<sub>3</sub> gives single band at about 765  $\text{cm}^{-1}$ , Si-(CH<sub>3</sub>)<sub>2</sub> bands at about 800 and 855  $\text{cm}^{-1}$ , whereas Si-(CH<sub>3</sub>)<sub>3</sub> bands at 841 and 755  $\text{cm}^{-1}$  [152,153].

Band assigned to C-H symmetric bending of Si-CH<sub>3</sub> also differ slightly in position between terminal trimethylsilyl groups and intrachain dimethyl groups. For hexamethyldisiloxane strong band at 1252  $\text{cm}^{-1}$  is observed, for octamethyltrisiloxane and decamethyltetrasiloxane bands at 1250 and 1258  $\text{cm}^{-1}$  are observed, the former of decreasing intensity, the latter of increasing intensity with elongation of oligomer chain, for longer siloxanes only strong band at 1258  $\text{cm}^{-1}$  is observed [148], which leads to the conclusion that 1250  $\text{cm}^{-1}$  band should be attributed to terminal Si-(CH<sub>3</sub>)<sub>3</sub> group, whereas 1258  $\text{cm}^{-1}$  band should be attributed to Si-(CH<sub>3</sub>)<sub>2</sub> group of siloxane backbone.

Si-H bond gives rise to strong Si-H stretching vibration mode observed in 2250-2100  $\text{cm}^{-1}$  region and strong Si-H deformation vibration mode observed in 985-800  $\text{cm}^{-1}$  region [150]. For poly(methylhydrosiloxane) those bands occur at 2174 and 893  $\text{cm}^{-1}$ , and Si-O-Si

stretching vibrations band is shifted towards shorter wavelengths (to about 1095-1048  $\text{cm}^{-1}$ ) compared to PDMS spectrum [154].

## 5 Chosen applications of organic semiconductors

### 5.1 Gas sensors

Nitrogen oxides are binary inorganic compounds composed of nitrogen and oxygen in variable proportions – depending on the oxidation state of the nitrogen atom. Among them  $\text{NO}_x$  – term referring to mixture of nitrogen(II) oxide (NO) and nitrogen(IV) oxide ( $\text{NO}_2$ ) – draw particular attention, as substantial atmospheric pollutants emitted mostly by burning fossil fuels in internal combustion engines (mostly in transportation sector), biomass burning and soil emissions.  $\text{NO}_x$  are among the main health-damaging air pollutants, along with particulate matter (PM), ozone ( $\text{O}_3$ ), sulphur dioxide ( $\text{SO}_2$ ) and carbon monoxide (CO).  $\text{NO}_x$  contribute to formation of smog and acid rains, since they are precursors of nitrous acid ( $\text{HNO}_2$ ) and nitric acid ( $\text{HNO}_3$ ), and catalyse tropospheric formation of ozone ( $\text{O}_3$ ), which is direct greenhouse gas [155],  $\text{NO}_2$  absorbs solar visible radiation and contributes to the deterioration of atmospheric visibility and potentially plays a direct role in global climate change [156]. What is more,  $\text{NO}_2$  is reddish-brown gas with characteristic pungent odour, toxic upon inhalation. High-intensity, confined space exposure to  $\text{NO}_2$  causes such effects as cough, dyspnoea, haemoptysis, respiratory tract irritation, pulmonary oedema, severe respiratory distress syndrome, bronchiolitis obliterans or even death. Exposure to ambient  $\text{NO}_2$  may increase the risk of respiratory tract infections due to the pollutant's interaction with the immune system [157].  $\text{NO}_2$ -induced adverse pulmonary effects in healthy humans are observed for  $\text{NO}_2$  concentrations exceeding 1 ppm, while in susceptible individuals, e.g. asthmatics, children or elders, for concentrations ranging from 0.2 to 0.6 ppm [158]. Meta-analysis studies find positive associations between exposure to long-term concentrations of  $\text{NO}_2$  at level of  $10 \mu\text{g}/\text{m}^3$  (recommended as a limit by Global Air Quality Guidelines) and incidence of Acute Lower Respiratory Infection (ALRI) mortality and Chronic Obstructive Pulmonary Disease (COPD) mortality [159].

$\text{NO}_2$  can be easily detected by smell, but its concentration of 4 ppm anaesthetizes olfactory sense [160]. Considering that – it is important to monitor and control  $\text{NO}_x$  emission to the atmosphere and to track concentrations of  $\text{NO}_2$  in the workplace environment in case

to alert the people about the risk of exposure exceeding safety standards. Sensor structures for detection and measurements of small concentrations of nitrogen oxides find potential applications in the industry [161], automotive sensors [162,163], environmental monitoring and medical practices [164] or in the detection of explosives [165]. Even domestic gas-burning appliances (stoves) may pose a threat to human health since stove usage can result in indoor NO<sub>2</sub> concentration of 100 ppb within 1 hour, especially in small kitchens with poor ventilation [166].

Currently, sensor market is dominated by metal oxide-based gas sensors (MOS). Metal oxide-based gas sensors made of WO<sub>3</sub>, SnO<sub>2</sub>, ZnO, TiO<sub>2</sub>, InO<sub>3</sub>, were extensively investigated in NO<sub>2</sub> detection [160]. Sensors based on semiconductor oxides are generally low cost and easy to manufacture, and show high sensitivity and stability [167]. Among the disadvantages of MOS low selectivity and high operating temperatures (within the range of 100-450°C, typically 200-300°C) should be mentioned.

Currently many efforts in the field of gas sensors are focused on the development of sensors with high performance, low energy consumption and low production cost, operating in room temperature. Gas sensors based on conjugated polymers are under investigation in this field, since interaction with reducing or oxidating agents influences their electric properties (resistance) allowing to detect the gases with high selectivity. Reports on the application of conjugated polymers in NO<sub>2</sub> sensors are collected in Tab. 5.1.

Tab. 5.1 NO<sub>2</sub> sensors based on conjugated polymers reported in literature

Material	Response (NO <sub>2</sub> concentration)	Limit of detection	Ref.
Polyaniline (PANI)	80% (1 ppm)	50 ppb	[168]
Polythiophene (PT)	9 (10 ppm)	-	[169]
Polypyrrole (PPy)	12 (10 ppm)	-	[170]
Hybrids of ethylenediamine-modified reduced graphene oxide and polythiophene (RGO-PT)	2636 (10 ppm)	0.52 ppm	[171]
Regioregular poly(3- hexylthiophene):poly(vinylcarbazole) (P3HT:PVK) blend (1:1)	20,000% (30 ppm) 700% (0.6 ppm)	139.3 ppb	[172]
Poly(3-hexylthiophene):poly(9-vinylcarbazole) (P3HT:PVK) blend 1:1	700% (600 ppb) 12,381% (15 ppm)	-	[173]

Poly(3,3'''-bisdodecylquaterthiophene) (PQT12)	24% (100 ppb)	100 ppb	[174]
Poly(3,3'''-bisdodecylquaterthiophene):polystyrene (PQTS12:PS) blend	25% (200 ppb) 400% (20 ppm)	200 ppb	[175]
Poly(3-hexylthiophene):poly[N,N'-bis(4-butylphenyl)-N,N'-bis(phenyl)benzidine] (P3HT:PTPD) blend 1:9	63% (0.3 ppm) 746% (30 ppm)	242.6 ppb	[176]
Poly(3-hexylthiophene):poly(methyl methacrylate) (P3HT:PMMA) blend 1:60	1,481% (30 ppm)	0.7 ppb	[177]
Alkylated diketopyrrolopyrrole-thiophene copolymer (PDPP4T)	157% (1 ppm) 258% (5 ppm) 571% (10 ppm) 614% (20 ppm)	-	[178]
Poly[4-(4,4-dihexadecyl-4H-cyclopenta[1,2-b:5,4-b']dithiophen-2-yl)- <i>alt</i> -[1,2,5]-thiadiazolo[3,4-c]pyridine] (PCDTPT)	3,110% (1 ppm) 2,460,000% (30 ppm)	<1 ppm	[179]
Poly(3-hexylthiophene):polystyrene (P3HT:PS) dense blend (P3HT:PS) porous blend	7,900% (20 ppm) 22,000% (20 ppm)	- -	[180]
Poly[2,5-bis(3-tetradecylthiophen-2-yl)thieno[3,2-b]thiophene]/graphene oxide (PBTTC:GO) nanohybrid composite	174% (10 ppm)	0.37 ppm	[181]
Two-dimensional polymer derived from a covalent triazine framework (T-2DP)	505 (1 ppm)	2.2 ppb	[182]
Poly(3-hexylthiophene):hydroxylated multi-walled carbon nanotube (P3HT:OH-MWCNTs) blend 10:1	282% (0.5 ppm) 1320% (30 ppm)	-	[183]
Polypyrrole:reduced graphene oxide functionalized with aryl 4-carboxybenzene diazonium salt (PPy:rGO-aryl-COOH)	40% (20 ppm)	2 ppm	[184]
Regioregular poly(3-hexylthiophene): polystyrene- <i>block</i> -poly(ethylene- <i>ran</i> -butylene)- <i>block</i> -polystyrene (RR P3HT:SEBS) blend 4:1	1,053% (30 ppm)	2.3 ppb	[185]

Presented above conjugated polymers-based NO<sub>2</sub> sensors offer lower operating temperature, easy application on transducers (via spin coating, printing, drop-coating, dip-coating), high sensitivities (relative responses) and low limit of detection. As such they provide an alternative to metal oxides-based sensors, showing potential to measure NO<sub>2</sub> in sub ppm concentrations.

## 5.2 Organic solar cells

Developing modern world is heavily dependent on the electricity, and with its growing population and rapidly increasing number of electric appliances in use, electric power usage continues to grow, with total energy consumption reaching globally  $620 \cdot 10^{18}$  J in 2023. Dominant energy sources are still fossil fuels (coal, oil and natural gas) which currently account for 84% global energy production [186]. Those resources are limited, moreover burning fossil fuels massively contributes to greenhouse gases emission, climate changes and environmental pollution, therefore there is an urgent need to develop and implement efficient renewable energy sources (among others, photovoltaic devices) that will help to diversify energy market and promote energy security, affordability and sustainability. Electricity generated by solar sources reached in global scale 1,322 TWh in 2022 and 1,642 TWh in 2023 (24% growth year by year) [186], making the development of photovoltaics an attractive field for academia and industry.

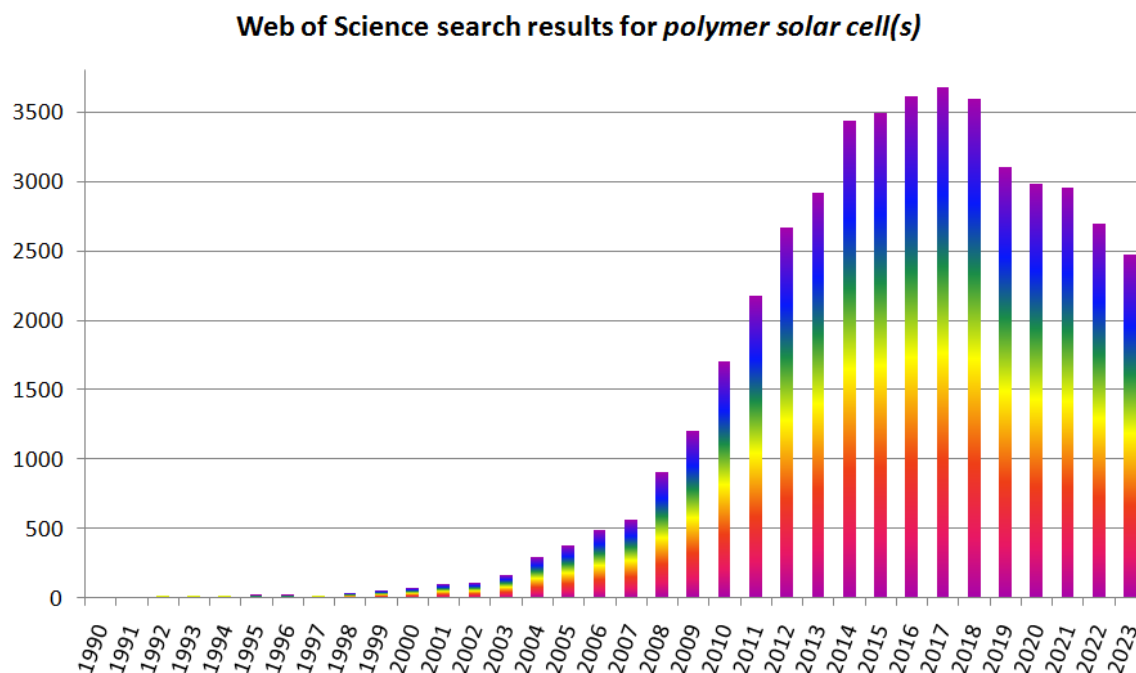


Fig. 5.1 Number of Web of Science records by year for query “polymer solar cell(s)”, acquired online 02.07.2024

Organic solar cells (OSCs) are photovoltaic devices that employ organic compounds (mostly conducting polymers, but also small organic molecules) as active layer for light absorption and charge transport to convert sunlight into direct current electricity by means of photovoltaic effect. They gained attention (Fig. 5.1) since molecular engineering offers

tunability of physical, chemical and optoelectronic properties of organic compounds for applications in organic photovoltaics.

Compared to well-established silicon solar cells, polymer solar cells, as emerging photovoltaic devices, are lightweight, flexible, might be fabricated as semi-transparent sheets, yet their main disadvantages are low efficiency, low stability and low durability. Organic semiconductors feature low charge-carrier mobility compared to inorganic semiconductors, but much higher light absorption coefficients, and may achieve efficient absorption in layers of thickness below 100 nm. Materials applied in OSC might be cheap in production and efficiently processable (employing, e.g., roll-to-roll processes) to ensure low-cost fabrication of large-area devices in high volume.

### 5.2.1 BHJ solar cells

There are several types of OSCs that differ in details of design, nevertheless, in general solar cells consist of light-absorbing layer sandwiched between two metallic electrodes (at least one electrode has to be transparent) of different work functions.

Working principle of polymer solar cell might be outlined as follows. When the energy of incident sunlight is equal to or greater than band gap ( $E_g$ ) of active layer material photons are absorbed, which allows for promotion of the electron from HOMO valence band to LUMO conduction band ( $\pi$ - $\pi^*$  transition) of the donor (electron donor material, typically p-type conjugated polymer), as depicted schematically in Fig. 5.2. Exciton state (electron-hole

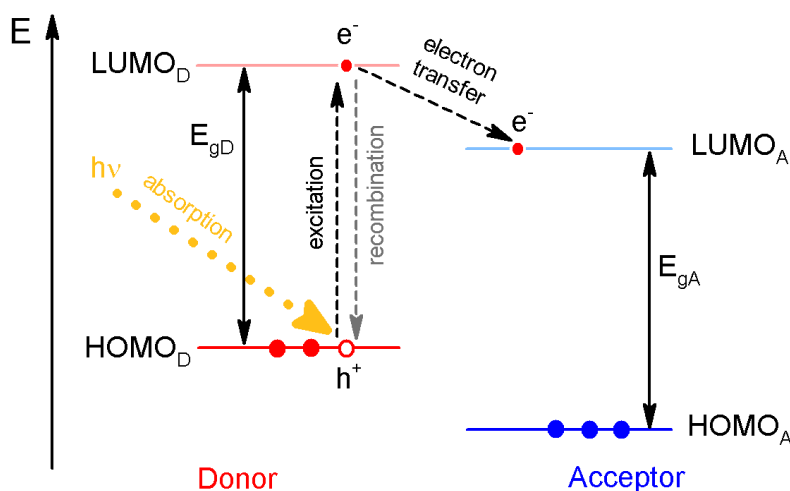


Fig. 5.2 Energy level diagram of donor and acceptor in organic solar cells



pair, bound together by electrostatic interactions, confined to a molecule or a region of a polymer chain) is created, which has to undergo dissociation into separate charge carriers (electrons and holes). Contrary to inorganic solar cells, exciton dissociation in OSCs cannot occur intrinsically, driven by thermal energy at room temperature alone, since exciton binding energies in semiconducting polymers are too high (0.3-0.8 eV) [187]. Dissociation may take place on the donor-acceptor interface (heterojunction), driven by the energy difference in LUMO levels of a donor and an acceptor. As a result, electron moves to acceptor material with lower LUMO level and the hole remains in the donor. Then separated charge carriers diffuse to appropriate electrodes (electrons to the cathode, holes to the anode), where are extracted. On the other hand, exciton and charge recombination on the way may occur resulting in the loss of absorbed energy [188]. Total efficiency of the solar cell is a product of efficiency of light absorption and exciton generation, exciton transport and dissociation at the interface, and charge carriers transport and extraction on the electrodes (Fig. 5.3).

Photocurrent efficiency ( $\eta_j$ ) is determined by the fraction of absorbed photons ( $\eta_{\text{abs}}$ ), the fraction of dissociated electron-hole pairs that ( $\eta_{\text{diss}}$ ), and the fraction of separated charge carriers that reached the electrodes ( $\eta_{\text{out}}$ ) [189]:

$$\eta_j = \eta_{\text{abs}} \times \eta_{\text{diss}} \times \eta_{\text{out}}$$

Exciton lifetime is expressed as its approximate diffusion pathway before it decays back to the ground state and is equal to 10 nm [190]. On the other hand, about 100 nm thickness of active layer is required to ensure high efficiency of light absorption in polymer

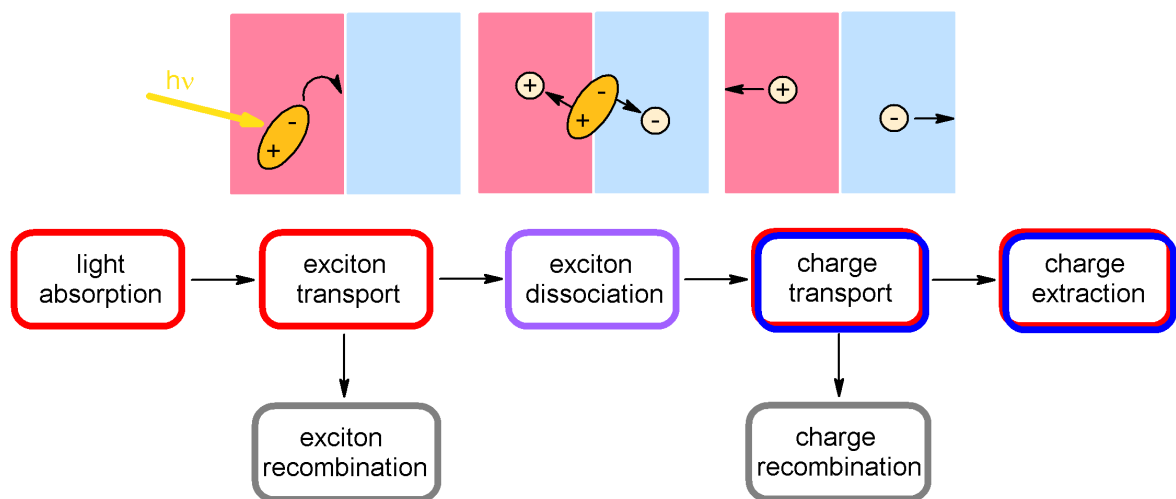


Fig. 5.3 Charge generation and transport in organic solar cells

solar cell. If solar cells are fabricated with separate layers of acceptor and donor, tradeoff between thickness of the layers high enough to absorb light efficiently and low enough to allow excitons to reach the interface and dissociate must be taken into account. Bulk heterojunction (BHJ) architecture solves this issue: active layer comprises nanoscale blend of electron donor (p-type) and acceptor (n-type) materials in form of percolating network. Typical, conventional BHJ OSC structure (Fig. 5.4) involves transparent indium-tin oxide (ITO) anode deposited on a glass or plastic support, poly(3,4-ethylenedioxythiophene):poly(styrene sulfonate) (PEDOT:PSS) layer (as hole transporting layer), active layer, and metal cathode, commonly aluminium. Thin (1 nm) LiF interlayer is usually deposited between active layer and negative electrode to improve contact efficiency [191].

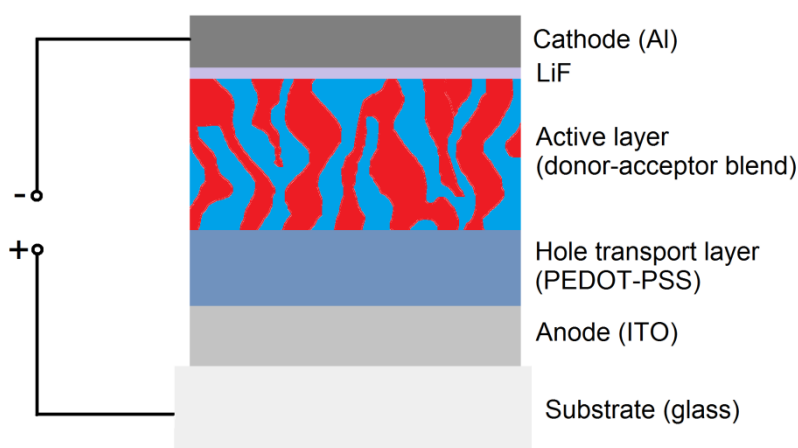


Fig. 5.4 Scheme of conventional bulk heterojunction organic solar cell

BHJ solar cells comprising P3HT as the donor and phenyl- $C_{61}$ -butyric acid methyl ester ( $PC_{61}BM$ ,  $PCBM$ ) as fullerene acceptor became the most extensively examined system and sort of reference point in field of organic photovoltaics [192]. Fabrication of BHJ active layer in such system typically involves spin-casting of binary solution of donor and acceptor and post treatment: annealing or solvent annealing, to develop interpenetrating donor-acceptor network. Blending morphology of the mixture significantly affects device performance: too fine mixing may cause problems with transport of charge carriers to electrodes due to the deterioration of percolating paths; on the other hand, too big domains of donor and acceptor phases may result in recombination of excitons before they reach heterojunction interface.

Sunlight intensity varies throughout the day and year, and with location at the globe. Currently, universally accepted reference for testing and comparing performance of photovoltaic plate module devices for terrestrial applications is AM1.5 Global spectrum

(irradiation spectrum of the sun positioned at an elevation of  $41.81^\circ$  above the horizon, passing through 1.5 air mass thickness, incident on sun-facing inclined surface tilted at  $37^\circ$  from the horizontal toward the equator) [193], according to ISO 9845-1 standard. AM1.5G spectrum has by definition an integrated power of  $1000 \text{ W/m}^2$  ( $100 \text{ mW/cm}^2$ ).

Solar cells are characterized by means of current-voltage analysis (Fig. 5.5) which provides information about device performance. The tested device is connected to source-measure unit, which sweeps the voltage within the defined range and simultaneously measures the output electric current.,

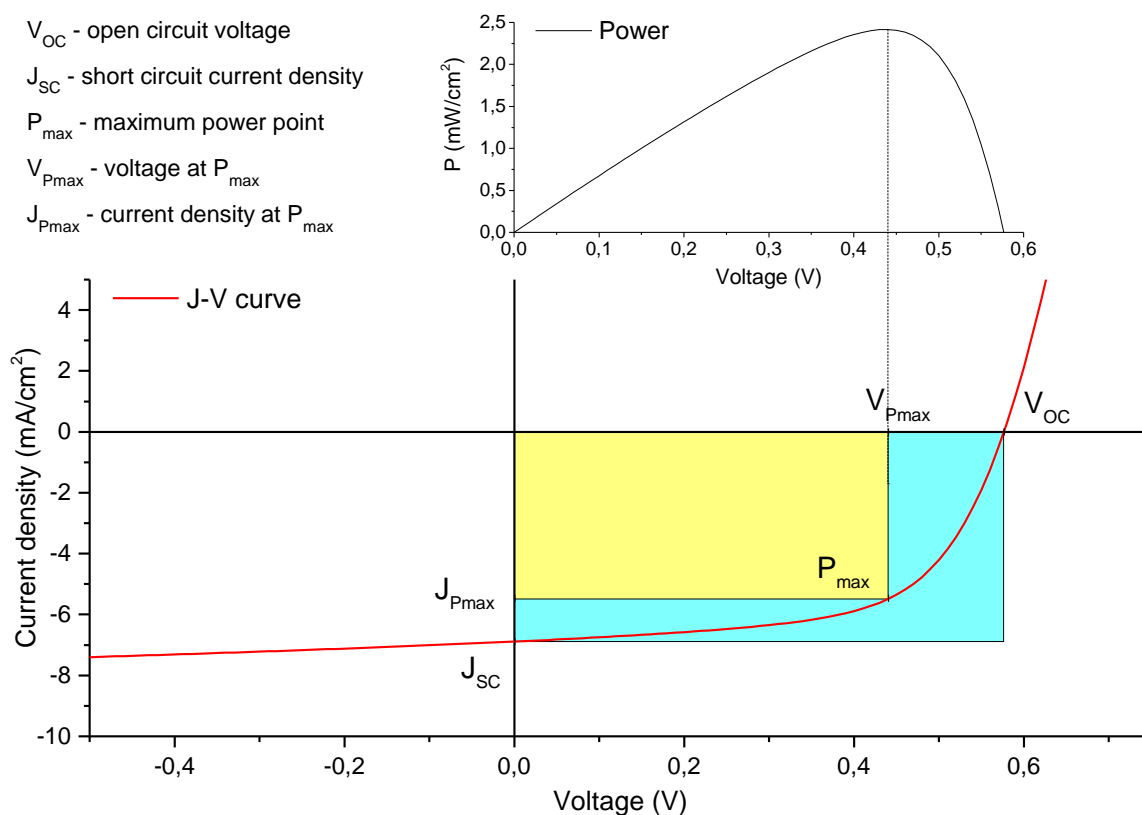


Fig. 5.5 J-V and power-voltage curves of organic solar cell

At 0 V the maximum generated photocurrent density ( $J_{SC}$ ) is achieved under short-circuit conditions, whereas at  $V_{OC}$  point photogenerated current is balanced to zero. Between 0 V and  $V_{OC}$ , the device generates power. At  $P_{max}$  point the power output (the product between current and voltage) is maximized.

Total efficiency of a solar cell indicates the proportion of power generated by the device ( $P_{out}$ ) to power of the incident sunlight ( $P_{in}$ ) equal  $100 \text{ mW/cm}^2$  for AM1.5G conditions:

$$\eta = \frac{P_{\text{out}}}{P_{\text{in}}}$$

Power conversion efficiency (PCE) can be therefore calculated from the equation:

$$\text{PCE} = \frac{P_{\text{out}}}{P_{\text{in}}} \times 100\% = \frac{P_{\text{max}}}{P_{\text{in}}} \times 100\% = \frac{V_{\text{OC}} \times J_{\text{SC}} \times \text{FF}}{P_{\text{in}}} \times 100\%$$

FF denotes fill factor, which represents the proportion of voltage and current density product which contribute to the power generation in the solar cell:

$$\text{FF} = \frac{V_{\text{Pmax}} \times J_{\text{Pmax}}}{V_{\text{OC}} \times J_{\text{SC}}}$$

$V_{\text{OC}}$  is determined by the difference in energy of acceptor's LUMO and donor's HOMO level (it can be estimated as donor-acceptor band gap reduced by about 0.3 V [194]).  $J_{\text{SC}}$  depends on the number of generated photoexcitations, the quantum efficiency for charge separation, and the efficiency of the transport of the charge carriers through the material. FF is determined by the competition between transport and extraction of photogenerated carriers and the recombination of the carriers to the ground state.

External quantum efficiency (EQE) defines probability that an incident photon is converted into photocurrent. It represents the ratio between the number of charge carriers collected from the device to the external circuit and the number of incident photons:

$$\text{EQE} = \frac{\text{electrons out}}{\text{photons in}}$$

The morphology of the BHJ blend can be altered by controlling the liquid-liquid phase separation during the deposition of the active layer or by post-treatment of the BHJ film. Solvent used for casting active layer, proportions between donor and acceptor, additives, concentration of the solution, thermal annealing, solvent annealing, molecular structure of the materials are among factors which influence the nanoscale morphology of the BHJ blends. The molecular structures of donor and acceptor determine their solubility in organic solvents and their miscibility in solution. The solvent influences the drying time during film formation. Thermal and solvent annealing promotes the crystallization and rearrangement of the solid film leading to the phase separation [195].

In case of P3HT:PCBM BHJ solar cell phase separation occurs upon thermal annealing, leading to improvement in solar cell performance resulting from the increase of current

density and fill factor [196]. Investigation of cross sections of such devices with transmission electron microscopy revealed column-like morphology: P3HT and fullerene domains were forming bicontinuous pathways from the top to the bottom of the active layer [197]. On the other hand, long annealing of P3HT:PC<sub>61</sub>BM solar cells may result in decrease in performance after initial increase of PCE, which may be caused by forming too large fullerene domains hindering charge transport [198,199].

### 5.2.2 Additives improving performance of solar cells

Additives to active layer can work like a matrix helping to assemble P3HT and PCBM into percolating pathways for excitons and charge carriers or they can be added in small amounts, in molecular dispersion, to promote miscibility of donor and acceptor. In subject literature many simple and complex (eg. copolymers bearing P3HT or PCBM) additives were reported as factors improving performance of P3HT:PCBM organic solar cells.

Numerous reports on investigation of block copolymers comprising P3HT and non-conjugated segments were published. P3HT-PEO diblock copolymer with oligomeric PEO chains demonstrated similar efficiency as parent P3HT in solar cells with PCBM. Introduction of PEO segment made size of phase separated domains smaller [200]. It was further elaborated that introduction of PEO segment contributed to the generation of ordered lamellar morphology with the smaller size compared with the P3HT/PCBM blend. For the devices based on P3HT-*b*-PEO:PCBM active layer, the favourable PEO content to obtain the high efficiency was found to be 7–9%. They exhibited slightly better (11%) performance than P3HT:PCBM solar cells, similar thermal behaviour, and similar decrease of efficiency with annealing time [201]. Addition of P3HT-*b*-PEO copolymer (5-10%) as compatibilizer was also reported. Additive induced finer phase segregation after thermal annealing and reduced fullerene domain size. At 5% additive  $V_{OC}$  of the solar cell was slightly increased, but  $J_{SC}$  was reduced which resulted in overall PCE decrease in comparison with P3HT:PCBM solar cells without the additive [202].

Donor–acceptor rod–coil terpolymer of P3HT segment, and polystyrene-acrylate segment with pending fullerene moiety segment was examined as additive to P3HT:PCBM solar cells. The copolymer self-assembled into nanofibrils, exhibiting a long-range nanofibrillar structure, similar to those of typical rod–coil block copolymer. 5% of addition to active layer resulted in enhancement of  $J_{SC}$  and consequently PCE by 35% compared to solar cell without additive [203].

Addition of polystyrene-poly(3-hexyothiophene) diblock copolymer increased  $J_{SC}$  and fill factor, resulting in overall increase of PCE by 26% compared to binary P3HT:PCBM blend. Addition of the PS-*b*-P3HT compatibilizer affected the PCBM segregation in the vertical direction – PCBM accumulation near the substrate interface was reduced with a corresponding increase in the middle region of the active layer. The most homogeneous profile was obtained at the PS-*b*-P3HT concentration of 5 wt. %, which was attributed to an increase in miscibility of P3HT and PCBM driven by the presence of the copolymer [204]. During thermal processes P3HT-*b*-PS block copolymer was found to assist the segregation of PCBM through microphase separation. Photovoltaic cell with P3HT-*b*-PS block additive provided conversion efficiency increased by 40% after thermal annealing compared to 1:1 P3HT:PCBM solar cell [205].

Well-defined coil-rod-coil triblock copolymer: poly(4-vinyltriphenylamine)-*block*-poly(3-hexylthiophene)-*block*-poly(4-vinyltriphenylamine) (PTPA-*b*-P3HT-*b*-PTPA) was used as a surfactant for P3HT:PCBM active layer. Power conversion efficiency of the device was enhanced from 3.9 to 4.4% (by increasing  $J_{SC}$ ) by adding 1.5% PTPA-*b*-P3HT-*b*-PTPA. According to authors, the morphology variation and the balance of the hole/electron mobility accounted for such enhancement. The fiber-like structure was observed for surfactant concentration range of 0-5%, while a sphere-like nanostructure was observed for the surfactant concentration of 1.5%. The sphere-like nanostructure led to a smaller domain size and enhanced interfacial area for charge separation as compared to the fiber-like structure. The incorporated PTPA-*b*-P3HT-*b*-PTPA surfactant extended the lifetime of solar cells and reduced the PCBM aggregation upon annealing as well, resulting in better thermal stability [206].

Styryl-functionalized polymerizable fullerene derivatives ([6,6]-phenyl-C61-butyric acid styryl ester - PCBS - and [6,6]-phenyl-C61-butyric acid styryl dendron ester - PCBSD) were in situ polymerized in P3HT:PCBM active layer for maintaining optimal nanomorphology of donor-acceptor blend. Solar cells with P3HT:PCBM:PCBSD ratios in active layers of 6:5:1 after long-time annealing (25 h in 150°C) exhibited PCE of 3.3-3.7%, (maximum PCE 4.0% - was recorded for solar cells annealed for 5-15 h). Devices with P3HT:PCBM:PCBS ratios in active layers of 6:5:1 demonstrated PCE of 3.8-3.6% (maximum PCE of 3.9% for devices annealed for 2-5h). Reference P3HT:PCBM solar cells featured dramatic decrease in PCE: from 4.1 to 0.7% upon annealing due to the phase segregation and resulting drop of  $J_{SC}$  and FF [207].

The increased crystallization of P3HT in the donor-acceptor mixture with PCBM was achieved by the addition of a block copolymer of P3HT and polyisoprene, P3HT-*b*-PI. The photovoltaic performance of devices comprising this blend was improved (maximum power conversion efficiency of 4.5% was achieved for copolymer containing 7 wt. % of the copolymer). It was concluded that P3HT-*b*-PI copolymer acted as a nucleation agent, promoting the crystallization of P3HT [208].

Poly(norbornene)-*graft*-poly(3-hexylthiophene) (PNB-*g*-P3HT) bottlebrush copolymers were investigated in ITO/PEDOT:PSS/active layer/ZnO/Al solar cells, but exhibited lower performance than P3HT:PCBM active layers [120].

Materials based on polysiloxanes are reported to improve parameters of solar cells as well. A surface-segregated thin layer of poly(dimethylsiloxane)-*block*-poly(methylmethacrylate) (PDMS-*b*-PMMA) formed by self-organization during spin-coating was utilized as an interfacial buffer layer in organic photovoltaic cells. PDMS-*b*-PMMA mixed into the spin-coating solution spontaneously accumulated at the surface of the active layer due to the low surface energy of PDMS while the PMMA block made the polymer solid and easy to handle. The introduction of the PDMS-*b*-PMMA layer improved PCE of the P3HT:PCBM cells from 3.05% to 3.56% on average. Addition of the proper amount of PDMS-*b*-PMMA (0.4 mg/ml) improved the OPV performance, while when an excessive amount (0.6-1.0 mg/ml) was added the performance decreased due to the insulation properties of PDMS-*b*-PMMA [209].

Incorporation of 1% of polyhedral oligomeric octaphenyl silsesquioxane (Ph-POSS) allowed for fabrication of the solar cell with PCE of 2.62% (26% increase with respect to P3HT:PCBM cells without modification). This enhancement was attributed to improved phase separation and light scattering within the film by Ph-POSS/PCBM aggregates, which increases the light absorbance efficiency in the device due to the increase of the photon absorption by extending the optical path traversed, resulting in increased exciton generation [210]. The layer of siloxane oligomers, inserted between the active layer and the electrode, formed by contact-printing with flat or structured PDMS stamp, was found to play the role in making the electrodes selective to their own charge carrier type and increasing PCE [211].

Diblock copolymer: poly(3-hexylthiophene)-*block*-poly(dimethylsiloxane) was reported as a donor material for organic photovoltaic devices. In P3HT-*b*-PDMS:PCBM blend films the phase-separated structure within several tens nanometer scale was obtained,

and the aggregation of PCBM was sufficiently suppressed by the incorporation of PDMS. PDMS segment is probably assembled into the interface between P3HT and PCBM to relieve the mismatch of the surface free energy. PCE of obtained devices increased with increasing length of PDMS segment. PCE of 2.45% was achieved in P3HT:PCBM (1:1) solar cells, 2.88% for the device with copolymer bearing short PDMS segment (400 g/mol, 3.5% PDMS content), 3.09% for the device with copolymer bearing medium PDMS segment (1000 g/mol, 5.4% PDMS content) and 3.24% for the device with copolymer bearing medium-long PDMS segment (1900 g/mol, 9.6% PDMS content). The increase in  $J_{SC}$  with maintained  $V_{OC}$  and FF accounted for PCE improvement of the devices. Nevertheless both P3HT:PCBM and P3HT-*b*-PDMS:PCBM active layers turned out to be prone to thermal degradation [98].

“Hairy” nanostructured hybrid material comprising RR P3HT chains densely grafted on silica nanoparticle core were prepared by grafting P3HT chains from activated organosilicon nanoparticles by means of KCTP. The nano-P3HT particles in a combination with PCBM (1:1) showed decent performance in solar cells with relatively large active area of 1 cm<sup>2</sup>, reaching PCE of 2.27% [212]. Poly(3-hexylthiophene)-functionalized siloxane nanoparticles (P3HT-SSQ NPs) were prepared by condensation of P3HT-silane compound. PCE of 2.5% was achieved for solar cell comprising 1:1 mixture of P3HT-SSQ NPs and PCBM as active layer, however fill factor was rather low (0.30) [213].



## VII. Experimental part

### 6 Materials, methods and equipment

Commercially available monomers, Grignard reagents, polysiloxanes and catalysts used in this work are collected in Tab. S.1.

#### 6.1 Syntheses of poly(3-hexylthiophene)s

**Nonregular poly(3-hexylthiophene) (NR P3HT)** was synthesized by means of chemical oxidation with iron(III) chloride ( $\text{FeCl}_3$ ) according to the method described by R. Sugimoto [214] with modifications based on V.M. Niemi's paper [215].

In a two-necked 500 mL flask equipped with an air condenser, a magnetic dipole and a gas capillary 18.90 g (0,117 mol) of  $\text{FeCl}_3$  and 225 mL of chloroform was placed followed by stirring for 10 min under nitrogen flow. Next, 5 mL (0,028 mol) of monomer (3-hexylthiophene) was added and polymerization was carried out in room temperature under nitrogen flow for 1.5 h followed by addition of 150 mL of deionized water to terminate the reaction and precipitation of polymer with 50 mL of acidic ethanol (acidified with HCl). Crude polymer was filtered under vacuum and fractionated by sequential Soxhlet extractions with ethanol (to wash off  $\text{FeCl}_3$ , inorganic salts and residual monomer), hexane (to extract oligomeric fraction) and chloroform (to extract polymeric fraction). Solutions of oligomeric and polymeric fractions were concentrated on rotary evaporator, poured on Petri dishes and allowed to air-dry, then dried in vacuum oven (60°C, 40 mbar). Obtained hexane fraction (FH 0.199 g, yield 4%) was sticky and brown-dark green in colour, while chloroform fraction (FC 1.799 g, yield 39%) formed slightly elastic opalescent dark green free-standing film.

**Regioregular poly(3-hexylthiophene) (RR P3HT)** was synthesized by means of GRIM/KCTP procedure developed by R.D. McCullough [61] with modifications based on J. De Girolamo's paper [216].

An oven-dried three-necked 100 mL flask equipped with a reflux condenser (cut off from the outside atmosphere), a gas capillary, a septum and a magnetic stirring bar was purged with nitrogen for 10 min, then 1.3 mL (6.13 mmol) of 2,5-dibromo-3-hexylthiophene, 21.5 mL of THF (distilled over metallic sodium prior to use) and 3.7 mL (7.46 mmol) of *t*-butylmagnesium chloride (2M diethyl ether solution) was placed in the flask followed by

heating at reflux, under nitrogen flow for 2 h. Then 0.0172 g (0.0317 mmol) of Ni(dppp)Cl<sub>2</sub> catalyst was added and polymerization was conducted for 1 h at gently reflux followed by quenching the reaction mixture in 150 mL of methanol. Crude polymer was filtered and fractionated by sequential Soxhlet extractions with methanol (to wash off catalyst, inorganic salts and residual monomer), hexane (to extract oligomeric fraction) and chloroform (to extract polymeric fraction). Solutions of oligomeric and polymeric fractions were concentrated on rotary evaporator, poured on Petri dishes and allowed to air-dry, then dried in vacuum oven (60°C, 40 mbar). Obtained hexane fraction (FH 0.071 g, yield 7%) was sticky and red-dark green, while chloroform fraction (FC 0.411 g, yield 40%) formed brittle and opalescent-dark green film.

To minimize contact of Grignard reagents used in syntheses of regioregular poly(3-hexylthiophene) with water and moisture in the air the following precautions were applied: laboratory glassware was oven-dried at 55°C for 48 h prior to use; reaction systems were sealed off from the atmosphere; inert gas (nitrogen) used to purge and fill reaction systems was dried by flow through Drierite™ gas drying unit; solvent (THF) was distilled over metallic sodium under dry nitrogen flow right before use; all reagents were dosed at Aldrich AtmosBag™ glove bag and transferred to the reaction system via syringes.

Syntheses of **vinyl-terminated regioregular poly(3-hexylthiophene) (P3HTvin)** was carried out by means of GRIM/KCTP route based on report of B.W. Boudouris [217], using the same reaction system and similar procedure as described for synthesis of regioregular poly(3-hexylthiophene).

Representative procedure for repeated syntheses of vinyl-terminated regioregular poly(3-hexylthiophene) was as follows. An oven-dried three-necked flask equipped with a reflux condenser (cut off from the outside atmosphere), a gas capillary, a septum and a magnetic stirring bar was purged with nitrogen for 10 min, then 1.3 mL (6.13 mmol) of 2,5-dibromo-3-hexylthiophene, 50 mL of THF (distilled over metallic sodium prior to use) and 3.71 mL (6.13 mmol) of *t*-butylmagnesium chloride (2M diethyl ether solution) was placed in the flask followed by heating at reflux, under nitrogen flow for 1.5 h. Then 0.0375 g (0.0692 mmol) of Ni(dppp)Cl<sub>2</sub> catalyst was added and polymerization was conducted for 1 h at room temperature followed by addition of 1.6 mL (1.15 mmol) vinylmagnesium bromide (0.7M solution in THF) and termination reaction conducted for 1 h at room temperature. Then the reaction mixture was quenched in 200 mL of methanol. Crude polymer was filtered and fractionated by sequential Soxhlet extractions with methanol (to wash off catalyst, inorganic

salts and residual monomer), hexane (to extract oligomeric fraction) and chloroform (to extract polymeric fraction). Solutions of oligomeric and polymeric fractions were concentrated on rotary evaporator, poured on Petri dishes and allowed to air-dry, then dried in vacuum oven (60°C, 40 mbar). Synthesis was repeated several times to provide enough P3HT for syntheses of copolymers. Obtained hexane fraction (FH 0.0623 g (average), yield 6%) was sticky and red-brown, while chloroform fraction (FCH 0.2998 g (average), yield 28%) formed brittle and opalescent-dark green film or flakes.

## 6.2 Syntheses of graft copolymers

Copolymers of polymethylsiloxanes grafted with poly(3-hexylthiophene) and, in most cases, other comonomers were synthesized by means of hydrosilylation reaction with poly(methylhydrosiloxane) (PMHS) and poly(dimethylsiloxane-*co*-methylhydrosiloxane), P(DMS-*co*-MHS), in facile, one-pot procedure. Synthetic paths are shown in the Fig. 6.1.

Procedure for synthesis of **poly(methylsiloxane) grafted with poly(3-hexylthiophene) (PMHS-*g*-P3HT)** was as follows. An oven-dried three-necked 100 mL flask, equipped with a reflux condenser (cut off from the outside atmosphere), a gas capillary, a septum and a magnetic stirring bar, was charged with 0.3500 g of vinyl terminated poly(3-hexylthiophene), chloroform fraction (P3HTvin FCH), purged with nitrogen for 10 min, then 30 mL of anhydrous toluene was added followed by heating to 60°C and stirring until P3HTvin dissolves. Then 0.5 mL of poly(methylhydrosiloxane) (PMHS) and 0.04 mL of Karstedt catalyst, platinum(0)-1,1,3,3-tetramethyl-1,3-divinyldisiloxane complex (PTDD, solution in xylene, Pt ~ 2%) were added and reaction was conducted under nitrogen flow for 24 h. Crude product was separated by evaporating solvent and purified by sequential Soxhlet extraction with methanol (to wash off catalyst and residual polysiloxane) and chloroform (to extract product). Copolymer Solution was concentrated on rotary evaporator, poured on Petri dish and allowed to air-dry, then dried in vacuum oven (60°C, 40 mbar). Obtained chloroform fraction of PMHS-*g*-P3HT (0.2055 g) formed sticky dark green film.

Procedure for synthesis of **poly(dimethylsiloxane-*co*-methylhydrosiloxane) grafted with poly(3-hexylthiophene) [P(DMS-*co*-MHS)-*g*-P3HT]** was as follows. An oven-dried three-necked 100 mL flask equipped with a reflux condenser (cut off from the outside atmosphere), a gas capillary, a septum, and a magnetic stirring bar was charged with vinyl

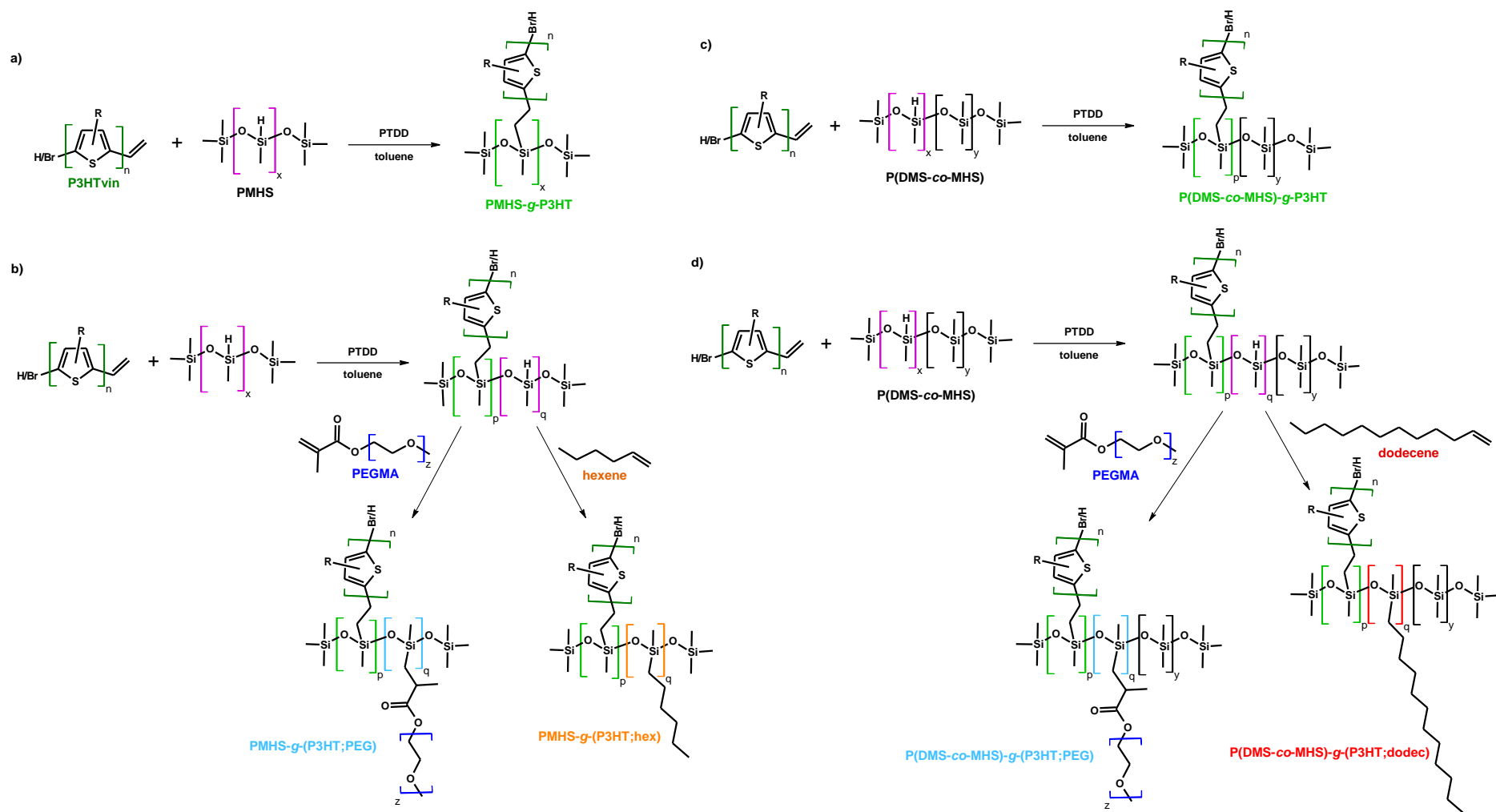


Fig. 6.1 Schematic paths for syntheses of graft copolymers: PMHS grafted with P3HT (a), PMHS grafted with P3HT and PEGMA or hexyl groups (b), PDMS-MHS copolymer grafted with P3HT (c), PDMS-MHS copolymer grafted with P3HT and PEGMA or dodecyl groups (d)

terminated poly(3-hexylthiophene), chloroform fraction (P3HTvin FC) (0.370 g), purged with nitrogen for 10 min, then anhydrous toluene (20 mL) was added followed by heating to 60°C and stirring until P3HTvin dissolves. Then 0.015 mL of trimethylsilyl terminated poly(dimethylsiloxane-co-methylhydrosiloxane) P(DMS-*co*-MHS) and 0.001 mL of Karstedt catalyst, platinum(0)-1,1,3,3-tetramethyl-1,3-divinyldisiloxane complex (PTDD, solution in xylene, Pt ~ 2%) were added and reaction was conducted under nitrogen flow for 24 h. Crude product was separated by evaporating solvent and purified by sequential Soxhlet extraction with methanol (to wash off catalyst and residual polysiloxane), and chloroform (to extract copolymer). Copolymer solution was concentrated on rotary evaporator, poured on Petri dish and allowed to air-dry, then dried in vacuum oven (60°C, 40 mbar). Obtained chloroform fraction (0.3485 g) of copolymer was similar in appearance to previously described poly(methylhydrosiloxane)-*graft*-poly(3-hexylthiophene) copolymer.

Representative procedure for **grafting poly(methylhydrosiloxane) with vinyl-terminated poly(3-hexylthiophene) and poly(ethylene glycol) methyl ether methacrylate or hexene [PMHS-*g*-(P3HT;*co*-*graft*)]** was as follows. An oven-dried three-necked 100 mL flask equipped with a reflux condenser (cut off from the outside atmosphere), a gas capillary, a septum, and a magnetic stirring bar was charged with vinyl terminated poly(3-hexylthiophene), purged with nitrogen for 10 min, then anhydrous toluene was added followed by heating to 60°C and stirring until P3HTvin dissolves. Then poly(methylhydrosiloxane) (PMHS) and Karstedt catalyst, platinum(0)-1,1,3,3-tetramethyl-1,3-divinyldisiloxane complex (PTDD, solution in xylene, Pt ~ 2%) were added and reaction was conducted under nitrogen flow for 12 h followed by adding poly(ethylene glycol) methyl ether methacrylate or hexane and continuing reaction for further 12 h. Crude product was separated by evaporating solvent and purified by sequential Soxhlet extraction with methanol (to wash off catalyst and residual polysiloxane), hexane (in some cases, to extract copolymer with P3HT short chains) and chloroform (to extract copolymer with P3HT long chains). Copolymer solution was concentrated on rotary evaporator, poured on Petri dish and allowed to air-dry, then dried in vacuum oven (60°C, 40 mbar). Obtained chloroform fraction of copolymers formed brown-dark green film, similar to RR P3HTvin, but a slightly more soft and sticky.

Copolymers were synthesised based on various PMHS backbone (different poly(methylhydrosiloxane) chain lengths, i.e.  $M_n$  390 g/mol (PMHS 390) and 1,700-3,200 g/mol (PMHS 1700-3200) and using P3HT of various chain lengths (hexane or chloroform

fraction of polymer). Feed composition and additional reaction conditions are summarized in Tab. 6.1.

Tab. 6.1 Copolymers grafted on PMHS backbone

Sample	PMS	V PMHS [ml]	P3HT	m P3HT [g]	V PTDD [mL]	V toluene [mL]	V cograft [mL]	Yield* [g]
PMHS-g-(P3HT;PEG) 1	PMHS 390	0.1	P3HTvin FH	0.387	0.03	30	PEGMA 2.75	<b>FH</b> 0.310 FC 0.076
PMHS-g-(P3HT;PEG) 2	PMHS 390	0.1	P3HTvin FC	0.892	0.03	60	PEGMA 2.75	FH 0.680 <b>FC</b> 0.739
PMHS-g-(P3HT;PEG) 3	PMHS 1700-3200	1.0	P3HTvin FC	0.901	0.04	60	PEGMA 7.50	FC 1.570
PMHS-g-(P3HT;hex) 1	PMHS 390	0.1	P3HTvin FC	0.342	0.01	30	Hex-1-ene 0.1	FC 0.369
PMHS-g-(P3HT;hex) 2	PMHS 1700-3200	0.04	P3HTvin FC	0.421	0.03	21	Hex-1-ene 0.07	FC 0.578

\* - fraction on which further investigation was focused is bolded

Representative procedure for **grafting poly(dimethylsiloxane-co-methylhydrosiloxane) with vinyl-terminated poly(3-hexylthiophene) and poly(ethylene glycol) methyl ether methacrylate or dodecene [P(DMS-co-MHS)-g-(P3HT;co-graft)]** was as follows. An oven-dried three-necked 100 mL flask equipped with a reflux condenser (cut off from the outside atmosphere), a gas capillary, a septum, and a magnetic stirring bar was charged with vinyl terminated poly(3-hexylthiophene), purged with nitrogen for 10 min, then anhydrous toluene was added followed by heating to 60°C and stirring until P3HTvin dissolves. Then trimethylsilyl terminated poly(dimethylsiloxane-co-methylhydrosiloxane) P(DMS-co-MHS) and Karstedt catalyst, platinum(0)-1,1,3,3-tetramethyl-1,3-divinyldisiloxane complex (PTDD, solution in xylene, Pt ~ 2%) were added and reaction was conducted under nitrogen flow for 12 h followed by adding hexene or dodecene and continuing reaction for further 12h. Crude product was separated by evaporating solvent and purified by sequential Soxhlet extraction with methanol (to wash off catalyst and residual polysiloxane), and chloroform (to extract copolymer with P3HT long chains). Copolymer solution was concentrated on rotary evaporator, poured on Petri dish and allowed to air-dry,

then dried in vacuum oven (60°C, 40 mbar). Obtained chloroform fractions of copolymers were similar in appearance to previously described polysiloxane graft copolymers.

Tab. 6.2 Copolymers grafted on P(DMS-*co*-MHS) backbone

Sample	V P(DMS- <i>co</i> -MHS) [mL]	P3HT	m P3HT [g]	V PTDD [mL]	V toluene [mL]	V cograft [mL]	Yield [g]
P(DMS- <i>co</i> -MHS)- <i>g</i> -(P3HT;PEG) 1	0.10	P3HTvin FH	0.102	0.034	10	PEGMA 0.40	0.120
P(DMS- <i>co</i> -MHS)- <i>g</i> -(P3HT;PEG) 2	0.07	P3HTvin FC	0.086	0.023	10	PEGMA 0.27	0.092
P(DMS- <i>co</i> -MHS)- <i>g</i> -(P3HT;dodec) 1	0.11	P3HTvin FH	0.112	0.038	11	Dodec-1-ene 0.21	0.224
P(DMS- <i>co</i> -MHS)- <i>g</i> -(P3HT;dodec) 2	0.04	P3HTvin FC	0.053	0.014	11	Dodec-1-ene 0.08	0.097

Copolymers were synthesised using P3HT of different chain lengths (hexane or chloroform fraction of polymer). Feed composition and additional reaction conditions are summarized in Tab. 6.2.

### 6.3 Molecular characterisation of polymers and copolymers

Nuclear magnetic resonance (NMR) spectra were recorded on a Varian Inova 300 MHz (100 MHz for  $^{13}\text{C}$  experiments), Varian 600 MHz, and Bruker Avance III 400 MHz (100 MHz for  $^{13}\text{C}$  experiments) spectrometers for solutions in deuterated chloroform ( $\text{CDCl}_3$ ) at room temperature (298 K), using tetramethylsilane (TMS) as an internal standard. Proton and carbon chemical shifts ( $\delta$ ) are reported in ppm downfield from TMS.

Fourier-transform infrared (FTIR) spectra were recorded on a Perkin Elmer Spectrum Two spectrometer with universal attenuated total reflectance (ATR) Single-Reflection Diamond module. In cases of band overlapping, band maxima were found through analysis of second derivative of the spectrum.

Gel permeation chromatography (GPC) in THF was performed on an Agilent 1260 Infinity chromatograph equipped with an isocratic pump, autosampler, degasser, column thermostat, multi-detector suite refractive index detector (MDS RID) calibrated on linear polystyrene standards (calibration points: 580, 1280, 2170, 4910, 11 440, 21 810, 28 770, 74

800, 139 400, 327 300 g/mol). The measurements were carried out in THF (HPLC grade) solutions of polymers (sample concentrations 1 mg/mL) at 40°C with a 0.8 ml/min flowrate. For separation a pre-column guard 5 µm 50 x 7.5 mm and PLGel 5 µm MIXED-C 300 x 7.5 mm column were used.

Matrix-assisted laser desorption/ionization–time of flight (MALDI-TOF) mass spectra were recorded on a Bruker Autoflex Speed spectrometer using *trans*-2-[3-(4-*tert*-butylphenyl)-2-methyl-2-propenylidene]malononitrile (DCTB) as a matrix.

#### 6.4 Fabrication and testing of gas sensors

Gas sensors were fabricated and tested at the Department of Optoelectronics at Silesian University of Technology by Marcin Procek PhD and Piotr Kałużyński MSc. Tested copolymers included: copolymers with P3HT and PEG grafted on PMHS backbone: PMHS-*g*-(P3HT;PEG) 1 and PMHS-*g*-(P3HT;PEG) 3; copolymers with P3HT and PEG grafted on P(DMS-*co*-MHS) backbone: P(DMS-*co*-MHS)-*g*-(P3HT;PEG) 1 and P(DMS-*co*-MHS)-*g*-(P3HT;PEG) 2; and copolymers with P3HT and alkyl, namely dodecyl, chains grafted on P(DMS-*co*-MHS) backbone: P(DMS-*co*-MHS)-*g*-(P3HT;dodec) 1 and P(DMS-*co*-MHS)-*g*-(P3HT;dodec) 2.

Investigated materials were tested as resistance (electronic) gas sensors for NO<sub>2</sub> detection. Thin polymer films were deposited either by spin coating from chloroform solutions (2.5 mg/mL, 500 rpm) or by drop coating from chlorobenzene (CB) solutions (2.5 mg/mL) on interdigital transducers (IDT) consisting of Au electrodes on Si/SiO<sub>2</sub> substrate, then dried under dry nitrogen atmosphere at elevated temperature. Roughness of fabricated layers was determined by AFM microscopy.

Sensors were tested under controlled temperature conditions: room temperature (23.5-25 °C), 50 °C and 100 °C. Resistance responses to the repeated exposure to NO<sub>2</sub> were measured for 50, 100, 200, 500 ppb and 1, 5, 10, 20 ppm concentrations of NO<sub>2</sub> in carrier gas – nitrogen or air, under continuous flow of 500 ml/min and relative humidity of 3.5 – 6 ± 1%. Cycling exposure and recovery periods were 30 min each.

Interaction of NO<sub>2</sub> (oxidizing gas) with P3HT and its copolymers, as *p*-type conducting materials, caused the decrease in the resistances of the sensors, which was monitored using multichannel switch unit. Response of the sensors was calculated as the ratio of the base



resistance in the carrier gas (ambient conditions): nitrogen or air, ( $R_a$ ) to the resistance upon the exposure to tested gas –  $\text{NO}_2$  ( $R_g$ ):

$$\text{Resistance response} = \frac{R_a}{R_g}$$

or as:

$$\text{Response} = \frac{R_a - R_g}{R_g} \times 100\%$$

UV irradiation with LED source of 393 nm wavelength was applied in some cases to improve dynamics of sensors recovery.

## 6.5 Fabrication and testing of photovoltaic devices

Solar cells of conventional architecture (glass/ITO/PEDOT:PSS/donor:PCBM/LiF/Al) were fabricated with active areas of 0.09 and 0.16 cm<sup>2</sup> on patterned indium tin oxide (ITO)/glass substrates, cleaned prior to use (sonicated sequentially in acetone, soap solution, water and isopropanol, dried under nitrogen and treated with UV-ozone for 30 min). Poly(ethylenedioxythiophene):poly(styrenesulfonate) (PEDOT:PSS) solution (Clevios<sup>TM</sup> P, VP Al4083), was spin coated on the substrates at 3000 rpm resulting in 40 nm conducting polymer contact layer, then active polymer layer was prepared by spin coating in from chlorobenzene (CB) solution at 1500-2500 RPM in the air, total concentration of 25-30 mg/ml. The thicknesses of the active layers were determined using a Veeco Dektak 150 profilometer, subtracting the thicknesses of PEDOT:PSS underlying layer. Materials investigated as donor included RR P3HT FC, PMHS-g-(P3HT;hex) 1 and PMHS-g-(P3HT;hex) 2, while [6,6]-phenyl-C<sub>61</sub>-butyric acid methyl ester (PCBM) was used as fullerene acceptor.

Preliminary optimization of the devices was performed. In tested solar cells P3HT (or copolymer):PCBM weight ratios were: 1:1, 3:2, 2:1. For all variants 3:2 donor:acceptor weight ratio was found optimal. The devices were annealed at 100°C for 5 min in nitrogen atmosphere prior or after deposition of contacts. The back electrode was deposited by means of high vacuum ( $5 \cdot 10^{-7}$  mbar) thermal evaporation: first thin layer of LiCl (1 nm) was deposited, followed by deposition of 100 nm Al contact. Then influence of further annealing in 5 or 10 min time increments, total of 60 min [180 min in case of P(DMS-co-MHS)-g-P3HT] on the parameters of the solar cells was investigated. Subsequently, influence of

storage in the room temperature under inert conditions (N<sub>2</sub> atmosphere) for up to 8 days was investigated as well. Active layer compositions and thicknesses are summarized in Tab. 6.3.

Tab. 6.3 Fabricated solar cells

Material	Concentration (total)	Spin coating speed	Device no.	Active layer thickness	Annealing
P3HT FCH	30 mg/ml	1500 RPM	1	94 (± 2) nm	prior to contact deposition
			2	96 (± 2) nm	prior to contact deposition
			3	96 (± 3) nm	after contact deposition
PMHS- <i>g</i> -(P3HT;hex) 1	25 mg/ml	2500 RPM	1	84 (± 5) nm	prior to contact deposition
			2	87 (± 3) nm	after contact deposition
PMHS- <i>g</i> -(P3HT;hex) 2	25 mg/ml	2500 RPM	1	67 (± 2) nm	prior to contact deposition
			2	72 (± 1) nm	after contact deposition
P(DMS- <i>co</i> -MHS)- <i>g</i> -P3HT	25 mg/ml	2000 RPM	1	61 (± 8) nm	after contact deposition

UV-vis spectroscopy of active layers was conducted on a PerkinElmer Lambda 1050 spectrophotometer equipped with a 3D WB PMT/InGaAs/PbS detector module.

Optical band gaps were calculated from the onset of the absorption peak on the UV-Vis spectrum according to the equation:

$$E = \frac{hc}{\lambda} [J] = \frac{1239.8}{\lambda} [eV]$$

$h$  – Planck constant ( $6.6261 \times 10^{-34}$  J·s),  $c$  – speed of light ( $2.9979 \times 10^8$  m/s),  $1 \text{ eV} = 1.602176634 \times 10^{-19}$  J

Current density-voltage (J-V) characteristics of tested solar cells were recorded using a Keithley 2400 source meter under  $\approx 100 \text{ mW/cm}^2$  white light illumination from a tungsten-halogen lamp filtered by a Hoya LB120 daylight filter simulating AM1.5G solar spectrum. No dependence of performance on the size (9 or 16 mm<sup>2</sup>) of solar cell was observed. Routinely power conversion efficiency values were calculated from short circuit current density ( $J_{sc}$ ), open circuit voltage ( $V_{oc}$ ) and fill factor (FF) values determined from J-V curve according to the equation (assuming power of incident sunlight equal to  $100 \text{ mW/cm}^2$ ):

$$\text{PCE} = \frac{V_{\text{OC}} \times J_{\text{SC}} \times \text{FF}}{100} \times 100\%$$

Since solar simulator spectrum is not a perfect match with AM1.5G spectrum, J-V response of solar cells recorded under illumination with solar simulator provide a good estimation of  $V_{\text{OC}}$  and FF values, but require spectral mismatch correction to obtain accurate  $J_{\text{SC}}$  and resulting PCE values. Precise values of short circuit current density ( $J_{\text{SC}}$  EQE) were calculated by integrating the AM1.5 G solar spectrum and the spectral response of the cells. EQEs were measured using modulated monochromatic light from a 50 W tungsten-halogen Philips Focusline lamp passing through an Oriel Cornerstone 130 monochromator with the use of a mechanical beam chopper. The response was recorded as the voltage produced by a Stanford Research Systems SR570 preamplifier with a lock-in SR830 amplifier. All measurements were done against a Si reference cell with known spectral response.

For the atomic force microscopy (AFM) investigation the NTGRA Prima system with a semi-contact mode, using HA-HR probes (NT-MDT) with a 260 kHz work frequency was applied. The typical curative radius of the tip of the used probes was less than 10 nm, the tip length was  $\leq 1 \mu\text{m}$ , and the cantilever length was 123  $\mu\text{m}$ . All of the measurements were performed using a scanning frequency of 0.5 Hz (scan speed for  $5 \times 5 \mu\text{m}$  areas was approximately 5  $\mu\text{m/s}$ ). Root mean square (RMS) values were used as estimation of surface roughness.

## VIII. Results and discussion

### 7 Structural analysis of polymers and copolymers

#### 7.1 Poly(3-hexylthiophene), polysiloxanes and poly(ethylene glycol)

**3-hexylthiophene (3HT)**, monomer for synthesis of nonregular poly(3-hexylthiophene), was used as purchased, without further purification, and characterized by NMR analysis prior to use:  $^1\text{H}$  NMR (300 MHz,  $\text{CDCl}_3$ ):  $\delta$  (ppm) 7.20 (dd,  $^4J_1=2.9$  Hz,  $^3J_2=4.9$  Hz, 1H, Ar-**H-5**), 6.91-6.89 (dd,  $^3J_2=4.9$  Hz,  $^4J_3=1.2$  Hz, Ar-**H-4** + dd,  $^4J_1=2.9$  Hz,  $^4J_3=1.2$  Hz, Ar-**H-2**, 2H), 2.61 (t,  $^3J_4=7.5$  Hz, 2H,  $\alpha$ -**CH<sub>2</sub>**), 1.61 (quint,  $^3J_4=7.5$  Hz, 2H,  $\beta$ -**CH<sub>2</sub>**), 1.30 (m, 6H, -(**CH<sub>2</sub>**)<sub>3</sub>-**CH<sub>3</sub>**), 0.88 (t,  $^3J_5=6.8$  Hz, 3H, -**CH<sub>3</sub>**). Obtained spectrum is consistent with data available in the literature [218] and in Spectral Database for Organic Compounds (SDBS) [219].

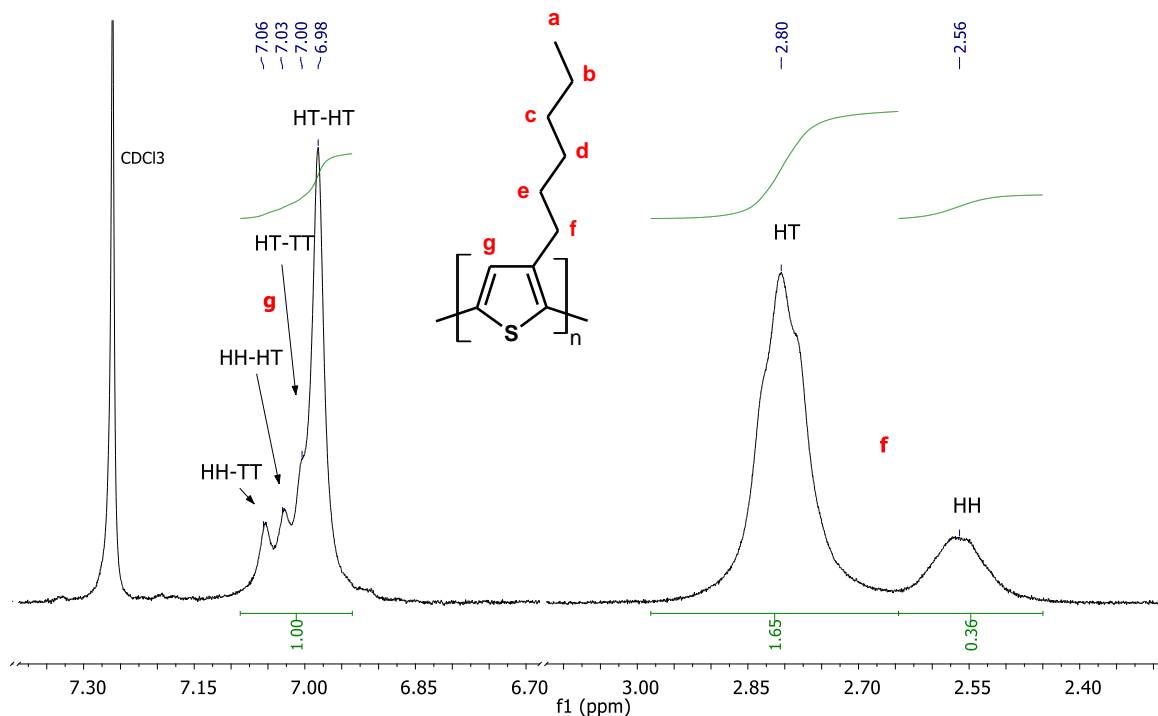


Fig. 7.1  $^1\text{H}$  NMR spectrum of NR P3HT FC (300 MHz,  $\text{CDCl}_3$ ), expansions of aromatic protons (g) region with peak assignments to regiomeric triads and  $\alpha$ - $\text{CH}_2$  protons (f) region with peak assignments to regiomeric dyads

$^1\text{H}$  NMR spectrum of synthesized **nonregular poly(3-hexylthiophene)** (chloroform fraction) (**NR P3HT FC**) (Fig. S.1) shows typical features characteristic for presence of regiomeric defects in the structure of the polymer [55,56,220]. Fig. 7.1 shows an

expansion of aromatic protons region and  $\alpha$ -methylene protons region. In the aromatic protons region four signals are present: dominant peak of regioregular, head-to-tail – head-to-tail (HT-HT) triad at 6.98 ppm, and three minor peaks at 7.00, 7.03 and 7.05 corresponding with nonregular connections: head-to-tail – tail-to-tail (HT-TT) triad, head-to-head – head-to-tail (HH-HT) triad, and head-to-head – tail-to-tail (HH-TT) triad, respectively. In the  $\alpha$ -methylene protons region 2 broad peaks are distinguishable: dominant signal of head-to-head (HT) dyads at 2.80 ppm and minor signal of head-to-head structural defects at 2.56 ppm. Based on the relative ratios of HT and HH peaks in the  $\alpha$ -methylene protons region regioregularity (percentage of HT couplings in polymer chain) of synthesized NR P3HT FC was estimated at 82%.

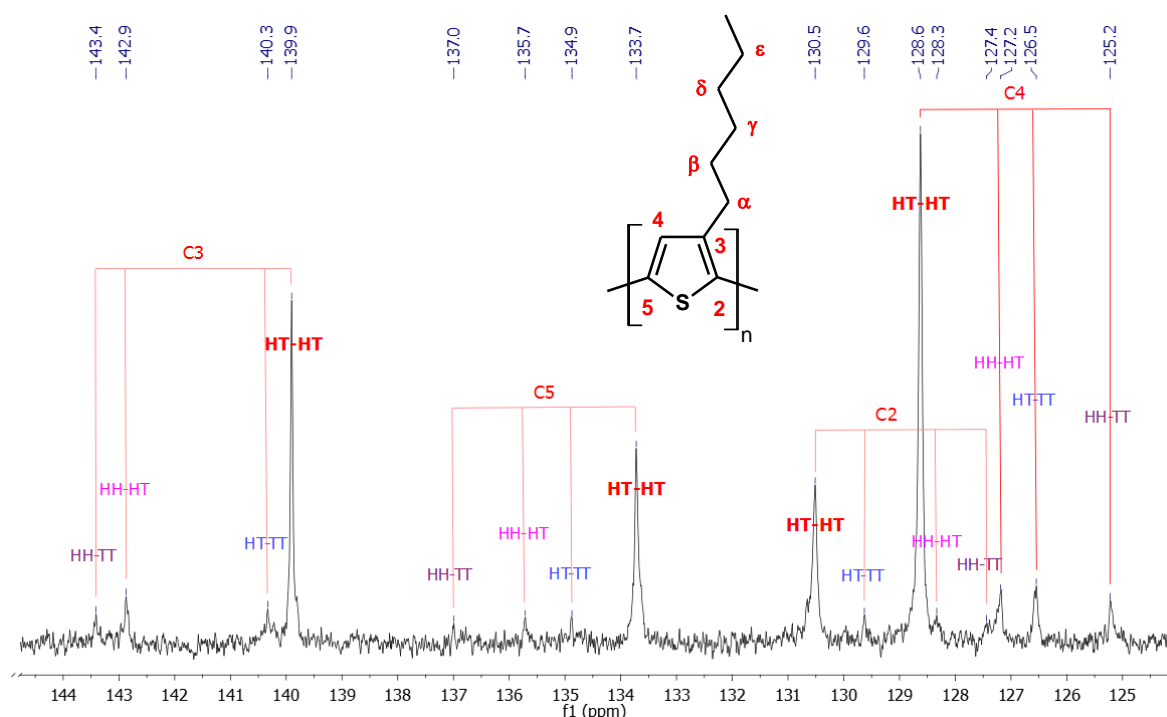


Fig. 7.2  $^{13}\text{C}$  NMR spectrum of NR P3HT FC (100 MHz,  $\text{CDCl}_3$ ), expansion of aromatic carbons region with assignment of the peaks to regioisomeric triads

Fig. S.2 presents  $^{13}\text{C}$  NMR spectrum of NR P3HT FC with the assignments of peaks. In Fig. 7.2 expansion of aromatic carbon region of  $^{13}\text{C}$  NMR spectrum is shown with 16 peaks and their assignments to regioisomeric triads based on literature [134–136] and heteronuclear single quantum correlation (HSQC) spectrum (Fig. S.3). Major peaks at 128.6, 130.5, 133.7 and 139.9 ppm are ascribed to carbons of thiophene ring in HT-HT triads, while minor peaks are ascribed to regioisomeric defects. What is more, peaks at 125.2, 126.5 and 127.2 ppm are more pronounced than the other minor peaks, and peak at 128.6 ppm has higher intensity than other HT-HT peaks, which suggests these carbons are bonded to protons

and their intensity is increased due to the nuclear Overhauser effect (NOE). Finally, HSQC spectrum shows correlations for pairs of peaks: 6.98 with 128.6 ppm, 7.01 with 126.7 ppm, 7.03 with 127.1 ppm and 7.05 with 125.2 ppm, which allows to assign those  $^{13}\text{C}$  NMR peaks to HT-HT, HT-TT, HH-HT and HH-TT triads, respectively. HSQC spectrum also confirms assignment of aliphatic carbons based on correlations with protons.

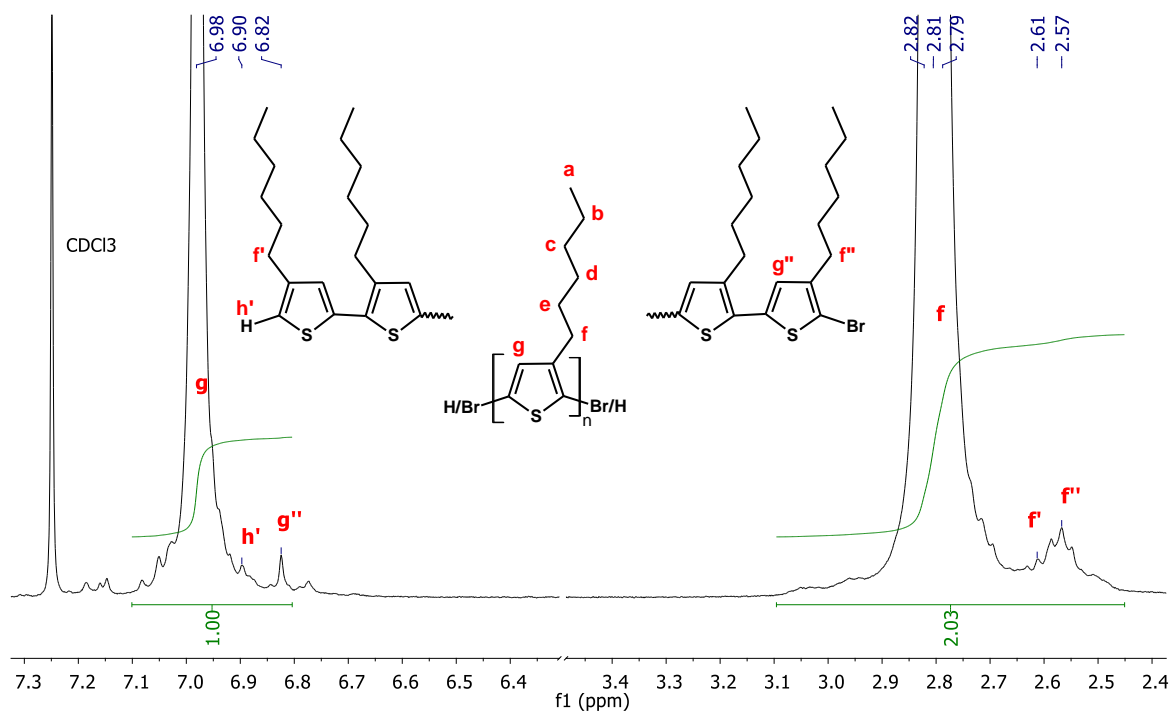


Fig. 7.3  $^1\text{H}$  NMR spectrum of RR P3HT FC (400 MHz,  $\text{CDCl}_3$ ), expansions of aromatic protons ( $g$ ) region and  $\alpha\text{-CH}_2$  protons ( $f$ ) region with assignments of end groups signals

$^1\text{H}$  NMR spectrum of **regioregular poly(3-hexylthiophene) (RR P3HT FC)** (Fig. S.4) synthesised by GRIM (KCTP) method shows typical features of P3HT with high regioregularity (almost exclusively made of HT-HT linkages) [55,56,61]: such as singlet at 6.98 ppm corresponding to thiophene aromatic proton in HT-HT couplings with no distinct accompanying peaks of regioregularity defects, and triplet-like multiplet of  $\alpha$ -methylene protons at 2.81 ppm accompanied with very small peak at 2.57 ppm, arising from terminal groups rather than HH defects. When investigated closer (Fig. 7.3), these two regions reveal more information. In aromatic region two more peaks are discernible: singlet at 6.82 ppm originating from aromatic proton at 4 position of HT Br-terminal thiophene unit ( $g'$ ), and singlet at 6.90 ppm originating from aromatic proton at 2 position of terminal HT thiophene unit ( $h'$ ) [139,221]. In  $\alpha$ -methylene region small triplet at 2.57 ppm ( $^3J=7.6$  Hz) is recognized originating from protons of  $\alpha\text{-CH}_2$  group in Br-terminal unit ( $f''$ ) [205], and much weaker, partially overlapping with 2.57 ppm signal, triplet at 2.61 ppm ( $^3J=7.5$  Hz) originating from

protons of  $\alpha$ -CH<sub>2</sub> group in H-terminal unit (*f'*) [70,222]. HSQC spectrum of RR P3HT FC (Fig. S.5) confirms considerations about high regioregularity showing in aromatic region main proton signal at 6.98 ppm correlated with carbon at 128.6 ppm (HT-HT coupling) and small proton signal at 7.00 ppm correlated with carbon at 126.6 ppm (HT-TT coupling), which is consistent with the mechanism of polymerization on Ni(dppp)Cl<sub>2</sub> catalyst which results in one HT-TT coupling defect in the polymer chain [62,69]. Also, small aromatic proton signal at 6.82 ppm correlated with carbon at 126.6 ppm confirms presence of Br-terminal unit [139].

Matrix-assisted laser desorption/ionization time of flight (MALDI-TOF) spectrum of RR P3HT FC (Fig. S.6) shows that all possible combinations of terminal units are present in the polymer, i.e. H-P3HT-Br, H-P3HT-H and Br-P3HT-Br, with H-P3HT-Br being dominant species, as expected based on literature [77].

Detailed NMR analysis was performed for chloroform fraction of **vinyl-terminated regioregular poly(3-hexylthiophene), (P3HTvin FC)**, as representative example of P3HTvin species. <sup>1</sup>H NMR spectrum of P3HTvin FC (Fig. S.7) shows features characteristic for regioregular P3HT, such as singlet peak of thiophene aromatic proton at 6.98 ppm and triplet-like peak of  $\alpha$ -CH<sub>2</sub> protons at 2.81 ppm, and also additional peaks revealing presence of vinyl end groups, among which the most important and easy to observe are two doublets at 5.51 and 5.12 ppm [83,223], accompanied with signals of -CH=CH<sub>2</sub> proton and aromatic proton of vinyl end-capped terminal thiophene unit located in 6.8-6.9 ppm region [82]. Detailed analysis of <sup>1</sup>H NMR and <sup>1</sup>H-<sup>1</sup>H Correlation Spectroscopy (COSY) spectra focused on vinyl group and other end groups leads to assignments shown in Fig. 7.4.

<sup>1</sup>H-<sup>1</sup>H COSY spectrum (Fig. 7.5) shows off-diagonal correlation of doublets at 5.13 and 5.51 ppm with multiplet signal at 6.85 ppm, which confirms coupling between them and leads to assignment of 6.85 ppm signal to -CH=CH<sub>2</sub> proton (*i*). Determined based on <sup>1</sup>H NMR spectrum coupling constants (5.51 ppm, d, <sup>3</sup>J<sub>1</sub>=17.2 Hz, *k*, 5.13, d, <sup>3</sup>J<sub>2</sub>=11.0 Hz, *j*), agree with typical values for such protons [224], and are in accordance with coupling constants of *i* proton doublet of doublets signal centered at 6.85 ppm, with individual peaks at 6.90, 6.86, 6.84 and 6.80 ppm (dd, <sup>3</sup>J<sub>1</sub>=17.2 Hz, <sup>3</sup>J<sub>2</sub>=11.0 Hz). Analysis of distances between individual lines of this multiplet (expressed in ppm) with changes of base frequency of NMR spectrometer (Fig. 7.6) shows that this distance changes, while coupling constant expressed in Hz remains unchanged, which confirms that it is in fact one multiplet, not a set of separate singlets. Integrals of *j*, *k* and sum of components of *i* protons are equal to each

other, and also equal to integration of singlet peak at 6.88 ppm, which confirms the assumption, that this signal belongs to aromatic proton of terminal thiophene unit bonded to vinyl group ( $g'$ ).

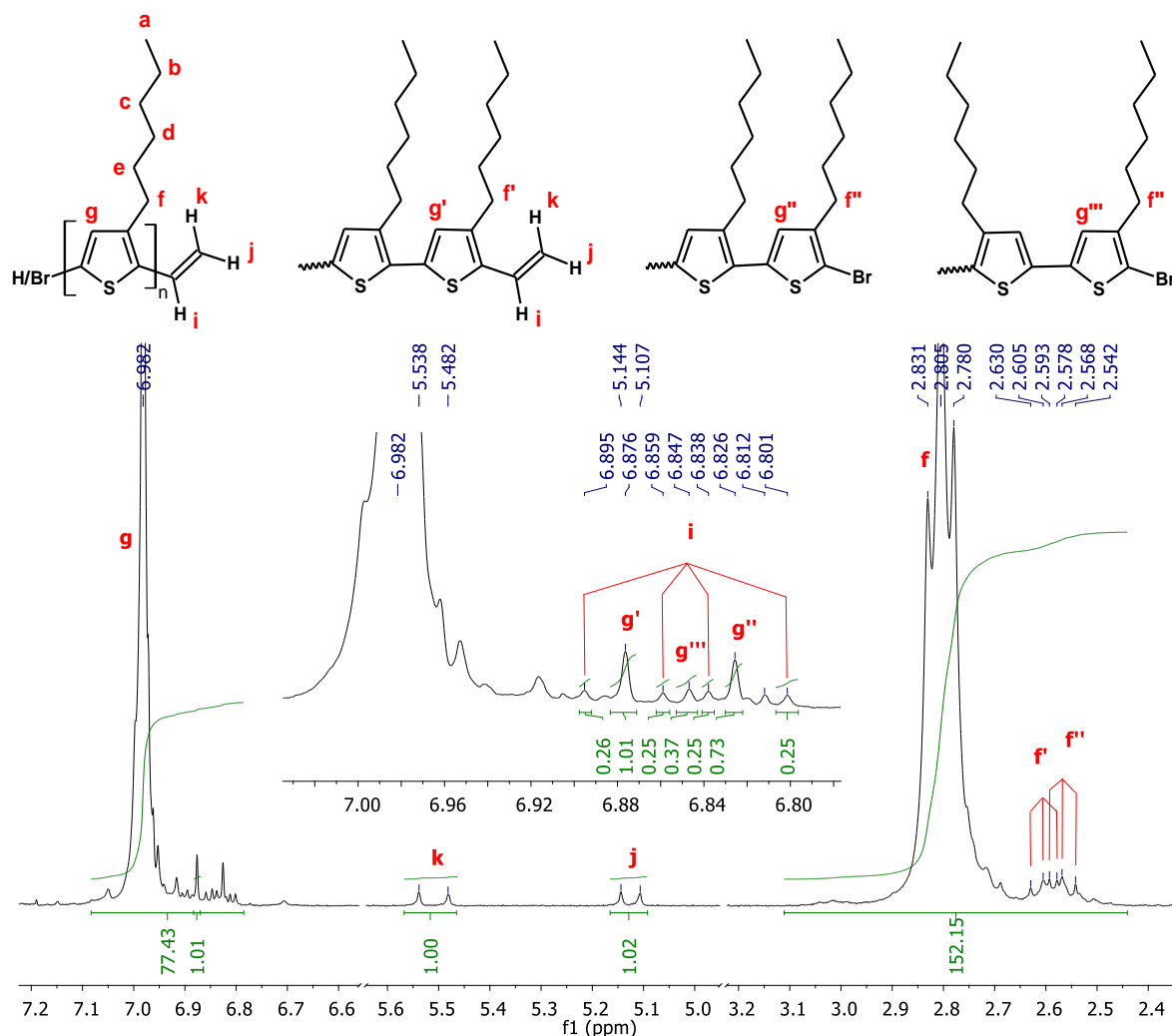


Fig. 7.4  $^1\text{H}$  NMR spectrum of P3HTvin FC (300 MHz,  $\text{CDCl}_3$ ), expansion of aromatic protons ( $g$ ) region, vinyl group protons ( $j$ ,  $k$ ) region, and  $\alpha\text{-CH}_2$  protons ( $f$ ) region with assignments of peaks

In the aromatic protons region, upfield to the signal of aromatic protons of thiophene rings in P3HT chain, there are a few more distinguishable peaks, among them most pronounced is singlet at 6.83 ppm, correlated with carbon signal at 126.7 ppm (see HSQC spectrum, Fig. S.8) – ascribed to aromatic proton at 4 position of Br-ended terminal HT thiophene unit ( $g'$ ), likewise in RR P3HT FCH. Another recognisable signal is small singlet at 6.85 ppm, which shows correlation with carbon signal at 124.3 ppm on HSQC spectrum (Fig. S.8), assigned to aromatic proton at 4 position of Br-ended terminal TT thiophene unit ( $g''$ ) [222].



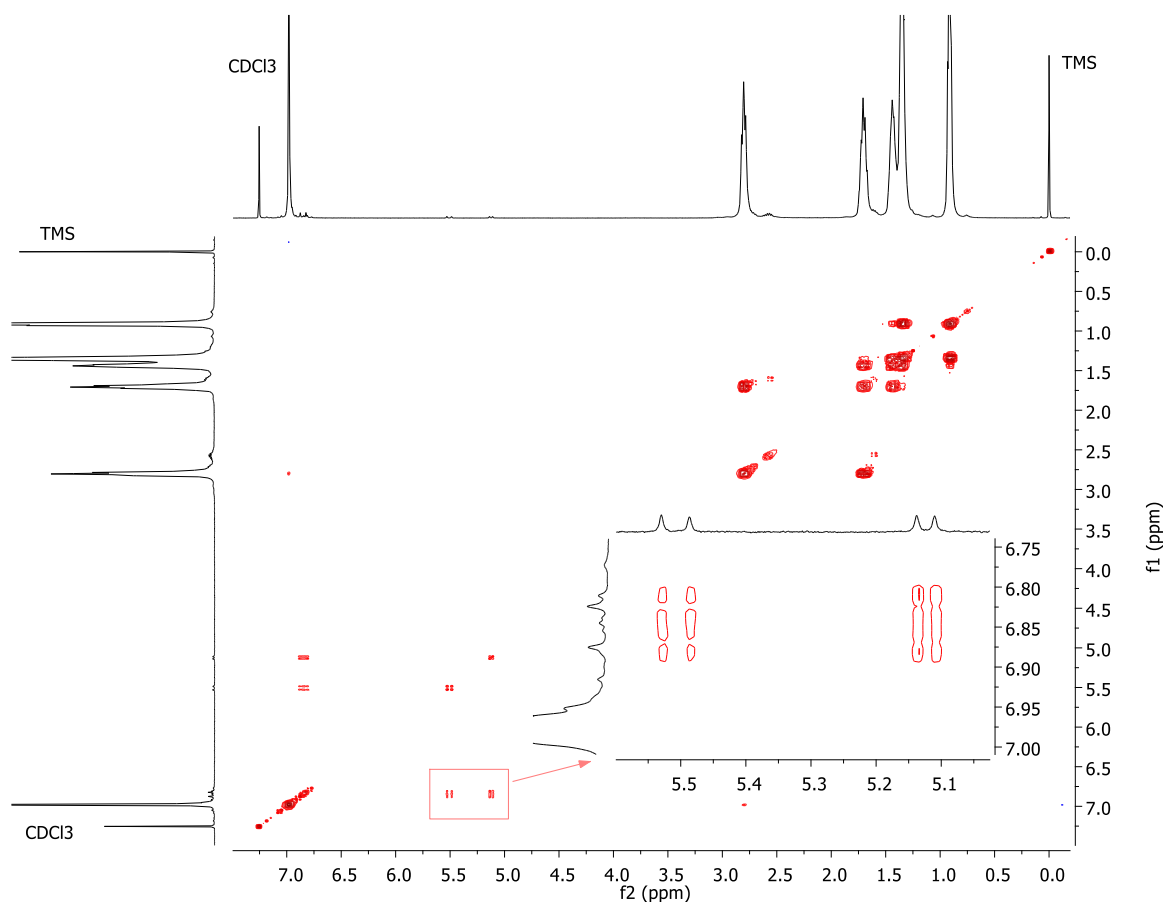


Fig. 7.5  $^1\text{H}$ - $^1\text{H}$  COSY spectrum of P3HTvin FC (400 MHz,  $\text{CDCl}_3$ ) with expansion of correlation peaks between  $-\text{CH}=\text{CH}_2$  proton and  $-\text{CH}=\text{CH}_2$  protons

Last region of P3HTvin FC NMR spectrum revealing important information about the structure is  $\alpha$ -methylene protons region. Besides main triplet-like peak of  $\alpha$ - $\text{CH}_2$  groups of regioregularly arranged 3-hexylthiophene units in P3HT chains at 2.81 ppm, for P3HTvin, two minor triplet-like peaks upfield to the main peak are observed. Small triplet centered at 2.57 ppm ( $^3J=7.6$  Hz) is ascribed to protons of  $\alpha$ - $\text{CH}_2$  group in Br-terminal unit ( $f''$ ), like in RR P3HT FC [70,222], and small triplet at 2.61 ppm ( $^3J=7.6$  Hz) is ascribed to protons of  $\alpha$ - $\text{CH}_2$  group in vinyl-terminal unit ( $f'$ ) (Fig. 7.4). Gradual separation of these triplets can be observed when frequency of used NMR spectrometer is increased and resolution of obtained spectrum is improved (Fig. 7.6).

MALDI-TOF spectrum of P3HTvin FCH (Fig. S.9) shows that vin-P3HT-Br is dominant combination of end groups for this type of polymer, but also Br-P3HT-Br, H-P3HT-vin and H-P3HT-Br polymer chains are present.

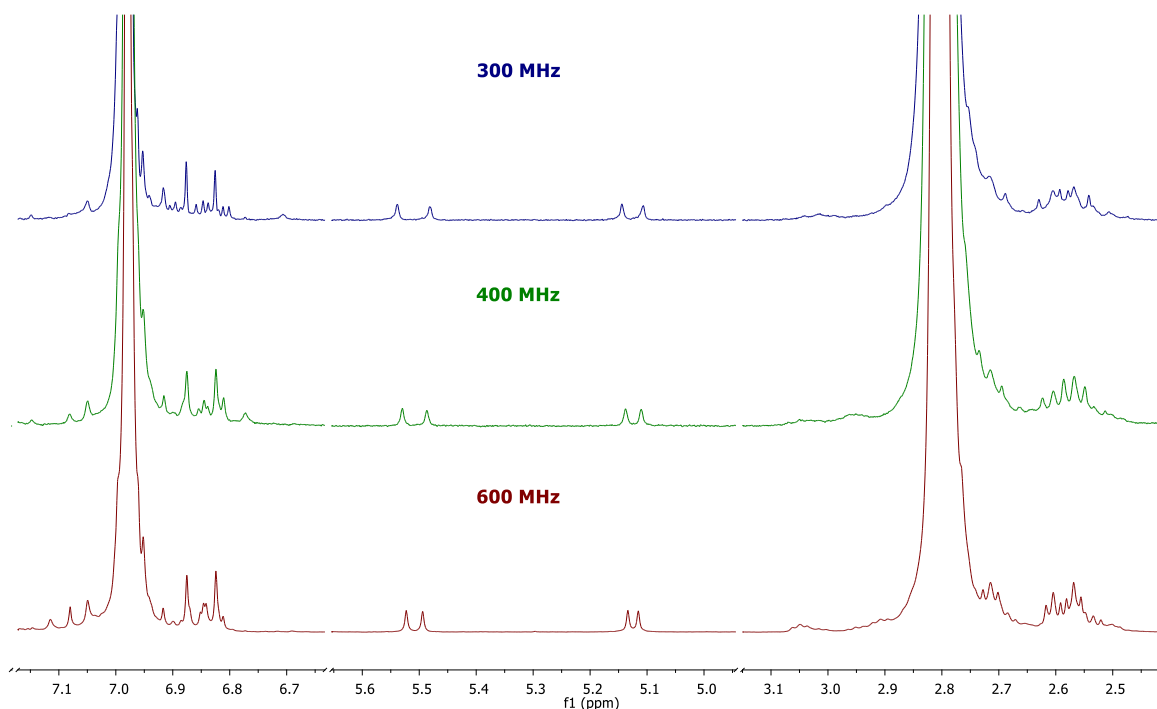


Fig. 7.6 Stacked spectra of P3HTvin FC obtained on 300 MHz (blue), 400 MHz (green) and 600 MHz (red) spectrometers showing changes of aromatic protons signals, vinyl protons signals and  $\alpha$ -CH<sub>2</sub> protons signals expressed in ppm with changing base frequency of the spectrometer

Fig. S.10 presents FTIR spectrum of vinyl terminated regioregular poly(3-hexylthiophene), chloroform fraction (P3HTvin FC), which is representative for all obtained vinyl-terminated P3HTs. It shows typical bands characteristic for regioregular P3HT. Thiophene ring gives rise to bands: stretching ( $\nu$ ) C-H vibrations at 3055 cm<sup>-1</sup> (weak), asymmetric (as; 1510 cm<sup>-1</sup>, medium-weak) and symmetric (s) stretching C=C vibrations (1454 cm<sup>-1</sup>, medium, broad due to the overlapping with bands of CH<sub>2</sub> and CH<sub>3</sub> deformations in hexyl chains), and out-of-plane C-H deformations in thiophene ring at 819 cm<sup>-1</sup> (medium, occurring at position which indicates high regioregularity [56]). Aliphatic hexyl side chains give rise to bands: at 2954 cm<sup>-1</sup> (strong, asymmetric C-H stretching of CH<sub>3</sub> group), 2922 cm<sup>-1</sup> (strong; asymmetric C-H stretching of CH<sub>2</sub> group) and 2854 cm<sup>-1</sup> (strong; symmetric C-H stretching of CH<sub>2</sub> group) overlapping with peak at about 2870 cm<sup>-1</sup> (medium-strong; symmetric C-H stretching of CH<sub>3</sub> group), complex peak (1454 cm<sup>-1</sup>, medium) covering bands of asymmetric C-H bending of CH<sub>3</sub> group and symmetric C-H bending of CH<sub>2</sub> groups, peak of symmetric C-H deformations of CH<sub>3</sub> group (1377 cm<sup>-1</sup>, medium-weak), and a band of rocking ( $\rho$ ) deformation of (CH<sub>2</sub>)<sub>5</sub> alkyl chain at 725 cm<sup>-1</sup> (weak). In addition, very weak band at 1650 cm<sup>-1</sup>, attributed to C=C stretching vibration of end vinyl group is present in the spectrum.

Three approaches were employed to estimate molecular weight of synthesized P3HTs: GPC, MALDI-TOF and  $^1\text{H}$  NMR analysis of end groups.  $^1\text{H}$  NMR end groups analysis was performed based on the ratio of integrals of dominant aromatic HT-HT signal at 6.98 ppm to signals of aromatic protons in end groups (sum of vinyl-terminated unit signal at 6.88 ppm, peaks of aromatic protons of Br-ended unit at 6.83 and 6.85 ppm, and peak of aromatic proton of H-ended unit at 6.81 ppm). Comparison of second group of  $^1\text{H}$  NMR signals: integrals of main  $\alpha\text{-CH}_2$  protons peak at 2,80 ppm with peaks of  $\alpha\text{-CH}_2$  protons in end groups at 2.6-2.5 ppm set for 4 protons (two  $\alpha\text{-CH}_2$  end groups, assuming linear P3HT chains) gave similar results as comparison of integrals of aromatic protons. Number average molecular weight based on MALDI-TOF analysis was calculated from equation:

$$M_n = \frac{\sum_i \text{Int}_i M_i}{\sum_i \text{Int}_i}$$

$\text{Int}_i$  – intensity of molecular peak for macromolecules of mass  $M_i$

From the results (Tab. 7.1) it is clear that GPC, as indirect chromatography technique, based on calibration with respect to set of polystyrene standards, tends to systematically overestimate  $M_n$ ,  $M_w$  and  $\bar{M}_w/\bar{M}_n$  of P3HT [77]. MALDI-TOF analysis seems a better choice, as a direct method for determination of  $M_n$ . However, taking into consideration rather high dispersities determined by GPC, especially for hexane fractions of P3HT, it is probable that MALDI-TOF underestimates  $M_n$  values to some extent since macromolecules with lower molecular weight desorb more easily than macromolecules with higher molecular weight and therefore molecular weight distribution might be shifted towards lower molar masses. Results obtained from  $^1\text{H}$  NMR end groups analysis give number of repeating units in P3HT chains even higher than GPC, which suggests that signals of end groups on NMR spectrum are too small and not well resolved due to the low spectrometer frequency routinely used (300 MHz), therefore do not give reliable values of integrals, (lower than expected), leading to systematic overestimation of  $M_n$  values. 600 MHz spectrometer was used for  $^1\text{H}$  NMR end group analysis of one P3HT sample (values with asterisk in Tab. 7.1). Multiplets in 600 MHz spectrum are narrower, better resolved, with higher signal to noise ratio than in 300 MHz spectrum, providing more accurate integrals. Analysis of integrals at 2.8-2.55 ppm region results in the following estimation: average number of repeating units ( $n$ ) equals 45 for chloroform fraction and 15 for hexane fraction.

Tab. 7.1 Number average molecular weights ( $M_n$ ), number of repeating thiophene units ( $n$ ) and dispersities ( $\mathcal{D}_M$ ) obtained based on GPC<sup>†</sup>, MALDI-TOF and end group analysis by <sup>1</sup>H NMR

P3HT	$M_n$ (GPC)	$n$ (GPC)	$\mathcal{D}_M$ (GPC)	$M_n$ (MALDI- TOF)	$n$ (MALDI- TOF)	$\mathcal{D}_M$ (MALDI- TOF)	$n$ (NMR)*
NR P3HT	47,900	288	5.12	-	-	-	-
RR P3HT (Br/H)	9,500	57	1.28	5,285	32	1.09	69
P3HTvin FH	3,300	19	1.86	2,302	13	1.15	28
	3,600	21	1.90				27
							30
							15*
P3HTvin FC	9,650	58	1.36	6,244	37	1.06	60
	9,550	57	1.40				61
	10,650	63	1.51				64
							52
							57
				54			
						45*	

\* Values without asterisk were obtained for 300 MHz spectrometer, with asterisk – for 600 MHz spectrometer

Taking all the above considerations into account it is concluded that MALDI-TOF and 600 MHz <sup>1</sup>H NMR end group analysis will give the best estimation of P3HT average molecular weight and average number of repeating units in polymer chain, closest to real values. Based on that,  $n$  was estimated at 37-45 units for chloroform fraction, and at 13-15 units for hexane fraction.

<sup>1</sup>H NMR analysis was performed to verify the structure of used polysiloxanes declared by a manufacturer (Sigma Aldrich). <sup>1</sup>H NMR spectra of poly(methylhydrosiloxane)s should exhibit typical features described in literature [143,144]. First one is the region of Si-CH<sub>3</sub> protons signals at 0.22-0.10 ppm in which 3 groups of signals can be distinguished: most downfield shifted group of -SiHCH<sub>3</sub>- protons signals at ~0.20 ppm, upfield shifted group of -SiHCH<sub>3</sub>-Si(CH<sub>3</sub>)<sub>3</sub> protons signals at ~0.15 ppm and terminal group, -Si(CH<sub>3</sub>)<sub>3</sub> protons signal (singlet) at ~0.12 ppm. Second one is -SiHCH<sub>3</sub>- protons region at ~4.65-4.72 ppm, divided into 2 groups: downfield shifted broad signal of -SiHCH<sub>3</sub>- protons in the repeating unit adjacent to another -SiHCH<sub>3</sub>- unit at 4.72 ppm and upfield shifted signal of -SiHCH<sub>3</sub>- protons in the repeating unit adjacent to terminal -Si(CH<sub>3</sub>)<sub>3</sub> unit at ~4.67 ppm.

$^1\text{H}$  NMR spectra of both poly(methylhydrosiloxane)s applied in synthesis of copolymers: **poly(methylhydrosiloxane) of Mn 390 g/mol (PMHS-S)** (Fig. S.11) and **poly(methylhydrosiloxane) of Mn 1,700-3,200 g/mol (PMHS-L)** (Fig. S.12) feature typical attributes described above. Comparison of integrals of  $-\text{CH}_3$  versus Si-H protons allows to estimate average number of repeating  $-\text{SiHCH}_3-$  units at about 4 for PMHS-S and at about 38 for PMH-L.

According to literature in poly(dimethylsiloxane-*co*-methylhydrosiloxane) copolymer triad effect can be observed for  $-\text{Si}(\text{CH}_3)_2-$  and  $-\text{Si}(\text{H})\text{CH}_3-$  groups [143]. In accordance, two sets of three signals (triad sequences) are expected in the region of methyl groups: signals at higher field come from  $-\text{Si}(\text{CH}_3)_2-$  group due to the shielding effect of methyl groups, and signals at lower field come from  $-\text{Si}(\text{H})\text{CH}_3-$  groups. In addition, for relatively low molecular weight polysiloxanes, signals of  $-\text{Si}(\text{CH}_3)_3$  end groups should be visible, and again, the signal of the end groups adjacent to  $-\text{Si}(\text{CH}_3)_2-$  group will be shifted upfield compared to the signal of the end groups adjacent to  $-\text{Si}(\text{H})\text{CH}_3-$  group. Also, set of three signals is expected in Si-H region.

In  $^1\text{H}$  NMR spectrum of poly(dimethylsiloxane-*co*-methylhydrosiloxane) of average Mn 950 g/mol [P(DMS-*co*-MHS)] (Fig. S.13) only two elaborate groups of signals: at 0.04-0.014 and 0.14-0.24 ppm can be distinguished in the region between 0 and 0.25 ppm due to the complexity of the spectrum and overlapping of the signals. Peaks originating from terminal  $-\text{CH}_3$  groups (*a* and *a'*) overlap with peaks emerging from  $-\text{Si}(\text{CH}_3)_2-$  groups resulting in shifted upfield group of signals, hindering direct determination of the structure. Group of broad signals shifted downfield (0.14-0.24 ppm) was ascribed to  $-\text{Si}(\text{H})\text{CH}_3-$  protons. Also silane protons ( $-\text{Si}(\text{H})\text{CH}_3-$ ) give complex group of signals at about 4.7 ppm that cannot be analyzed as separate peaks. Nevertheless, average number of methylhydrosiloxane units in P(DMS-*co*-MHS) was estimated for about 7, and number of dimethylsiloxane units for about 5 based on ratio of the  $-\text{CH}_3$  integrals versus Si-H integrals in  $^1\text{H}$  NMR spectrum and information that  $M_n$  declared by manufacturer was about 950 g/mol.

ATR-FTIR spectra of both poly(methylhydrosiloxane)s and poly(dimethylsiloxane-*co*-methylhydrosiloxane) collected in Fig. S.14 show similar bands, compliant with methylhydrosiloxane structure: In 4000-1000  $\text{cm}^{-1}$  region all three compounds feature similar pattern of bands arising from asymmetric C-H stretching of Si- $\text{CH}_3$  group (2966-2962  $\text{cm}^{-1}$ , medium), symmetric C-H stretching of Si- $\text{CH}_3$  (2902-2905  $\text{cm}^{-1}$ , weak), Si-H stretching

(2162-2159  $\text{cm}^{-1}$ , medium to strong), asymmetric C-H deformation of Si-CH<sub>3</sub> group (weak, 1411-1408  $\text{cm}^{-1}$ ), symmetric C-H deformation of Si-CH<sub>3</sub> (1259  $\text{cm}^{-1}$ , strong), asymmetric Si-O-Si stretching (broad band spreading between 1100 and 1000  $\text{cm}^{-1}$ , with maxima at about 1088 and 1040-1020  $\text{cm}^{-1}$ ). 950-600  $\text{cm}^{-1}$  region is more variable, since bands of skeletal vibrations (C-Si-C stretching) are observed there along with Si-H and Si-CH<sub>3</sub> deformations.

Closer investigation of band assigned to symmetric C-H deformation in Si-CH<sub>3</sub> reveals that in case of PMHS-S two close bands are overlapping: band of terminal Si-(CH<sub>3</sub>)<sub>3</sub> groups at 1253  $\text{cm}^{-1}$  and band of Si-(CH<sub>3</sub>)<sub>2</sub> segments within the siloxane chain at 1258  $\text{cm}^{-1}$ . It is expected, since according to literature terminal Si-(CH<sub>3</sub>)<sub>3</sub> group gives peak at longer wavelength [148] and PMHS-S has oligomeric chains short enough to observe this effect. Under analysis, 1100-100  $\text{cm}^{-1}$  region of Si-O-Si stretching band also shows complexity and reveals some differences between investigated polysiloxanes. The mode is composed of broad band centered at 1088-1087  $\text{cm}^{-1}$ , and stronger, sharper band with maximum at about 1040  $\text{cm}^{-1}$  for PMHS-S, 1036  $\text{cm}^{-1}$  for PMHS-L and 1024  $\text{cm}^{-1}$  for P(DMS-co-MHS).

Spectra of PMHS-S and PMHS-L show similar features in the region 1300-700  $\text{cm}^{-1}$ : weak band 925  $\text{cm}^{-1}$  (for PMHS-S) and 916  $\text{cm}^{-1}$  (for PMHS-L), set of overlapping bands is spreading from 930 to 890  $\text{cm}^{-1}$ , sharp, strong band at 827 (PMHS-S) and 829  $\text{cm}^{-1}$  (PMHS-L) and combination mode of bands with maxima centered at 764 and 753-751  $\text{cm}^{-1}$ . In the spectrum of P(DMS-co-MHS) band at 909  $\text{cm}^{-1}$  is discernible, whereas band at 827  $\text{cm}^{-1}$  is present only as medium intensity shoulder of band positioned at 820  $\text{cm}^{-1}$ , discernible at second derivative of the spectrum. On the other hand strong band, absent in PMHSs spectra, is present in P(DMS-co-MHS) spectrum at 794  $\text{cm}^{-1}$ . Band at 827-829  $\text{cm}^{-1}$  are therefore identified as related to the presence of Si-H segment, namely Si-H bending vibration [225], whereas band at 794  $\text{cm}^{-1}$  is attributed to vibrations of Si(CH<sub>3</sub>)<sub>2</sub> groups (methyl rocking) in dimethylsiloxane segment. Band at about 753  $\text{cm}^{-1}$  is a rocking mode of Si(CH<sub>3</sub>)<sub>3</sub> terminal groups, whereas band at about 764  $\text{cm}^{-1}$  is a rocking mode of intrachain Si-CH<sub>3</sub> (single CH<sub>3</sub> group attached to Si). Other medium-weak and weak bands in 850-650  $\text{cm}^{-1}$  region are arising from skeletal Si-C stretching vibrations.

**Poly(ethylene glycol) methyl ether methacrylate (PEGMA)** of average Mn 500 g/mol as co-graft for synthesis of copolymers was used as purchased, without further purification, and characterized by NMR and FT-IR analysis prior to use: <sup>1</sup>H NMR (300 MHz, CDCl<sub>3</sub>): δ (ppm) 6.13 (dq, <sup>3</sup>J=1.6 Hz <sup>4</sup>J=1.0 Hz, 1H, HHC=C(CH<sub>3</sub>)-C=O), 5.83 (dq, <sup>3</sup>J=1.6 Hz, <sup>4</sup>J=1.6 Hz, 1H, HHC=C(CH<sub>3</sub>)-C=O), 4.30 (m, 2H, O=C-O-CH<sub>2</sub>-CH<sub>2</sub>-), 3.53-3.77 (m,

32 H,  $\text{O}=\text{C}-\text{O}-\text{CH}_2-\text{CH}_2-[\text{O}-\text{CH}_2-\text{CH}_2-]_n$ , 3.38 (s, 3H,  $\text{O}-\text{CH}_3$ ), 1.951 (dd,  $^3J=1.6$  Hz,  $^4J=1.6$  Hz, 3H,  $=\text{C}(\text{CH}_3)-\text{C}=\text{O}$ ). From the analysis it was estimated that used PEGMA has in average 8.5 ethylene oxide repeating units per macromolecule.

In ATR-FTIR spectrum of PEGMA (Fig. S.15) bands characteristic for methacrylate group are present: C=O stretching vibration ( $1716\text{ cm}^{-1}$ ), C=C stretching vibration ( $1637\text{ cm}^{-1}$ ), C-O-C asymmetric stretching vibration (dual band,  $1296$  and  $1330\text{ cm}^{-1}$ ) and C-O-C symmetric stretching vibration ( $1168\text{ cm}^{-1}$ ) and  $=\text{CH}_2$  wagging vibration at  $944\text{ cm}^{-1}$ . Also, bands characteristic for aliphatic ethers are recorded: stretching C-H vibrations (broad, complex peak at  $2870\text{ cm}^{-1}$ ), C-H deformation vibrations of  $\text{OCH}_2$  ( $1454\text{ cm}^{-1}$ ) and  $\text{OCH}_3$  ( $1350\text{ cm}^{-1}$ ) groups, and C-O-C asymmetric stretching vibrations at  $1099\text{ cm}^{-1}$  accompanied by smaller sideband of C-O-C symmetric stretching vibrations at  $1038\text{ cm}^{-1}$ .

## 7.2 Graft copolymers

Fig. S.16 presents  $^1\text{H}$  NMR spectrum of **poly(methylhydrosiloxane)-graft-poly(3-hexylthiophene) (PMHS-g-P3HT)** copolymer. It demonstrates all expected features, i.e. signals arising from P3HT protons (*a-g*), as well as polysiloxane protons (*j,k*) and complete disappearance of vinyl protons signals, which were present at 5.12, 5.51 and 6.85 ppm in parent P3HTvin FC (lack of signal at 6.85 ppm can be seen on the expansion of aromatic protons region). Also, disappearance of one of the small high field triplet signals accompanying main peak of  $\alpha\text{-CH}_2$  groups is observed and only small triplet-like peak at 2.57 ppm ( $^3J=7.5$  Hz), ascribed to protons of  $\alpha\text{-CH}_2$  group in Br-terminal unit (*f'*) remains, as can be seen in the expansion of the spectrum. Likewise, in aromatic region of the spectrum only small signal of Br-terminal unit (*g'*) at 6.83 ppm can be readily distinguished upfield to the main HT-HT triad signal at 6.98 ppm. Decrease of Si-H signal at about 4.66-4.71 ppm is observed, however not complete, which suggests some residual Si-H groups left in the resulting copolymer after copolymerization and purification.

Signals of newly formed  $-\text{CH}_2-\text{CH}_2-$  linkage group between P3HT and PMHS probably overlap with P3HT signals: Si- $\text{CH}_2-$  (*i*) with peak of  $-\text{CH}_3$  alkyl protons (*a*) at about 0.90 ppm, and  $-\text{CH}_2-\text{Th}$  (*h*) with peak of  $\alpha$ -methylene protons (*f*) at about 2.6-2.8 ppm (positions of these signals were estimated based on  $^1\text{H}$  NMR shifts reported in literature for similar system: Si- $\text{CH}_2-\text{CH}_2$ -phenyl [96,98,226]. Those new peaks may be also broadened and therefore even more difficult to locate precisely in NMR spectrum if they overlap with other,

much stronger signals. Individual signals of Si-CH<sub>3</sub> protons are not distinguishable, but merged in one very broad peak centered at about 0.10 ppm, which suggests side reactions, such as cross-coupling and crosslinking of PMHS chains during the hydrosilylation reaction or later, in the course of purification. What is more, analysis of integration values in <sup>1</sup>H NMR spectrum of PMHS-*g*-P3HT copolymer supports this hypothesis. Si-CH<sub>3</sub> protons are overrepresented – when the integral of Si-CH<sub>3</sub> protons is set for 30 (the same as in starting PMHS-S) integration value of peak around 6.98 ppm (aromatic protons in thiophene ring) corresponds to only four thiophene units per one starting PMHS chain, whereas starting P3HTvin FCH had about 37-45 repeating units. This suggests crosslinking and therefore extension of polysiloxane segments during grafting process. One more unexpected peak emerges at about 3.48 ppm – most likely corresponding to –OCH<sub>3</sub> moiety attached to polysiloxane chain, since residual Si-H groups may react with methanol during first purification step in Soxhlet apparatus. Dehydrocoupling between Si-H bond and C-OH groups in the presence of platinum catalysts, including Karstedt catalyst, is a reaction reported in the literature [227,228]. PMHS-*g*-P3HT copolymer isolated after post-synthesis purification is quite well soluble in chloroform, however its solubility decreases with storage time, suggesting further crosslinking reactions of Si-H active groups, possibly with water. Another explanation of underrepresentation of P3HT signals in NMR spectrum is situation in which obtained material is a blend of PMHS-P3HT graft copolymer and high molecular weight polysiloxane matrix formed during the reaction (since excess of PMHS was employed in the reaction feed). However, degree of crosslinking is presumably low, since at the macroscopic scale material seems homogenous, so miscibility of graft copolymer and polysiloxane matrix is sufficient, and the whole composite remains soluble in solvents such as CHCl<sub>3</sub>, toluene or dichlorobenzene.

GPC analysis (1 mg/ml solution in THF) of PMHS-*g*-P3HT results in monomodal elution curve allowing to determine M<sub>n</sub> of about 10,300 g/mol (comparable or slightly higher than parent P3HT) and Đ<sub>M</sub> of 1,46 (comparable with parent P3HT), which suggests that single P3HT chains are attached to rather short polysiloxane backbone.

Results described above allows to conclude that vinyl-terminated P3HT chains pose too big steric hindrance to fully saturate all Si-H graft sites and to form dense bottlebrush-type copolymer on the polysiloxane chain. Unsaturated Si-H bond gives rise to potential crosslinking and uncontrolled saturation of active Si-H groups with random compounds present in the reaction system, environment or during purification steps, such as methanol or



molecules bearing vinyl groups. To overcome this issue copolymer comprising methylhydrosiloxane, as well as dimethylsiloxane units was used as a backbone for grafting P3HT chains in the next attempt to synthesise well-defined graft copolymer.

Fig. S.17 presents  $^1\text{H}$  NMR spectrum of **poly(dimethylsiloxane-*co*-methylhydrosiloxane)-graft-poly(3-hexylthiophene) [P(DMS-*co*-MHS)-*g*-P3HT]** copolymer. It is quite similar to spectrum of PMHS-*g*-P3HT copolymer. Almost complete decay of vinyl group peaks and Si-H peak is observed. However peak at 3.48 ppm is present again, suggesting side reactions with methanol. Analysis of integrals values allows to estimate P3HT chain to starting P(DMS-*co*-MHS) chain ratio for about 1, which again suggests crosslinking, since starting P(DMS-*co*-MHS) had about 7 grafting sites per macromolecule and the amount of  $-\text{OCH}_3$  groups potentially attached in the course of side reactions does not cover the remaining sites. However, obtained P3HT:polysiloxane ratio in the final product is improved.

GPC analysis (1 mg/ml solution in THF) of P(DMS-*co*-MHS)-*g*-P3HT results in monomodal elution curve allowing to determine  $M_n$  of about 10,300 g/mol, almost identical to PMHS-*g*-P3HT, comparable or slightly higher than parent P3HT and  $D_M$  of 1,69 (noticeably higher compared with parent P3HT), which suggests that single P3HT chains are attached to rather short polysiloxane backbone, and that molar mass distribution of P(DMS-*co*-MHS) used is higher than for PMHS-S.

Fig. S.18 presents ATR-FTIR spectra of PMHS-*g*-P3HT and P(DMS-*co*-MHS)-*g*-P3HT in comparison with spectra of parent components: P3HT<sub>vin</sub>, PMHS-S and P(DMS-*co*-MHS). In both cases characteristic bands of P3HT aromatic ring and hexyl side chains are preserved for copolymers, except the weak band of stretching vibrations of vinyl group at about  $1650\text{ cm}^{-1}$ . When it comes to bands which arise from polysiloxane segment more changes are observed. Distinct and readily observable band of Si-H stretching vibrations at  $2159\text{ cm}^{-1}$  decreases noticeably in case of PMHS-*g*-P3HT and completely in case of P(DMS-*co*-MHS)-*g*-P3HT – which complies with conclusions drawn from analysis of  $^1\text{H}$  NMR spectra. Also band at  $829\text{ cm}^{-1}$ , related to the presence of H-Si-CH<sub>3</sub> segments decreases in graft copolymers, but this change is more difficult to follow due to the overlapping with other peaks in this region. In the spectrum of PMHS-*g*-P3HT bands at  $841$  and  $754\text{ cm}^{-1}$  are observed, characteristic for Si(CH<sub>3</sub>)<sub>3</sub> terminal groups, suggesting short polysiloxane chains, whereas in the spectrum of P(DMS-*co*-MHS)-*g*-P3HT band at  $798\text{ cm}^{-1}$  is observed, characteristic for Si(CH<sub>3</sub>)<sub>2</sub> segments. Band of Si-CH<sub>3</sub> deforming vibrations in parent

polysiloxanes appearing as sharp, narrow peak of medium-strong intensity at  $1259\text{ cm}^{-1}$  transforms into double band, suggesting significant changes in behaviour of methyl groups attached to polysiloxane backbone. For PMHS-*g*-P3HT, originating from short PMHS, two separated maxima at about  $1269$  and  $1253\text{ cm}^{-1}$  are observed. For P(DMS-*co*-MHS)-*g*-P3HT, originating from P(DMS-*co*-MHS) backbone, broadened band with maximum at about  $1258\text{ cm}^{-1}$  is observed, but analysis of second derivative of the spectrum reveals that it is combination mode composed of two bands:  $1269$  and  $1258\text{ cm}^{-1}$ . It may suggest formation of Si-CH<sub>2</sub> fragments due to the grafting as well as occurrence of crosslinking between polysiloxane chains, yet occurrence of  $1253\text{ cm}^{-1}$  band for PMHS-*g*-P3HT, characteristic for short polysiloxane chains, makes hypothesis about elongation of polysiloxane chains during hydrosilylation procedure less probable.

In the next attempt additional co-grafted groups were introduced to copolymers structure – to saturate active Si-H sites in the controlled manner. This approach allowed also for further modification of properties of obtained copolymers by incorporation of new functional groups featuring unique properties, such as polyether chains, or just neutral fillers, such as alkyl chains, to further facilitate molecular dilution of P3HT and prevent aggreration. Investigation covers copolymers composed of PMHS with P3HT (oligomeric hexane fraction or polymeric chloroform fraction) and hexyl chains or polyether chains in form of polyethylene glycol methacrylate methyl ether.

Fig. S.19 presents <sup>1</sup>H NMR spectrum of **poly(methylhydrosiloxane)-graft-[poly(3-hexylthiophene); hexene], copolymer 1: [PMHS-*g*-(P3HT;hex) 1]**, bearing short PMHS-S backbone, hexyl co-grafts and chloroform fraction of P3HT. It demonstrates all expected features, proving grafting of vinyl-terminated P3HT chains on PMHS backbone like in case of PMHS-*g*-P3HT copolymer (disappearance of vinyl protons signals and one of the small high field triplet-like signals, centered at 2.61 ppm is observed, and only one small triplet-like peak at 2.57 ppm, ascribed to protons of α-CH<sub>2</sub> group in Br-terminal unit (*f'*) remains, in aromatic region of the spectrum only one minor signal of Br-terminal unit (*g'*) at 6.83 ppm can be observed upfield to main HT-HT triad signal at 6.98 ppm. Practically complete decrease of Si-H signal at about 4.66-4.71 ppm is observed. Broad signal of Si-CH<sub>3</sub> protons is observed at 0.11 ppm, and a new, broad signal of Si-CH<sub>2</sub> protons arising from co-grafted hexyl chains at 0.50 ppm. Peak of -CH<sub>3</sub> protons of co-grafted hexyl chains overlaps with -CH<sub>3</sub> protons signal from 3-hexylthiophene segment at 0.91 ppm, and -CH<sub>2</sub>-(CH<sub>2</sub>)<sub>4</sub>-CH<sub>3</sub> protons of co-grafted hexyl chains overlaps with analogous -(CH<sub>2</sub>)<sub>3</sub>-CH<sub>3</sub> segments of 3-

hexylthiophene in 1.44-1.34 region. Analysis of integrals reveals that 1 P3HT chain is grafted on starting short PMHS backbone, accompanied by about 2 co-grafted hexyl chains.

Fig. S.20 presents  $^1\text{H}$  NMR spectrum of **poly(methylhydrosiloxane)-graft-[poly(3-hexylthiophene); hexene], copolymer 2: [PMHS-g-(P3HT;hex) 2]**, bearing long PMHS-L backbone, hexyl co-grafts and chloroform fraction of P3HT. It features basically the same signals as discussed above PMHS-g-(P3HT;hex) 1, with the main difference in integral values and presence of a signal at 3.49, which might arise from O-CH<sub>3</sub> protons. Analysis of integrals reveals that about 2 P3HT chains are grafted on starting long PMHS backbone, accompanied by about 18 co-grafted hexyl chains and about 4 methoxy groups. It again leads to the conclusion that long PMHS chains promote side reactions during grafting process.

Fig. S.21 presents ATR-FTIR spectrum of PMHS-g-(P3HT;hex) 1 and PMHS-g-(P3HT;hex) 2 in comparison with spectra of P3HTvin, PMHS-S and PMHS-L. Spectra of both copolymers feature all bands characteristic for P3HTvin, except C=C stretching vibrations of vinyl group at about 1650 cm<sup>-1</sup> (however at the spectrum of PMHS-g-(P3HT;hex) 1 this weak band is visible, which may suggest that the material isn't homogenous and composition of the sample analysed by NMR is slightly different than composition of sample characterised by IR, since in  $^1\text{H}$  NMR spectrum of PMHS-g-(P3HT;hex) 1 signals from vinyl groups are absent). Si-H stretching mode at 2159 cm<sup>-1</sup> and Si-H bending mode at 829 cm<sup>-1</sup> are practically absent in both spectra. In the spectrum of PMHS-g-P3HT;hex 1 complex mode is present with band maxima at 1269 and 1251 cm<sup>-1</sup> due to the Si-CH<sub>3</sub> symmetric deformations. 1251 cm<sup>-1</sup> band suggests again short oligosiloxane chains. In the spectrum of PMHS-g-P3HT;hex 2 this mode is present at 1269 and 1258 cm<sup>-1</sup>, suggesting long polysiloxane chains. This is consistent with the spectra of parent short and long PMHS. In spectra of both alkyl co-grafted copolymers asymmetric Si-O-Si stretching mode is broadened to cover the range from 1170 to 960 cm<sup>-1</sup>, and the low-frequency maximum is shifted to 1024 cm<sup>-1</sup>.

Fig. S.22 presents  $^1\text{H}$  NMR spectrum of **poly(methylhydrosiloxane)-graft-[poly(3-hexylthiophene); (poly(ethylene glycol) methyl ether methacrylate) [PMHS-g-(P3HT;PEG) 1]**, bearing short PMHS-S backbone, polyether co-grafts and hexane fraction of P3HT. Hexane fraction of this graft copolymer was investigated in this work. Complete decay of peaks originating from vinyl protons in P3HTvin and peaks originating from Si-H protons is observed. Broad signal of Si-CH<sub>3</sub> protons is observed at about 0.11 ppm, like in cases of previously described copolymers. Additional peaks arising from PEG co-grafts are

present at 3.38 ppm (O-CH<sub>3</sub>) and 3.55-3.64 ppm (O-CH<sub>2</sub>-CH<sub>2</sub>-O). The rest of the peaks are relatively small and overlapping with signals of P3HT alkyl protons. According to literature methacrylate group attaches via -C(CH<sub>3</sub>)=CH<sub>2</sub> group to Si-H bond in the presence of Karstedt catalyst forming β-adduct [97]. In the product of the reaction the following signals arise in <sup>1</sup>H NMR spectrum: two signals (doublet) at the range 0.65-0.93 ppm (Si-CH<sub>2</sub>-CH), doublet at 1.20 ppm CH(CH<sub>3</sub>), and multiplet at 2.5 ppm CH<sub>2</sub>-CH(CH<sub>3</sub>)-C=O [97]. From the comparison of integrals of Si-CH<sub>3</sub> and thiophene aromatic protons can be seen that proportion of the starting PMHS-S chains to P3HT FH oligomeric chains is about 1:1 and marginal amount of co-grafted PEG chains is present, which again suggests occurrence of side reactions.

Fig. S.23 presents <sup>1</sup>H NMR spectrum of **poly(methylhydrosiloxane)-graft-[poly(3-hexylthiophene); (poly(ethylene glycol) methyl ether methacrylate), PMHS-g-(P3HT;PEG) 2**, bearing short PMHS-S backbone and chloroform fraction of grafted P3HT. Chloroform fraction of the copolymer was investigated in this work. It resembles the spectrum of PMHS-g-(P3HT;PEG) 1 copolymer, but PEG co-grafted chains are present only in trace amount. P3HT polymeric chains to starting PMHS 390 chains ratio is about 1:1-1.5:1.

Fig. S.24 presents ATR-FTIR spectrum of PMHS-g-(P3HT;PEG) 1 and PMHS-g-(P3HT;PEG) 2. Spectrum of PMHS-g-(P3HT;PEG) 1 features bands arising mostly from P3HT and polysiloxane, like spectrum of PMHS-g-P3HT copolymer. In both copolymers Si-H stretching band at 2159 cm<sup>-1</sup> and Si-H deformation band at 829 cm<sup>-1</sup> almost completely disappear. For PMHS-g-(P3HT;PEG) 1 band of Si-(CH<sub>3</sub>) deformation vibrations is split into two peaks with maxima at 1269 and 1258 cm<sup>-1</sup> which seems unusual for the copolymer built on PMHS-S and may suggest significant changes in polysiloxane backbone, including branching and incorporation of Si-(CH<sub>3</sub>)<sub>2</sub> segments, since 1258 cm<sup>-1</sup> band is characteristic for all linear, cyclic and branched oligodimethylsiloxanes [148]. Additionally, it can be seen that weak C=O stretching band at about 1700 cm<sup>-1</sup> appears originating from PEG segment. In ATR-FTIR spectrum of PMHS-g-(P3HT;PEG) 2 bands arising from PEGMA segment are practically absent.

Fig. S.25 presents <sup>1</sup>H NMR spectrum of poly(methylhydrosiloxane)-graft-[poly(3-hexylthiophene); (poly(ethylene glycol) methyl ether methacrylate)], bearing long PMHS-L-derived backbone and chloroform fraction of P3HT – PMHS-g-(P3HT;PEG) 3. Complete decay of peaks originating from vinyl protons in P3HTvin and peaks originating from Si-H

protons is observed. In this copolymer P3HT polymeric chains to starting PMHS-L chains ratio is about 2.5:1-3:1, and about 50 PEGMA co-grafted chains are present per starting long PMHS polysiloxane. Dominant signals are well resolved peaks of protons in co-grafted on polysiloxane backbone PEG chains at: 3.38 ppm (O-CH<sub>3</sub>, *t*) and 3.55-3.64 ppm (O-CH<sub>2</sub>-CH<sub>2</sub>-O, *s*) and 4.07 ppm (O=C-O-CH<sub>2</sub>-CH<sub>2</sub>, *r*). Peaks typical for P3HT and polysiloxane are also present.

In ATR-FTIR spectrum of PMHS-*g*-(P3HT;PEG) 3 (Fig. S.26) bands arising from PEG co-grafts are distinct. Area of stretching C-H vibrations (2955-2860 cm<sup>-1</sup>) contains bands characteristic not only for P3HT but also pronounced band at 2870 cm<sup>-1</sup> arising from C-H stretching vibrations in PEG segments. Quite strong band of stretching C=O vibrations appear at 1728 cm<sup>-1</sup>, band of deforming vibrations of OCH<sub>3</sub> terminal group in PEG appears at 1350 cm<sup>-1</sup>, band of Si-(CH<sub>3</sub>) deformation vibrations is broad and complex, with distinct maximum at 1270 cm<sup>-1</sup>, area between 1180 and 1000 cm<sup>-1</sup> features combination of stretching Si-O-Si vibrations in polysiloxane backbone and stretching C-O-C vibrations in PEGMA chains. What is worth noting – medium intensity band of C-O-C asymmetric stretching characteristic for methacrylate group decays in PMHS-*g*-(P3HT;PEG) 2 copolymer, confirming attachment of PEGMA chains to PMHS backbone through methacrylate C=C double bond, as expected, not through C=O double bond, since stretching band of carbonyl group does not decrease in intensity for graft copolymer.

Poly(dimethylsiloxane-*co*-methylhydrosiloxane) [P(DMS-*co*-MHS)] was used as polysiloxane backbone bearing both active Si-H grafting sites, as well as dimethylsiloxane segments to promote molecular dilution and facilitate grafting and co-grafting with both P3HT and alkyl or polyether. Investigation covers copolymers composed of P(DMS-*co*-MHS) backbone grafted with P3HT (oligomeric hexane fraction or polymeric chloroform fraction) and dodecyl chains.

Fig. S.27 presents <sup>1</sup>H NMR spectrum of **poly(dimethylsiloxane-*co*-methylhydrosiloxane)-*graft*-[poly(3-hexylthiophene); dodecene], copolymer 1: P(DMS-*co*-MHS)-*g*-(P3HT;dodec) 1**, with dodecyl co-grafts and hexane fraction of P3HT. It demonstrates peaks characteristic for P3HT, but without signals coming from vinyl groups, similar as in case of PMHS-*g*-(P3HT;hex) 1. Si-CH<sub>3</sub> protons give rise to group of overlapping peaks, but this time with distinct maxima at 0.04, 0.07 and 0.08 ppm and broad shoulder extending downfield, to 0.14 ppm. There are no traces of Si-H proton signals around 4.6-4.7 ppm, Si-H active sites are fully saturated. Peaks emerging from dodecyl

chains grafted on polysiloxane are present at 0.50 ppm (Si-CH<sub>2</sub>), 0.88-0.90 ppm (-CH<sub>3</sub>, overlapping with -CH<sub>3</sub> signal of hexylthiophene segment at 0.91 ppm) and 1.25 ppm (Si-CH<sub>2</sub>-(CH<sub>2</sub>)<sub>10</sub>-CH<sub>3</sub>). Small peak at 3.47 ppm is present again – probably due to the methoxy group grafted on polysiloxane chains resulting from side reactions. P3HT to starting P(DMS-*co*-MHS) chains is surprisingly low, about 0.5:1, and additional about 4 co-grafted dodecyl chains are statistically present in the copolymer chain.

Fig. S.28 presents <sup>1</sup>H NMR spectrum of **poly(dimethylsiloxane-*co*-methylhydrosiloxane)-graft-[poly(3-hexylthiophene); dodecene], copolymer 2: P(DMS-*co*-MHS)-*g*-(P3HT;dodec) 2**, with dodecyl co-grafts and chloroform fraction of P3HT. It demonstrates peaks very similar to P(DMS-*co*-MHS)-*g*-(P3HT;dodec) 1 spectrum, but essentially with different integral values. There are no traces of vinyl and Si-H proton signals. Very small peak at 3.47 ppm is present once again. P3HT to starting P(DMS-*co*-MHS) chains is even lower than in case of P(DMS-*co*-MHS)-*g*-(P3HT;dodec) 1, about 0.15:1, and additional about 4 co-grafted dodecyl chains are statistically present in the copolymer chain.

Fig. S.29 presents ATR-FTIR spectrum of P(DMS-*co*-MHS)-*g*-(P3HT;dodec) 1 and 2 copolymers in comparison with spectra of P3HTvin, and P(DMS-*co*-MHS). Spectra of both copolymers feature all bands characteristic for P3HTvin, except C=C stretching vibrations of vinyl group at about 1650 cm<sup>-1</sup>. Si-H stretching mode at 2159 cm<sup>-1</sup> and Si-H bending mode at 829 cm<sup>-1</sup> are practically absent in both spectra. Si-CH<sub>3</sub> symmetric deformations appear as medium-strong sharp band in spectra of both copolymers. Medium-strong band of Si(CH<sub>3</sub>)<sub>2</sub> rocking vibrations is present in spectrum of PDMScoMHS, as well as in spectra of both copolymers. In spectra of both grafted copolymers asymmetric Si-O-Si stretching mode is just slightly broadened in comparison with P(DMS-*co*-MHS) spectrum and low frequency maximum is shifted from 1024 to 1020-1018 cm<sup>-1</sup>.

<sup>1</sup>H NMR spectrum of **poly(dimethylsiloxane-*co*-methylhydrosiloxane)-graft-[poly(3-hexylthiophene); (poly(ethylene glycol) methyl ether methacrylate), copolymer 1: P(DMS-*co*-MHS)-*g*-(P3HT;PEG) 1**, with polyether co-grafts and hexane fraction of P3HT is shown in Fig. S.30. Signals arising from P3HT are clearly visible, but without signals coming from vinyl groups. Si-CH<sub>3</sub> protons give rise to group of overlapping peaks with distinct maxima at 0.07 and 0.08 ppm and broad shoulder extending downfield, to 0.18 ppm. There are no traces of Si-H proton signal about 4.6-4.7 ppm, PMHS backbone seems fully saturated. Peaks emerging from PEGMA chains grafted on polysiloxane are present at 3.38 ppm (O-CH<sub>3</sub>), 3.55-3.64 ppm (O-CH<sub>2</sub>-CH<sub>2</sub>-O), 4.23 ppm (-C(O)-O-CH<sub>2</sub>-CH<sub>2</sub>-), and

small doublet at 1.20-1.22 ppm (C(CH<sub>3</sub>)-C(O)) overlapping with the base of hexyl -(CH<sub>2</sub>)- protons signal. The rest of the peaks are fully overlapping with much bigger signals of P3HT alkyl protons and are not distinguishable. P3HT to starting P(DMS-*co*-MHS) chains ratio is about 1:1, and additional 1 co-grafted PEGMA chain is statistically present in the copolymer chain.

<sup>1</sup>H NMR spectrum of **poly(dimethylsiloxane-*co*-methylhydrosiloxane)-graft-[poly(3-hexylthiophene); (poly(ethylene glycol) methyl ether methacrylate), copolymer 2: P(DMS-*co*-MHS)-g-(P3HT;PEG) 2**, with polyether co-grafts and chloroform fraction of P3HT is shown in Fig. S.31. It is very similar to <sup>1</sup>H NMR spectrum of P(DMS-*co*-MHS)-g-(P3HT;PEG) 1 copolymer, except for ratio of the components resulting from analysis of integrals: P3HT to starting PDMScoMHS chains ratio is about 0.3:1, and additional 1 co-grafted PEGMA chain is statistically present in copolymer chain.

Fig. S.32 presents ATR-FTIR spectrum of P(DMS-*co*-MHS)-g-(P3HT;PEG) 1 and 2 copolymers in comparison with spectra of P3HTvin, P(DMS-*co*-MHS) and PEGMA. Spectra of both copolymers feature bands arising mostly from P3HT and polysiloxane, like spectrum of P(DMS-*co*-MHS)-g-P3HT copolymer, but bands arising from PEGMA co-grafts are also visible: weak band of C=O stretching vibrations at 1735 cm<sup>-1</sup> and C-O-C stretching band in the range from 1200 to 1000 cm<sup>-1</sup>, overlapping with asymmetric Si-O-Si stretching band. In both copolymers Si-H stretching band at 2159 cm<sup>-1</sup> and Si-H deformation band at 829 cm<sup>-1</sup> decrease completely. Si-(CH<sub>3</sub>) deformation band broadens towards higher frequency – shoulder at about 1270 cm<sup>-1</sup> appears in addition to the original band at 1258 cm<sup>-1</sup> in P(DMS-*co*-MHS).

### 7.3 Summary of the copolymers composition

Since obtained copolymers have surprising and unexpected ratios of components, some summary based on the content of thiophene rings, polysiloxane, and co-grafted moieties is collected in the Tab. 7.2.

In case of almost all copolymers grafted on PMHS-S (except for PMHS-g-P3HT) on average about 1 P3HT chain per starting PMHS chain is present in the copolymer molecule, so those copolymers may be considered as P3HT chains of different lengths decorated on one end with polysiloxane segment. Virtually, in all copolymers apparent excess of polysiloxane is observed with respect to the stoichiometry, which suggests occurrence of side reactions

leading to crosslinking. Crosslinking may occur due to the presence of labile divinyl ligand (1,1,3,3-tetramethyl-1,3-divinyldisiloxane) in applied Karstedt catalyst, which can be incorporated into polysiloxane network [229]. Very broad signal of siloxane protons, with no distinct peaks, supports this hypothesis. In copolymers with co-grafts, significant amount of co-grafted moieties is found but not enough to saturate all active Si-H sites in PMHS – yet Si-H protons are absent or almost absent in practically all copolymers (small peak of Si-H protons is observed only for PMHS-*g*-P3HT copolymer). For copolymers grafted on P(DMS-*co*-MHS) P3HT:polysiloxane ratio is even lower than for copolymers grafted on PMHS – in many cases <1 P3HT chain per starting P(DMS-*co*-MHS) chain, and number of co-grafts is lower than the amount required to saturate all the Si-H sites. The above considerations lead to the conclusion that attachment of one P3HT chain (oligomeric or polymeric) creates steric hindrance around grafting site and prevents grafting of subsequent P3HT molecules on adjacent active sites.

Tab. 7.2 Composition of synthesised copolymers

Copolymer	PMHS	P3HT fraction	Co-graft	Thiophene units per siloxane chain	Co-graft units per siloxane chain
PMHS- <i>g</i> -P3HT	PMHS-S	FC	-	4	-
PMHS- <i>g</i> -(P3HT;hex) 1	PMHS-S	FC	hexene	15	1
PMHS- <i>g</i> -(P3HT;hex) 2	PMHS-L	FC	hexene	79	16
PMHS- <i>g</i> -(P3HT;PEG) 1	PMHS-S	FH	PEGMA	12	0.1
PMHS- <i>g</i> -(P3HT;PEG) 2	PMHS-S	FC	PEGMA	47	0.03
PMHS- <i>g</i> -(P3HT;PEG) 3	PMHS-L	FC	PEGMA	110	51
P(DMS- <i>co</i> -MHS)- <i>g</i> -P3HT	P(DMS- <i>co</i> -MHS)	FC	-	48	-
P(DMS- <i>co</i> -MHS)- <i>g</i> -(P3HT;dodec) 1	P(DMS- <i>co</i> -MHS)	FH	dodecene	6	3.5
P(DMS- <i>co</i> -MHS)- <i>g</i> -(P3HT;dodec) 2	P(DMS- <i>co</i> -MHS)	FC	dodecene	6	3.5
P(DMS- <i>co</i> -MHS)- <i>g</i> -(P3HT;PEG) 1	P(DMS- <i>co</i> -MHS)	FH	PEGMA	13	1
P(DMS- <i>co</i> -MHS)- <i>g</i> -(P3HT;PEG) 2	P(DMS- <i>co</i> -MHS)	FC	PEGMA	15	1

Abbreviations: PMHS-S – poly(methylhydrosiloxane), short, average Mn 390; PMHS-L – poly(methylhydrosiloxane), long, average Mn 1700-3200; P(DMS-*co*-MHS) - poly(dimethylsiloxane-*co*-methylhydrosiloxane), medium, average Mn 950; FC - chloroform fraction (37-45 repeating thiophene units); FH - hexane fraction (13-15 repeating Th units)



## 7.4 Spectroelectrochemical characteristics

Spectroelectrochemical investigation of chosen copolymers was performed at the Department of Physical Chemistry and Technology of Polymers at the Silesian University of Technology, and was a subject of Tomasz Jarosz, PhD, doctoral thesis and a publication [230]. It will not be discussed hereby.

## 8 Application of obtained copolymers

Introduction of polysiloxane segment to the copolymers aimed at boosting material processability and mechanical characteristics of obtained thin films compared to pristine P3HT. Polysiloxane backbone of copolymers was expected to improve film-forming properties and adhesion to the surface of metal, indium tin oxide (ITO) and Si/SiO<sub>2</sub> substrates by lowering surface tension during deposition of polymer layers from the solution and increasing affinity to the surface, which is important for preparation of thin films in various devices, such as sensors, solar cells or thin film transistors. Increase in thermal and oxidative stability of devices fabricated from obtained copolymers is also expected. In addition, it should positively influence flexibility of materials in low temperatures. On the other hand polysiloxanes exhibit high gas diffusion rates and high permeabilities for gases [231], therefore their presence in copolymer structure is expected to facilitate gas sorption and transport of gas molecules in sensing layers, shortening both response and regeneration time of the sensors.

### 8.1 Gas sensors

Chosen copolymers were investigated towards application as low temperature NO<sub>2</sub> sensing materials. Sensing responses and morphologies of copolymers were also compared with results obtained for regioregular and nonregular P3HT. Results are described in details and discussed in the set of publications [232–234]. In this dissertation some highlights are presented.

Fig. 8.1 presents AFM height images of 3x3 μm gold electrode and substrate (between the electrodes) regions of interdigital transducer (IDT) covered by RR P3HT and PMHS-g-(P3HT;PEG) 3 copolymer layers prepared by spin coating of chloroform solution. Deposited films feature homogenous surface, covering the metal electrodes and SiO<sub>2</sub> substrates

uniformly. Tab. 8.1 summarises root mean square (RMS) values calculated from AFM measurements to determine surface roughness.

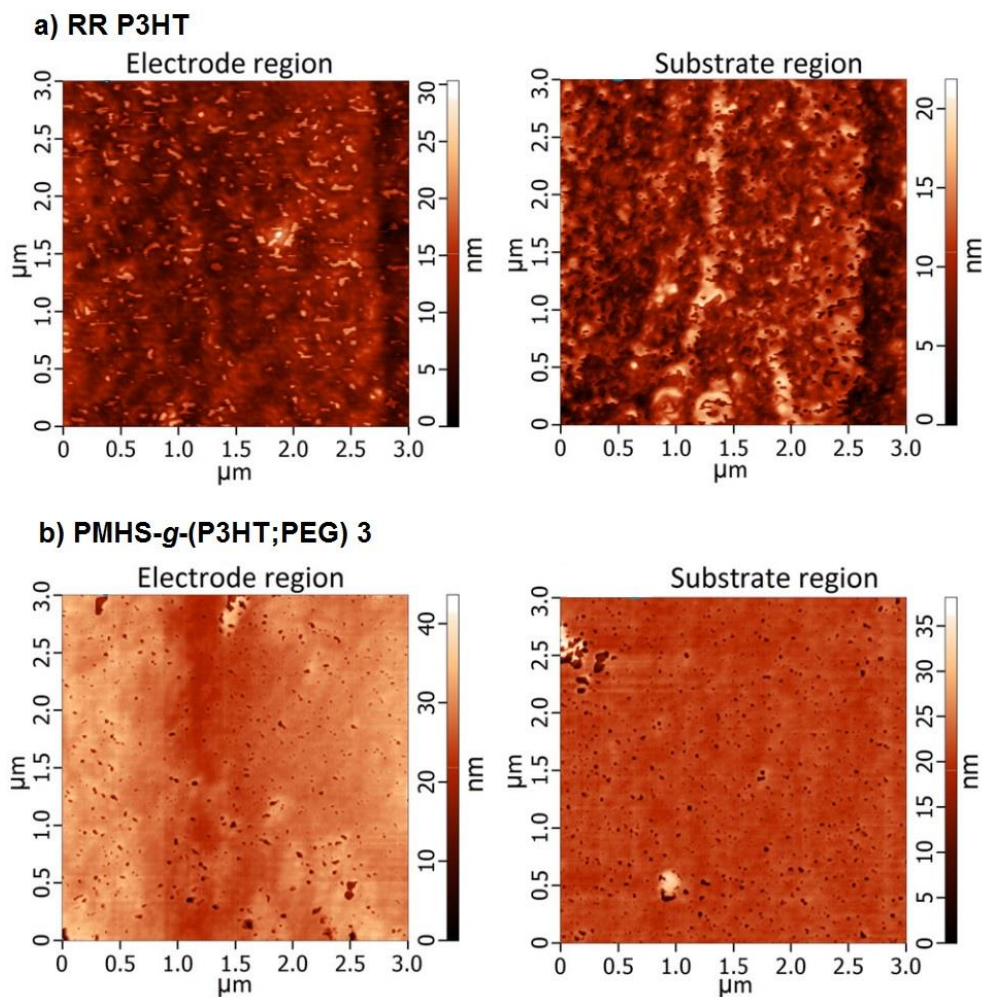


Fig. 8.1 AFM height images of electrode region and substrate region of IDT for: a) RR P3HT and b) PMHS-*g*-(P3HT;PEG) 3 copolymer films spin coated from CHCl<sub>3</sub> solutions [232]

Tab. 8.1 Surface roughness of RR P3HT, NR P3HT and copolymers (PMHS-*g*-(P3HT;PEG) 1 and 3) films deposited on IDT

Polymer/copolymer	RMS (3x3 μm area) [nm]	
	Au electrode	Si/SiO <sub>2</sub> substrate
RR P3HT	3.4	2.5
NR P3HT	6.7	2.6
PMHS- <i>g</i> -(P3HT;PEG) 1	2.7	1.5
PMHS- <i>g</i> -(P3HT;PEG) 3	3.6	2.3

Determined RMS values are quite low. In general, in all cases layers on the Si/SiO<sub>2</sub> surface were slightly smoother than on Au electrode surface, and RMS values were comparable for all materials, except for NR P3HT film on Au electrode, which featured RMS twice as large than RR P3HT and copolymers. The lowest RMS value, for films deposited both on the gold electrode and Si/SiO<sub>2</sub> substrate, was observed for PMHS-*g*-(P3HT;PEG) 1 copolymer bearing short polysiloxane backbone and short P3HT chains. RR P3HT layers show some fibrillar patterns suggesting self-assembly of polymer chains, whereas surface of the copolymer is featureless and smooth.

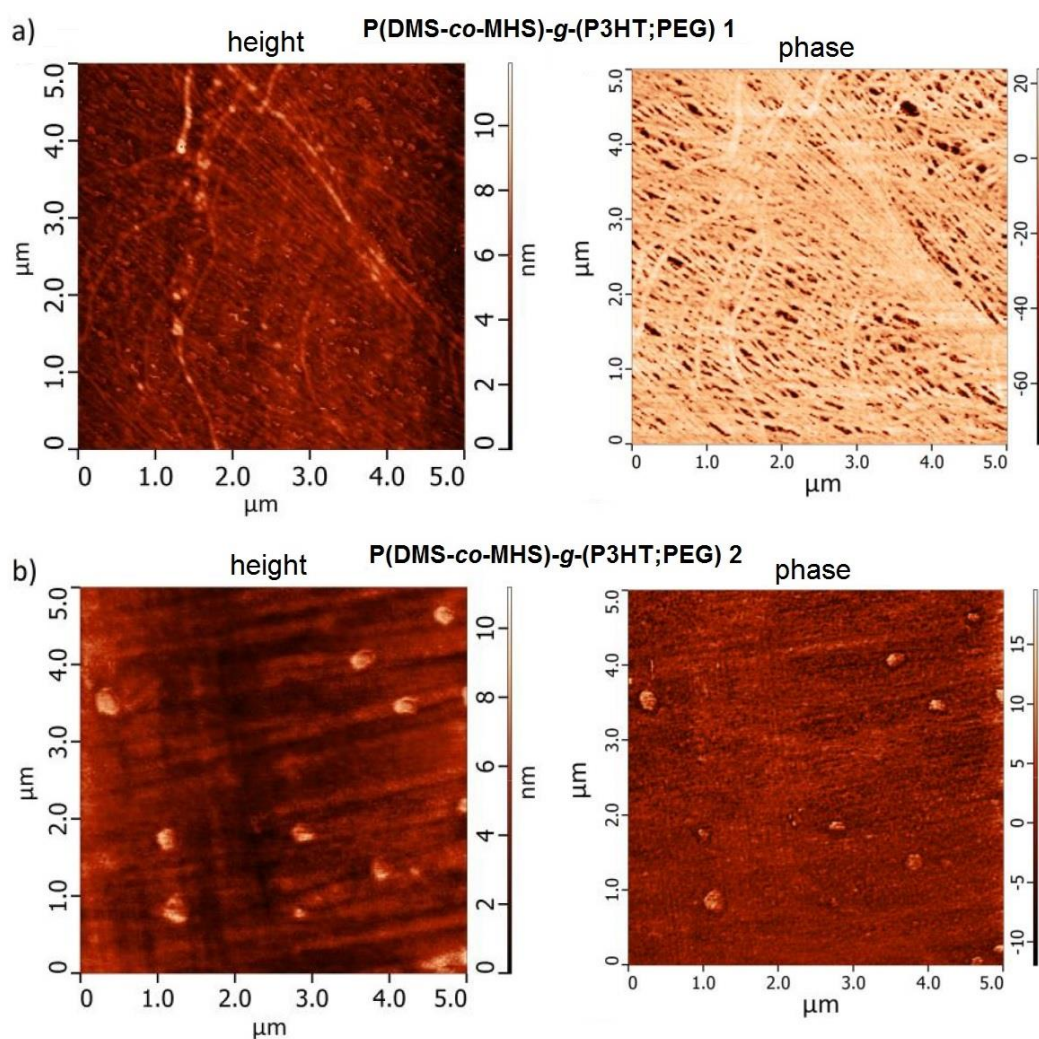


Fig. 8.2 AFM height and phase images (5x5  $\mu\text{m}$  area) of copolymer films spin coated from  $\text{CHCl}_3$  solutions on IDT (substrate region): a) P(DMS-*co*-MHS)-*g*-(P3HT;PEG) 1, b) P(DMS-*co*-MHS)-*g*-(P3HT;PEG) 2 [233]

Fig. 8.2 presents AFM height and phase images (5 x 5  $\mu\text{m}$  region) of copolymer films deposited by spin coating on the SiO<sub>2</sub> substrate of IDT: P(DMS-*co*-MHS)-*g*-(P3HT;PEG) 1 and P(DMS-*co*-MHS)-*g*-(P3HT;PEG) 2. Fig. 8.3 presents AFM height and phase images

(5x5  $\mu\text{m}$  region) of copolymer films deposited by spin coating on the  $\text{SiO}_2$  substrate of IDT: P(DMS-*co*-MHS)-*g*-(P3HT;dodec) 1 and P(DMS-*co*-MHS)-*g*-(P3HT;dodec) 2. In all cases copolymer films cover the surface uniformly and quite smoothly (as can be seen from RMS values in Tab. 8.2), RMS values are about half the values for P3HT and PMHS-*g*-(P3HT;PEG) 1 and 3 copolymers (Tab. 8.1). Circular structures (islands) can be distinguished in AFM images, especially pronounced in case of P(DMS-*co*-MHS)-*g*-(P3HT;PEG) 2. They are attributed to the formation of agglomerates in the films during solvent evaporation and annealing. Fibrillar morphology was observed in case of copolymers with alkyl co-grafts, similar to RR P3HT spin coated film.

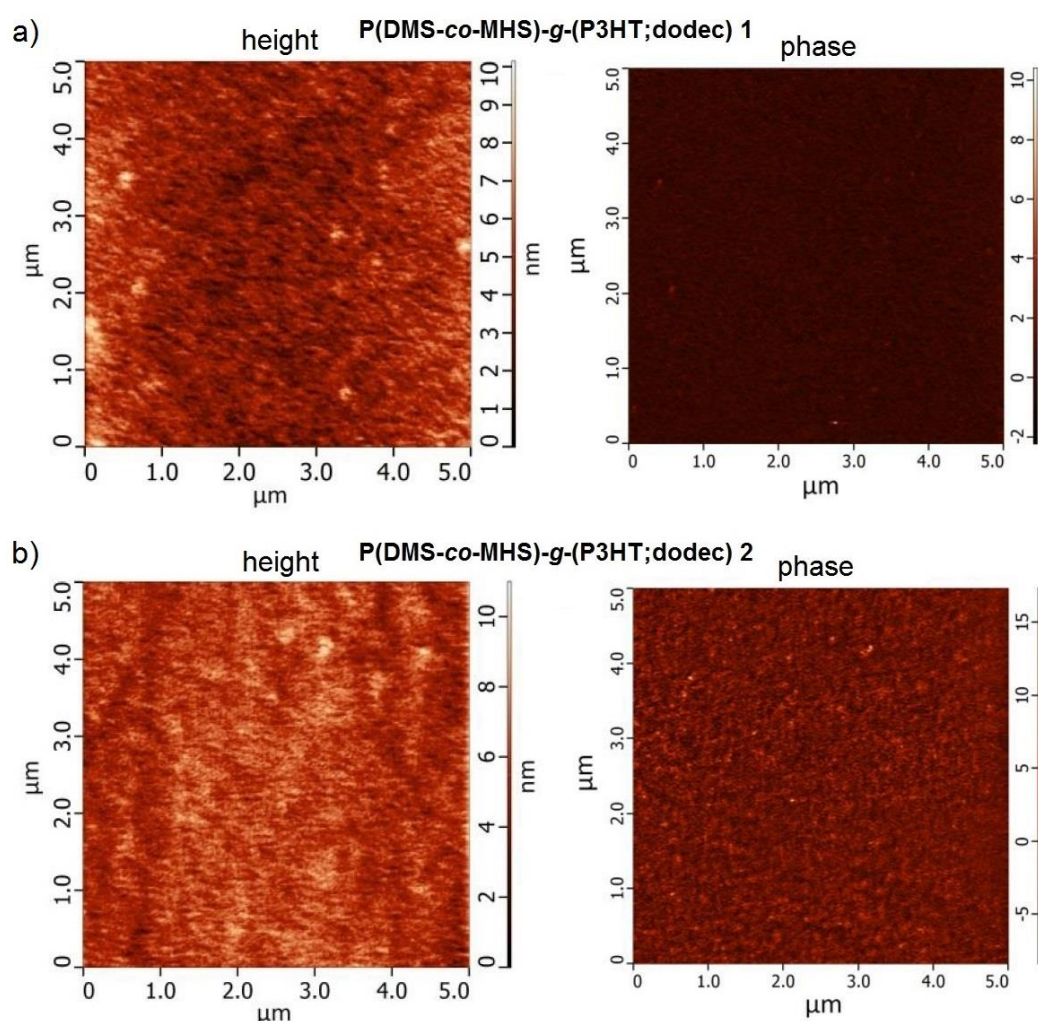


Fig. 8.3 AFM height and phase images (5x5  $\mu\text{m}$  area) of copolymer films spin coated from  $\text{CHCl}_3$  solutions on IDT (substrate region): a) P(DMS-*co*-MHS)-*g*-(P3HT;dodec) 1, b) P(DMS-*co*-MHS)-*g*-(P3HT;dodec) 2 [233]

Tab. 8.2 Surface roughness of P(DMS-*co*-MHS)-*g*-(P3HT;PEG) 1 and 2, and P(DMS-*co*-MHS)-*g*-(P3HT;dodec) 1 and 2 copolymer films spin coated on IDT from CHCl<sub>3</sub> solution

Polymer/copolymer	RMS [nm] (5x5 μm area, Si/SiO <sub>2</sub> substrate)
P(DMS- <i>co</i> -MHS)- <i>g</i> -(P3HT;PEG) 1	1.24
P(DMS- <i>co</i> -MHS)- <i>g</i> -(P3HT;PEG) 2	1.21
P(DMS- <i>co</i> -MHS)- <i>g</i> -(P3HT;dodec) 1	1.05
P(DMS- <i>co</i> -MHS)- <i>g</i> -(P3HT;dodec) 2	1.06

Films of P(DMS-*co*-MHS)-*g*-(P3HT;PEG) 2 and P(DMS-*co*-MHS)-*g*-(P3HT;dodec) 2 drop coated from chlorobenzene solution feature morphology similar to spin coated films (Fig. 8.4). Circular islands of agglomerates in P(DMS-*co*-MHS)-*g*-(P3HT;PEG) 2 drop coated film are more numerous and more pronounced than for spin-coated film, but still isolated. It is due to the fact that slower solvent evaporation (drop coating and less volatile chlorobenzene solvent) promotes agglomeration and self assembling of P3HT [235]. If there are some free P3HT chains, not chemically attached to polysiloxane backbone, phase separation and creation of P3HT micro-domains in polysiloxane based matrix may occur. In case of P(DMS-*co*-MHS)-*g*-(P3HT;dodec) 2 there was no significant difference in AFM images between spin coated (Fig. 8.3) and drop coated (Fig. 8.4) layers.

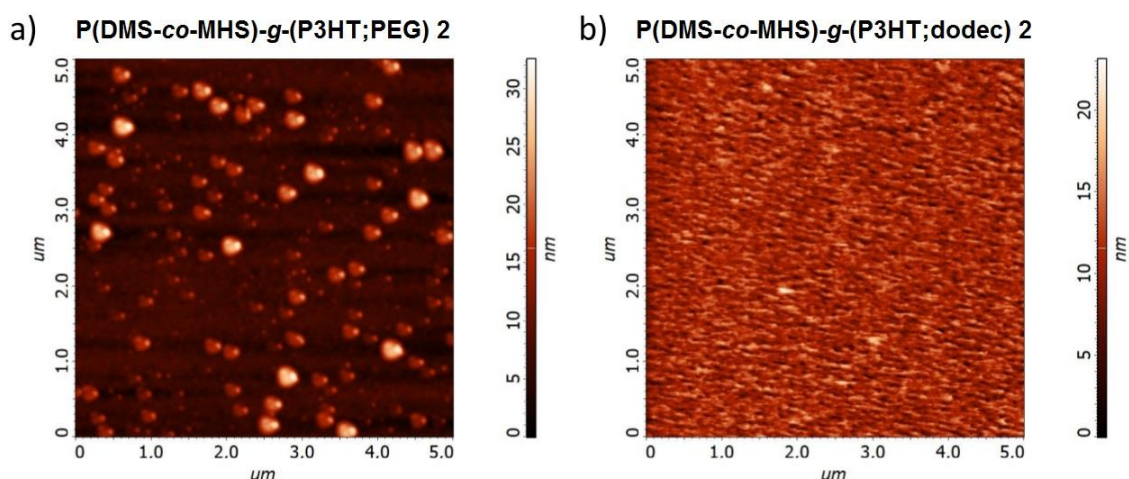


Fig. 8.4 AFM height images of copolymer films drop coated from CB solutions on IDT (substrate region): a) P(DMS-*co*-MHS)-*g*-(P3HT;PEG) 2, b) P(DMS-*co*-MHS)-*g*-(P3HT;dodec) 2 [234]

Sensor responses were recorded for repeating exposure to NO<sub>2</sub> in nitrogen carrier gas. Sorption was reversible, when NO<sub>2</sub> was removed sensor resistance returned to initial values. At RT recovery process was slow, therefore subsequent measurements were performed at

elevated temperatures (50 and 100°C). Fig. 8.5 presents resistance responses to the repeated exposition to 5 ppm of NO<sub>2</sub> in nitrogen carrier gas for RR P3HT, NR P3HT, PMHS-*g*-(P3HT;PEG) 1 and PMHS-*g*-(P3HT;PEG) 3 at 50 °C.

In general, responses of graft copolymers were higher than responses of pristine P3HT, both regioregular and nonregular. RR P3HT showed the lowest response, whereas PMHS-*g*-(P3HT;PEG) 3 copolymer (with long P3HT chains and long polysiloxane backbone) the highest. Recovery of the sensors (except for RR P3HT) in 30 min was incomplete, resulting in baseline drift, especially for PMHS-*g*-(P3HT;PEG) 3.

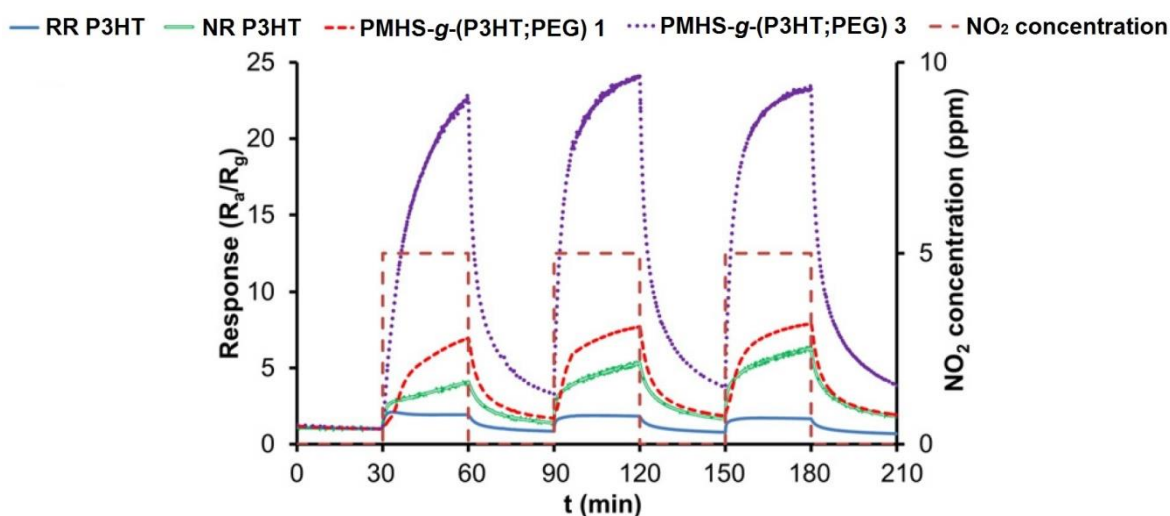


Fig. 8.5 Resistance responses of RR and NR P3HT, and graft copolymers (PMHS-*g*-(P3HT;PEG) 1, PMHS-*g*-(P3HT;PEG) 3) to the repeated exposure to 5 ppm of NO<sub>2</sub> at 50°C [232]

Fig. 8.6 presents resistance responses to the repeated exposition to the increasing concentration of NO<sub>2</sub> in nitrogen carrier gas (1 ppm, 5 ppm, 10 ppm and 20 ppm) for copolymers grafted on P(DMS-*co*-MHS) backbone: P(DMS-*co*-MHS)-*g*-(P3HT;PEG) 1, P(DMS-*co*-MHS)-*g*-(P3HT;PEG) 2, P(DMS-*co*-MHS)-*g*-(P3HT;dodec) 1 and P(DMS-*co*-MHS)-*g*-(P3HT;dodec) 2 at 50°C (a) and 100°C (b). At 50°C P(DMS-*co*-MHS)-*g*-(P3HT;PEG) 1 with hexane fraction of P3HT and PEG co-graft showed the highest responses for lower concentrations of NO<sub>2</sub> (1 and 5 ppm), whereas for 20 ppm of NO<sub>2</sub> P(DMS-*co*-MHS)-*g*-(P3HT;PEG) 2 with chloroform fraction of P3HT outperforms its analogue with shorter P3HT chains. At 100°C similar trend is observed, however response profiles are smoother and recovery times of sensor layers are faster. Copolymers with dodecyl co-grafts show lower responses, comparable with RR P3HT. In general, highest responses, best stability and operation dynamics of sensing layers fabricated by spin-coating copolymers bearing P(DMS-*co*-MHS) backbone from chloroform solutions are observed at 100°C,

whereas copolymers bearing PMHS backbone exhibited stable response to NO<sub>2</sub> exposure in lower temperature (50°C).

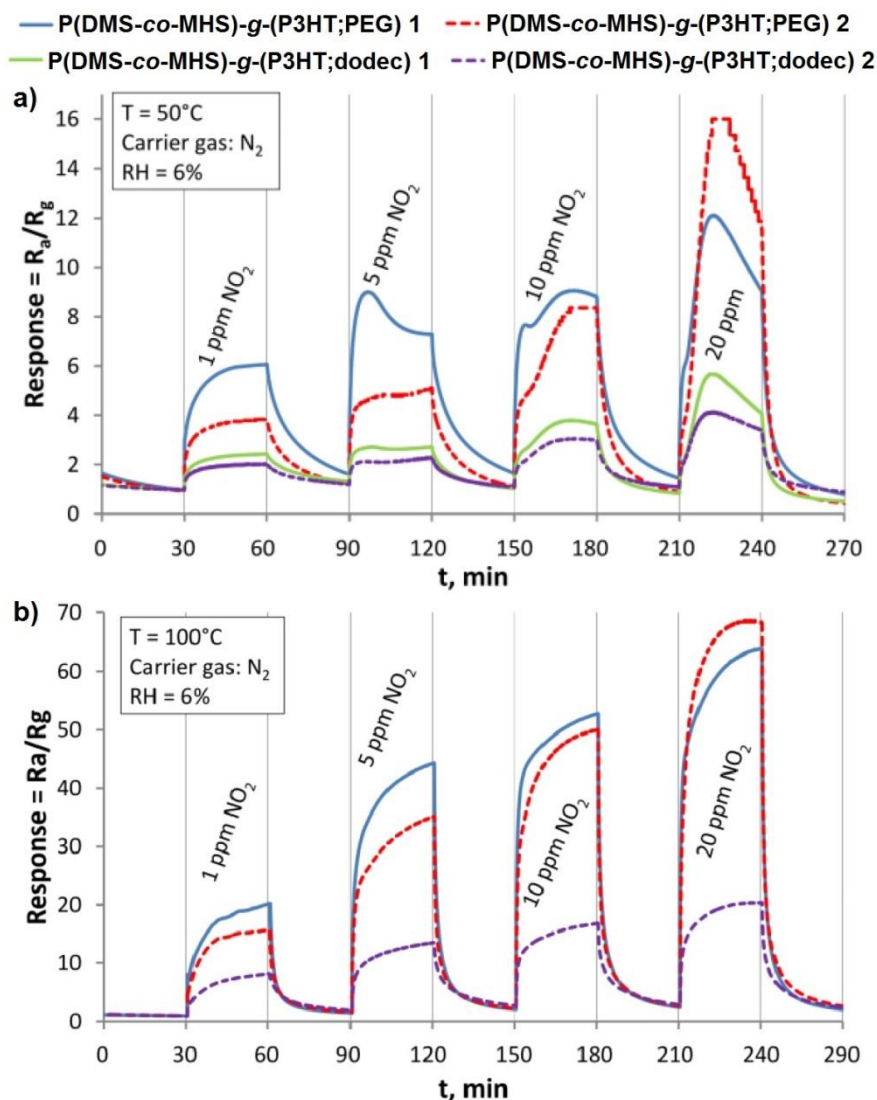


Fig. 8.6 Resistance responses of graft copolymers (P(DMS-co-MHS)-g-(P3HT;PEG) 1, P(DMS-co-MHS)-g-(P3HT;PEG) 2, P(DMS-co-MHS)-g-(P3HT;dodec) 1, P(DMS-co-MHS)-g-(P3HT;dodec) 2) to the repeated exposure to different concentrations of NO<sub>2</sub> at 50°C (a) and 100°C (b) [233]

P(DMS-co-MHS)-g-(P3HT;PEG) 2 and P(DMS-co-MHS)-g-(P3HT;dodec) 2 copolymers were selected for further investigation as NO<sub>2</sub> sensors. Preliminary investigations described above were conducted in inert N<sub>2</sub> carrier gas, but in the environmental conditions gas sensors operate in the air. Oxygen present in the air is an oxidizing agent which may interact with the sensing layer lowering its response to the target NO<sub>2</sub> gas, therefore it is important to test proposed materials in air. Another aim was to lower the operating temperature of gas sensor as it is required in case to reduce power consumption of the

working device, but at lower temperatures dynamics of the sensors is decreased. Sensing layers were fabricated by drop coating chlorobenzene solutions of the copolymers, and the sensors were tested at room temperature in dark conditions and under UV irradiation in N<sub>2</sub> and air atmosphere. UV irradiation was applied to improve dynamics of the sensors and to decrease baseline drift throughout the exposure-recovery cycles.

In the nitrogen as the carrier gas P(DMS-*co*-MHS)-*g*-(P3HT;PEG) 2 is much more sensitive to NO<sub>2</sub> (about 4-5 times) than P(DMS-*co*-MHS)-*g*-(P3HT;dodec) 2 (Fig. 8.7). Responses under UV irradiation were stronger than for the dark conditions. Both materials exhibited distinct response to NO<sub>2</sub> concentrations as low as 200 ppb and strong baseline drift for dark conditions as well as for UV irradiation at room temperature.

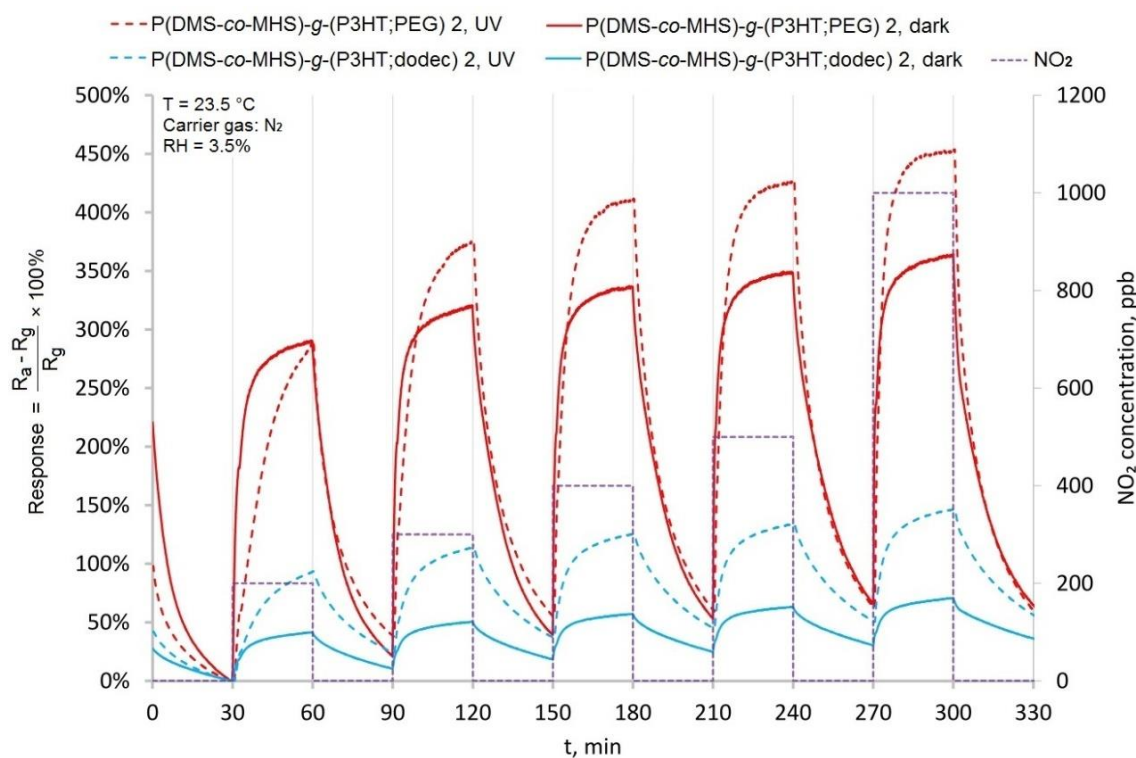


Fig. 8.7 Resistance responses of graft copolymers P(DMS-*co*-MHS)-*g*-(P3HT;PEG) 2, and P(DMS-*co*-MHS)-*g*-(P3HT;dodec) 2 to the repeated exposure to different concentrations of NO<sub>2</sub> in N<sub>2</sub> at RT under dark and UV conditions [234]

In case of measurements conducted in the air as the carrier gas relative responses under UV irradiation were much lower compared to results obtained in nitrogen for both copolymers, but in exchange baseline drift was suppressed (Fig. 8.8), especially in the case of copolymer bearing co-grafted PEG chains, for which upon recovery baseline returned to a value below 10% increase of the initial resistance throughout all investigated NO<sub>2</sub>



concentrations. This suggests that UV irradiation enhances desorption of NO<sub>2</sub>, assisting sensor recovery.

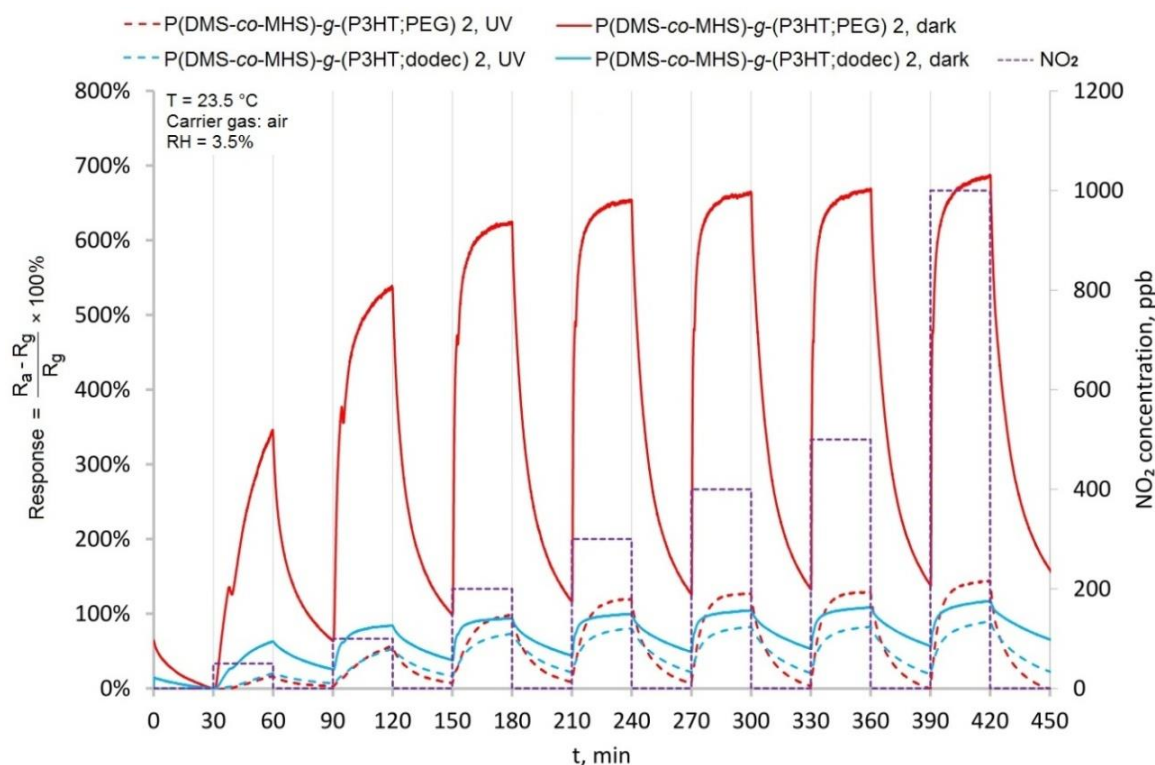


Fig. 8.8 Resistance responses of graft copolymers P(DMS-*co*-MHS)-*g*-(P3HT;PEG) 2, and P(DMS-*co*-MHS)-*g*-(P3HT;dodec) 2 to the repeated exposure to different concentrations of NO<sub>2</sub> in the air at RT under dark and UV conditions [234]

Under dark conditions in the air baseline drift was even more pronounced compared to that observed in the nitrogen carrier gas. On the other hand, under dark conditions the response of P(DMS-*co*-MHS)-*g*-(P3HT;dodec) 2 increased slightly, whereas for P(DMS-*co*-MHS)-*g*-(P3HT;PEG) 2 about 2-fold increase of the response was observed. Lower sensitivity of the sensors irradiated with UV light in the air might be attributed to the lower base resistance ( $R_a$ ) resulting from the presence of photogenerated charge carriers in the copolymer films. Indeed, upon UV irradiation in the presence of the air photocurrent increasing with irradiation time was recorded [234].

Continuous UV irradiation of the sensor made of P(DMS-*co*-MHS)-*g*-(P3HT;PEG) 2 copolymer under air flow resulted in its gradual degradation. “Fresh” sensor (after 1 hour of work) showed response of 260% to 500 ppb of NO<sub>2</sub>. After 1 day and 14 days of continuous exposure to UV irradiation and the air the response of the sensor decreased to 145% and 18.5% respectively (Fig. 8.9 a). After 2 weeks of the ageing changes in the film morphology

were observed as well: the agglomerates on the surface have grown higher (from 30 to 60 nm) and the RMS increased to 4.9 nm (Fig. 8.9 b).

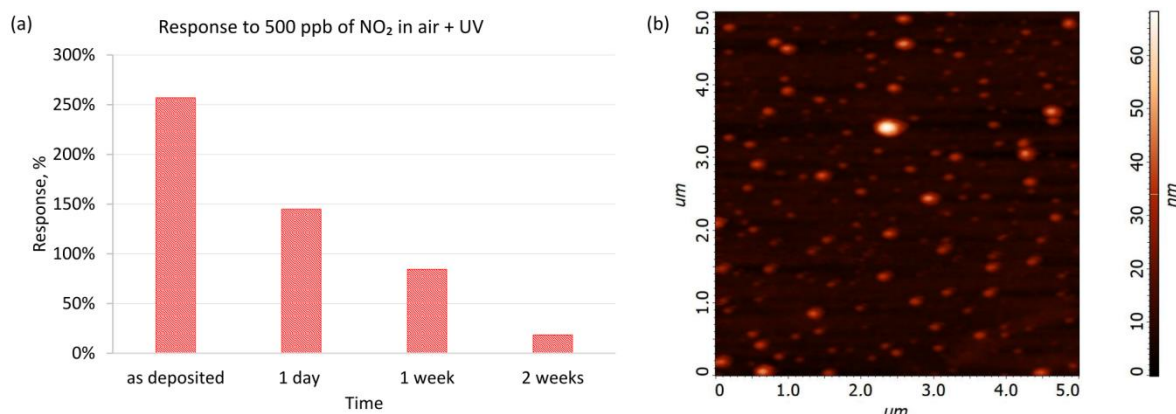


Fig. 8.9 a) P(DMS-*co*-MHS)-*g*-(P3HT;PEG) 2 response to 500 ppb of NO<sub>2</sub> in the air under continuous UV illumination, b) AFM surface image of P(DMS-*co*-MHS)-*g*-(P3HT;PEG) 2 after two weeks of ageing under UV in the air [234]

NO<sub>2</sub> sensors of IDT structure were prepared based on thin films of P3HT and its copolymers by spin coating chloroform solution or drop casting from chlorobenzene solution. This method allowed for simple and inexpensive sensors fabrication. Pristine RR P3HT is a poor material for NO<sub>2</sub> gas sensors, NR P3HT outperformed it. Copolymers bearing RR P3HT side chains and polysiloxane backbone featured increased sensitivity compared to pure RR P3HT. Especially in case of copolymers with co-grafted polyether chains response to NO<sub>2</sub> was significantly enhanced. It seems that co-grafted alkyl chains act mostly as internal plasticizer, improving film-forming and mechanical properties of sensor layers, whereas PEG can absorb NO<sub>x</sub> particles [236], therefore presence of PEG segments in copolymers greatly improves NO<sub>2</sub> sensing properties of tested materials.

## 8.2 Photovoltaic devices

RR P3HT and 3 of its copolymers were investigated in BHJ solar cells with phenyl-C<sub>61</sub>-butyric acid methyl ester (PCBM) as fullerene acceptor: PMHS-*g*-P3HT bearing short PMHS-S and P3HT FC, PMHS-*g*-(P3HT;hex) 1, bearing short PMHS-S and P3HT FC and PMHS-*g*-(P3HT;hex) 2 bearing long PMHS-L and P3HT FC. Results of J-V measurements (average measured J<sub>SC</sub>, V<sub>OC</sub>, calculated FF and PCE are summarised in Tab. S.2).

For P3HT:PCBM solar cells, it was found that annealing the active layer at 100°C for 5 min prior to Al contact deposition resulted in solar cells with the highest efficiency (average

PCE 2.35%, PCE of the best solar cell 2.42%). However, these solar cells showed a gradual deterioration of the performance after storage for 8 days in N<sub>2</sub> atmosphere (PCE decrease from 2.33 to 2.11%), mostly due to the decrease of J<sub>SC</sub> (from 6.80 to 6.44 mA/cm<sup>2</sup>) (J-V curves are shown in Fig. 8.10). P3HT:PCBM solar cells annealed prior to contact deposition, after further annealing at 100°C exhibited a decrease in performance – slight after 10 min, and significant after 30-60 min (J-V curves are plotted in Fig. 8.11). Average PCE decreased from 2.37 to 2.24% after 10 min, 1.75% after 30 min and finally to 1.67% after 60 min, mainly due to a decrease of J<sub>SC</sub> (from 6.90 to 6.76 mA/cm<sup>2</sup> after 10 min, 5.54 mA/cm<sup>2</sup> after 30 min and 5.45 mA/cm<sup>2</sup> after 60 min).

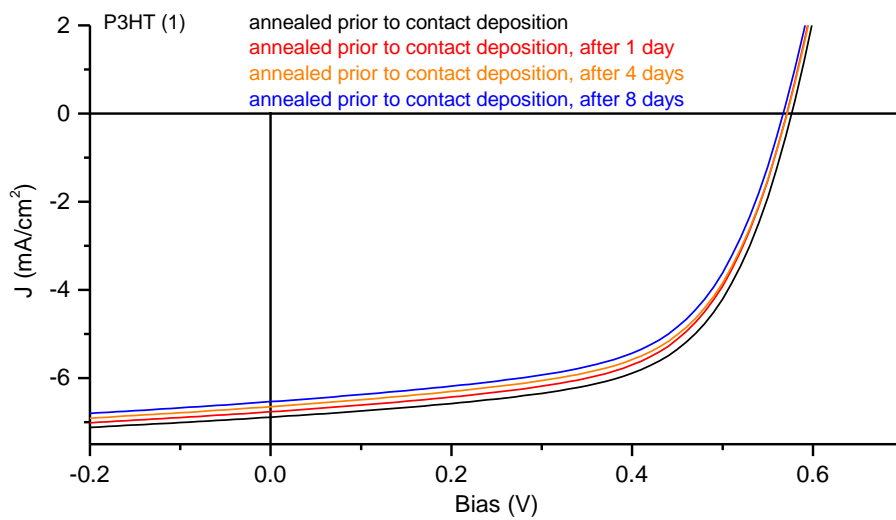


Fig. 8.10 J-V curves of P3HT:PCBM (1) solar cell stored under nitrogen

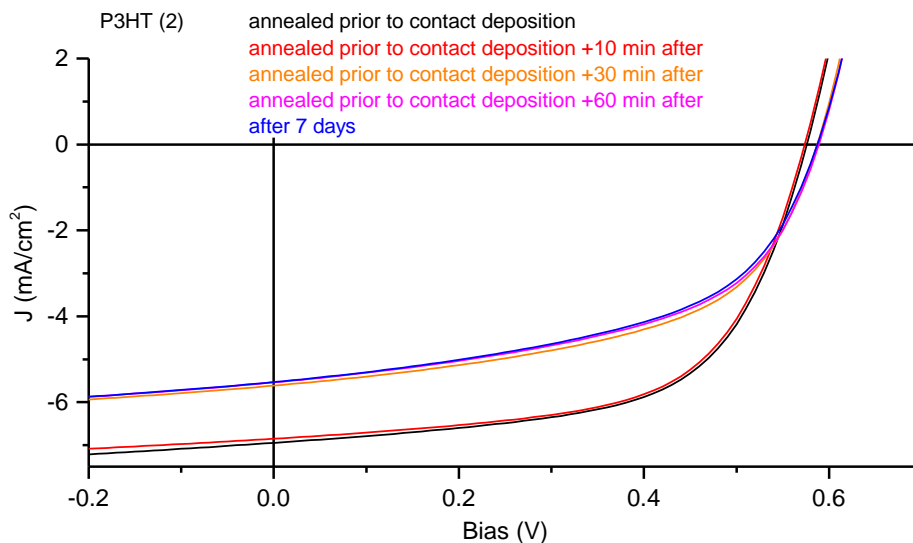


Fig. 8.11 J-V curves of P3HT:PCBM (2) solar cell annealed before contact deposition

In case of not annealed P3HT:PCBM solar cells initial annealing after Al contact deposition resulted in an initial increase in performance after 10 min annealing (average PCE increase from 0.91 to 2.01%) due to the increase of  $J_{SC}$  (from 3.29 to 6.48 mA/cm<sup>2</sup>) and FF (from 0.395 to 0.523), with a simultaneous decrease of  $V_{OC}$  (from 0.696 to 0.592 V). Further annealing results in PCE drop to 1.72% after 60 min due to the decrease of  $J_{SC}$  and FF. Performance of long annealed P3HT:PCBM solar cells was virtually not influenced by storing for 7 days in an inert atmosphere (J-V curves are shown in Fig. 8.12).

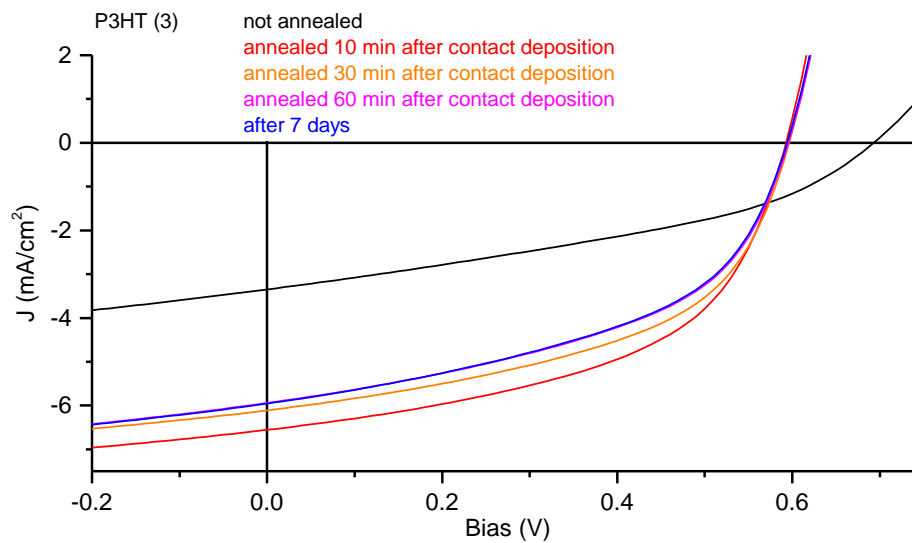


Fig. 8.12 J-V curves of P3HT:PCBM (3) solar cell annealed after contact deposition

For PMHS-g-(P3HT:hex) 1:PCBM solar cells, it was found that annealing the active layer at 100°C for 10 min after Al contact deposition resulted in solar cells with the highest efficiency (average PCE 2.30%, , PCE of the best solar cell 2.32% - value comparable with P3HT:PCBM solar cells). For solar cells based on PMHS-g-(P3HT:hex) 1 copolymer annealing at 100°C was found to improve the efficiency for both types of devices: annealed prior and after contact deposition. In general long annealing (for 30 min and more) did not have significant deteriorating effect on the performance of such devices. For solar cells annealed for 5 min prior to contact deposition average PCE increased gradually from 1.70 to 2.00% upon further annealing for 60 min (J-V curves are shown in Fig. 8.13). PCE increase resulted from the increase of  $J_{SC}$  from 4.93 to 5.58 mA/cm<sup>2</sup> and  $V_{OC}$  from 0.589 to 0.624 V.

For the devices based on PMHS-g-(P3HT;hex) 1 copolymer annealed after contact deposition high increase in average PCE was achieved after 10 min (from 0.95 to 2.30%) and further annealing for up to 60 min did not influence performance significantly (J-V curves are shown in Fig. 8.14). Rise in PCE resulted from the initial increase and stabilisation of  $J_{SC}$

(from 3.50 to 6.13 mA/cm<sup>2</sup>) and FF (from 0.381 to 0.588) after 10 min of annealing. On the other hand initial decrease in  $V_{OC}$  from 0.714 to 0.637 V was observed for 10 min annealing, followed by stabilisation upon further annealing. Similar drop of  $V_{OC}$  was observed for P3HT:PCBM solar cells annealed after contact deposition. Storage of PMHS-g-(P3HT;hex) 1-based solar cells for 8 days in N<sub>2</sub> atmosphere had very low influence on the performance of devices (Fig. 8.13, Fig. 8.14).

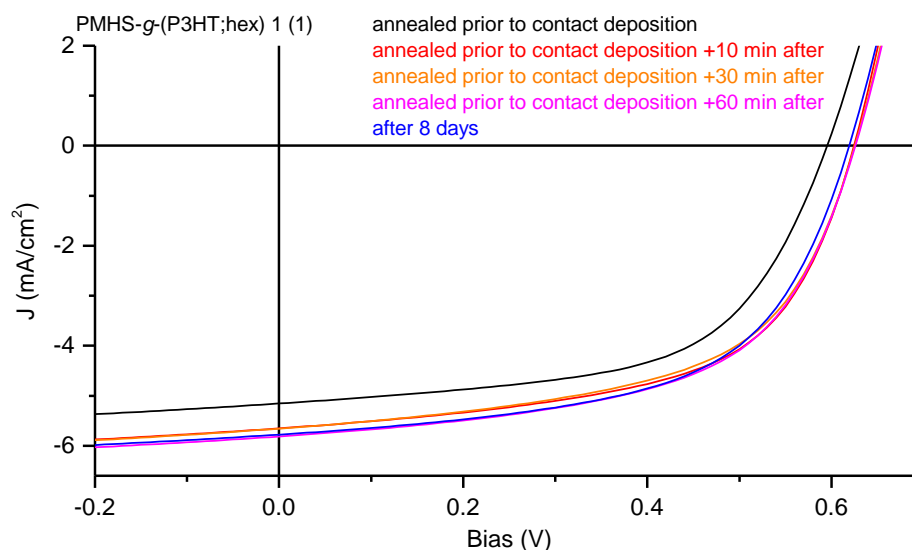


Fig. 8.13 J-V curves of PMHS-g-(P3HT;hex) 1:PCBM (1) solar cell annealed before contact deposition and further annealed after contact deposition

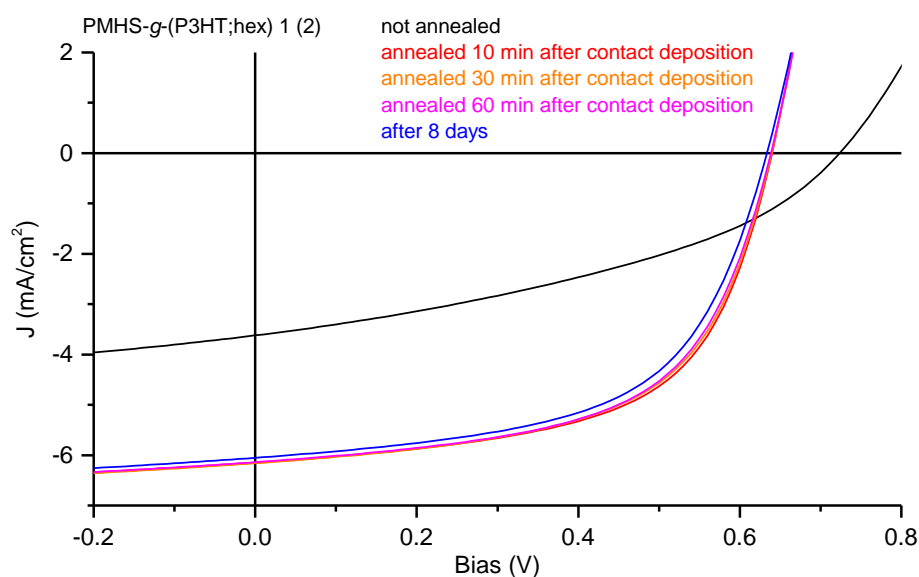


Fig. 8.14 J-V curves of PMHS-g-(P3HT;hex) 1:PCBM (2) solar cell annealed after contact deposition

For solar cells based on PMHS-*g*-(P3HT:hex) 2 highest PCE (average 1.56%, PCE of the best solar cell 1.59%) was found for the device annealed 5 min after contact deposition. For the device annealed prior to contact deposition further annealing, even for short time, resulted in slight decrease of the parameters (J-V curves are shown in Fig. 8.15).

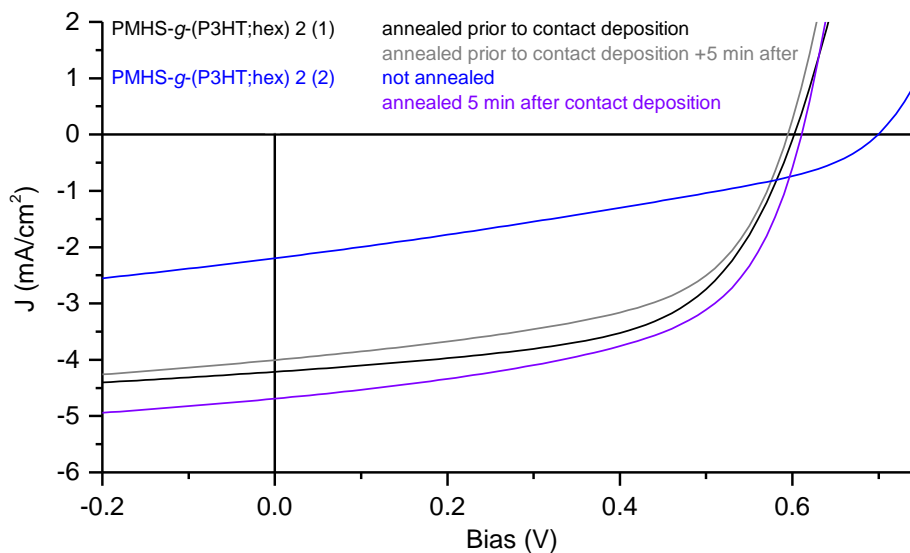


Fig. 8.15 J-V curves of PMHS-*g*-(P3HT;hex) 2:PCBM (1) and (2) solar cells annealed before and after contact deposition

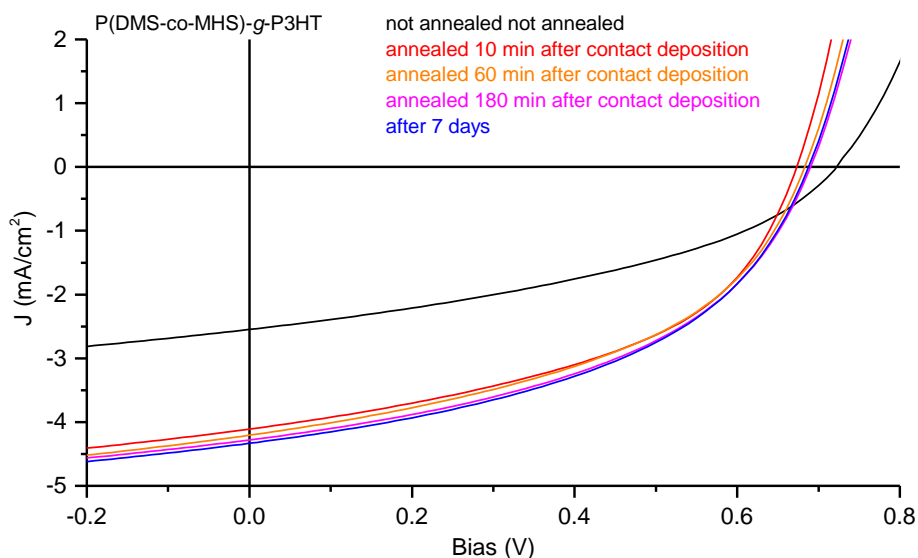


Fig. 8.16 J-V curves of P(DMS-*co*-MHS)-*g*-P3HT:PCBM solar cell annealed after contact deposition

For solar cells based on P(DMS-*co*-MHS)-*g*-P3HT influence of long thermal annealing (up to 180 min) after contact deposition was investigated. Annealing at 100°C resulted in

gradual increase of average PCE (from 0.69 to 1.30% after 10 min of annealing, 1.33% after 60 min and 1.37% after 180 min) due to the increase of JSC (from 2.44 to 4.04 mA/cm<sup>2</sup> after 10 min, 4.14 mA/cm<sup>2</sup> after 60 min and 4.21 mA/cm<sup>2</sup> after 180 min).  $V_{OC}$  initially dropped from 0.719 to 0.672 V after 10 min annealing, then stabilized at 0.690 V after 180 min J-V curves are shown in Fig. 8.16). Storage for 7 days under nitrogen had virtually no influence on the efficiency of these solar cells. Lower PCEs may result to some extent from thinner active layer: for P3HT:PCBM and PMHS-*g*-(P3HT:hex) 1:PCBM solar cells measured thickness of active layers were accordingly 94-96 and 84-87 nm, whereas for PMHS-*g*-(P3HT:hex) 2:PCBM and PMHS-*g*-P3HT solar cells active layers were 67-72 and 61 nm thick, respectively.

EQE measurements resulted in similar absorption profile in the 300-900 nm range for P3HT:PCBM and copolymer-based solar cells (Fig. 8.17). Broad absorption bands cover 300-650 nm range with medium absorption in 430-630 nm region and high absorption at 480-550 nm region for all tested devices. Bathochromic shift of absorption maximum is observed in the series: P3HT (500 nm), PMHS-*g*-(P3HT:hex) 1 (520 nm) and PMHS-*g*-(P3HT:hex) 2 (530 nm) solar cells. Highest EQE was recorded for P3HT solar cell, but PMHS-*g*-(P3HT:hex) 1 showed very similar light absorption profile, almost identical in 540-590 nm region of the spectrum.

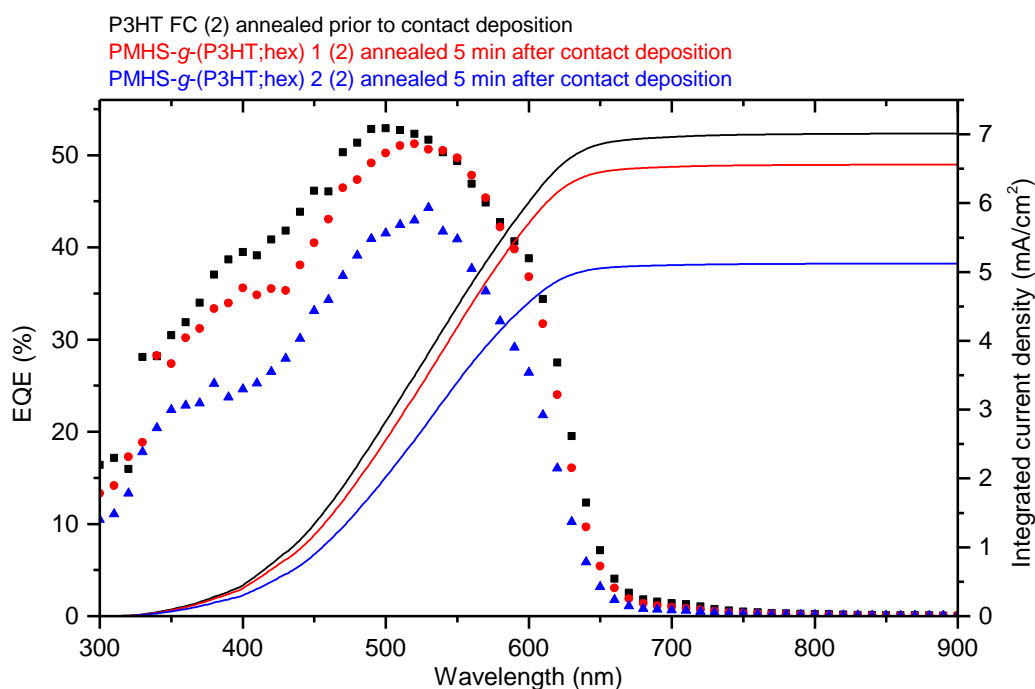


Fig. 8.17 EQE characteristic of solar cells with AM1.5G integrated current densities

Tab. 8.3 summarizes  $J_{SC}$  values determined from EQE measurements of the best solar cells tested and resulting PCE values. It can be seen that for investigated solar cells J-V measurements underestimated current density values in all cases. For P3HT:PCBM solar cell  $J_{SC}$  value differs only by 1.6%, but in case of PMHS-g-(P3HT;hex) 1:PCBM solar cells  $J_{SC}$  underestimation reaches 8.3-8.4%. Based on EQE measurements PMHS-g-(P3HT;hex) 1:PCBM solar cell slightly outperformed P3HT:PCBM solar cell mostly due to achieving higher  $V_{OC}$  value: 0.637 V compared to 0.576 V of P3HT:PCBM solar cells.

Tab. 8.3 Parameters of solar cells calculated based on EQE measurements

No.	Solar cell	$J_{SC}$ [mA/cm <sup>2</sup> ]	$J_{SC}$ EQE [mA/cm <sup>2</sup> ]	$V_{OC}$ [V]	FF	PCE [%]
1	P3HT (2) annealed prior to contact deposition	6.887	7.000	0.576	0.609	2.46
2	PMHS-g-(P3HT;hex) 1 (2) annealed 5 min after contact deposition	6.005	6.550	0.637	0.606	2.53
3	PMHS-g-(P3HT;hex) 2 (2) annealed 5 min after contact deposition	4.691	5.120	0.611	0.554	1.73

UV-Vis spectra of thin film representing active layers of investigated solar cells (blends of P3HT or the copolymers with PCBM mixed in 3:2 ratio): as cast from CB solution and after annealing under  $N_2$  for 5 min at 100°C are collected in Fig. 8.18. UV-Vis spectra of all thin films featured PCBM peak located at 333 nm, and absorption bands of P3HT in the range 400-650 nm. Position and shape of PCBM peak was the same for all thin films investigated and did not change upon annealing. In case of P3HT:PCBM blend 3 bands originating from P3HT are discernible in the UV-Vs spectrum of as cast thin film:  $\pi$ - $\pi^*$  transition absorption band with maximum at 510 nm and vibronic shoulders at 556 and 609 nm characteristic for P3HT in solid state [237]. Upon annealing slight bathochromic shift of 510 nm maximum to 516 nm was observed and all three bands became better resolved. In case of P(DMS-co-MHS)-g-P3HT, PMHS-g-(P3HT;hex) 1 and PMHS-g-(P3HT;hex) 2 copolymer blends before annealing broad bands with maxima at accordingly 496, 493 and 486 nm are observed in the region 400-650 nm. After annealing the maximum of  $\pi$ - $\pi^*$  transition band redshifted to 513-516 nm and two vibronic shoulders at 554-556 and 606-607 nm emerged in the spectra of all copolymer blends. Longer annealing (up to 30 min) did not affect significantly absorption profiles of investigated thin films. In general, progressive broadening of P3T absorption bands towards longer wavelengths with increasing intensity were observed in all cases upon annealing. This indicates that annealing promoted self-organisation and



crystallisation of P3HT domains, and copolymer blends with PCBM develop vibronic structure characteristic for P3HT. It also implies enhancement of  $J_{SC}$  of the solar cells upon annealing as resulting from increase in crystallinity degree and  $\pi$ - $\pi$  interactions promoting development of conducting pathways in BHJ lattice.

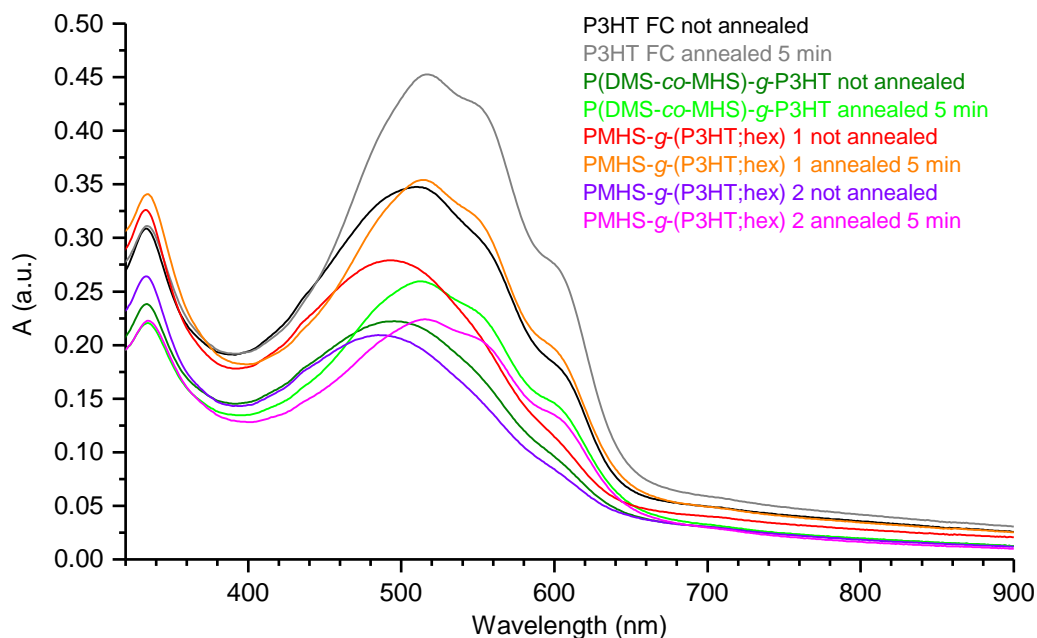


Fig. 8.18 UV-Vis absorption spectra of thin films (P3HT and copolymers blend with PCBM) as cast and annealed for 5 min

Optical band gaps determined from UV-Vis spectra (from the onset of the absorption peak) were practically the same for all investigated blends (1.90-1.92 eV – value characteristic for regioregular P3HT [238]).

In the Fig. 8.19 AFM height (left column) and phase images (right column) of surfaces of P3HT-based solar cell are collected. In case of P3HT:PCBM solar cells annealed 5 min prior to contact deposition (Fig. 8.19 a) big circular islands of up to about 350 nm diameter are clearly visible in surface and phase AFM images. Images of P3HT:PCBM solar cells annealed for 60 min after contact deposition (Fig. 8.19 b) demonstrate more uniform surface with lower roughness (slightly lower RMS and much smaller peak to peak distance – see Tab. 8.4). Especially 1x1  $\mu\text{m}$  images show smoother surface, yet scattered aggregates of diameter up to about 300 nm are still present.

In the Fig. 8.20 AFM height (left column) and phase (right column) images of the surface of PMHS-g-(P3HT;hex) 1 copolymer-based solar cell are presented. Copolymer:PCBM blend surface exhibits different pattern than P3HT:PCBM blend. It is

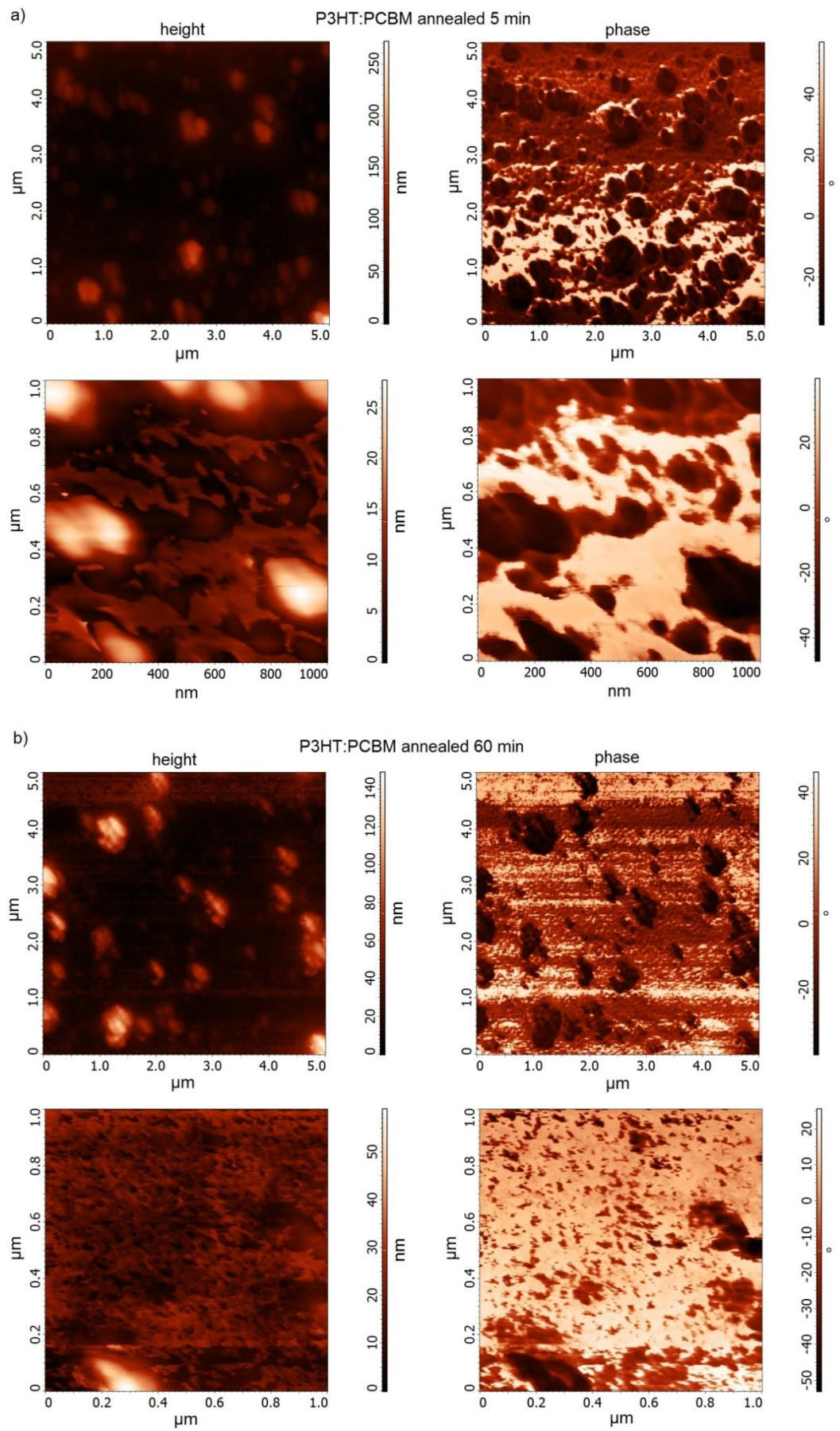


Fig. 8.19 AFM images of P3HT:PCBM solar cells surface: annealed 5 min (a) and 60 min (b)

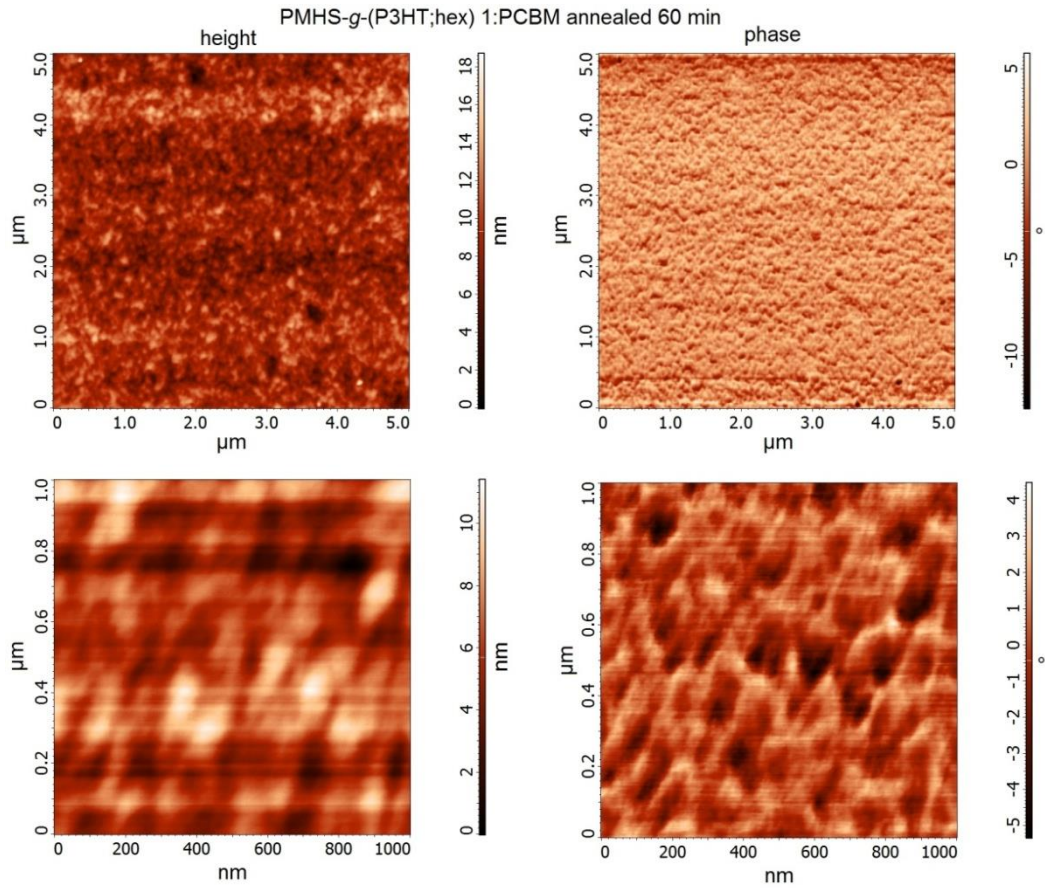


Fig. 8.20 AFM images of PMHS-*g*-(P3HT;hex) 1:PCBM solar cells surface annealed 60 min

much smoother (see Tab. 8.4), without pronounced aggregates, and features uniform pattern with 30-80 nm valeys distributed evenly across the plane. This supports the hypothesis about molecaular dilution of P3HT in the sythesised copolymers, which prevents large scale  $\pi$ -stacking and aggregation. Moreover, polysiloxanes demonstrate a tendency to assemble into the interface between P3HT and PCBM [98] which facilitates miscibility of P3HT donor component with fullerene acceptor component in the BHJ active layers of tested solar cells.

Tab. 8.4 RMS and peak to peak distances (maximum heights) of the solar cells surfaces determined from AFM images

Solar cell	RMS (5x5 $\mu\text{m}$ area) [nm]	Peak to peak (5x5 $\mu\text{m}$ area) [nm]
P3HT (1) annealed 5 min prior to contact deposition	22.7	271.2
P3HT (2) annealed prior to contact deposition +60 min after	20.4	148.5
PMHS- <i>g</i> -(P3HT;hex) (2) annealed 60 min after contact deposition	1.9	18.7

It seems that nanoscale blending of components in siloxane copolymer:PCBM thin film resulted in the creation of domains better fitted to diffusion pathway of the exciton, facilitating transport of excitons to the heterojunction interface. On the other hand sufficient percolating channels of donor and acceptor domains are maintained to provide transport of electrons and holes to the electrodes. Series of block copolymers of P3HT and PDMS reported in literature allowed for fabrication of P3HT-*b*-PDMS:PC<sub>61</sub>BM BHJ solar cells exhibiting higher PCE than reference P3HT:PC<sub>61</sub>BM solar cell, but prone to thermal degradation upon prolonged annealing, similar to reference P3HT-based devices [98]. Polysiloxane-P3HT graft copolymers reported in this work allowed for thermal stabilisation of active layer's optimal architecture. They prevent aggregation of PCBM and P3HT into too large domains (resulting in too extensive phase separation), without suppressing P3HT crystallisation to achieve higher light absorption.

## IX. Summary and conclusions

Copolymers in this work were designed as multifunctional  $\pi$ -conjugated materials able to be tailored on molecular and supramolecular levels to adjust physicochemical properties. Variable lengths of P3HT side chains and polysiloxane backbone, as well as different co-grafted moieties (none, alkyl or PEG) were employed to tune morphology and optoelectronic properties of resulting materials.

Regioregular poly(3-hexylthiophene) was chosen for macromolecular manipulations as a representative, solution-processable conjugated polymer – as well recognised hole transporting conjugated system, referred to as a benchmark among conducting polymers. Polymethylsiloxane backbone was incorporated into graft macromolecules as an inert, flexible, non-toxic, non-flammable scaffold to further promote solubility of investigated materials in organic solvents by limiting  $\pi$ - $\pi$  stacking of polythiophene chains and enhance miscibility with n-type component in bulk heterojunction solar cell active layer. Polysiloxane acts also as a surfactant, lowering the surface tension of polymer solution, improving deposition of smooth polymer layers. Different co-grafts were implemented as additional molecular dispersers for P3HT chains, as well as moieties saturating remaining active sites remaining on the PMHS backbone after grafting P3HT. Two types of co-grafts were applied: polar medium-length polyether (PEG) chains ( $M_n$  500 g/mol) and nonpolar hydrocarbon component (alkyl chains of different lengths: hexyl and dodecyl) were used as filler, plasticizer and agents enhancing solubility of the resulting copolymers.

Grafting onto approach via hydrosilylation reaction was adapted to obtain copolymers. Hydrosilylation was selected as an easy, one-pot reaction proceeding under mild conditions, resulting in coupling between active Si-H sites on polysiloxane backbone and unsaturated bonds, especially effective for C=C moiety, such as vinyl group. To obtain vinyl-functionalised regioregular P3HT Grignard Metathesis (GRIM) with in-situ end-functionalisation method was employed.

NMR analysis suggests that molecular composition of obtained copolymers diverges from stoichiometry assumed based on reaction feed, nevertheless series of indirect evidences (disappearance of reactive groups present in the individual building blocks, consumed in the course of coupling reaction) point to occurrence of grafting process and chemical bonding of the segments.

Graft copolymers with PEG [PMHS-*g*-(P3HT;PEG) 1 and 3, P(DMS-*co*-MHS)-*g*-(P3HT;PEG) 1 and 2] and dodecyl moieties [P(DMS-*co*-MHS)-*g*-(P3HT;dodec) 1 and 2] co-grafted on polysiloxane backbone were tested as low-temperature resistance gas sensors for NO<sub>2</sub> detection. The key objective of this part of the work was to develop new materials of improved performance for highly sensitive and stable chemoresistive sensors with low power consumption based on conducting polymer. Graft copolymers demonstrated higher responses to NO<sub>2</sub> than P3HT, both regular and nonregular. Especially presence of PEG co-grafts in copolymer structure improved response of the sensors: PMHS-*g*-(P3HT;PEG) 3, P(DMS-*co*-MHS)-*g*-(P3HT;PEG) 1 and P(DMS-*co*-MHS)-*g*-(P3HT;PEG) 2 copolymers were found the most efficient sensor materials. For all tested sensors dynamics of regeneration process at room temperature was slow, but was improved by elevating operating temperature of the sensors to 50-100°C and irradiation of the sensor with UV. Implementation of these modifications resulted in faster target gas desorption and more efficient restoration to base conditions.

Graft copolymers bearing co-grafted alkyl chains (PMHS-*g*-(P3HT;hex) 1 and 2), and with no co-grafts (P(DMS-*co*-MHS)-*g*-P3HT) along with parent P3HT were tested as photovoltaic devices of BHJ architecture with fullerene PC<sub>61</sub>BM acceptor.

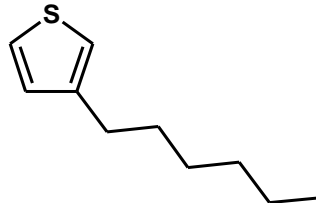
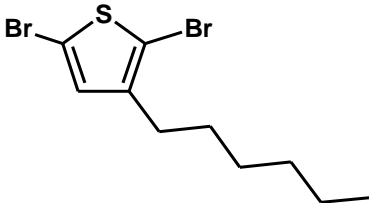

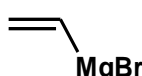
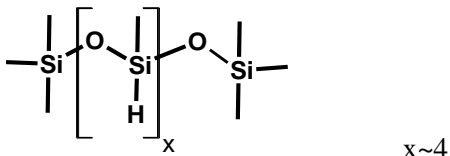
Different annealing conditions were found optimal for fabrication of solar cells based on P3HT and siloxane copolymers. P3HT:PCBM solar cells demonstrated the best performance upon short time annealing prior to contact deposition, whereas solar cells based on copolymers demonstrated the best performance upon annealing after metal contact deposition. PMHS-*g*-(P3HT;hex) 1 and 2 devices demonstrated the best efficiency upon short time annealing (5-10 min). PMHS-*g*-P3HT:PCBM devices performed best upon long annealing (180 min). What is more, PMHS-*g*-P3HT:PCBM solar cells were immune to deterioration during 7-days storage under nitrogen, whereas P3HT:PCBM showed 9.5% drop of PCE after 8-days storage under nitrogen. Solar cells based on P3HT and PMHS-*g*-(P3HT;hex) 1 copolymer demonstrated comparable efficiency (PCE about 2.5%) (and only 3.9% PCE drop after 8-days storage under nitrogen for PMHS-*g*-(P3HT;hex) 1-based device), while for solar cells based on PMHS-*g*-(P3HT;hex) 2 and PMHS-*g*-P3HT copolymers efficiencies were much lower (1.7-1.4%).

P3HT and PMHS-*g*-(P3HT;hex) 1 copolymer demonstrated differences in blending behaviour with PCBM upon annealing. In general, annealing of active layers improves the charge collection efficiency by promoting generation of P3HT and PCBM crystalline

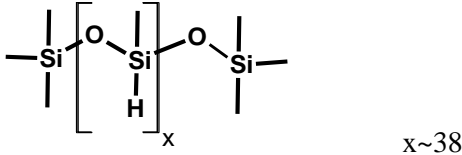
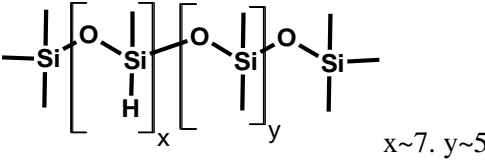
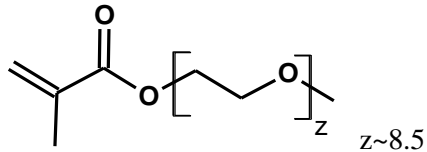
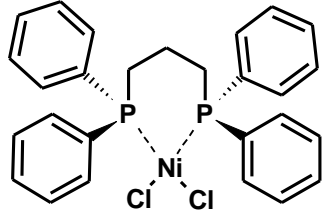
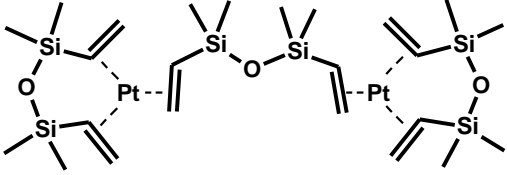
domains and paths for charge transport. Obtained copolymer blends featured surface roughness much lower than P3HT blend with PCBM, as well as different patterns of phase separation (domain sizes and shapes). In case of PMHS-*g*-(P3HT;hex) 1:PCBM solar cell long annealing promoted development of quite fine nanoscale mixing as a result of suppressing PCBM aggregation without hindering P3HT crystallisation and development of vibronic structure. PCE of long annealed PMHS-*g*-(P3HT;hex) 1-based solar cell was comparable with optimal, short annealed P3HT:PCBM solar cells with more pronounced phase separation of active layer components. In summary – obtained siloxane-P3HT copolymers seem promising materials for further investigation in photovoltaic devices.

## X. Supplement

Tab. S.1 List of commercially available thiophenes, polysiloxanes, poly(ethylene glycol), Grignard compounds and catalysts used in this work

Description	Chemical structure/symbol	Purity	CAS	Molar mass [g/mol]	Density [g/cm <sup>3</sup> ]	Manufacturer
3-hexylthiophene		> 98.0%	1693-86-3	168.30	0.94	TCI Chemicals
2,5-dibromo-3-hexylthiophene		> 97.0%	116971-11-0	326.09	1.54	TCI Chemicals
<i>tert</i> -Butylmagnesium chloride, 2M solution in diethyl ether		-	677-22-5	116.87	0.828	Sigma Aldrich
Vinylmagnesium bromide, 0.7M solution in THF		-	1826-67-1	131.25	0.9800	ACROS Organics
Poly(methylhydrosiloxane), trimethylsilyl terminated. average Mn ~ 390 PMHS 390		-	63148-57-2	-	0.85	Sigma Aldrich



Poly(methylhydrosiloxane), average Mn 1,700, 3.200 PMHS-L		-	63148-57-2	-	1.006	Sigma Aldrich
Poly(dimethylsiloxane-co-methylhydrosiloxane), trimethylsilyl terminated. average Mn ~ 950. methylhydrosiloxane 50 mol % P(DMS-co-MHS)		-	68037-59-2	-	0.99	Sigma Aldrich
Poly(ethylene glycol) methyl ether methacrylate, average Mn 500, contains 200 ppm BHT as inhibitor, 100 ppm MEHQ as inhibitor PEGMA		-	26915-72-0	-	1.08	Sigma Aldrich
1,3-Bis(diphenylphosphino)propane nickel(II) chloride Ni(dppp)Cl <sub>2</sub>		99%	15629-92-2	542.04	-	Sigma Aldrich
Platinum(0) -1,1,3,3-tetramethyl-1,3-divinyldisiloxane complex solution in xylene Karstedt catalyst, PTDD		Pt ~ 2 %	68478-92-2	381.48	-	Sigma Aldrich

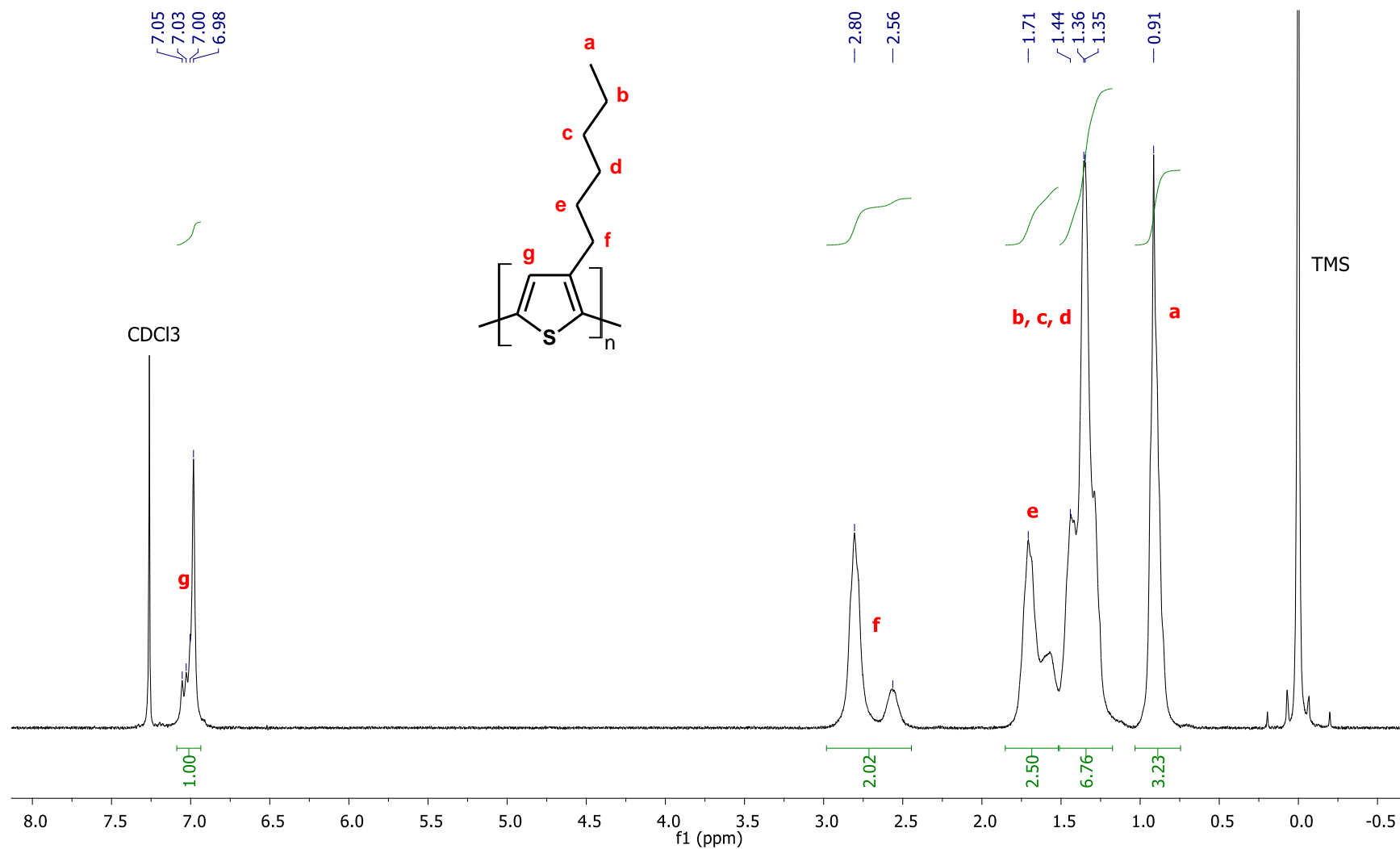


Fig. S.1  $^1\text{H}$  NMR spectrum of NR P3HT FC (300 MHz,  $\text{CDCl}_3$ ) with assignments of peaks:  $\delta$  (ppm) 7.05, 7.03, 7.00, 6.98 (4 singlets, 1H), 2.80, 2.56 (2 broad singlets, 2H), 1.71 (m, 2H), 1.44-1.35 (m, 6H), 0.91 (m, 3H)

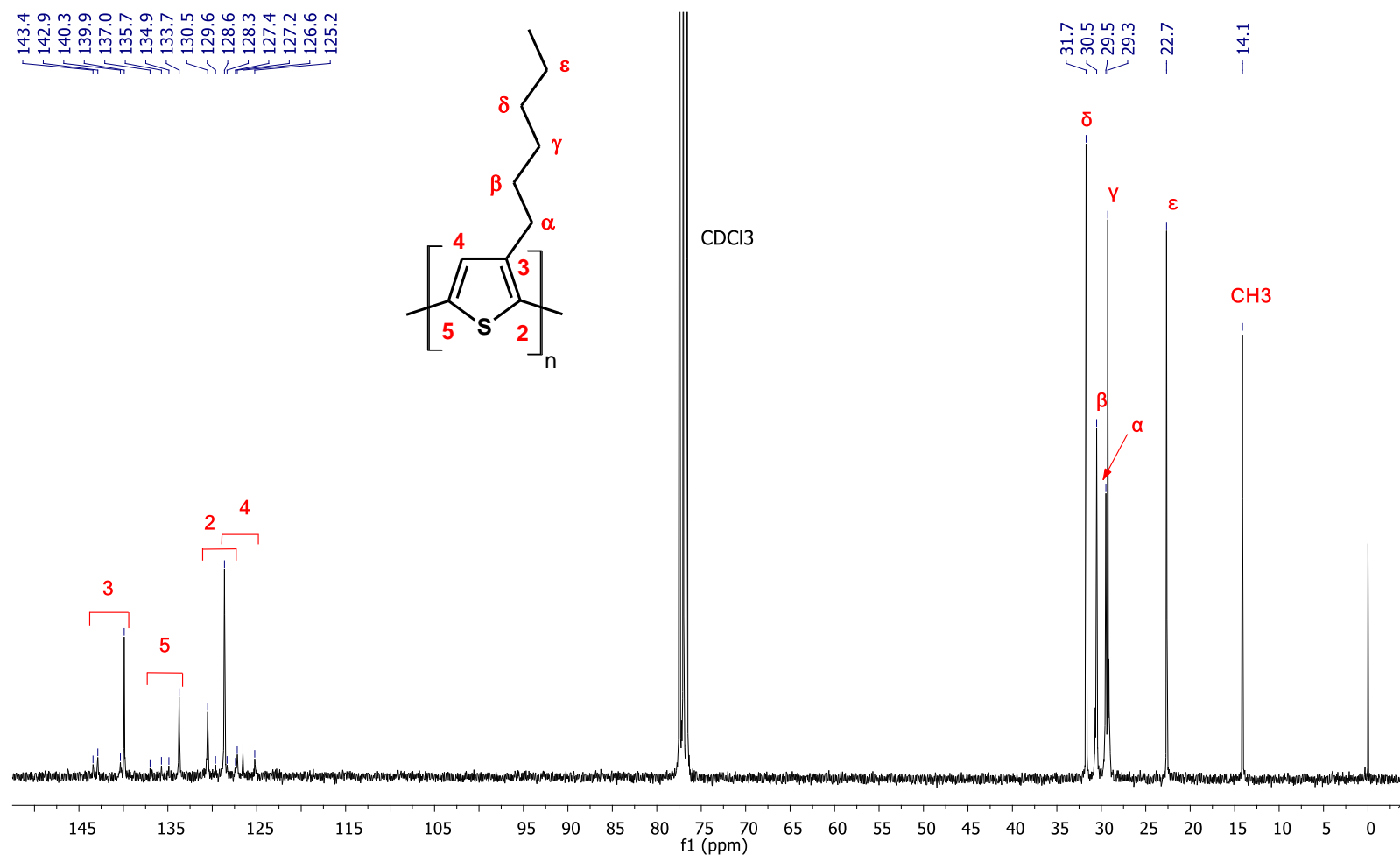


Fig. S.2  $^{13}\text{C}$  NMR spectrum of NR P3HT FCH (100 MHz,  $\text{CDCl}_3$ ) with assignments of peaks:  $\delta$  (ppm) 143.4 (C3 HH-TT), 142.9 (C3 HH-HT), 140.3 (C3 HT-TT), **139.9 (C3 HT-HT)**, 137.0 (C5 HH-TT), 135.7 (C5 HH-HT), 134.9 (C5 HT-TT), **133.7 (C5 HT-HT)**, **130.5 (C2 HT-HT)**, 129.6 (C2 HT-TT), **128.6 (C4 HT-HT)**, 128.3 (C2 HH-HT), 127.4 (C2 HH-TT), 127.2 (C4 HT-HH), 126.6 (C4 HT-TT), 125.2 (C4 HH-TT), **31.7, 30.5, 29.5, 29.3, 22.7, 14.1**

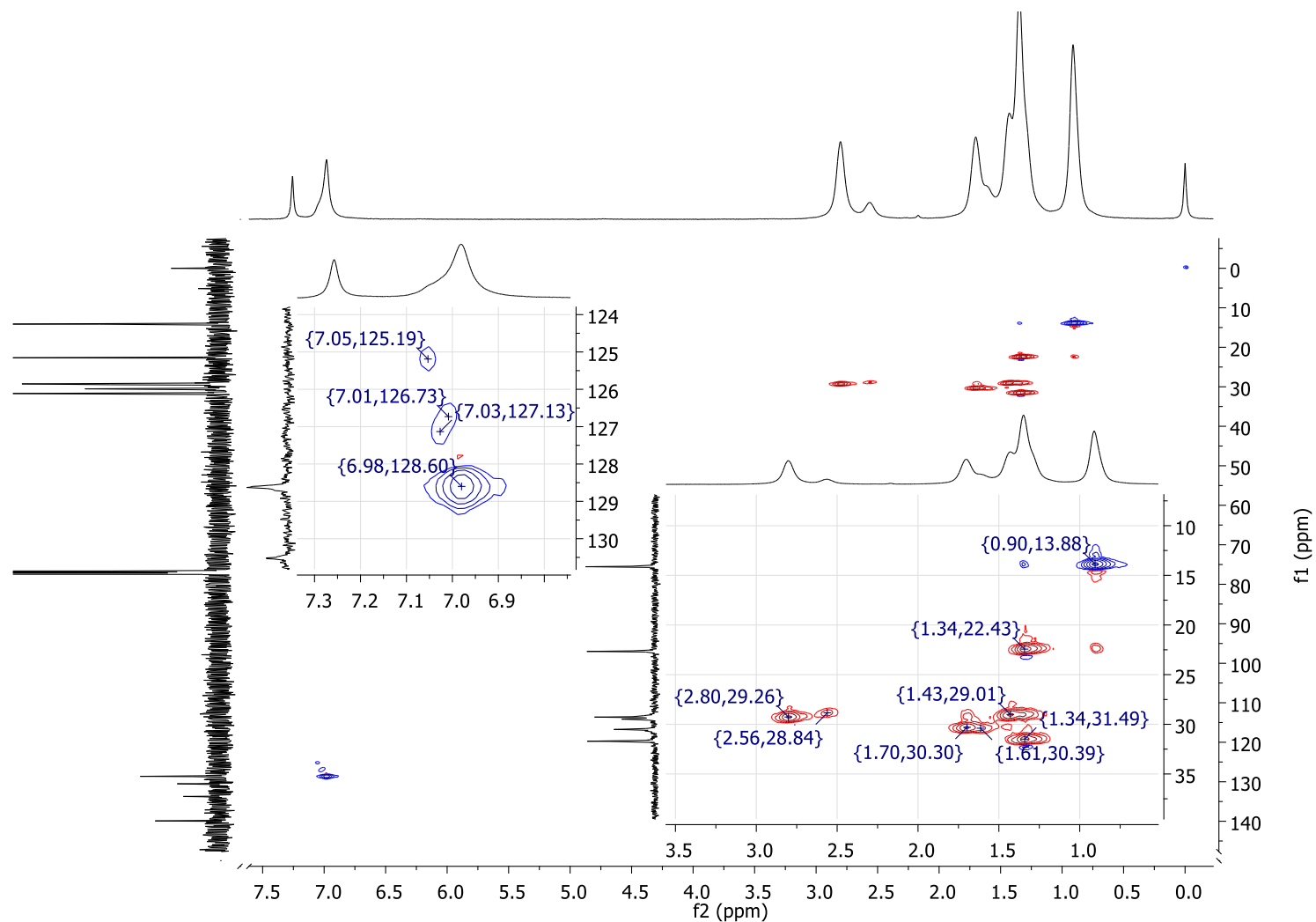


Fig. S.3 HSQC spectrum of NR P3HT FCH with expansions of aliphatic and aromatic regions; CH and CH<sub>3</sub> groups are negative in phase (blue), CH<sub>2</sub> groups are positive in phase (red)

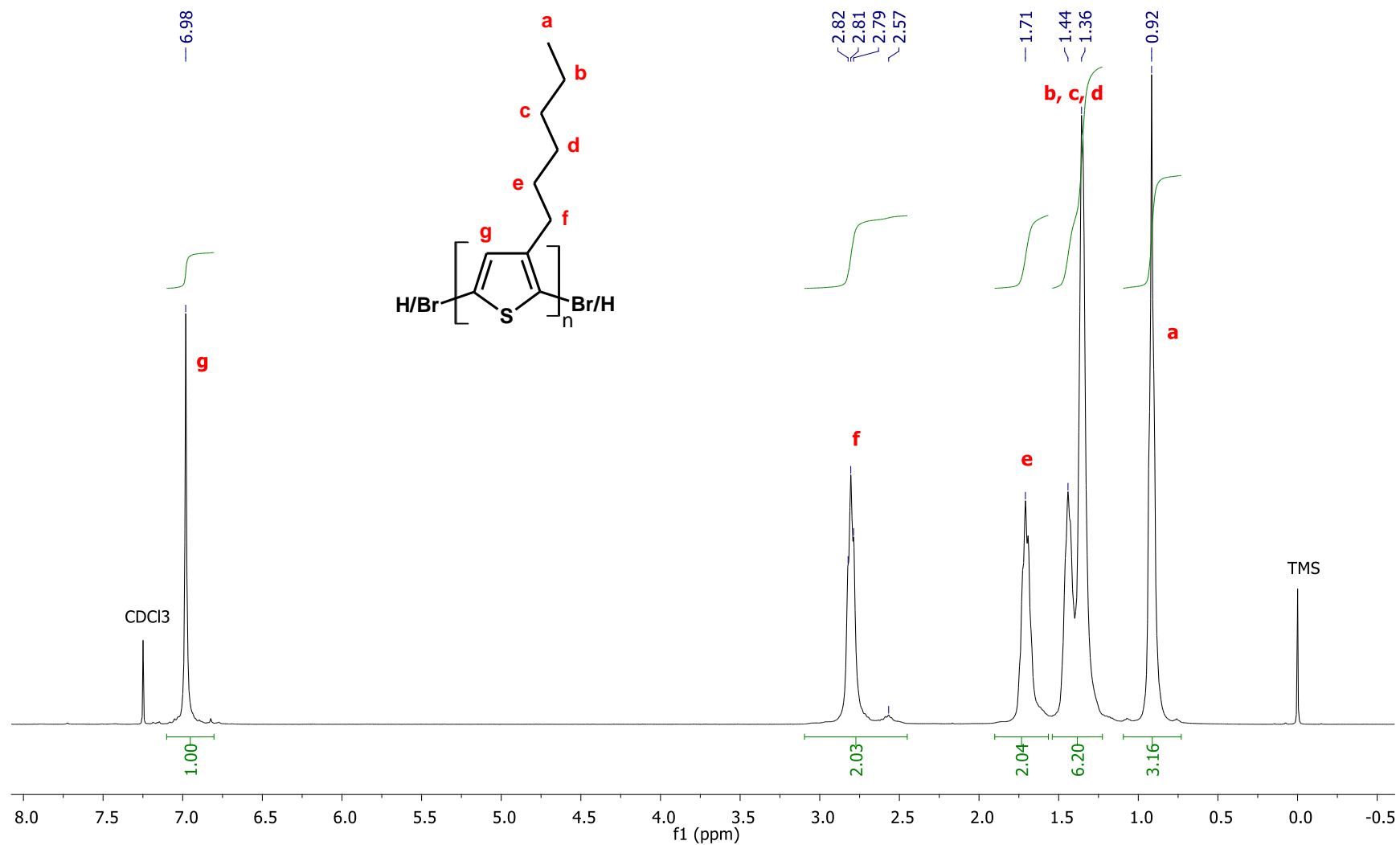


Fig. S.4 <sup>1</sup>H NMR spectrum of RR P3HT (300 MHz, CDCl<sub>3</sub>) with assignments of peaks: δ (ppm) 6.98 (s, 1H), 2.81-2.57 (m, 2H), 1.71 (m, 2H), 1.44-1.36 (m, 6H), 0.92 (m, 3H)

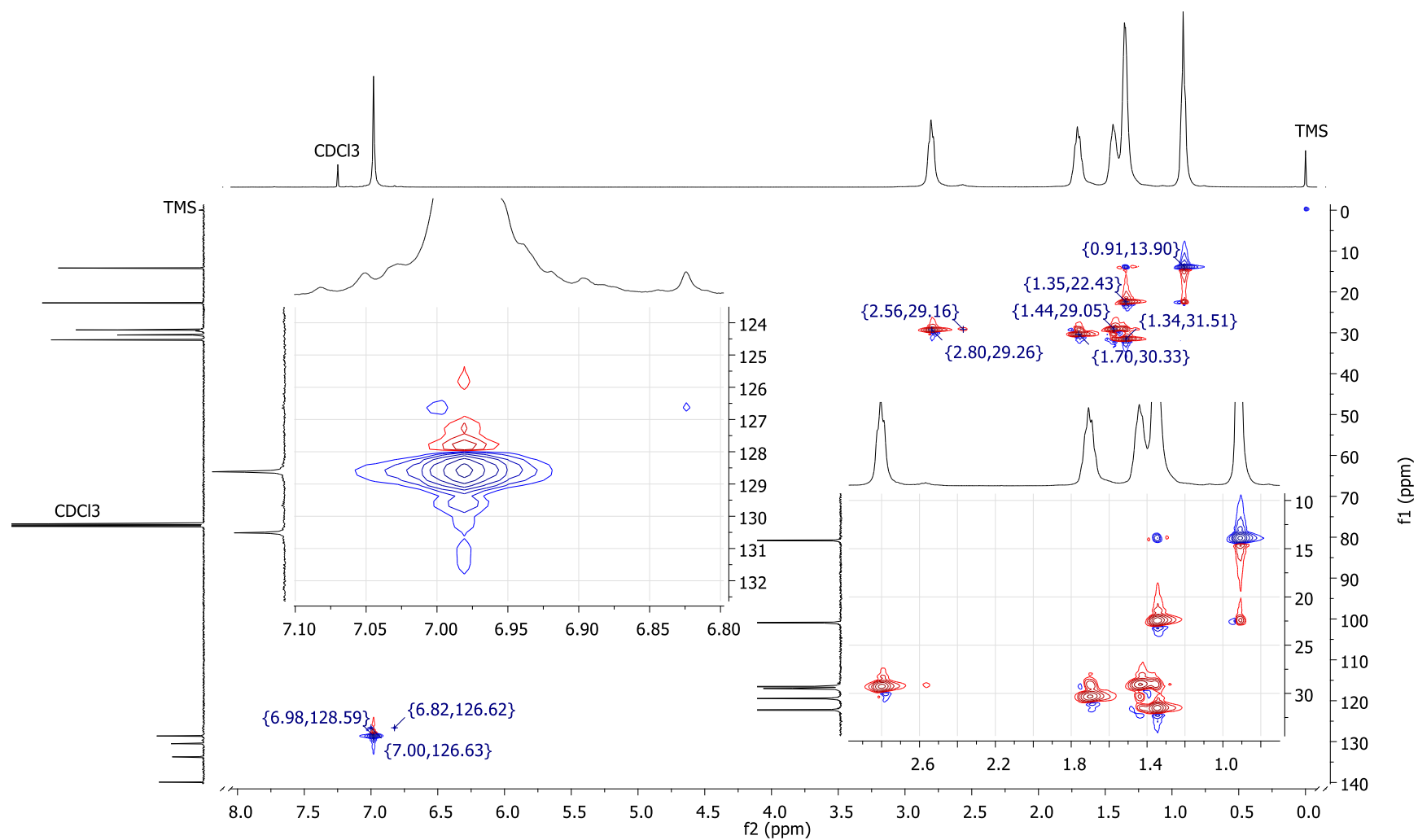


Fig. S.5 HSQC ( $^1\text{H}$  400 MHz,  $^{13}\text{C}$  100 MHz,  $\text{CDCl}_3$ ) spectrum of RR P3HT with expansions of aliphatic and aromatic regions; CH and  $\text{CH}_3$  groups are negative in phase (blue),  $\text{CH}_2$  groups are positive in phase (red)

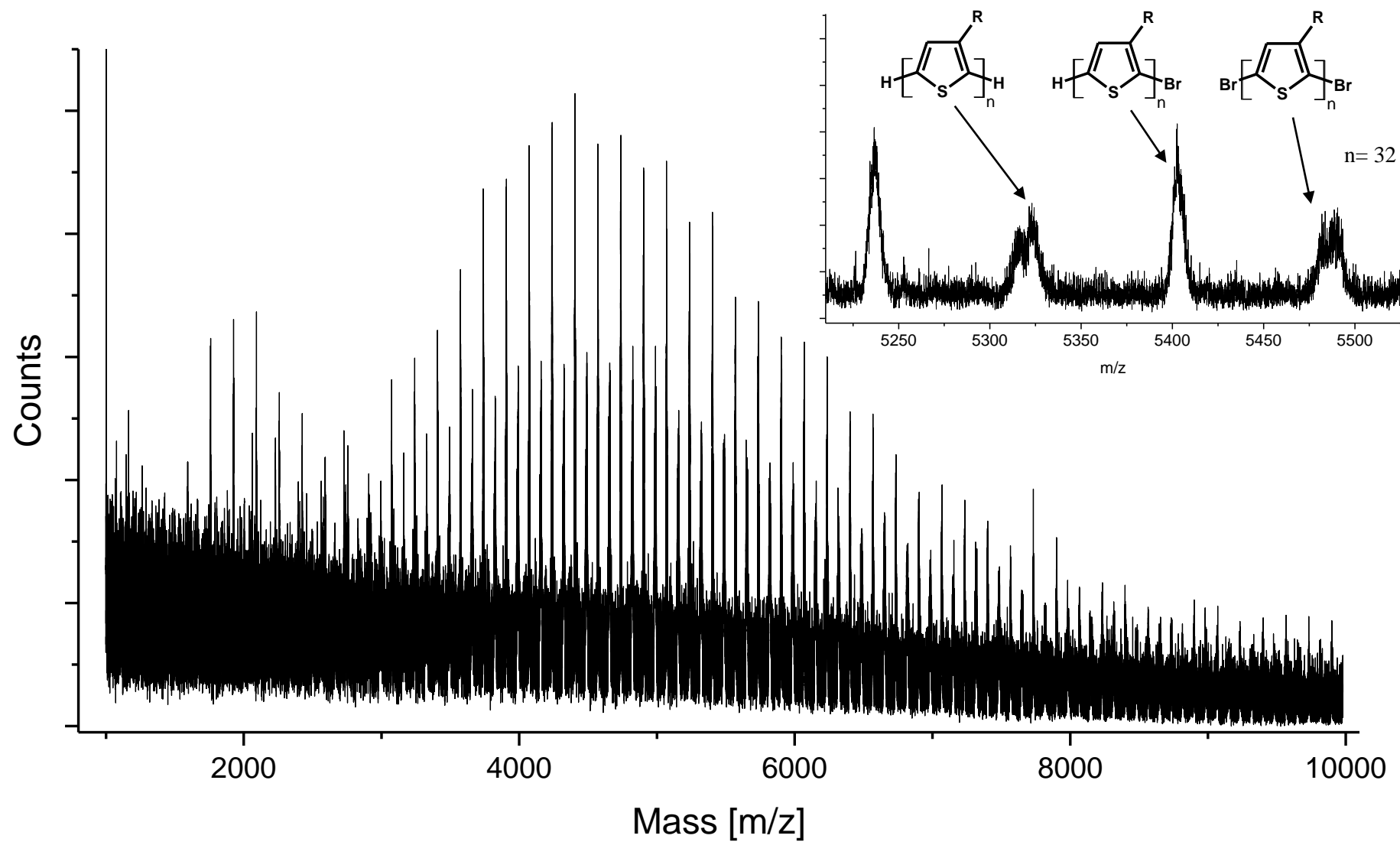


Fig. S.6 MALDI-TOF spectrum of RR P3HT with zoom showing assignment of series of peaks to polymer chains with different end groups

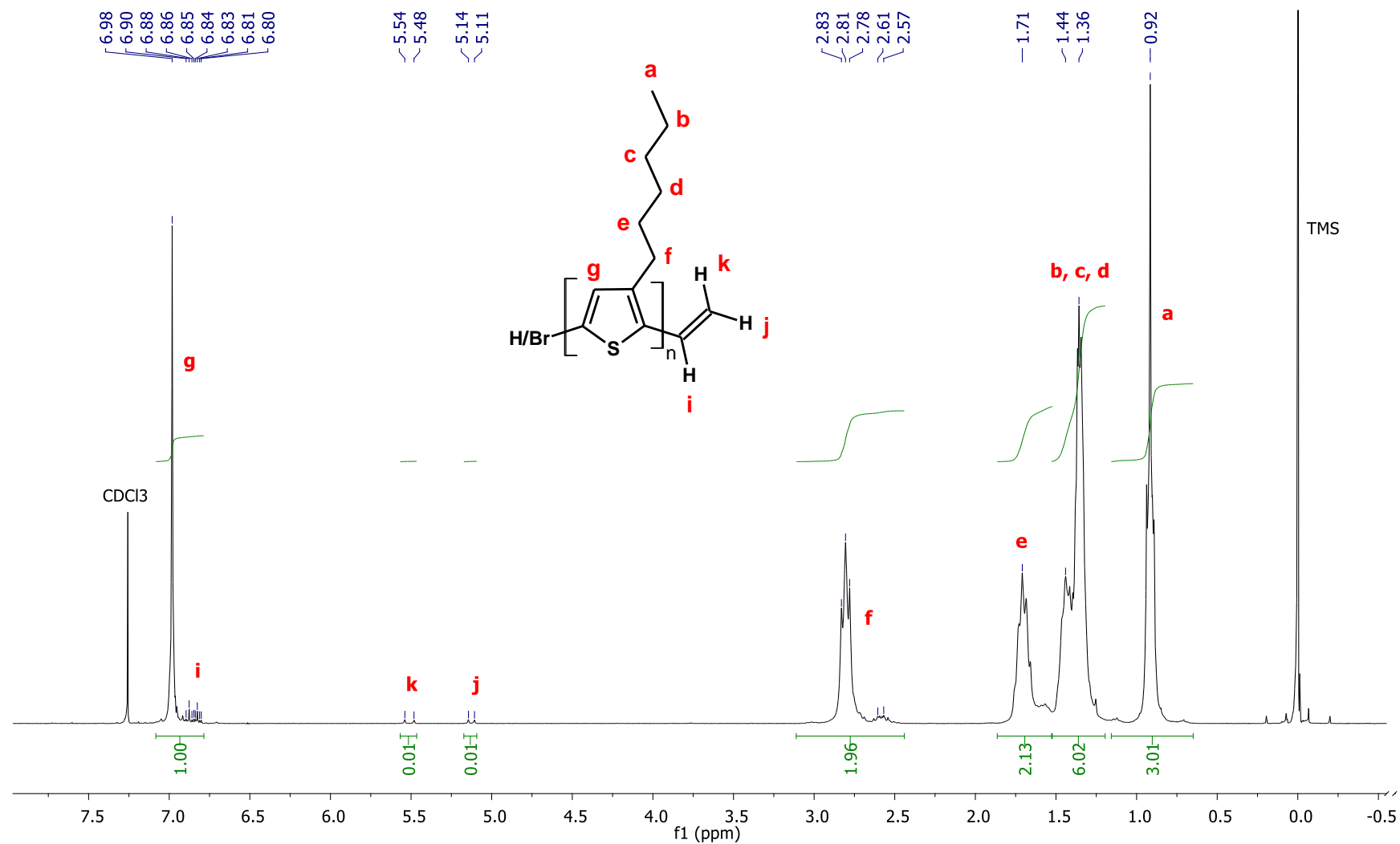


Fig. S.7  $^1\text{H}$  NMR spectrum of P3HTvin FC (300 MHz,  $\text{CDCl}_3$ ) with assignments of peaks:  $\delta$  (ppm) 6.98 (s, 1H), 5.51 (d,  $^3J_1=17.2$  Hz, 0.013 H), 5.13 (d,  $^3J_2=11.0$  Hz, 0.013 H), 2.81-2.57 (m, 2H), 1.71 (m, 2H), 1.44-1.36 (m, 6H), 0.92 (m, 3H)



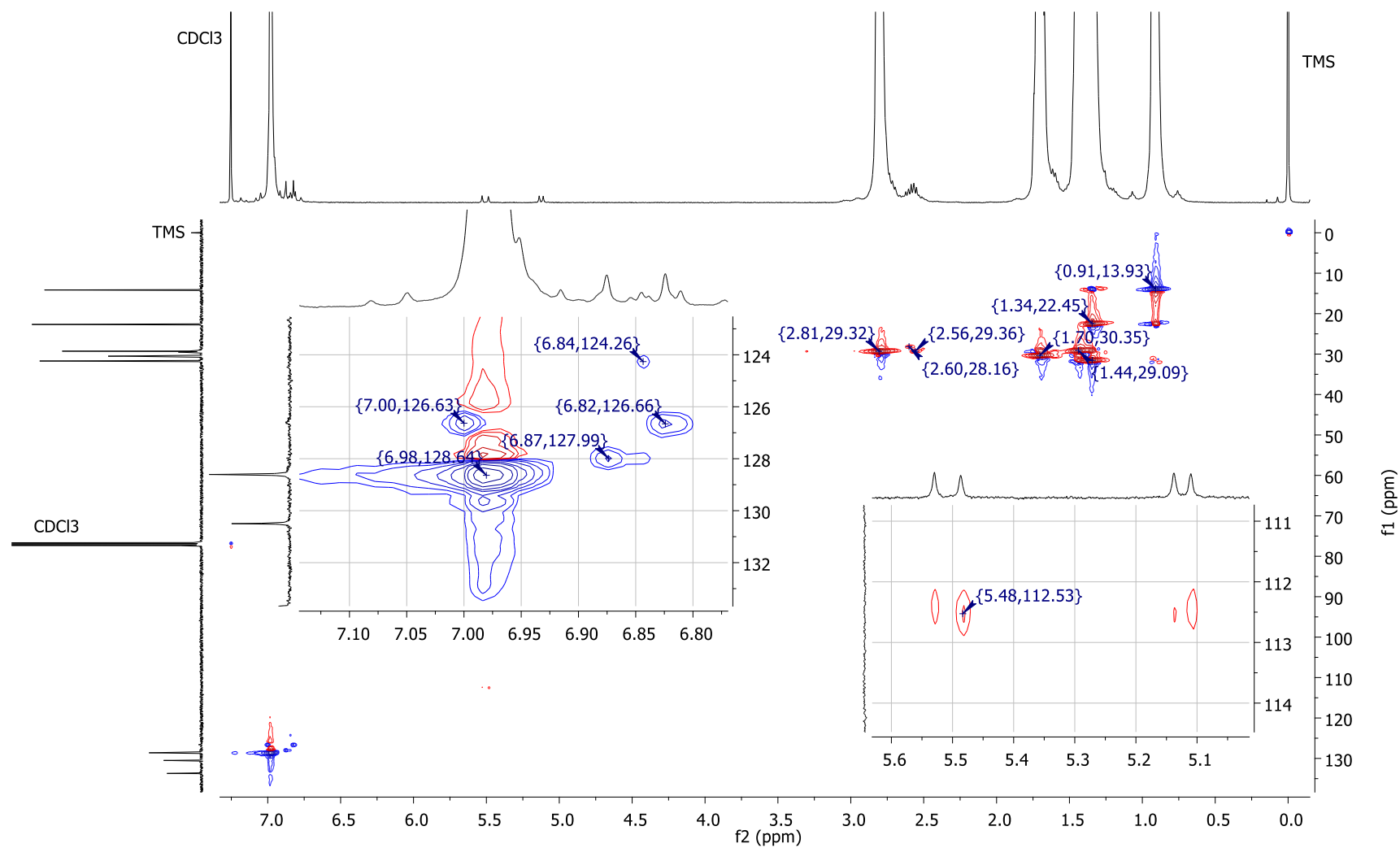


Fig. S.8 HSQC ( $^1\text{H}$  400 MHz,  $^{13}\text{C}$  100 MHz,  $\text{CDCl}_3$ ) spectrum of P3HTvin FC with expansions of vinyl and aromatic regions; CH and  $\text{CH}_3$  groups are negative in phase (blue),  $\text{CH}_2$  groups are positive in phase (red)

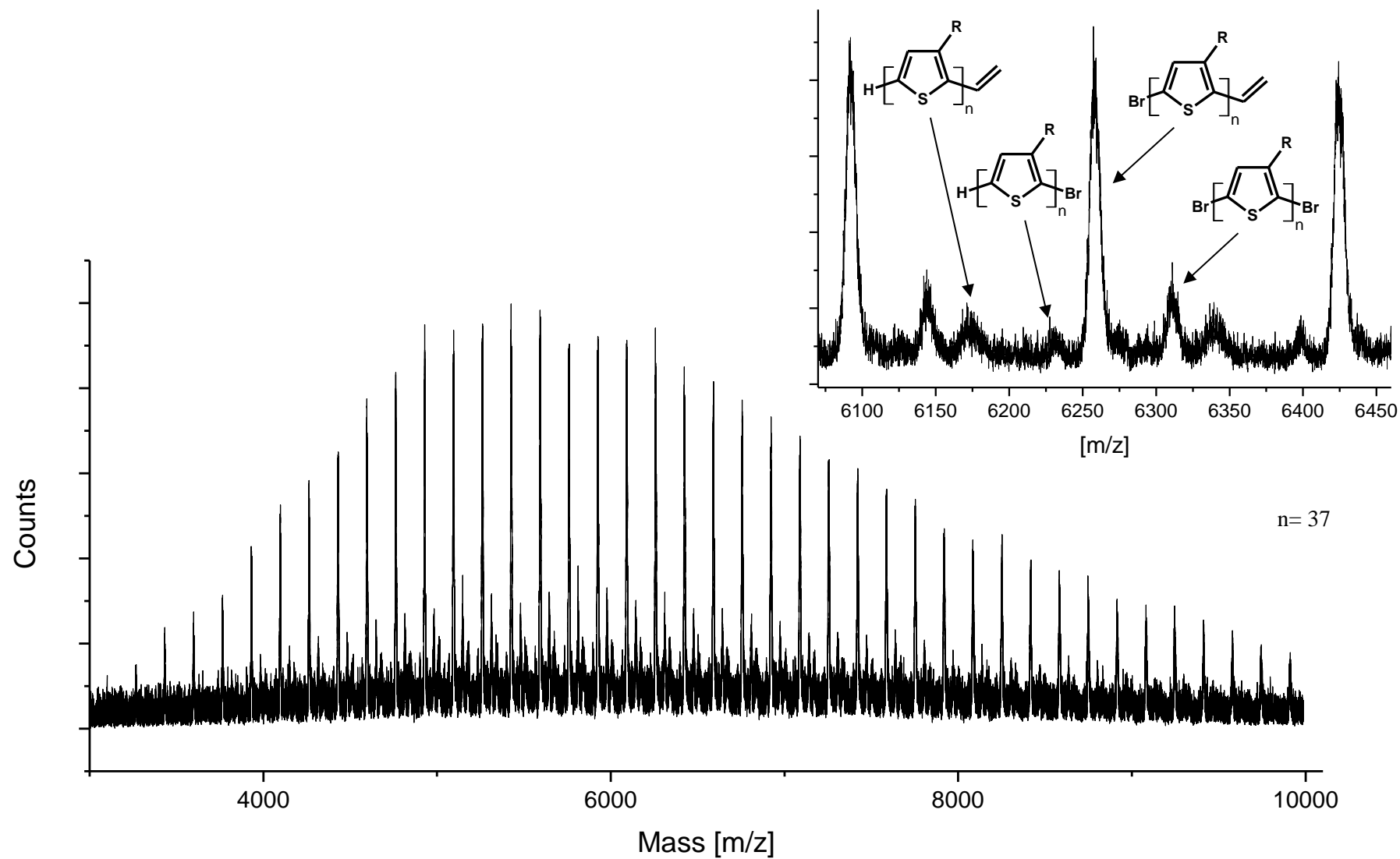


Fig. S.9 MALDI-TOF spectrum of P3HTvin FC with zoom showing assignment of series of peaks to polymer chains with different end groups

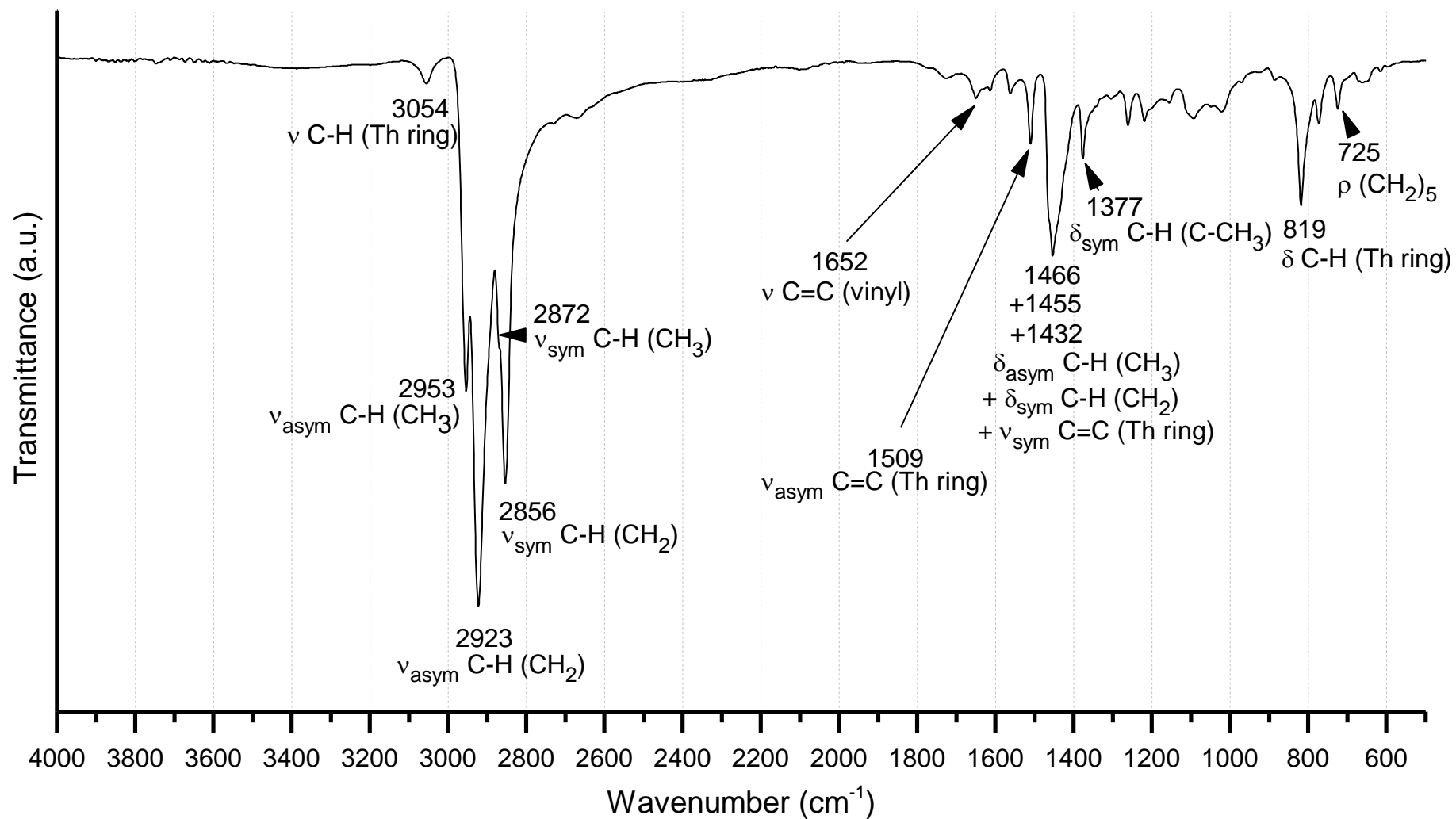


Fig. S.10 ATR-FTIR spectrum of P3HTvin FC; vibrations:  $\nu$  – stretching,  $\delta$  – deforming,  $\rho$  – rocking, asym – asymmetric, sym – symmetric, Th ring – thiophene ring

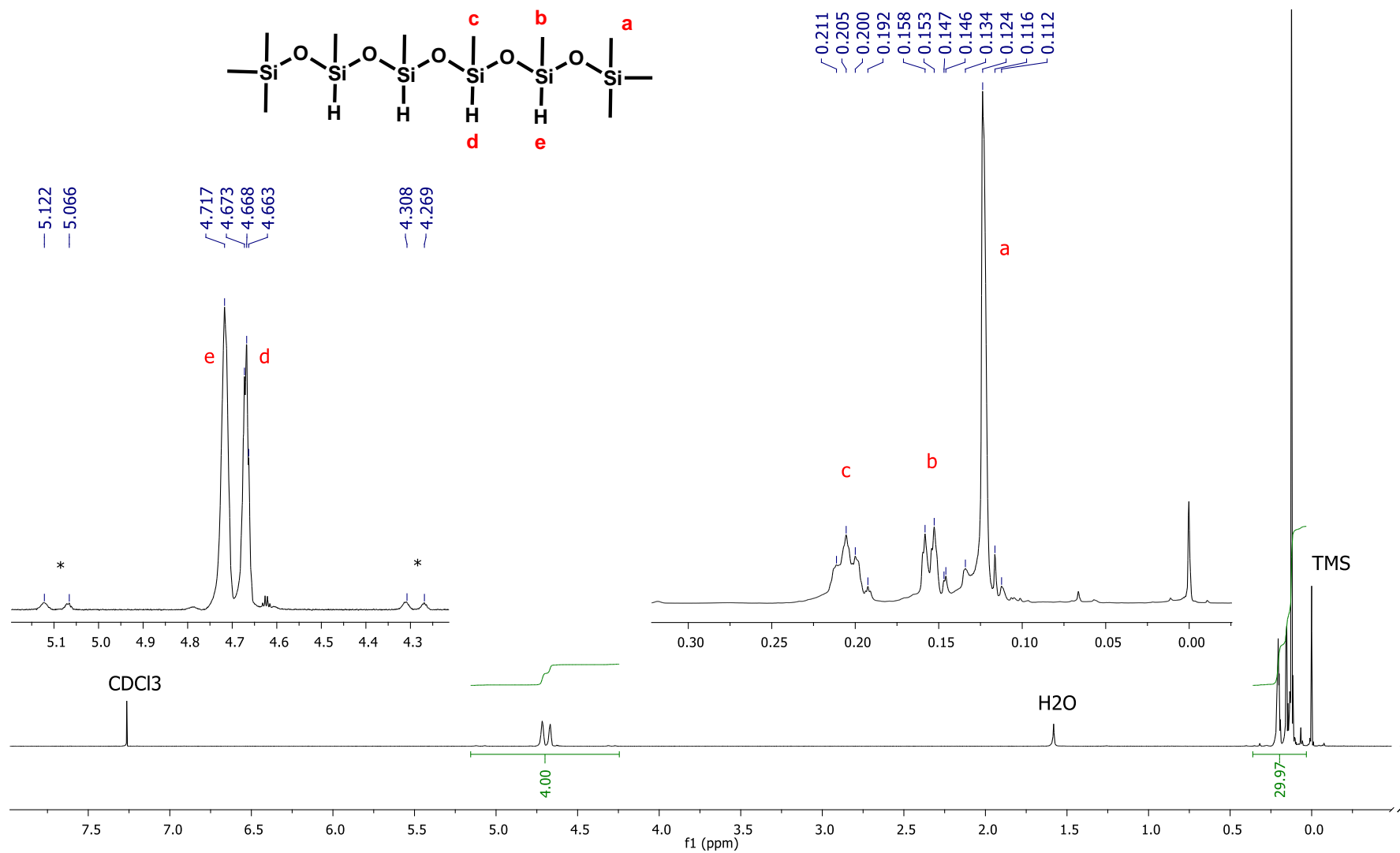


Fig. S.11 <sup>1</sup>H NMR spectrum of PMHS-S (300 MHz, CDCl<sub>3</sub>) with assignments of peaks; \* - <sup>29</sup>Si satellite peaks

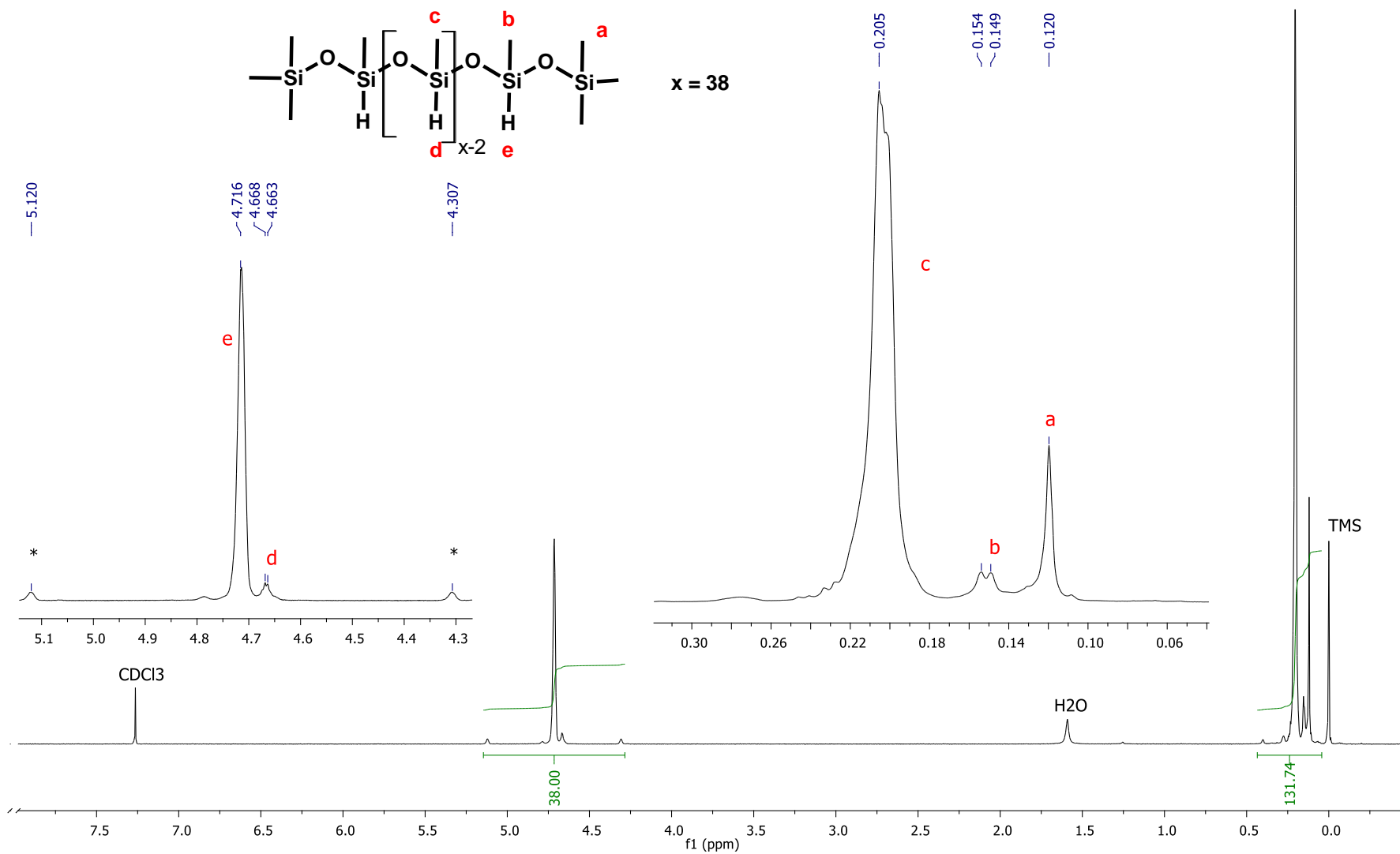


Fig. S.12 <sup>1</sup>H NMR spectrum of PMHS-L (300 MHz, CDCl<sub>3</sub>) with assignments of peaks; \* - <sup>29</sup>Si satellite peaks

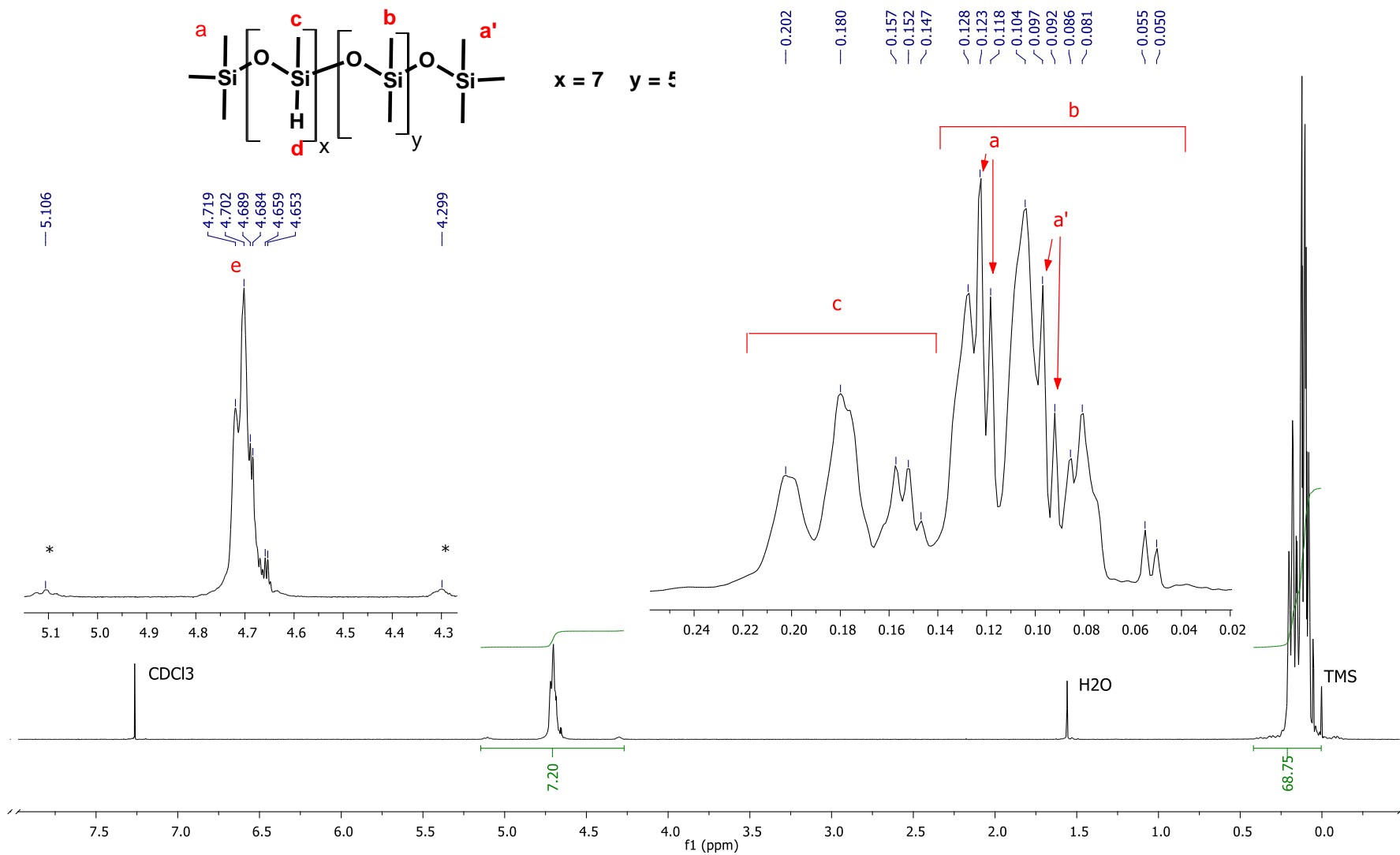


Fig. S.13 <sup>1</sup>H NMR spectrum of P(DMS-co-MHS) (300 MHz, CDCl<sub>3</sub>) with assignments of peaks; \* - <sup>29</sup>Si satellite peaks

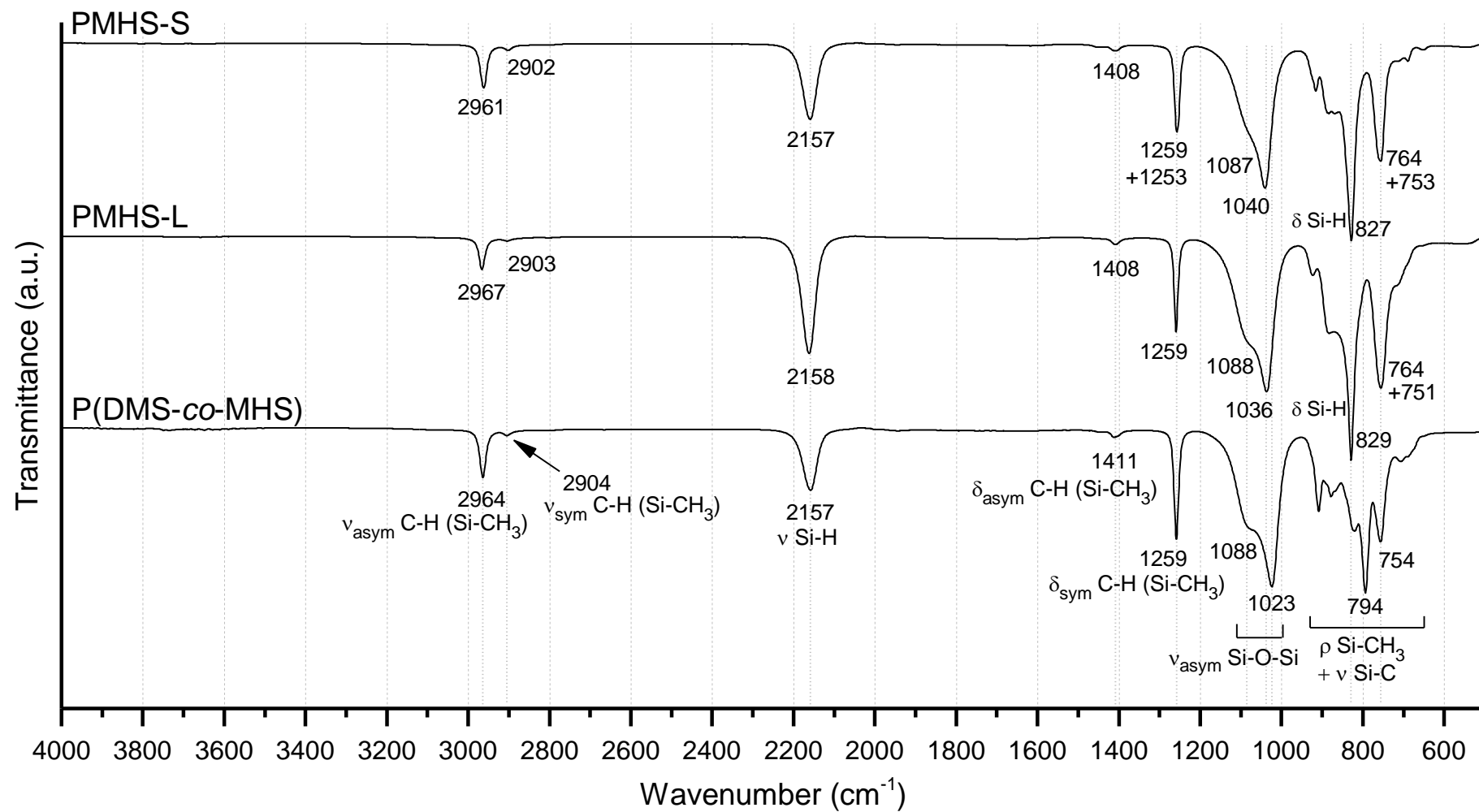


Fig. S.14 ATR-FTIR spectrum of PMHS-S, PMHS-L, and P(DMS-co-MHS); vibrations:  $\nu$  – stretching,  $\delta$  – deforming, asym – asymmetric, sym – symmetric

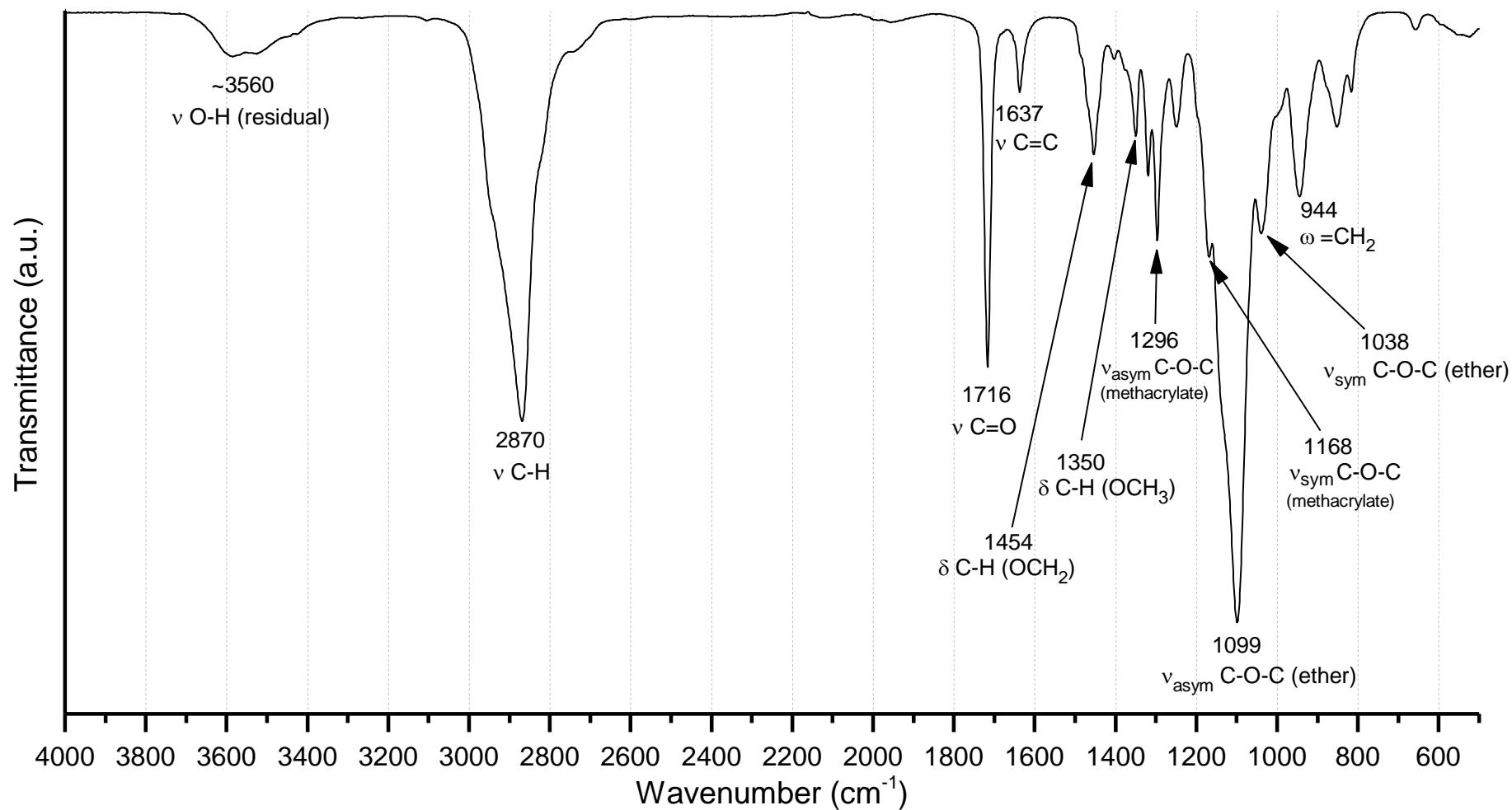
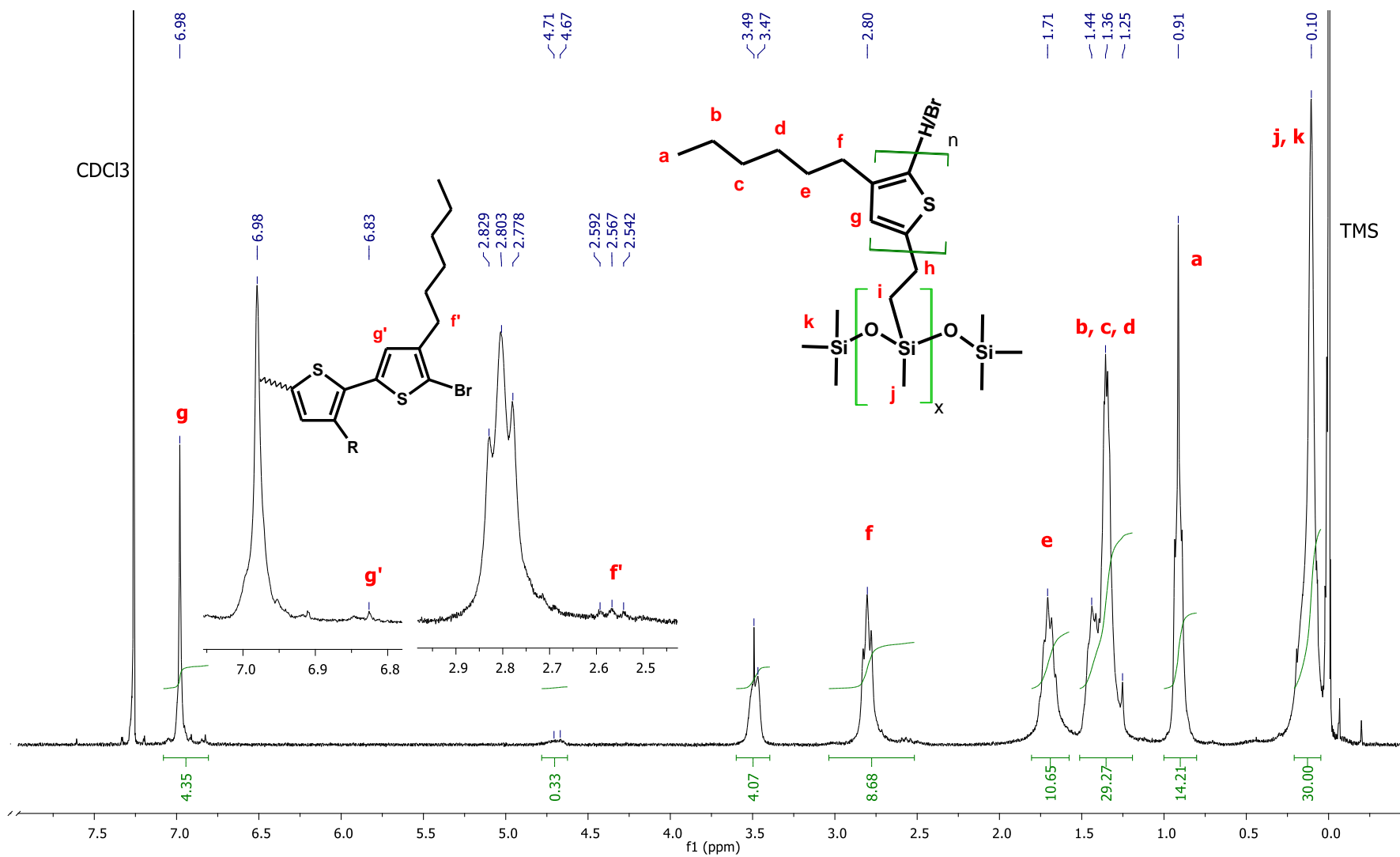
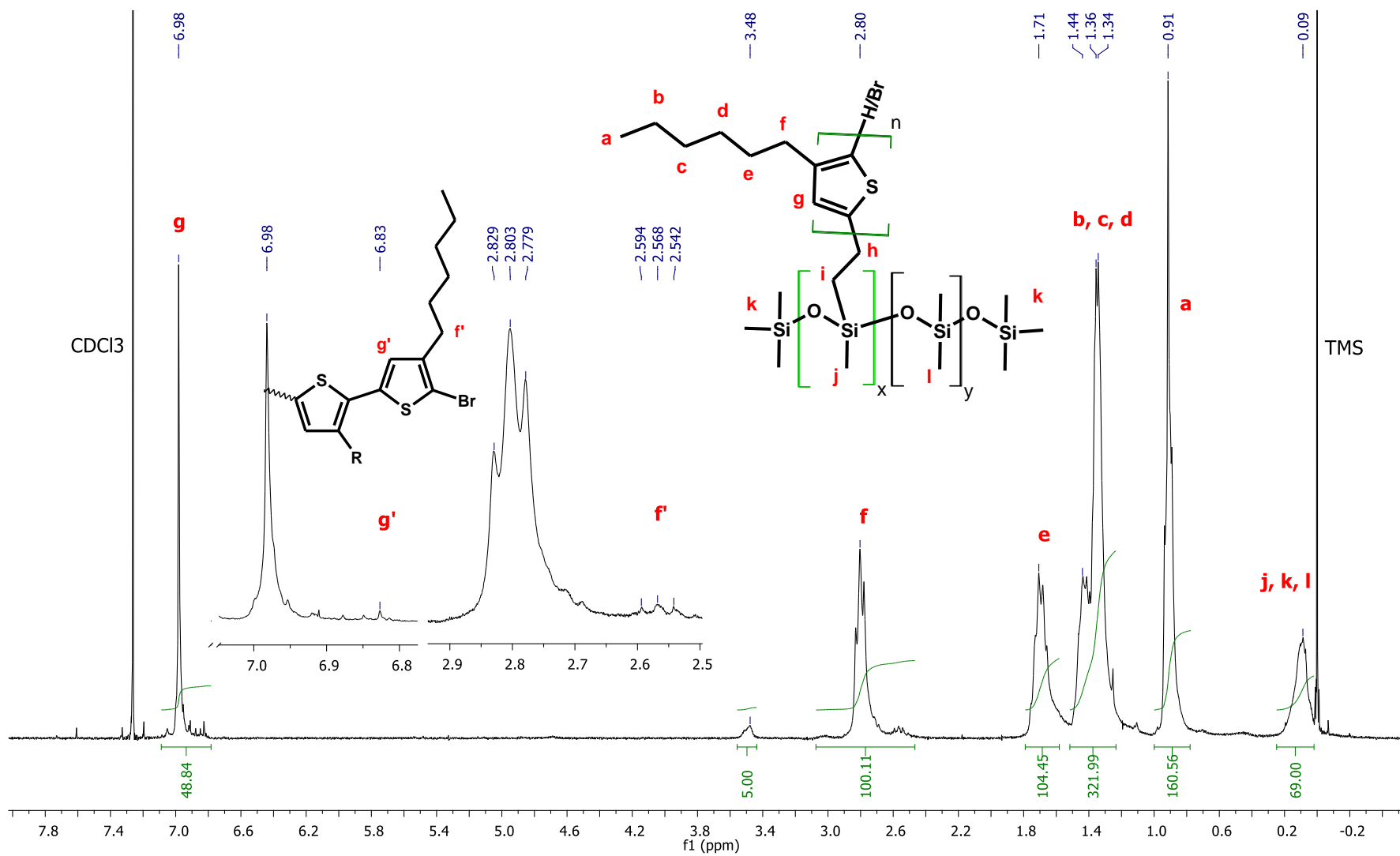


Fig. S.15 ATR-FTIR spectrum of PEGMA; vibrations:  $\nu$  – stretching,  $\delta$  – deforming,  $\omega$  – wagging, asym – asymmetric, sym – symmetric



Fig. S.16  $^1\text{H}$  NMR spectrum of PMHS-g-P3HT copolymer (300 MHz,  $\text{CDCl}_3$ ) with assignments of peaks

Fig. S.17  $^1\text{H}$  NMR spectrum of P(DMS-co-MHS)-g-P3HT copolymer (300 MHz,  $\text{CDCl}_3$ )

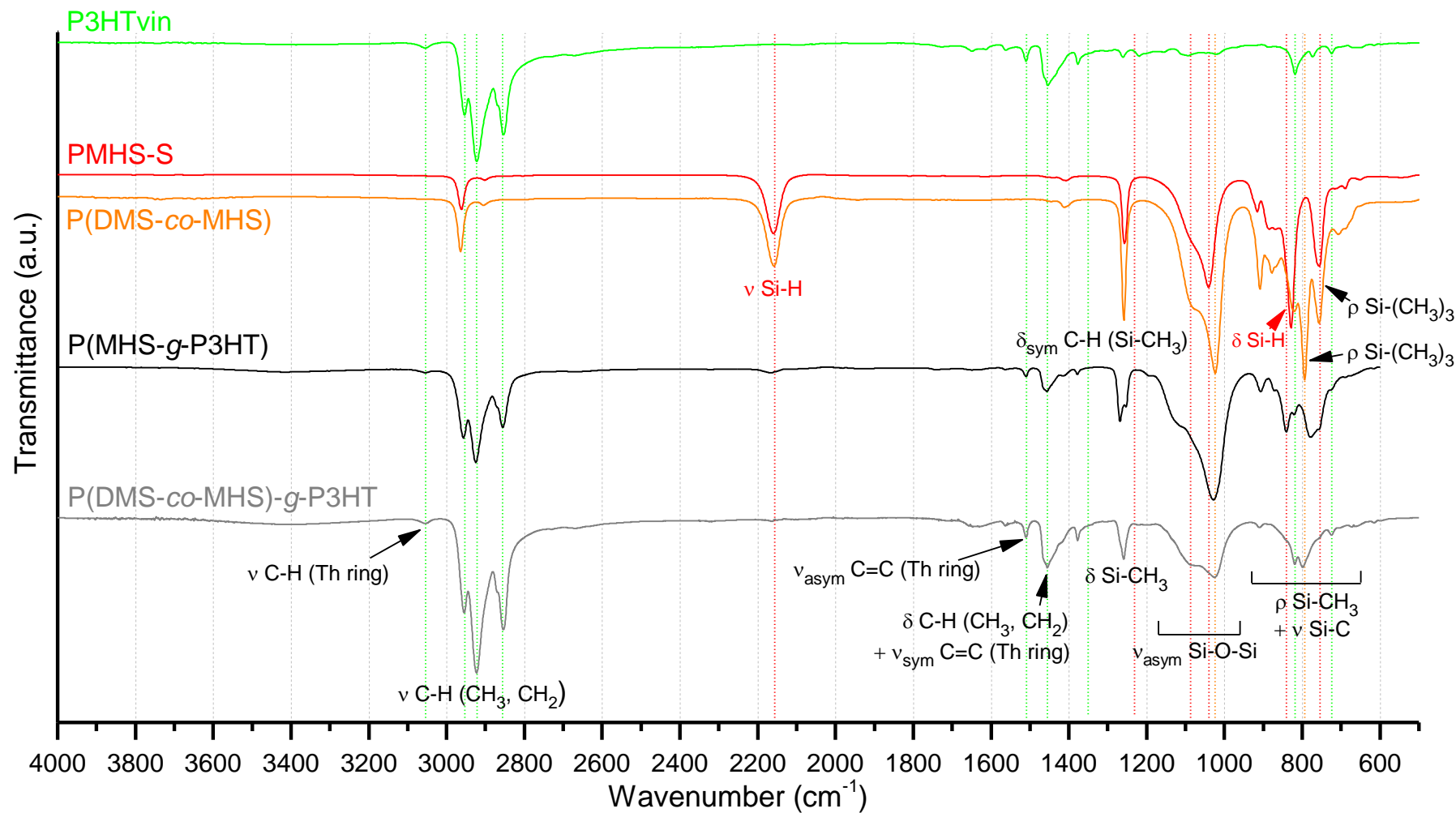
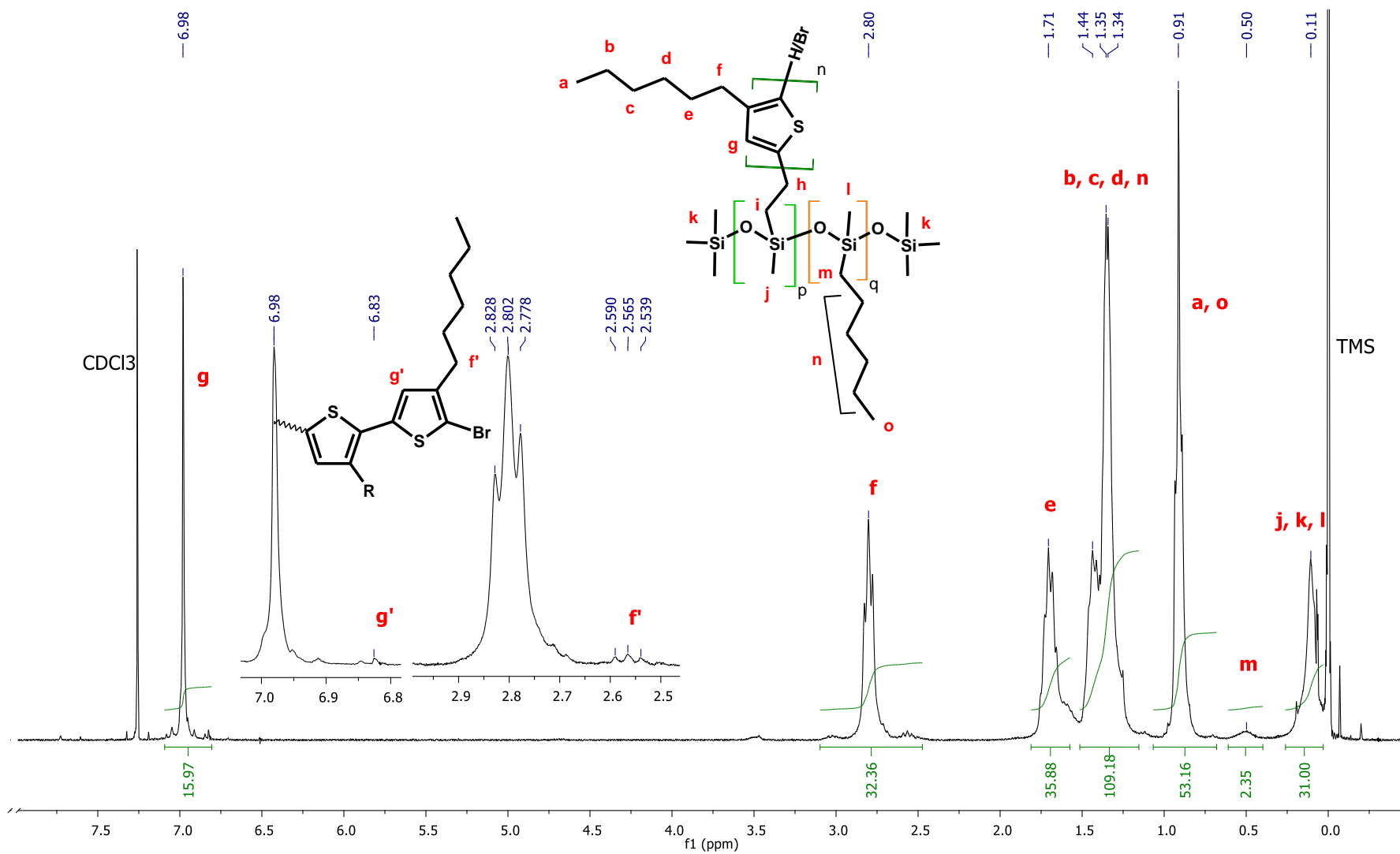
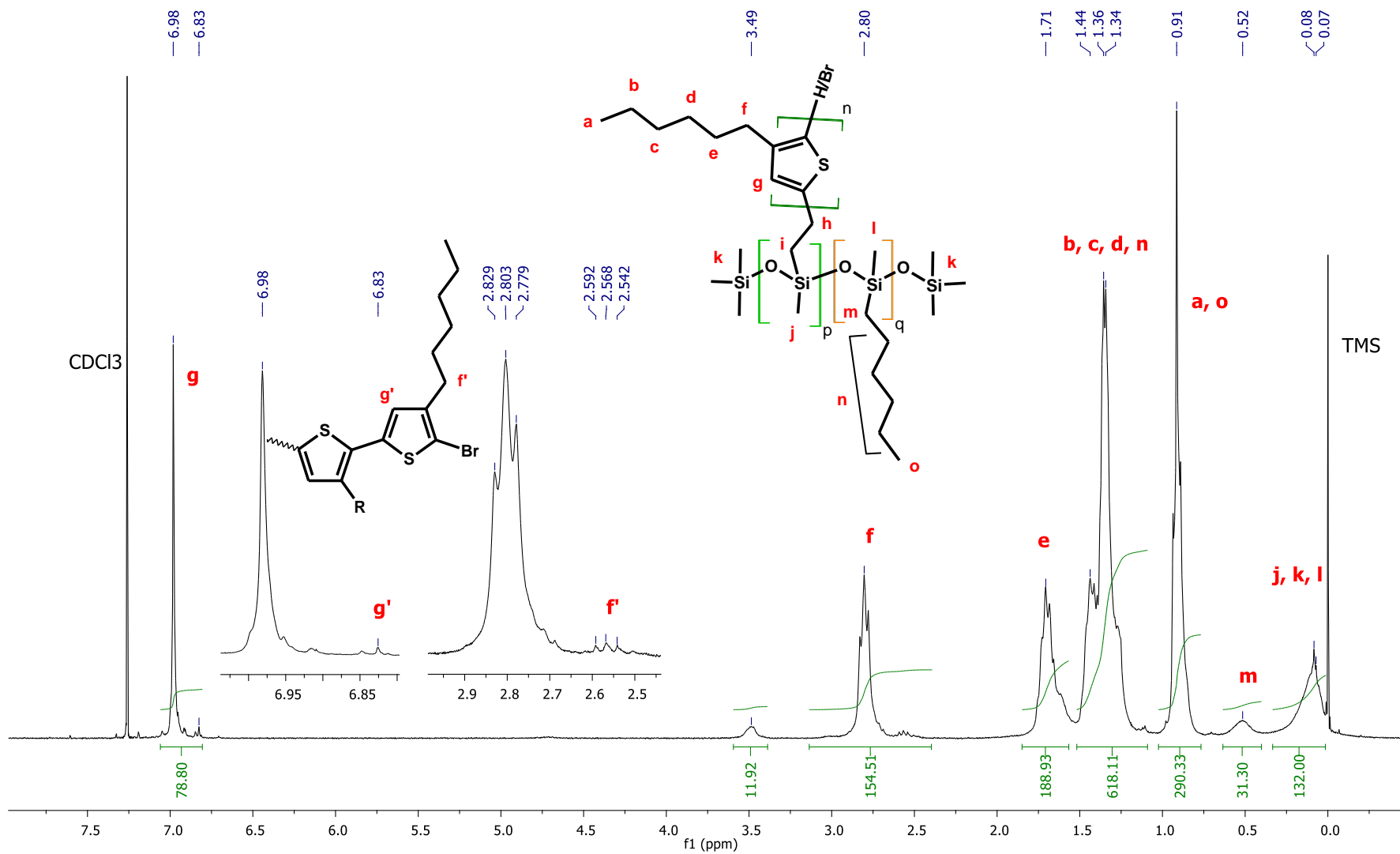


Fig. S.18 ATR-FTIR spectrum of P3HTvin, PMHS-S, P(DMS-co-MHS), PMHS-g-P3HT and P(DMS-co-MHS)-g-P3HT; vibrations:  $\nu$  – stretching,  $\delta$  – deforming, asym – asymmetric, sym – symmetric

Fig. S.19  $^1\text{H}$  NMR spectrum of PMHS-g-(P3HT;hex) 1 copolymer (300 MHz,  $\text{CDCl}_3$ )

Fig. S.20  $^1\text{H}$  NMR spectrum of PMHS-g-(P3HT;hex) 2 copolymer (300 MHz,  $\text{CDCl}_3$ )

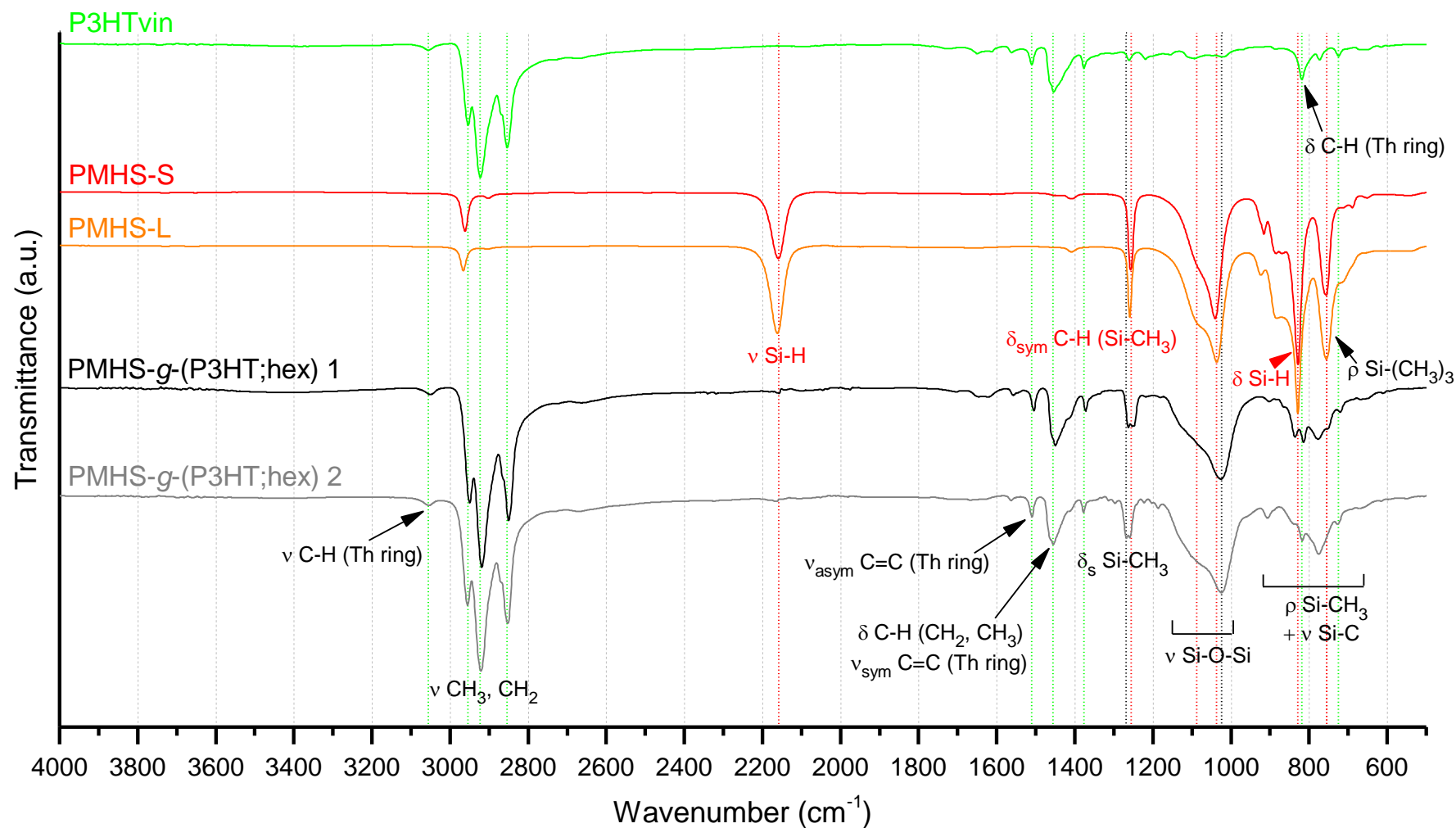
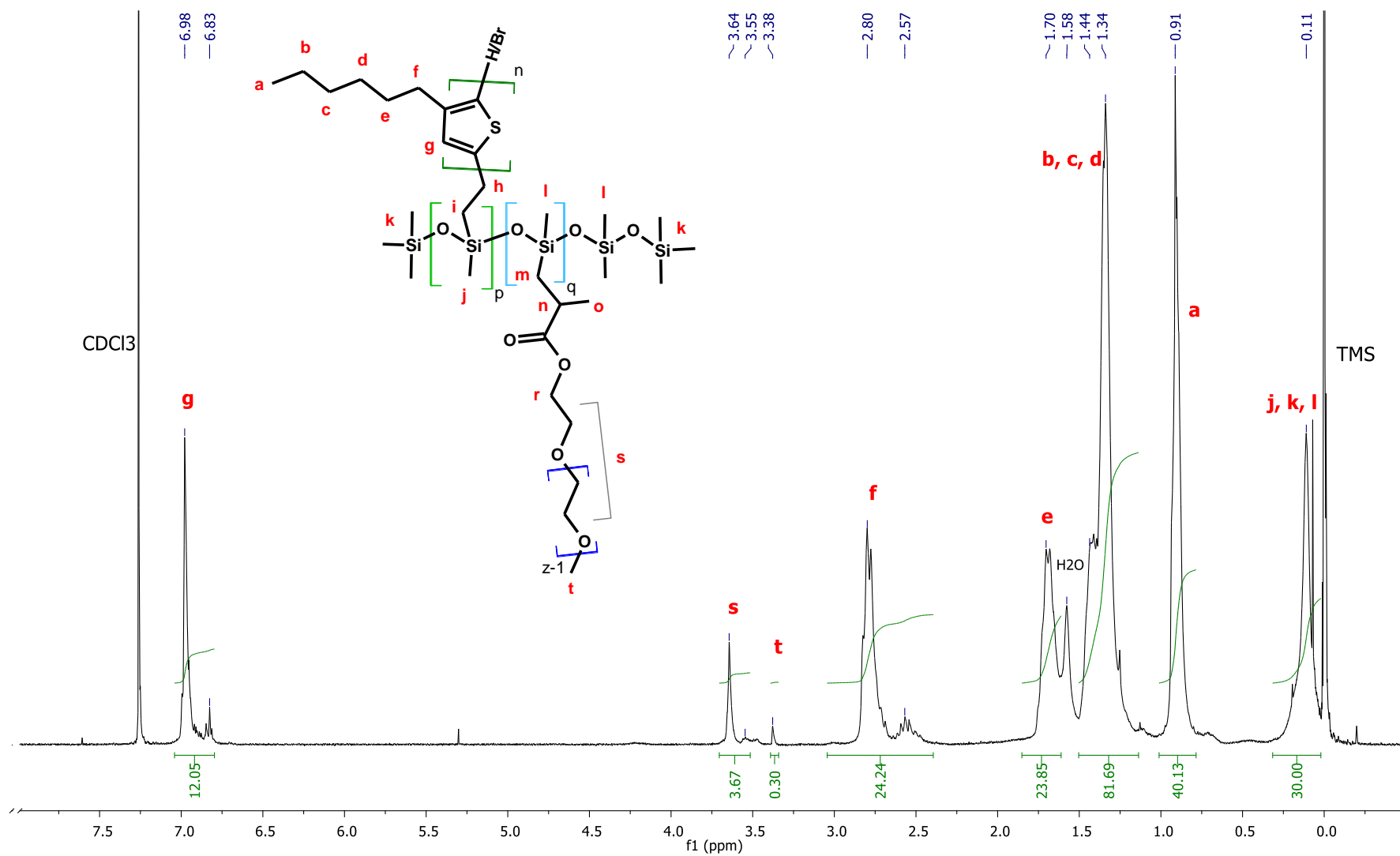
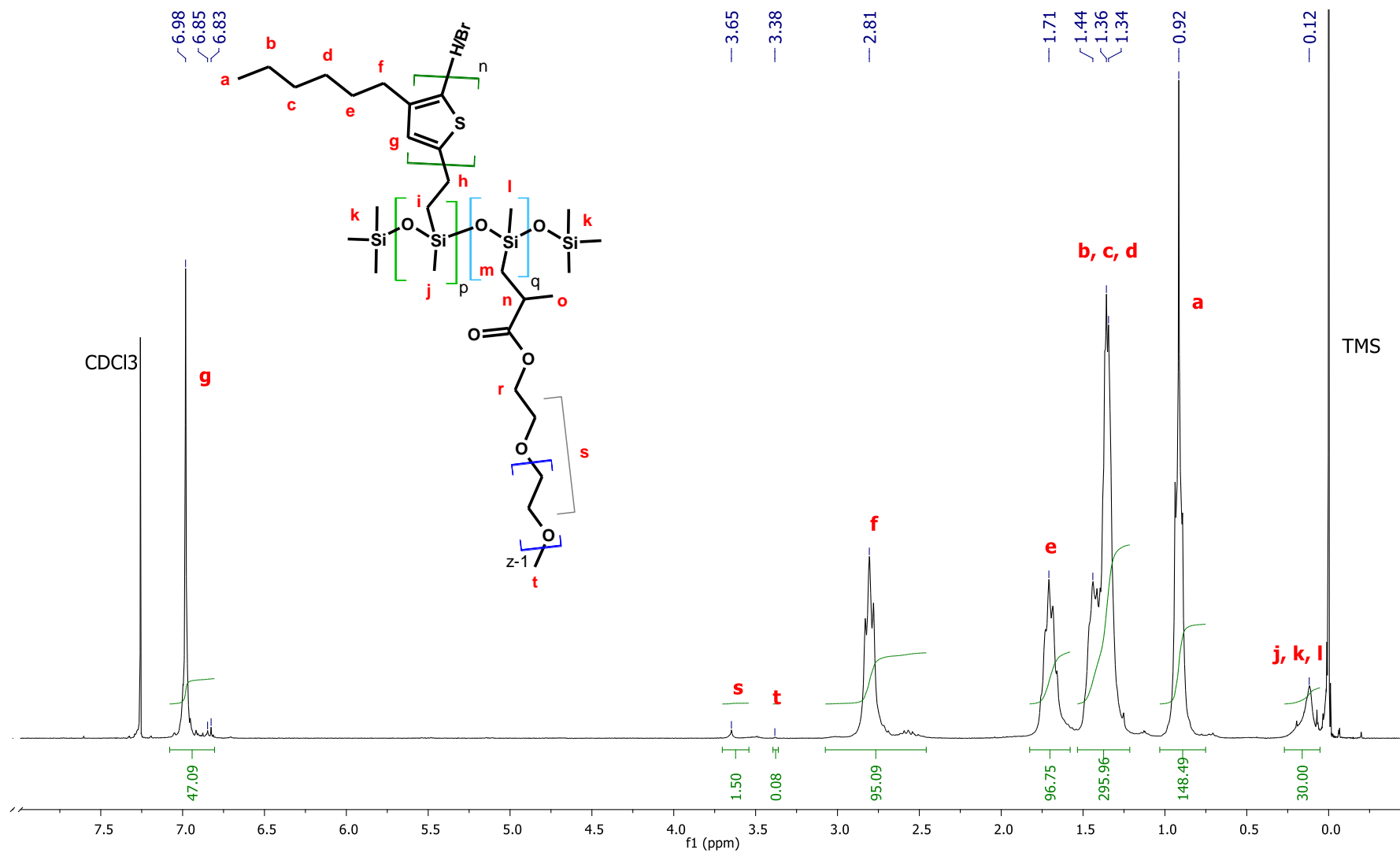


Fig. S.21 ATR-FTIR spectrum of P3HTvin, PMHS-S, PMHS-L, PMHS-g-(P3HT;hex) 1, PMHS-g-(P3HT;hex) 2; vibrations:  $\nu$  – stretching,  $\delta$  – deforming, asym – asymmetric, sym – symmetric

Fig. S.22  $^1\text{H}$  NMR spectrum of PMHS-g-(P3HT;PEG) 1 copolymer (300 MHz,  $\text{CDCl}_3$ )

Fig. S.23 <sup>1</sup>H NMR spectrum of PMHS-g-(P3HT;PEG) 2 copolymer (300 MHz, CDCl<sub>3</sub>)



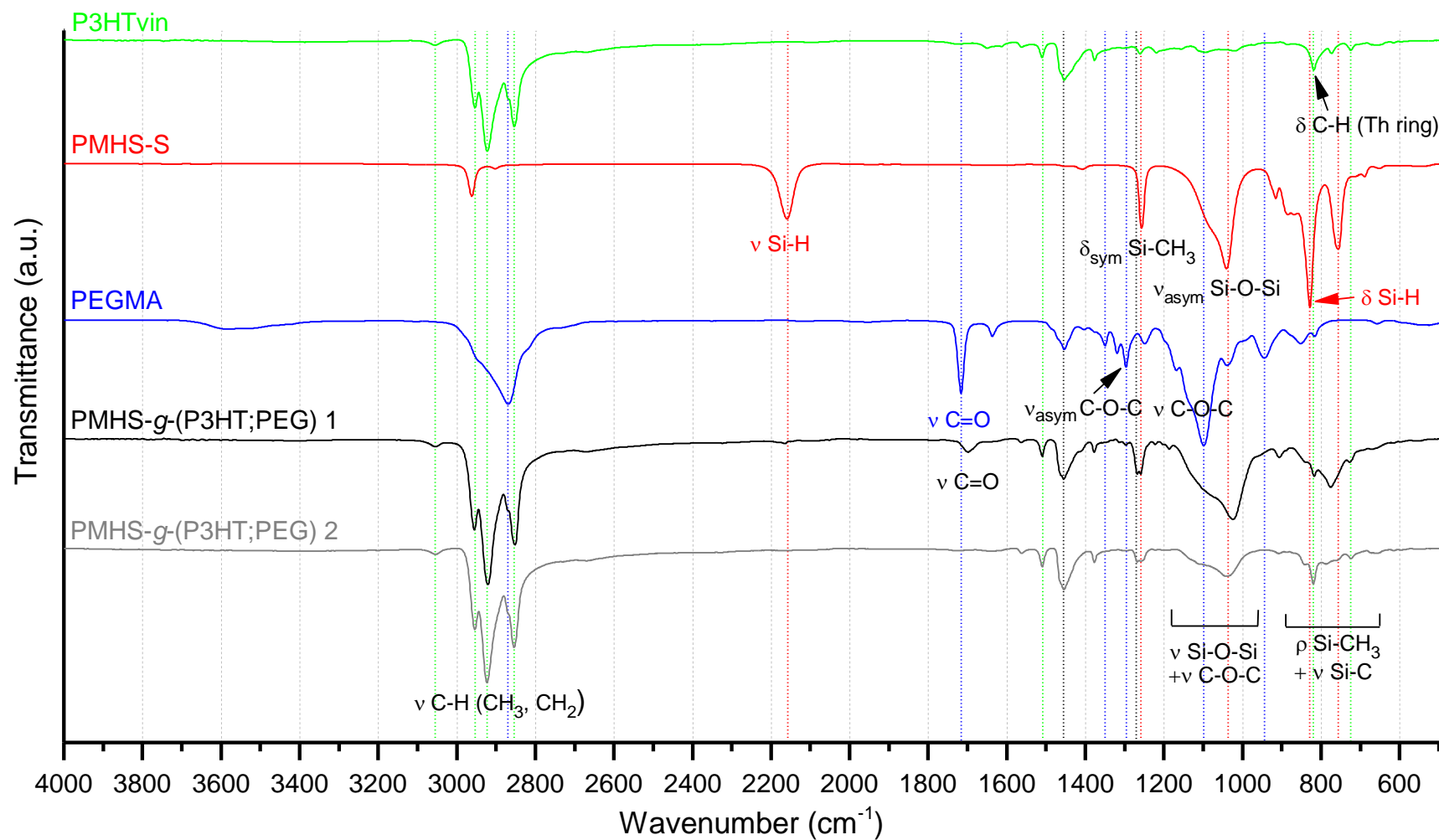


Fig. S.24 ATR-FTIR spectrum of P3HTvin, PMHS-S, PEGMA, PMHS-g-(P3HT;PEG) 1, and PMHS-g-(P3HT;PEG) 2; vibrations:  $\nu$  – stretching,  $\delta$  – deforming, asym – asymmetric, sym – symmetric

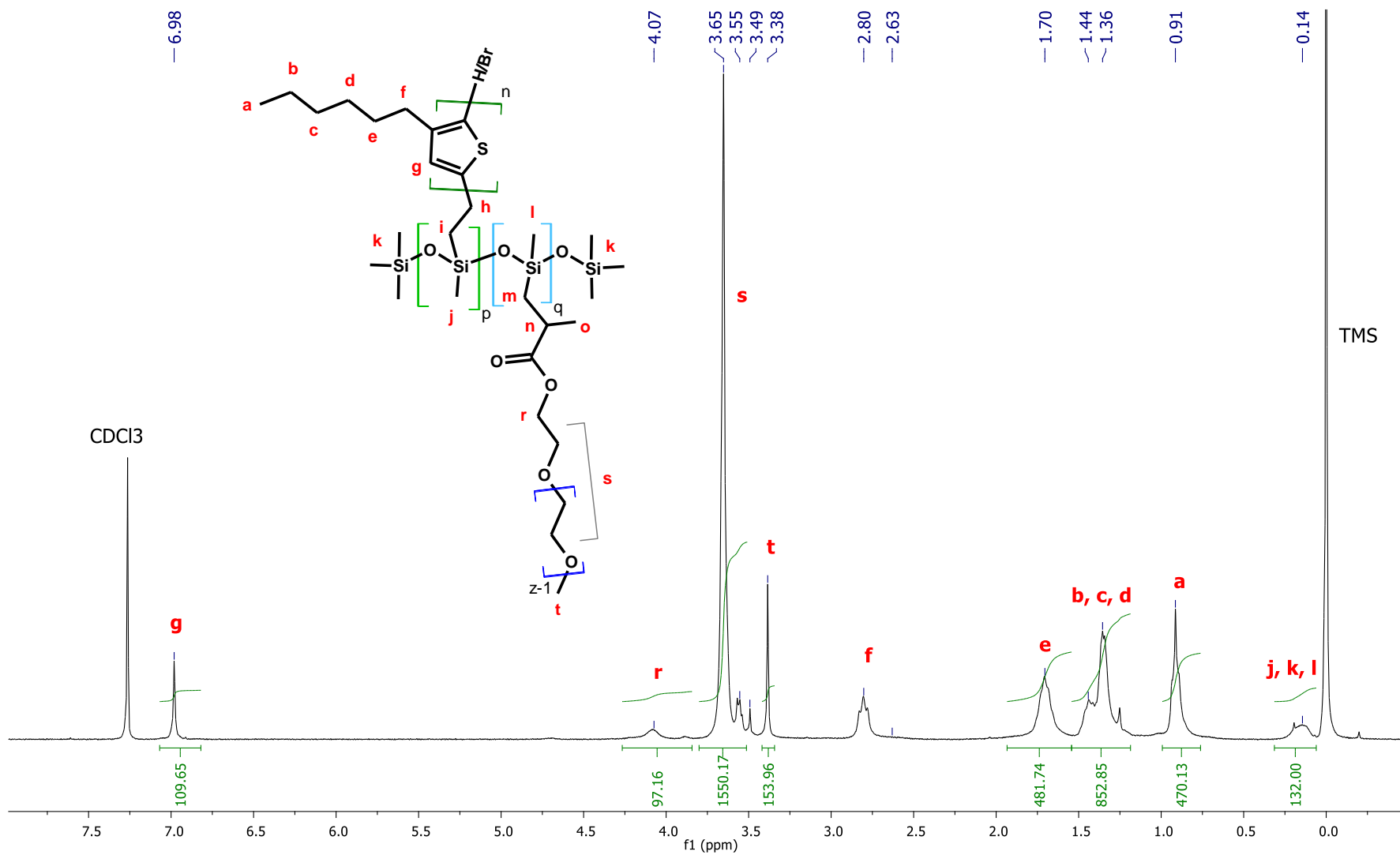


Fig. S.25 <sup>1</sup>H NMR spectrum of PMHS-g-(P3HT;PEG) 3 copolymer (300 MHz, CDCl<sub>3</sub>)

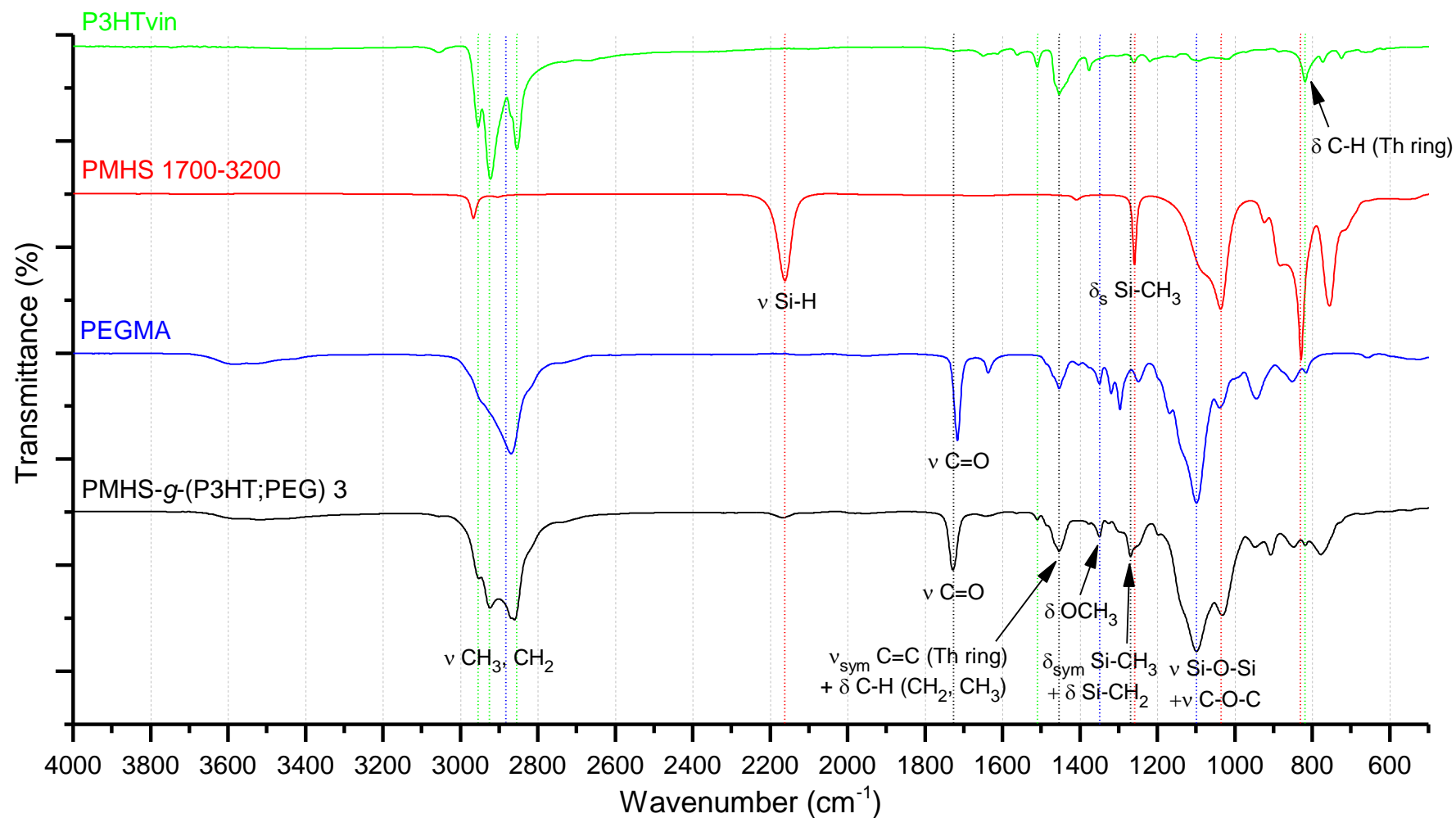


Fig. S.26 ATR-FTIR spectrum of P3HTvin, PMHS-L, PEGMA, and PMHS-g-(P3HT;PEG) 3; vibrations:  $\nu$  – stretching,  $\delta$  – deforming, asym – asymmetric, sym – symmetric

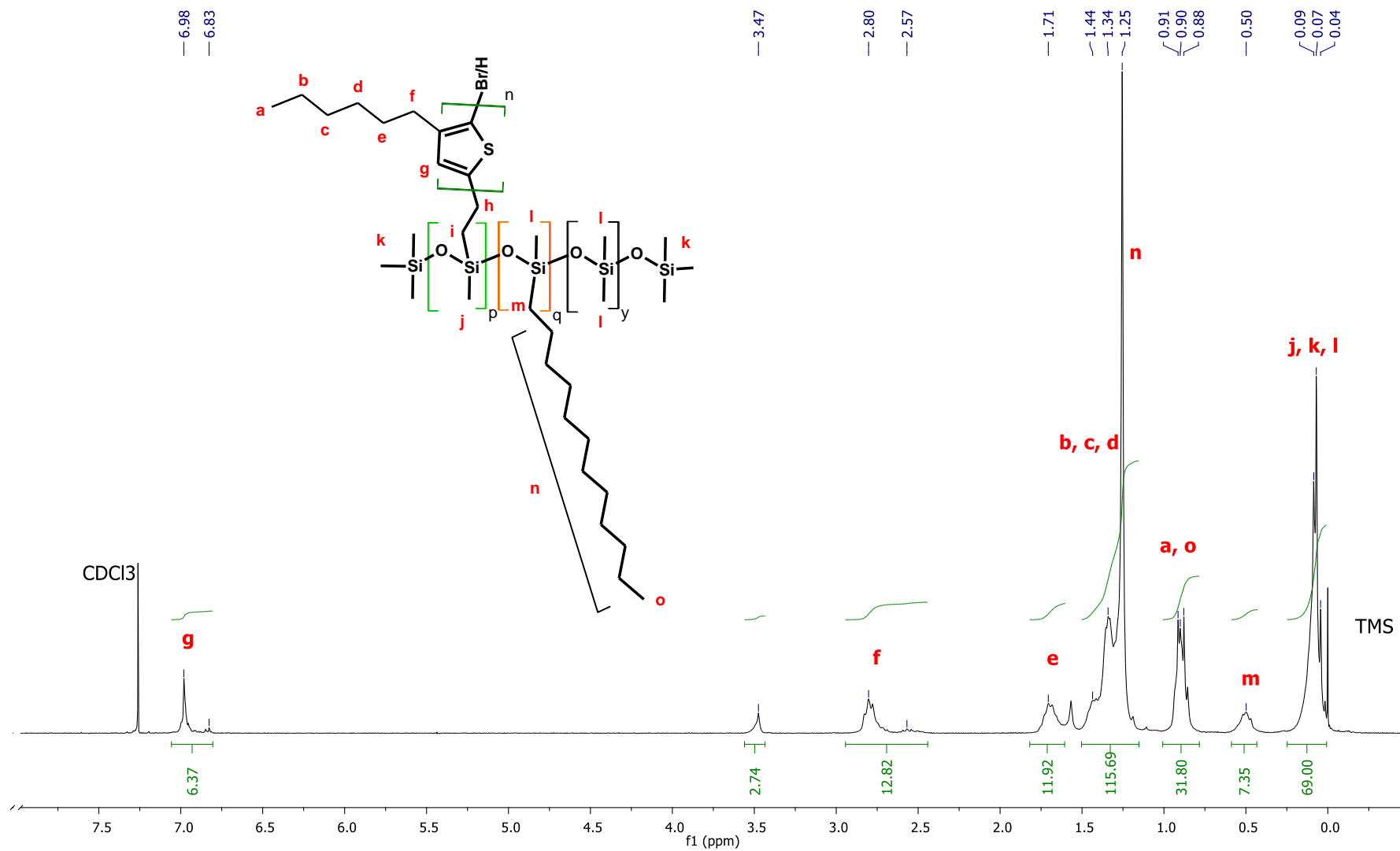


Fig. S.27 <sup>1</sup>H NMR spectrum of P(DMS-co-MHS)-g-(P3HT;dodec) 1 copolymer (300 MHz, CDCl<sub>3</sub>)

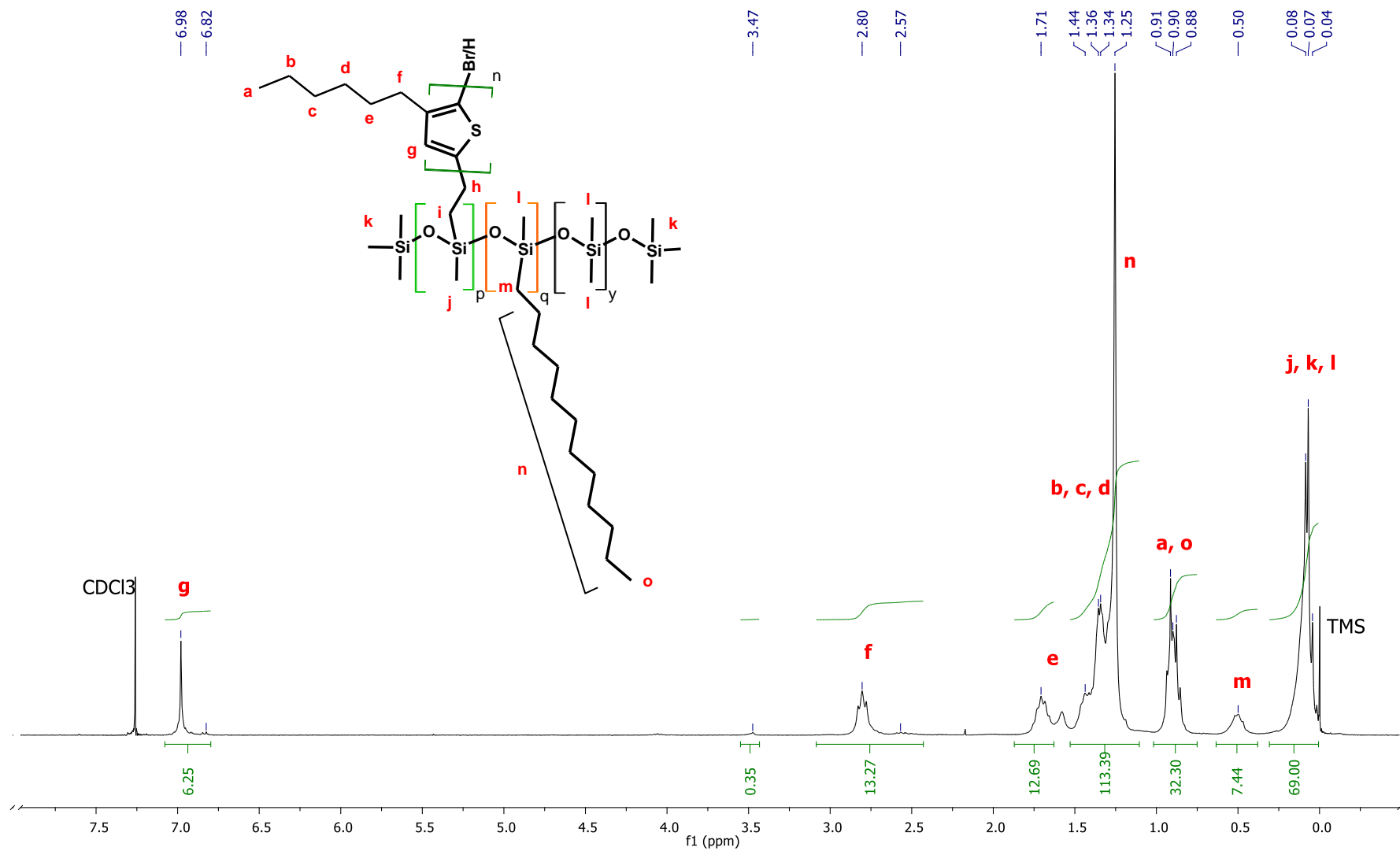


Fig. S.28 <sup>1</sup>H NMR spectrum of P(DMS-co-MHS)-g-(P3HT;dodec) 2 copolymer (300 MHz, CDCl<sub>3</sub>)

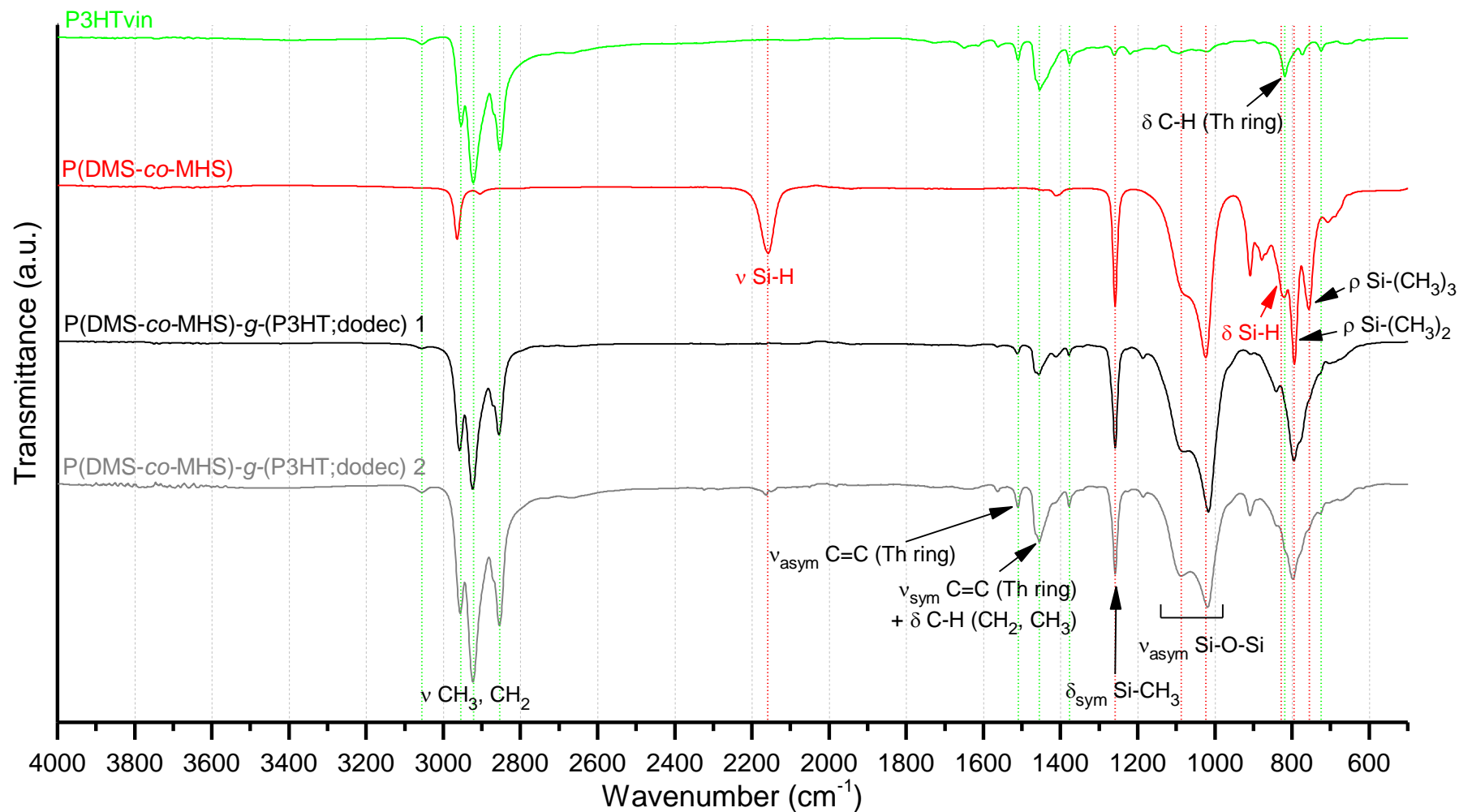


Fig. S.29 ATR-FTIR spectrum of P3HTvin, P(DMS-co-MHS), P(DMS-co-MHS)-g-(P3HT;dodec) 1, and P(DMS-co-MHS)-g-(P3HT;dodec) 2; vibrations:  $\nu$  – stretching,  $\delta$  – deforming, asym – asymmetric, sym – symmetric

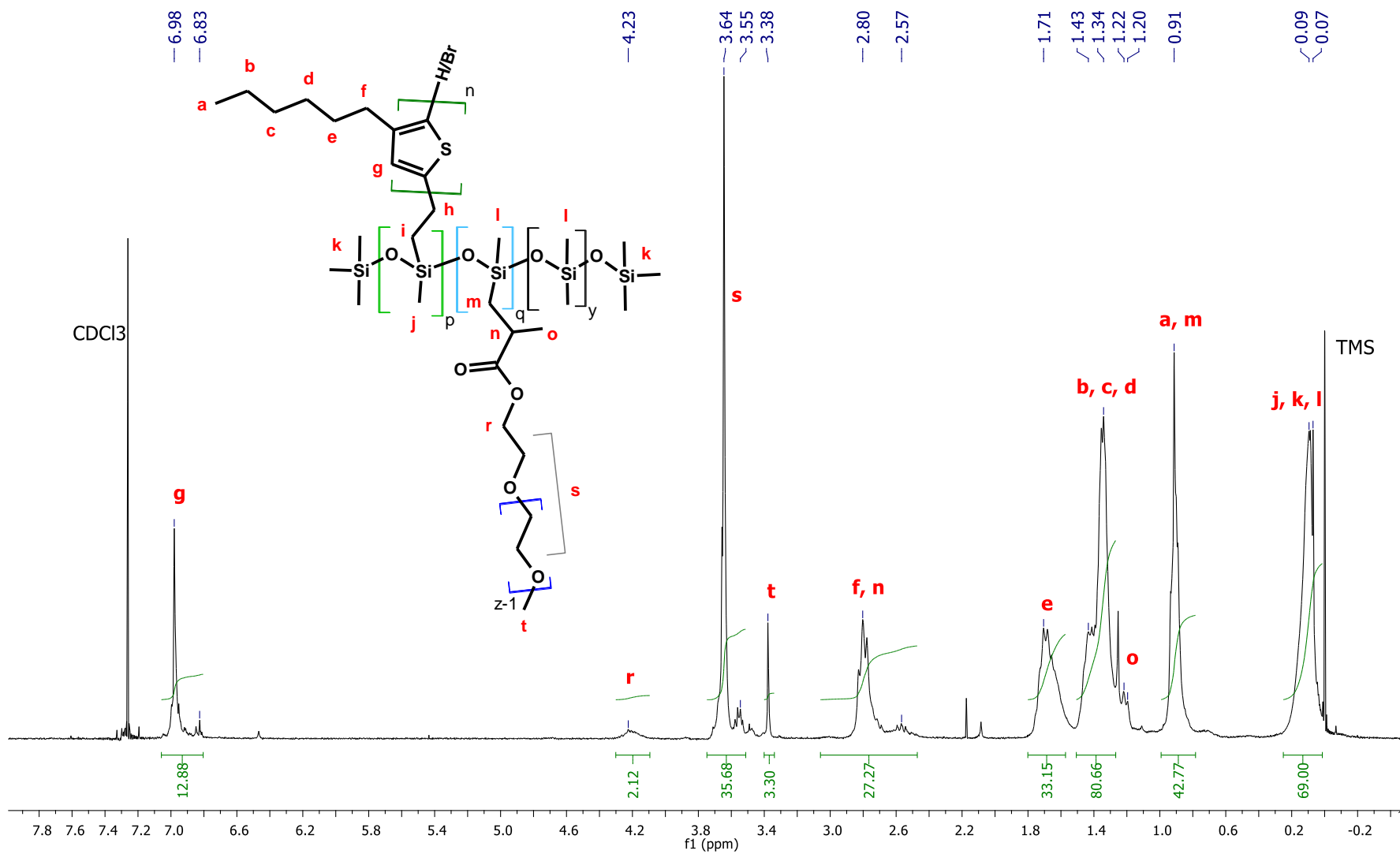
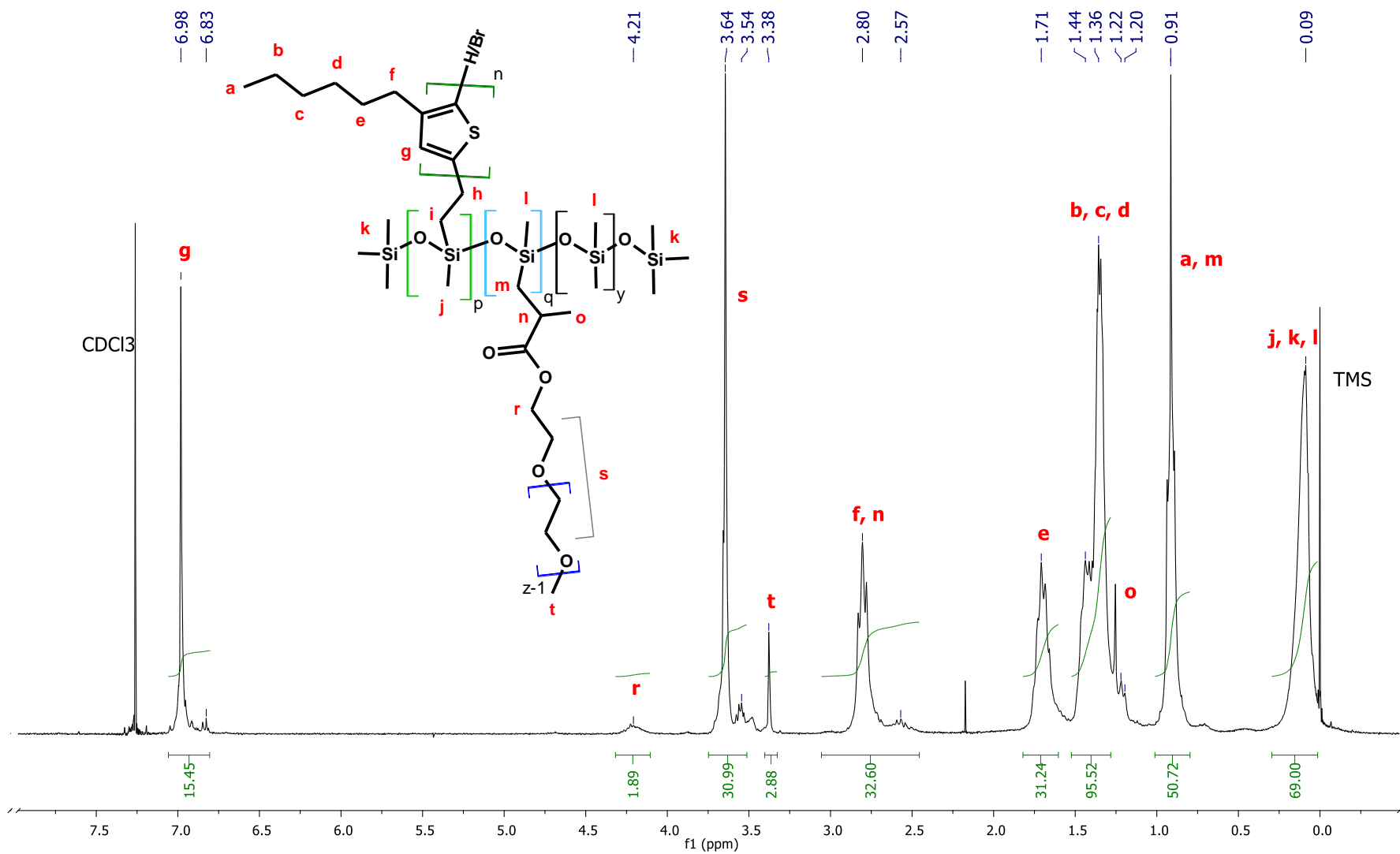


Fig. S.30 <sup>1</sup>H NMR spectrum of P(DMS-co-MHS)-g-(P3HT;PEG) 1 copolymer (300 MHz, CDCl<sub>3</sub>)

Fig. S.31  $^1\text{H}$  NMR spectrum of P(DMS-co-MHS)-g-(P3HT;PEG) 2 copolymer (300 MHz,  $\text{CDCl}_3$ )



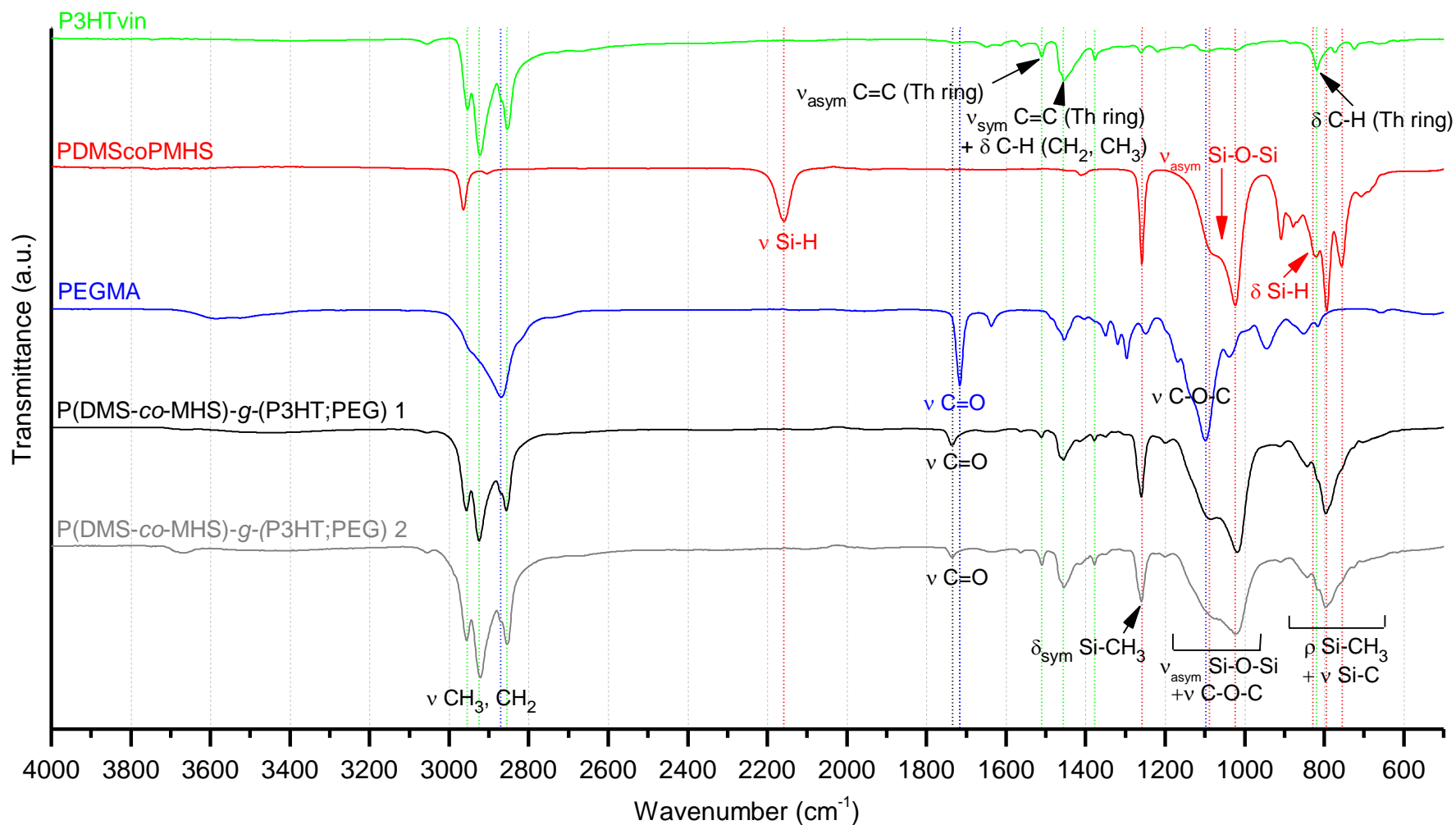


Fig. S.32 ATR-FTIR spectrum of P3HTvin, P(DMS-co-MHS), PEGMA, P(DMS-co-MHS)-g-(P3HT;PEG) 1, and P(DMS-co-MHS)-g-(P3HT;PEG) 2; vibrations:  $\nu$  – stretching,  $\delta$  – deforming, asym – asymmetric, sym – symmetric

Tab. S.2 Parameters of the solar cells measured under illumination with solar simulator

No.	Solar cell	$J_{sc}$ [mA/cm <sup>2</sup> ]	$u(J_{sc})$	$V_{oc}$ [V]	$u(V_{oc})$	FF	$u(FF)$	PCE [%]	$u_c$ (PCE)
1	P3HT FCH (1) annealed prior to contact deposition	6.803	0.047	0.57500	0.00058	0.5958	0.0062	2.331	0.029
2	P3HT FCH (1) annealed prior to contact deposition. after 1 day	6.665	0.046	0.5680	0.0011	0.578	0.0084	2.189	0.036
3	P3HT FCH (1) annealed prior to contact deposition. after 4 days	6.494	0.054	0.5688	0.0011	0.559	0.022	2.066	0.085
4	P3HT FCH (1) annealed prior to contact deposition. after 8 days	6.440	0.050	0.5653	0.0013	0.5790	0.0088	2.109	0.036
5	P3HT FCH (2) annealed prior to contact deposition	6.900	0.034	0.5758	0.0025	0.5958	0.0076	2.367	0.034
6	P3HT FCH (2) annealed prior to contact deposition +10 min after	6.760	0.045	0.5705	0.0013	0.5813	0.0087	2.242	0.037
7	P3HT FCH (2) annealed prior to contact deposition +30 min after	5.540	0.048	0.5885	0.0012	0.5378	0.0028	1.753	0.018
8	P3HT FCH (2) annealed prior to contact deposition +60 min after	5.454	0.046	0.59100	0.00091	0.5245	0.0034	1.690	0.018
9	P3HT FCH (2) after 7 days	5.453	0.047	0.5885	0.0010	0.5215	0.0031	1.673	0.018
10	P3HT FCH (3) not annealed	3.294	0.027	0.6958	0.0028	0.3953	0.0080	0.906	0.020
11	P3HT FCH (3) annealed 10 min after contact deposition	6.479	0.038	0.59200	0.00071	0.5233	0.0034	2.007	0.018
12	P3HT FCH (3) annealed 30 min after contact deposition	6.048	0.036	0.59400	0.00082	0.5043	0.0036	1.811	0.017
13	P3HT FCH (3) annealed 60 min after contact deposition	5.895	0.036	0.59450	0.00065	0.4915	0.0029	1.722	0.015
14	P3HT FCH (3) after 7 days	5.911	0.034	0.59350	0.00065	0.4890	0.0033	1.715	0.015
15	PMHS-g-(P3HT;hex) 1 (1) annealed prior to contact deposition	4.931	0.080	0.5890	0.0025	0.5840	0.0039	1.696	0.030
16	PMHS-g-(P3HT;hex) 1 (1) annealed prior to contact deposition +10 min after	5.409	0.090	0.62250	0.00065	0.5790	0.0020	1.950	0.033
17	PMHS-g-(P3HT;hex) 1 (1) annealed prior to contact deposition +30 min after	5.479	0.070	0.62350	0.00065	0.5693	0.0023	1.944	0.026
18	PMHS-g-(P3HT;hex) 1 (1) annealed prior to contact deposition +60 min after	5.584	0.086	0.6235	0.0010	0.5735	0.0033	1.996	0.033
19	PMHS-g-(P3HT;hex) 1 (1) after 2 days	5.543	0.087	0.6203	0.0011	0.5753	0.0035	1.977	0.034
20	PMHS-g-(P3HT;hex) 1 (1) after 8 days	5.542	0.086	0.6175	0.00065	0.5755	0.0031	1.969	0.032

21	PMHS-g-(P3HT;hex) 1 (2) not annealed	3.497	0.045	0.7140	0.0061	0.3813	0.003	0.952	0.017
22	PMHS-g-(P3HT;hex) 1 (2) annealed 5 min after contact deposition	5.975	0.035	0.6338	0.0025	0.6020	0.0041	2.280	0.017
22	PMHS-g-(P3HT;hex) 1 (2) annealed 10 min after contact deposition	6.134	0.012	0.63725	0.00095	0.5878	0.002	2.297	0.010
23	PMHS-g-(P3HT;hex) 1 (2) annealed 30 min after contact deposition	6.149	0.012	0.6375	0.00065	0.5773	0.0026	2.263	0.011
24	PMHS-g-(P3HT;hex) 1 (2) annealed 60 min after contact deposition	6.1358	0.0086	0.6358	0.001	0.5783	0.0025	2.256	0.011
25	PMHS-g-(P3HT;hex) 1 (2) after 2 days	6.077	0.012	0.63375	0.00048	0.5778	0.0024	2.225	0.010
26	PMHS-g-(P3HT;hex) 1 (2) after 8 days	6.054	0.011	0.632	0.00091	0.5668	0.0024	2.168	0.010
27	PMHS-g-(P3HT;hex) 2 (1) annealed prior to contact deposition	3.76	0.21	0.5928	0.0038	0.549	0.013	1.231	0.076
28	PMHS-g-(P3HT;hex) 2 (1) annealed prior to contact deposition + 5 min after	3.65	0.18	0.5793	0.0059	0.5328	0.0090	1.131	0.060
29	PMHS-g-(P3HT;hex) 2 (2) not annealed	2.240	0.025	0.676	0.033	0.331	0.019	0.505	0.038
30	PMHS-g-(P3HT;hex) 2 (2) annealed 5 min after contact deposition	4.574	0.068	0.61000	0.00071	0.5590	0.0024	1.559	0.024
31	PMHS-g-P3HT not annealed	2.438	0.041	0.719	0.0015	0.3925	0.0038	0.688	0.013
32	PMHS-g-P3HT annealed 10 min after contact deposition	4.036	0.029	0.67175	0.00048	0.4793	0.0016	1.299	0.010
33	PMHS-g-P3HT annealed 30 min after contact deposition	4.063	0.034	0.67775	0.00085	0.4725	0.0034	1.301	0.014
34	PMHS-g-P3HT annealed 60 min after contact deposition	4.135	0.028	0.6838	0.0011	0.4700	0.0039	1.329	0.014
35	PMHS-g-P3HT annealed 120 min after contact deposition	4.194	0.029	0.6870	0.0011	0.4703	0.0042	1.355	0.016
36	PMHS-g-P3HT annealed 180 min after contact deposition	4.214	0.030	0.6900	0.0011	0.4725	0.0036	1.374	0.014
37	PMHS-g-P3HT after 7 days	4.262	0.033	0.6888	0.0011	0.4728	0.0033	1.387	0.015

## XI. List of figures

Fig. IV.1	Number of Web of Science records by year for query “conducting polymer” or “conductive polymer”, acquired online 17.05.2024.....	11
Fig. 1.1	Diagram of energy levels in metals, semiconductors and insulators .....	14
Fig. 1.2	Examples of the most common conjugated polymers .....	15
Fig. 1.3	Types of thiophene rings couplings in polythiophene .....	17
Fig. 1.4	Scheme of synthetic route of Ni-catalysed polymerization of 2,5-dibromothiophene; Ni catalyst: Ni(bpy)Cl <sub>2</sub> [30] or Ni(acac) <sub>2</sub> [34] .....	17
Fig. 1.5	Structural difference between poly(thiophene-2,5-diyl) and poly(thiophene-2,4-diyl)....	18
Fig. 2.1	Numbering of atoms in the thiophene ring and the configurations of the regioisomeric couplings of the thiophene rings: dyads: 2,5 - head-to-tail (HT); 2,2 - head-to-head (HH); 5,5 - tail-to-tail (TT) and triads resulting from the combination of two dyads.....	20
Fig. 2.2	Out-of-plane deformation of the P3HT chain due to the structure defect (HH connection) .....	20
Fig. 2.3	Crystal structure of P3HT .....	22
Fig. 2.4	Mechanism of Grignard Metathesis (GRIM) polymerization proposed by McCullough [69,70]; L: PPh <sub>3</sub> , R: <i>n</i> -hexyl.....	28
Fig. 2.5	Mechanism of Kumada catalyst transfer polycondensation (KCTP) proposed by Yokozawa [68]; NiL <sub>2</sub> : Ni(dppp), R: <i>n</i> -hexyl .....	29
Fig. 3.1	Architectures of chosen copolymer macromolecules and their nomenclature .....	33
Fig. 3.2	General approaches to the synthesis of graft copolymers.....	34
Fig. 3.3	Schematic structure of polysiloxane (a); polysiloxanes: poly(dimethylsiloxane) and poly(methylhydrosiloxane) (b); structural units distinguished based on functionality (c) 35	
Fig. 3.4	Structural parameters of PDMS chain .....	36
Fig. 3.5	Addition of silanes to double bonds .....	37
Fig. 3.6	Schematic structure of Karstedt catalyst.....	38
Fig. 3.7	Chalk-Harrod and modified Chalk-Harrod mechanism of platinum-catalysed hydrosilylation .....	39
Fig. 3.8	Formation of $\alpha$ - and $\beta$ -adducts in hydrosilylation .....	39
Fig. 4.1	Dimethylsiloxane-methylhydrosiloxane compositional triads and their designation .....	49
Fig. 5.1	Number of Web of Science records by year for query “polymer solar cell(s)”, acquired online 02.07.2024 .....	55
Fig. 5.2	Energy level diagram of donor and acceptor in organic solar cells .....	56
Fig. 5.3	Charge generation and transport in organic solar cells.....	57
Fig. 5.4	Scheme of conventional bulk heterojunction organic solar cell .....	58
Fig. 5.5	J-V and power-voltage curves of organic solar cell.....	59
Fig. 6.1	Schematic paths for syntheses of graft copolymers: PMHS grafted with P3HT (a), PMHS grafted with P3HT and PEGMA or hexyl groups (b), PDMS-MHS copolymer grafted with P3HT (c), PDMS-MHS copolymer grafted with P3HT and PEGMA or dodecyl groups (d) .....	68
Fig. 7.1	<sup>1</sup> H NMR spectrum of NR P3HT FC (300 MHz, CDCl <sub>3</sub> ), expansions of aromatic protons (g) region with peak assignments to regioisomeric triads and $\alpha$ -CH <sub>2</sub> protons (f) region with peak assignments to regioisomeric dyads .....	76
Fig. 7.2	<sup>13</sup> C NMR spectrum of NR P3HT FC (100 MHz, CDCl <sub>3</sub> ), expansion of aromatic carbons region with assignment of the peaks to regioisomeric triads .....	77

Fig. 7.3	$^1\text{H}$ NMR spectrum of RR P3HT FC (400 MHz, $\text{CDCl}_3$ ), expansions of aromatic protons ( <i>g</i> ) region and $\alpha\text{-CH}_2$ protons ( <i>f</i> ) region with assignments of end groups signals.....	78
Fig. 7.4	$^1\text{H}$ NMR spectrum of P3HTvin FC (300 MHz, $\text{CDCl}_3$ ), expansion of aromatic protons ( <i>g</i> ) region, vinyl group protons ( <i>j, k</i> ) region, and $\alpha\text{-CH}_2$ protons ( <i>f</i> ) region with assignments of peaks .....	80
Fig. 7.5	$^1\text{H}\text{-}^1\text{H}$ COSY spectrum of P3HTvin FC (400 MHz, $\text{CDCl}_3$ ) with expansion of correlation peaks between $\text{-CH=CH}_2$ proton and $\text{-CH=CH}_2$ protons .....	81
Fig. 7.6	Stacked spectra of P3HTvin FC obtained on 300 MHz (blue), 400 MHz (green) and 600 MHz (red) spectrometers showing changes of aromatic protons signals, vinyl protons signals and $\alpha\text{-CH}_2$ protons signals expressed in ppm with changing base frequency of the spectrometer.....	82
Fig. 8.1	AFM height images of electrode region and substrate region of IDT for: a) RR P3HT and b) PMHS- <i>g</i> -(P3HT;PEG) 3 copolymer films spin coated from $\text{CHCl}_3$ solutions [232]...	98
Fig. 8.2	AFM height and phase images ( $5 \times 5 \mu\text{m}$ area) of copolymer films spin coated from $\text{CHCl}_3$ solutions on IDT (substrate region): a) P(DMS- <i>co</i> -MHS)- <i>g</i> -(P3HT;PEG) 1, b) P(DMS- <i>co</i> -MHS)- <i>g</i> -(P3HT;PEG) 2 [233] .....	99
Fig. 8.3	AFM height and phase images ( $5 \times 5 \mu\text{m}$ area) of copolymer films spin coated from $\text{CHCl}_3$ solutions on IDT (substrate region): a) P(DMS- <i>co</i> -MHS)- <i>g</i> -(P3HT;dodec) 1, b) P(DMS- <i>co</i> -MHS)- <i>g</i> -(P3HT;dodec) 2 [233] .....	100
Fig. 8.4	AFM height images of copolymer films drop coated from CB solutions on IDT (substrate region): a) P(DMS- <i>co</i> -MHS)- <i>g</i> -(P3HT;PEG) 2, b) P(DMS- <i>co</i> -MHS)- <i>g</i> -(P3HT;dodec) 2 [234].....	101
Fig. 8.5	Resistance responses of RR and NR P3HT, and graft copolymers (PMHS- <i>g</i> -(P3HT;PEG) 1, PMHS- <i>g</i> -(P3HT;PEG) 3) to the repeated exposure to 5 ppm of $\text{NO}_2$ at $50^\circ\text{C}$ [232]..	102
Fig. 8.6	Resistance responses of graft copolymers (P(DMS- <i>co</i> -MHS)- <i>g</i> -(P3HT;PEG) 1, P(DMS- <i>co</i> -MHS)- <i>g</i> -(P3HT;PEG) 2, P(DMS- <i>co</i> -MHS)- <i>g</i> -(P3HT;dodec) 1, P(DMS- <i>co</i> -MHS)- <i>g</i> -(P3HT;dodec) 2) to the repeated exposure to different concentrations of $\text{NO}_2$ at $50^\circ\text{C}$ (a) and $100^\circ\text{C}$ (b) [233] .....	103
Fig. 8.7	Resistance responses of graft copolymers P(DMS- <i>co</i> -MHS)- <i>g</i> -(P3HT;PEG) 2, and P(DMS- <i>co</i> -MHS)- <i>g</i> -(P3HT;dodec) 2 to the repeated exposure to different concentrations of $\text{NO}_2$ in $\text{N}_2$ at RT under dark and UV conditions [234].....	104
Fig. 8.8	Resistance responses of graft copolymers P(DMS- <i>co</i> -MHS)- <i>g</i> -(P3HT;PEG) 2, and P(DMS- <i>co</i> -MHS)- <i>g</i> -(P3HT;dodec) 2 to the repeated exposure to different concentrations of $\text{NO}_2$ in the air at RT under dark and UV conditions [234] .....	105
Fig. 8.9	a) P(DMS- <i>co</i> -MHS)- <i>g</i> -(P3HT;PEG) 2 response to 500 ppb of $\text{NO}_2$ in the air under continuous UV illumination, b) AFM surface image of P(DMS- <i>co</i> -MHS)- <i>g</i> -(P3HT;PEG) 2 after two weeks of ageing under UV in the air [234] .....	106
Fig. 8.10	J-V curves of P3HT:PCBM (1) solar cell stored under nitrogen.....	107
Fig. 8.11	J-V curves of P3HT:PCBM (2) solar cell annealed before contact deposition .....	107
Fig. 8.12	J-V curves of P3HT:PCBM (3) solar cell annealed after contact deposition .....	108
Fig. 8.13	J-V curves of PMHS- <i>g</i> -(P3HT;hex) 1:PCBM (1) solar cell annealed before contact deposition and further annealed after contact deposition .....	109
Fig. 8.14	J-V curves of PMHS- <i>g</i> -(P3HT;hex) 1:PCBM (2) solar cell annealed after contact deposition.....	109
Fig. 8.15	J-V curves of PMHS- <i>g</i> -(P3HT;hex) 2:PCBM (1) and (2) solar cells annealed before and after contact deposition.....	110
Fig. 8.16	J-V curves of P(DMS- <i>co</i> -MHS)- <i>g</i> -P3HT:PCBM solar cell annealed after contact deposition.....	110
Fig. 8.17	EQE characteristic of solar cells with AM1.5G integrated current densities .....	111

Fig. 8.18	UV-Vis absorption spectra of thin films (P3HT and copolymers blend with PCBM) as cast and annealed for 5 min .....	113
Fig. 8.19	AFM images of P3HT:PCBM solar cells surface: annealed 5 min (a) and 60 min (b) ..	114
Fig. 8.20	AFM images of PMHS-g-(P3HT;hex) 1:PCBM solar cells surface annealed 60 min ...	115
Fig. S.1	<sup>1</sup> H NMR spectrum of NR P3HT FC (300 MHz, CDCl <sub>3</sub> ) with assignments of peaks: δ (ppm) 7.05. 7.03. 7.00. 6.98 (4 singlets, 1H), 2.80. 2.56 (2 broad singlets, 2H), 1.71 (m, 2H), 1.44-1.35 (m, 6H), 0.91 (m, 3H) .....	122
Fig. S.2	<sup>13</sup> C NMR spectrum of NR P3HT FCH (100 MHz, CDCl <sub>3</sub> ) with assignments of peaks: δ (ppm) 143.4 (C3 HH-TT), 142.9 (C3 HH-HT), 140.3 (C3 HT-TT), <b>139.9 (C3 HT-HT)</b> , 137.0 (C5 HH-TT), 135.7 (C5 HH-HT), 134.9 (C5 HT-TT), <b>133.7 (C5 HT-HT)</b> , <b>130.5 (C2 HT-HT)</b> , 129.6 (C2 HT-TT), <b>128.6 (C4 HT-HT)</b> , 128.3 (C2 HH-HT), 127.4 (C2 HH-TT), 127.2 (C4 HT-HH), 126.6 (C4 HT-TT), 125.2 (C4 HH-TT), <b>31.7, 30.5, 29.5, 29.3, 22.7, 14.1</b> .....	123
Fig. S.3	HSQC spectrum of NR P3HT FCH with expansions of aliphatic and aromatic regions; CH and CH <sub>3</sub> groups are negative in phase (blue), CH <sub>2</sub> groups are positive in phase (red)...	124
Fig. S.4	<sup>1</sup> H NMR spectrum of RR P3HT (300 MHz, CDCl <sub>3</sub> ) with assignments of peaks: δ (ppm) 6.98 (s, 1H), 2.81-2.57 (m, 2H), 1.71 (m, 2H), 1.44-1.36 (m, 6H), 0.92 (m, 3H) .....	125
Fig. S.5	HSQC ( <sup>1</sup> H 400 MHz, <sup>13</sup> C 100 MHz, CDCl <sub>3</sub> ) spectrum of RR P3HT with expansions of aliphatic and aromatic regions; CH and CH <sub>3</sub> groups are negative in phase (blue), CH <sub>2</sub> groups are positive in phase (red) .....	126
Fig. S.6	MALDI-TOF spectrum of RR P3HT with zoom showing assignment of series of peaks to polymer chains with different end groups .....	127
Fig. S.7	<sup>1</sup> H NMR spectrum of P3HTvin FC (300 MHz, CDCl <sub>3</sub> ) with assignments of peaks: δ (ppm) 6.98 (s, 1H), 5.51 (d, <sup>3</sup> J <sub>1</sub> =17.2 Hz, 0.013 H), 5.13 (d, <sup>3</sup> J <sub>2</sub> =11.0 Hz, 0.013 H), 2.81-2.57 (m, 2H), 1.71 (m, 2H), 1.44-1.36 (m, 6H), 0.92 (m, 3H) .....	128
Fig. S.8	HSQC ( <sup>1</sup> H 400 MHz, <sup>13</sup> C 100 MHz, CDCl <sub>3</sub> ) spectrum of P3HTvin FC with expansions of vinyl and aromatic regions; CH and CH <sub>3</sub> groups are negative in phase (blue), CH <sub>2</sub> groups are positive in phase (red) .....	129
Fig. S.9	MALDI-TOF spectrum of P3HTvin FC with zoom showing assignment of series of peaks to polymer chains with different end groups .....	130
Fig. S.10	ATR-FTIR spectrum of P3HTvin FC; vibrations: ν – stretching, δ – deforming, ρ – rocking, asym – asymmetric, sym – symmetric, Th ring – thiophene ring .....	131
Fig. S.11	<sup>1</sup> H NMR spectrum of PMHS-S (300 MHz, CDCl <sub>3</sub> ) with assignments of peaks; * - <sup>29</sup> Si satellite peaks .....	132
Fig. S.12	<sup>1</sup> H NMR spectrum of PMHS-L (300 MHz, CDCl <sub>3</sub> ) with assignments of peaks; * - <sup>29</sup> Si satellite peaks .....	133
Fig. S.13	<sup>1</sup> H NMR spectrum of P(DMS-co-MHS) (300 MHz, CDCl <sub>3</sub> ) with assignments of peaks; * - <sup>29</sup> Si satellite peaks .....	134
Fig. S.14	ATR-FTIR spectrum of PMHS-S, PMHS-L, and P(DMS-co-MHS); vibrations: ν – stretching, δ – deforming, asym – asymmetric, sym – symmetric .....	135
Fig. S.15	ATR-FTIR spectrum of PEGMA; vibrations: ν – stretching, δ – deforming, ω – wagging, asym – asymmetric, sym – symmetric .....	136
Fig. S.16	<sup>1</sup> H NMR spectrum of PMHS-g-P3HT copolymer (300 MHz, CDCl <sub>3</sub> ) with assignments of peaks .....	137
Fig. S.17	<sup>1</sup> H NMR spectrum of P(DMS-co-MHS)-g-P3HT copolymer (300 MHz, CDCl <sub>3</sub> ) .....	138
Fig. S.18	ATR-FTIR spectrum of P3HTvin, PMHS-S, P(DMS-co-MHS), PMHS-g-P3HT and P(DMS-co-MHS)-g-P3HT; vibrations: ν – stretching, δ – deforming, asym – asymmetric, sym – symmetric .....	139
Fig. S.19	<sup>1</sup> H NMR spectrum of PMHS-g-(P3HT;hex) 1 copolymer (300 MHz, CDCl <sub>3</sub> ) .....	140

Fig. S.20	<sup>1</sup> H NMR spectrum of PMHS- <i>g</i> -(P3HT;hex) 2 copolymer (300 MHz, CDCl <sub>3</sub> )	141
Fig. S.21	ATR-FTIR spectrum of P3HTvin, PMHS-S, PMHS-L, PMHS- <i>g</i> -(P3HT;hex) 1, PMHS- <i>g</i> -(P3HT;hex) 2; vibrations: $\nu$ – stretching, $\delta$ – deforming, asym – asymmetric, sym – symmetric	142
Fig. S.22	<sup>1</sup> H NMR spectrum of PMHS- <i>g</i> -(P3HT;PEG) 1 copolymer (300 MHz, CDCl <sub>3</sub> )	143
Fig. S.23	<sup>1</sup> H NMR spectrum of PMHS- <i>g</i> -(P3HT;PEG) 2 copolymer (300 MHz, CDCl <sub>3</sub> )	144
Fig. S.24	ATR-FTIR spectrum of P3HTvin, PMHS-S, PEGMA, PMHS- <i>g</i> -(P3HT;PEG) 1, and PMHS- <i>g</i> -(P3HT;PEG) 2; vibrations: $\nu$ – stretching, $\delta$ – deforming, asym – asymmetric, sym – symmetric	145
Fig. S.25	<sup>1</sup> H NMR spectrum of PMHS- <i>g</i> -(P3HT;PEG) 3 copolymer (300 MHz, CDCl <sub>3</sub> )	146
Fig. S.26	ATR-FTIR spectrum of P3HTvin, PMHS-L, PEGMA, and PMHS- <i>g</i> -(P3HT;PEG) 3; vibrations: $\nu$ – stretching, $\delta$ – deforming, asym – asymmetric, sym – symmetric	147
Fig. S.27	<sup>1</sup> H NMR spectrum of P(DMS- <i>co</i> -MHS)- <i>g</i> -(P3HT;dodec) 1 copolymer (300 MHz, CDCl <sub>3</sub> )	148
Fig. S.28	<sup>1</sup> H NMR spectrum of P(DMS- <i>co</i> -MHS)- <i>g</i> -(P3HT;dodec) 2 copolymer (300 MHz, CDCl <sub>3</sub> )	149
Fig. S.29	ATR-FTIR spectrum of P3HTvin, P(DMS- <i>co</i> -MHS), P(DMS- <i>co</i> -MHS)- <i>g</i> -(P3HT;dodec) 1, and P(DMS- <i>co</i> -MHS)- <i>g</i> -(P3HT;dodec) 2; vibrations: $\nu$ – stretching, $\delta$ – deforming, asym – asymmetric, sym – symmetric	150
Fig. S.30	<sup>1</sup> H NMR spectrum of P(DMS- <i>co</i> -MHS)- <i>g</i> -(P3HT;PEG) 1 copolymer (300 MHz, CDCl <sub>3</sub> )	151
Fig. S.31	<sup>1</sup> H NMR spectrum of P(DMS- <i>co</i> -MHS)- <i>g</i> -(P3HT;PEG) 2 copolymer (300 MHz, CDCl <sub>3</sub> )	152
Fig. S.32	ATR-FTIR spectrum of P3HTvin, P(DMS- <i>co</i> -MHS), PEGMA, P(DMS- <i>co</i> -MHS)- <i>g</i> -(P3HT;PEG) 1, and P(DMS- <i>co</i> -MHS)- <i>g</i> -(P3HT;PEG) 2; vibrations: $\nu$ – stretching, $\delta$ – deforming, asym – asymmetric, sym – symmetric	153

## XII. List of tables

Tab. 2.1	Synthetic routes to regioregular poly(3-alkylthiophenes)	24
Tab. 3.1	Selection of block copolymers containing RR P3HT segment	40
Tab. 3.2	Graft copolymers bearing P3HT side chains reported in literature	42
Tab. 4.1	Assignments of signals of aromatic protons and carbons in main chains of poly(3-alkylthiophene)s	47
Tab. 4.2	<sup>1</sup> H NMR chemical shifts, multiplicities and coupling constants of aromatic and $\alpha$ -CH <sub>2</sub> protons in different end groups resulting from GRIM/KCTP polymerization protocol	48
Tab. 4.3	Characteristic infrared absorption bands of regioregular P3HT	50
Tab. 5.1	NO <sub>2</sub> sensors based on conjugated polymers reported in literature	53
Tab. 6.1	Copolymers grafted on PMHS backbone	70
Tab. 6.2	Copolymers grafted on P(DMS- <i>co</i> -MHS) backbone	71
Tab. 6.3	Fabricated solar cells	74
Tab. 7.1	Number average molecular weights ( $M_n$ ), number of repeating thiophene units ( $n$ ) and dispersities ( $\mathcal{D}_M$ ) obtained based on GPC <sup>†</sup> , MALDI-TOF and end group analysis by <sup>1</sup> H NMR	84
Tab. 7.2	Composition of synthesised copolymers	96

Tab. 8.1	Surface roughness of RR P3HT, NR P3HT and copolymers (PMHS- <i>g</i> -(P3HT;PEG) 1 and 3) films deposited on IDT.....	98
Tab. 8.2	Surface roughness of P(DMS- <i>co</i> -MHS)- <i>g</i> -(P3HT;PEG) 1 and 2, and P(DMS- <i>co</i> -MHS)- <i>g</i> -(P3HT;dodec) 1 and 2 copolymer films spin coated on IDT from CHCl <sub>3</sub> solution.....	101
Tab. 8.3	Parameters of solar cells calculated based on EQE measurements .....	112
Tab. 8.4	RMS and peak to peak distances (maximum heights) of the solar cells surfaces determined from AFM images.....	115
Tab. S.1	List of commercially available thiophenes, polysiloxanes, poly(ethylene glycol), Grignard compounds and catalysts used in this work .....	120
Tab. S.2	Parameters of the solar cells measured under illumination with solar simulator.....	154



### XIII. Bibliography

1. Shirakawa, H.; Ikeda, S. Infrared Spectra of Poly(Acetylene). *Polym. J.* **1971**, *2*, 231–244, doi:10.1295/polymj.2.231.
2. Shirakawa, H.; Ito, T.; Ikeda, S. Raman Scattering and Electronic Spectra of Poly(Acetylene). *Polym. J.* **1973**, *4*, 460–462, doi:10.1295/polymj.4.460.
3. Shirakawa, H.; Louis, J.; MacDiarmid, A.G. Synthesis of Electrically Conducting Organic Polymers: Halogen Derivatives of Polyacetylene, (CH)<sub>x</sub>. *J. Chem. Soc. Chem. Commun.* **1977**, 578–580, doi:10.1039/C39770000578.
4. Chiang, C.K.; Fincher, C.R.; Park, Y.W.; Heeger, A.J.; Shirakawa, H.; Louis, E.J.; Gau, S.C.; MacDiarmid, A.G. Electrical Conductivity in Doped Polyacetylene. *Phys. Rev. Lett.* **1977**, *39*, 1098–1101, doi:10.1103/PhysRevLett.39.1098.
5. Guo, X.; Facchetti, A. The Journey of Conducting Polymers from Discovery to Application. *Nat. Mater.* **2020**, *19*, 922–928, doi:10.1038/s41563-020-0778-5.
6. Angelopoulos, M. Conducting Polymers in Microelectronics. *IBM J. Res. Dev.* **2001**, *45*, 57–75, doi:10.1147/rd.451.0057.
7. Xu, H.; Zhang, Y. A Review on Conducting Polymers and Nanopolymer Composite Coatings for Steel Corrosion Protection. *Coatings* **2019**, *9*, 1–22, doi:10.3390/coatings9120807.
8. Sengodu, P.; Deshmukh, A.D. Conducting Polymers and Their Inorganic Composites for Advanced Li-Ion Batteries: A Review. *RSC Adv.* **2015**, *5*, 42109–42130, doi:10.1039/c4ra17254j.
9. Jia, X.; Ge, Y.; Shao, L.; Wang, C.; Wallace, G.G. Tunable Conducting Polymers: Toward Sustainable and Versatile Batteries. *ACS Sustain. Chem. Eng.* **2019**, *7*, 14321–14340, doi:10.1021/acssuschemeng.9b02315.
10. Wang, Y.; Ding, Y.; Guo, X.; Yu, G. Conductive Polymers for Stretchable Supercapacitors. *Nano Res.* **2019**, *12*, 1978–1987, doi:10.1007/s12274-019-2296-9.
11. Cai, X.; Sun, K.; Qiu, Y.; Jiao, X. Recent Advances in Graphene and Conductive Polymer Composites for Supercapacitor Electrodes: A Review. *Crystals* **2021**, *11*, 947, doi:10.3390/cryst11080947.
12. Rai, V.; Singh, R.S.; Blackwood, D.J.; Zhili, D. A Review on Recent Advances in Electrochromic Devices: A Material Approach. *Adv. Eng. Mater.* **2020**, *22*, doi:10.1002/adem.202000082.
13. Cai, Q.; Yan, H.; Yao, R.; Luo, D.; Li, M.; Zhong, J.; Yang, Y.; Qiu, T.; Ning, H.; Peng, J. From Traditional to Novel Printed Electrochromic Devices: Material, Structure and Device. *Membranes (Basel)*. **2022**, *12*, 1039, doi:10.3390/membranes12111039.
14. Hou, W.; Xiao, Y.; Han, G.; Lin, J.-Y. The Applications of Polymers in Solar Cells: A Review. *Polym.* **2019**, *11*, 143, doi:10.3390/polym11010143.
15. Murad, A.R.; Iraqi, A.; Aziz, S.B.; Abdullah, S.N.; Brza, M.A. Conducting Polymers for Optoelectronic Devices and Organic Solar Cells: A Review. *Polymers (Basel)*. **2020**, *12*, 1–47, doi:10.3390/polym12112627.
16. Kumar, B.; Kaushik, B.K.; Negi, Y.S. Organic Thin Film Transistors: Structures, Models, Materials, Fabrication, and Applications: A Review. *Polym. Rev.* **2014**, *54*, 33–111, doi:10.1080/15583724.2013.848455.
17. Sekine, C.; Tsubata, Y.; Yamada, T.; Kitano, M.; Doi, S. Recent Progress of High Performance Polymer OLED and OPV Materials for Organic Printed Electronics. *Sci. Technol. Adv. Mater.* **2014**, *15*, 034203, doi:10.1088/1468-6996/15/3/034203.
18. Bhuvana, K.P.; Joseph Bensingh, R.; Abdul Kader, M.; Nayak, S.K. Polymer Light Emitting Diodes: Materials, Technology and Device. *Polym. - Plast. Technol. Eng.* **2018**, *57*, 1784–1800, doi:10.1080/03602559.2017.1422269.
19. Nayak, D.; Choudhary, R.B. Conducting Polymer-Based Emissive Layer on Efficiency of

- OLEDs. In *Light-Emitting Diodes and Photodetectors - Advances and Future Directions*; Casalino, M., Thirumalai, J., Eds.; IntechOpen, 2021 ISBN 978-1-83968-556-9.
20. Cavallari, M.R.; Pastrana, L.M.; Sosa, C.D.F.; Marquina, A.M.R.; Izquierdo, J.E.E.; Fonseca, F.J.; de Amorim, C.A.; Paterno, L.G.; Kymissis, I. Organic Thin-Film Transistors as Gas Sensors: A Review. *Materials (Basel)*. **2021**, *14*, 1–32, doi:10.3390/ma14010003.
  21. Lakard, B. Electrochemical Biosensors Based on Conducting Polymers: A Review. *Appl. Sci.* **2020**, *10*, 6614, doi:10.3390/APP10186614.
  22. Sun, C.; Wang, X.; Auwalu, M.A.; Cheng, S.; Hu, W. Organic Thin Film Transistors-Based Biosensors. *EcoMat* **2021**, *3*, 1–22, doi:10.1002/eom2.12094.
  23. Ling, Q.D.; Song, Y.; Lim, S.L.; Teo, E.Y.H.; Tan, Y.P.; Zhu, C.; Chan, D.S.H.; Kwong, D.L.; Kang, E.T.; Neoh, K.G. A Dynamic Random Access Memory Based on a Conjugated Copolymer Containing Electron-Donor and -Acceptor Moieties. *Angew. Chemie - Int. Ed.* **2006**, *45*, 2947–2951, doi:10.1002/anie.200504365.
  24. Baek, S.; Lee, D.; Kim, J.; Hong, S.H.; Kim, O.; Ree, M. Novel Digital Nonvolatile Memory Devices Based on Semiconducting Polymer Thin Films. *Adv. Funct. Mater.* **2007**, *17*, 2637–2644, doi:10.1002/adfm.200600892.
  25. Grancarić, A.M.; Jerković, I.; Koncar, V.; Cochrane, C.; Kelly, F.M.; Soulat, D.; Legrand, X. Conductive Polymers for Smart Textile Applications. *J. Ind. Text.* **2018**, *48*, 612–642, doi:10.1177/1528083717699368.
  26. Jadoun, S.; Rathore, D.S.; Riaz, U.; Chauhan, N.P.S. Tailoring of Conducting Polymers via Copolymerization – A Review. *Eur. Polym. J.* **2021**, *155*, 110561, doi:10.1016/j.eurpolymj.2021.110561.
  27. Kanazawa, K.K.; Diaz, A.F.; Geiss, R.H.; Gill, W.D.; Kwak, J.F.; Logan, J.A.; Rabolt, J.F.; Street, G.B. “Organic Metals”: Polypyrrole, a Stable Synthetic “metallic” Polymer. *J. Chem. Soc. Chem. Commun.* **1979**, 854–855, doi:10.1039/C39790000854.
  28. Tourillon, G.; Garnier, F. New Electrochemically Generated Organic Conducting Polymers. *J. Electroanal. Chem.* **1982**, *135*, 173–178, doi:10.1016/0022-0728(82)90015-8.
  29. Pfluger, P.; Street, G.B. Chemical, Electronic, and Structural Properties of Conducting Heterocyclic Polymers: A View by XPS. *J. Chem. Phys.* **1984**, *80*, 544–553, doi:10.1063/1.446428.
  30. Yamamoto, T.; Sanechika, K.; Yamamoto, A. Preparation of Thermostable and Electric-Conducting Poly(2,5-Thienylene). *J. Polym. Sci. Polym. Lett. Ed.* **1980**, *18*, 9–12, doi:10.1002/pol.1980.130180103.
  31. Ewbank, P.C.; Stefan, M.C.; Sauve, G.; McCullough, R.D. Synthesis, Characterization and Properties of Regioregular Polythiophene-Based Materials. In *Handbook of Thiophene-based Materials: Applications in Organic Electronics and Photonics*; Perepichka, I.F., Perepichka, D.F., Eds.; John Wiley & Sons Ltd, 2009; pp. 157–218 ISBN 978-0-470-05732-2.
  32. McCullough, R.D.; Ewbank, P.C. Regioregular, Head-to-Tail Coupled Poly(3-Alkylthiophene) and Its Derivatives. In *Handbook of Conducting Polymers. Second Edition. Revised and Expanded*; Skotheim, T.A., Elsenbaumer, R.L., Reynolds, J.R., Eds.; Marcel Dekker Inc.: New York, 1998 ISBN 0-8247-0050-3.
  33. Sato, M.A.; Tanaka, S.; Kaeriyama, K. Soluble Conducting Polythiophenes. *J. Chem. Soc. Chem. Commun.* **1986**, 873–874, doi:10.1039/C39860000873.
  34. Lin, J.W.-P.; Dudek, L.P. Synthesis and Properties of Poly(2,5-Thienylene). *J. Polym. Sci. Polym. Chem. Ed.* **1980**, *18*, 2869–2873, doi:10.1002/pol.1980.170180910.
  35. Yamamoto, T.; Sanechika, K.; Yamamoto, A. Preparation of Poly(2,4-Thienylene) and Comparison of Its Optical and Electrical Properties With Those of Poly(2,5-Thienylene). *Chem. Lett.* **1981**, *10*, 1079–1082, doi:10.1246/cl.1981.1079.
  36. Sanechika, K.; Yamamoto, T.; Yamamoto, A. Preparation of Copolymers Composed of 2,5-Thienylene and 2,4-Thienylene Units. Effect of Copolymer Composition on Electronic Spectrum, Electric Conductivity, and Chemical Properties. *J. Polym. Sci. Polym. Lett. Ed.*

- 1982**, 20, 365–371, doi:10.1002/pol.1982.130200703.
37. Yamamoto, T.; Sanechika, K.I.; Yamamoto, A. Preparation and Characterization of Poly(Thienylene)S. *Bull. Chem. Soc. Jpn.* **1983**, 56, 1497–1502.
  38. Elsenbaumer, R.L.; Jen, K.Y.; Oboodi, R. Processible and Environmentally Stable Conducting Polymers. *Synth. Met.* **1986**, 15, 169–174.
  39. Jen, K.-Y.; Miller, G.G.; Elsenbaumer, R.L. Highly Conducting, Soluble, and Environmentally-Stable Poly(3-Alkylthiophenes). *J. Chem. Soc., Chem. Commun.* **1986**, 17, 1346–1347, doi:10.1039/C39860001346.
  40. Kobayashi, M.; Chen, J.; Chung, T.-C.; Moraes, F.; Heeger, A.J.; Wudl, F. Synthesis and Properties of Chemically Coupled Poly(Thiophene). *Synth. Met.* **1984**, 9, 77–86, doi:10.1016/0379-6779(84)90044-4.
  41. Sato, M.A.; Morii, H. Nuclear Magnetic Resonance Studies on Electrochemically Prepared Poly(3-Dodecylthiophene). *Macromolecules* **1991**, 24, 1196–1200, doi:10.1021/ma00005a035.
  42. Jeffries-El, M.; McCullough, R.D. Regioregular Polythiophenes. In *Handbook of Conducting Polymers, Third Edition. Conjugated Polymers. Theory, Synthesis, Properties and Characterization*; Skotheim, T.A., Reynolds, J.R., Eds.; CRC Press: Boca Raton, 2007 ISBN 1-4200-4358-7.
  43. Osaka, I.; McCullough, R.D. Advanced Functional Regioregular Polythiophenes. In *Design and Synthesis of Conjugated Polymers*; Leclerc, M., Morin, J.-F., Eds.; WILEY-VCH Verlag GmbH & Co. KGaA: Weinheim, 2010 ISBN 978-3-527-32474-3.
  44. Perepichka, I.F.; Perepichka, D.F. *Handbook of Thiophene-Based Materials: Applications in Organic Electronics and Photonics*; John Wiley & Sons Ltd, 2009; ISBN 978-0-470-05732-2.
  45. Siringhaus, P.; Brown, P.J.; Friend, R.H.; Nielsem, M.M.; Bechgaard, K.; Langeveld-Voss, B.M.W.; Spiering, A.J.H.; Janssen, R.A.J.; Meijer, E.W.; Herwig, P.; et al. Two-Dimensional Charge Transport in Self-Organized, High-Mobility Conjugated Polymers. *Nature* **1999**, 401, 685–688, doi:10.1038/44359.
  46. Kawai, T.; Nakazono, M.; Sugimoto, R.; Yoshino, K. Crystal Structure of Poly(3-Alkylthiophene) and Its Doping Effect. *J. Phys. Soc. Jpn.* **1992**, 61, 3400–3406, doi:10.1143/JPSJ.61.3400.
  47. Mena-Osteritz, E.; Meyer, A.; Langeveld-Voss, B.M.W.; Janssen, R.A.J.; Meijer, E.W.; Bäuerle, P. Two-Dimensional Crystals of Poly(3-Alkylthiophene)s: Direct Visualization of Polymer Folds in Submolecular Resolution. *Angew. Chemie - Int. Ed.* **2000**, 39, 2679–2684, doi:10.1002/1521-3773(20000804)39:15<2679::aid-anie2679>3.0.co;2-2.
  48. Grevin, B.; Rannou, P.; Payerne, R.; Pron, A.; Travers, J.P. Multi-Scale Scanning Tunneling Microscopy Imaging of Self-Organized Regioregular Poly(3-Hexylthiophene) Films. *J. Chem. Phys.* **2003**, 118, 7097–7102, doi:10.1063/1.1561435.
  49. Zen, A.; Saphiannikova, M.; Neher, D.; Grenzer, J.; Grigorian, S.; Pietsch, U.; Asawapirom, U.; Janietz, S.; Scherf, U.; Lieberwirth, I.; et al. Effect of Molecular Weight on the Structure and Crystallinity of Poly(3-Hexylthiophene). *Macromolecules* **2006**, 39, 2162–2171, doi:10.1021/ma0521349.
  50. McCullough, R.D.; Lowe, R.D. Enhanced Electrical Conductivity in Regioselectively Synthesized Poly(3-Alkylthiophenes). *J. Chem. Soc. Chem. Commun.* **1992**, 70–72, doi:10.1039/C39920000070.
  51. McCullough, R.D.; Lowe, R.D.; Jayaraman, M.; Anderson, D.L. Design, Synthesis, and Control of Conducting Polymer Architectures: Structurally Homogeneous Poly(3-Alkylthiophenes). *J. Org. Chem.* **1993**, 58, 904–912, doi:10.1021/jo00056a024.
  52. McCullough, R.D.; Lowe, R.D.; Jayaraman, M.; Ewbank, P.C.; Anderson, D.L.; Tristram-Nagle, S. Synthesis and Physical Properties of Regiochemically Well-Defined, Head-to-Tail Coupled Poly(3-Alkylthiophenes). *Synth. Met.* **1993**, 55, 1198–1203, doi:10.1016/0379-

- 6779(93)90224-K.
53. McCullough, R.D.; Williams, S.P.; Tristram-Nagle, S.; Jayaraman, M.; Ewbank, P.C.; Miller, L. The First Synthesis and New Properties of Regioregular, Head-to-Tail Coupled Polythiophenes. *Synth. Met.* **1995**, *69*, 237–238, doi:10.1016/0379-6779(94)02449-9.
  54. Liu, J.; McCullough, R.D. End Group Modification of Regioregular Polythiophene through Postpolymerization Functionalization. *Macromolecules* **2002**, *35*, 9882–9889, doi:10.1021/ma021362p.
  55. Chen, T.; Rieke, R.D. The First Regioregular Head-to-Tail Poly(3-Hexylthiophene-2,5-Diyl) and a Regiorandom Isopolymer: Ni vs Pd Catalysis of 2(5)-Bromo-5(2)-(Bromozincio)-3-Hexylthiophene Polymerization. *J. Am. Chem. Soc.* **1992**, *114*, 10087–10088, doi:10.1021/ja00051a066.
  56. Chen, T.; Wu, X.; Rieke, R.D. Regiocontrolled Synthesis of Poly(3-Alkylthiophenes) Mediated by Rieke Zinc: Their Characterization and Solid-State Properties. *J. Am. Chem. Soc.* **1995**, *117*, 233–244, doi:10.1021/ja00106a027.
  57. Iraqi, A.; Barker, G.W. Synthesis and Characterisation of Telechelic Regioregular Head-to-Tail Poly(3-Alkylthiophenes). *J. Mater. Chem.* **1998**, *8*, 25–29, doi:10.1039/a706583c.
  58. Guillerez, S.; Bidan, G. New Convenient Synthesis of Highly Regioregular Poly(3-Octylthiophene) Based on the Suzuki Coupling Reaction. *Synth. Met.* **1998**, *93*, 123–126, doi:10.1016/s0379-6779(97)04102-7.
  59. Liversedge, I.A.; Higgins, S.J.; Giles, M.; Heeney, M.; McCulloch, I. Suzuki Route to Regioregular Polyalkylthiophenes Using Ir-Catalysed Borylation to Make the Monomer, and Pd Complexes of Bulky Phosphanes as Coupling Catalysts for Polymerisation. *Tetrahedron Lett.* **2006**, *47*, 5143–5146, doi:10.1016/j.tetlet.2006.05.063.
  60. Yokozawa, T.; Suzuki, R.; Nojima, M.; Ohta, Y.; Yokoyama, A. Precision Synthesis of Poly(3-Hexylthiophene) from Catalyst-Transfer Suzuki-Miyaura Coupling Polymerization. *Macromol. Rapid Commun.* **2011**, *32*, 801–806, doi:10.1002/marc.201100037.
  61. Loewe, R.S.; Khersonsky, S.M.; McCullough, R.D. A Simple Method to Prepare Head-to-Tail Coupled, Regioregular Poly(3-Alkylthiophenes) Using Grignard Metathesis. *Adv. Mater.* **1999**, *11*, 250–253, doi:10.1002/(SICI)1521-4095(199903)11:3<250::AID-ADMA250>3.0.CO;2-J.
  62. Loewe, R.S.; Ewbank, P.C.; Liu, J.; Zhai, L.; McCullough, R.D. Regioregular, Head-to-Tail Coupled Poly(3-Alkylthiophenes) Made Easy by the GRIM Method: Investigation of the Reaction and the Origin of Regioselectivity. *Macromolecules* **2001**, *34*, 4324–4333, doi:10.1021/ma001677+.
  63. Wang, Q.; Takita, R.; Kikuzaki, Y.; Ozawa, F. Palladium-Catalyzed Dehydrohalogenative Polycondensation of 2-Bromo-3-Hexylthiophene: An Efficient Approach to Head-to-Tail Poly(3-Hexylthiophene). *J. Am. Chem. Soc.* **2010**, *132*, 11420–11421, doi:10.1021/ja105767z.
  64. Pouliot, J.R.; Wakioka, M.; Ozawa, F.; Li, Y.; Leclerc, M. Structural Analysis of Poly(3-Hexylthiophene) Prepared via Direct Heteroarylation Polymerization. *Macromol. Chem. Phys.* **2016**, *217*, 1493–1500, doi:10.1002/macp.201600050.
  65. Sévignon, M.; Papillon, J.; Schulz, E.; Lemaire, M. New Synthetic Method for the Polymerization of Alkylthiophenes. *Tetrahedron Lett.* **1999**, *40*, 5873–5876, doi:10.1016/S0040-4039(99)01164-8.
  66. Sista, P.; Luscombe, C.K. Progress in the Synthesis of Poly(3-Hexylthiophene). *Adv. Polym. Sci.* **2014**, *265*, 1–38, doi:10.1007/12\_2014\_278.
  67. Echavarren, A.M.; Cardenas, D.J. Mechanistic Aspects of Metal-Catalyzed C,C- and C,X-Bond-Forming Reactions. In *Metal-Catalyzed Cross-Coupling Reactions. Second, Completely Revised and Enlarged Edition*; Meijere, A. de, Diederich, F., Eds.; WILEY-VCH Verlag GmbH & Co. KGaA: Weinheim, 2004; Vol. 1 ISBN 3-527-30518-1.
  68. Yokoyama, A.; Miyakoshi, R.; Yokozawa, T. Chain-Growth Polymerization for Poly(3-Hexylthiophene) with a Defined Molecular Weight and a Low Polydispersity.

- Macromolecules* **2004**, *37*, 1169–1171, doi:10.1021/ma035396o.
69. Sheina, E.E.; Liu, J.; Iovu, M.C.; Laird, D.W.; McCullough, R.D. Chain Growth Mechanism for the Regioregular Nickel Initiated Cross-Coupling Polymerisations. *Macromolecules* **2004**, *37*, 3526–3528, doi:10.1021/ma0357063.
  70. Iovu, M.C.; Sheina, E.E.; Gil, R.R.; McCullough, R.D. Experimental Evidence for the Quasi-"living" Nature of the Grignard Metathesis Method for the Synthesis of Regioregular Poly(S-Alkylthiophenes). *Macromolecules* **2005**, *38*, 8649–8656, doi:10.1021/ma051122k.
  71. Beryozkina, T.; Senkovskyy, V.; Kaul, E.; Kiriy, A. Kumada Catalyst-Transfer Polycondensation of Thiophene-Based Oligomers: Robustness of a Chain-Growth Mechanism. *Macromolecules* **2008**, *41*, 7817–7823, doi:10.1021/ma801660x.
  72. Achord, B.C.; Rawlins, J.W. Evidence of Ni(0) Complex Diffusion during Grignard Metathesis Polymerization of 2,5-Dibromo-3-Hexylthiophene. *Macromolecules* **2009**, *42*, 8634–8639, doi:10.1021/ma901644k.
  73. Boyd, S.D.; Jen, A.K.Y.; Luscombe, C.K. Steric Stabilization Effects in Nickel-Catalyzed Regioregular Poly(3-Hexylthiophene) Synthesis. *Macromolecules* **2009**, *42*, 9387–9389, doi:10.1021/ma902190p.
  74. Wang, Y.; Mills, A.A.; Euler, W.B.; Lucht, B.L. Effect of Residual Monomer on the Spectroscopic Properties of Polythiophenes. *Chem. Commun.* **2006**, 2121–2122, doi:10.1039/b600793g.
  75. Urien, M.; Wantz, G.; Cloutet, E.; Hirsch, L.; Tardy, P.; Vignau, L.; Cramail, H.; Parneix, J.P. Field-Effect Transistors Based on Poly(3-Hexylthiophene): Effect of Impurities. *Org. Electron.* **2007**, *8*, 727–734, doi:10.1016/j.orgel.2007.06.003.
  76. Trznadel, M.; Pron, A.; Zagorska, M.; Chrzaszcz, R.; Pielichowski, J. Effect of Molecular Weight on Spectroscopic and Spectroelectrochemical Properties of Regioregular Poly(3-Hexylthiophene). *Macromolecules* **1998**, *31*, 5051–5058, doi:10.1021/ma970627a.
  77. Liu, J.; Loewe, R.S.; McCullough, R.D. Employing MALDI-MS on Poly(Alkylthiophenes): Analysis of Molecular Weights, Molecular Weight Distributions, End-Group Structures, and End-Group Modifications. *Macromolecules* **1999**, *32*, 5777–5785, doi:10.1021/ma9905324.
  78. Liu, J.; Sheina, E.; Kowalewski, T.; McCullough, R.D. Tuning the Electrical Conductivity and Self-Assembly of Regioregular Polythiophene by Block Copolymerization: Nanowire Morphologies in New Di- and Triblock Copolymers. *Angew. Chemie Int. Ed.* **2002**, *41*, 329–332, doi:10.1002/1521-3773(20020118)41:2<329::AID-ANIE329>3.0.CO;2-M.
  79. Langeveld-voss, B.M.W.; Janssen, R.A.J.; Spiering, A.J.H.; Dongen, J.L.J. Van; Vonk, E.C.; Claessens, H.A. End-Group Modification of Regioregular Poly(3-Alkylthiophene)S. *Chem. Commun.* **2000**, 81–82, doi:10.1039/A908848B.
  80. Liu, J.; Tanaka, T.; Sivula, K.; Alivisatos, A.P.; Fre, J.M.J. Employing End-Functional Polythiophene To Control the Morphology of Nanocrystal - Polymer Composites in Hybrid Solar Cells. *J. Am. Chem. Soc.* **2004**, *126*, 6550–6551, doi:10.1021/ja0489184.
  81. Jeffries-EL, M.; Sauv e, G.; McCullough, R.D. In-Situ End-Group Functionalization of Regioregular Poly(3-Alkylthiophene) Using the Grignard Metathesis Polymerization Method. *Adv. Mater.* **2004**, *16*, 1017–1019, doi:10.1002/adma.200400137.
  82. Jeffries-EL, M.; Sauv e, G.; McCullough, R.D. Facile Synthesis of End-Functionalized Regioregular Poly (3-Alkylthiophene)s via Modified Grignard Metathesis Reaction. *Macromolecules* **2005**, *38*, 10348–10352, doi:10.1021/ma051096q.
  83. Iovu, M.C.; Jeffries-EL, M.; Sheina, E.E.; Cooper, J.R.; McCullough, R.D. Regioregular Poly(3-Alkylthiophene) Conducting Block Copolymers. *Polymer (Guildf)*. **2005**, *46*, 8582–8586, doi:10.1016/J.POLYMER.2005.05.035.
  84. Rudin, A.; Choi, P. *The Elements of Polymer Science and Engineering*; Third.; 2013; ISBN 9780123821782.
  85. Hadjichristidis, N.; Pitsikalis, M.; Iatrou, H.; Driva, P.; Chatzichristidi, M.; Sakellariou, G.; Lohse, D. Graft Copolymers. *Encycl. Polym. Sci. Technol.* 2011, *6*, 348–385.

86. Mitra, A.; Atwood, D.A. Polysiloxanes & Polysilanes. In *Encyclopedia of Inorganic Chemistry*; John Wiley & Sons, Ltd., 2006 ISBN 9780470862100.
87. Chruściel, J.J. Hydrosilyl-Functional Polysiloxanes: Synthesis, Reactions and Applications. In *Reactive and Functional Polymers. Volume One: Biopolymers, Polyesters, Polyurethanes, Resins and Silicones*; Gutiérrez, T.J., Ed.; Springer Cham, 2020; pp. 329–414 ISBN 978-3-030-43403-8.
88. Lavis, J.M.; Maleczka, R.E.; Chandrasekaran, V.; Collier, S.J. Poly(Methylhydrosiloxane). In *Encyclopedia of Reagents for Organic Synthesis Reagents for Organic Synthesis*; John Wiley & Sons, 2016 ISBN 9780470842898.
89. Moretto, H.-H.; Schulze, M.; Wagner, G. Silicones. In *Ullmann's Encyclopedia of Industrial Chemistry*; Wiley-VCH Verlag GmbH & Co. KGaA: Weinheim, 2012; pp. 675–712 ISBN 9783527306732.
90. Marciniak, B.; Gulinski, J.; Urbaniak, W.; Kornetka, Z.W. *Comprehensive Handbook on Hydrosilylation*; 1992; ISBN 9780080402727.
91. Bogdan Marciniak *Hydrosilylation. A Comprehensive Review on Recent Advances*; Springer, 2009; ISBN 9781402081712.
92. Speier, J.L.; Webster, J.A.; Barnes, G.H. The Addition of Silicon Hydrides to Olefinic Double Bonds. Part II. The Use of Group VIII Metal Catalysts. *J. Am. Chem. Soc.* **1957**, *79*, 974–979, doi:10.1021/ja01561a054.
93. Karstedt, B. Platinum Complexes of Unsaturated Siloxanes and Platinum Containing Organopolysiloxanes. *Gen. Electr. Company, U.S. Pat. No. 3775452A* 1973.
94. Troegel, D.; Stohrer, J. Recent Advances and Actual Challenges in Late Transition Metal Catalyzed Hydrosilylation of Olefins from an Industrial Point of View. *Coord. Chem. Rev.* **2011**, *255*, 1440–1459, doi:10.1016/j.ccr.2010.12.025.
95. Sakaki, S.; Mizoe, N.; Sugimoto, M. Theoretical Study of Platinum(0)-Catalyzed Hydrosilylation of Ethylene. Chalk-Harrod Mechanism or Modified Chalk-Harrod Mechanism. *Organometallics* **1998**, *17*, 2510–2523, doi:10.1021/om980190a.
96. Poyatos, M.; Maisse-François, A.; Bellemin-Lapponnaz, S.; Gade, L.H. Coordination Chemistry of a Modular N,C-Chelating Oxazole-Carbene Ligand and Its Applications in Hydrosilylation Catalysis. *Organometallics* **2006**, *25*, 2634–2641, doi:10.1021/om060166u.
97. Risangud, N.; Li, Z.; Anastasaki, A.; Wilson, P.; Kempe, K.; Haddleton, D.M. Hydrosilylation as an Efficient Tool for Polymer Synthesis and Modification with Methacrylates. *RSC Adv.* **2015**, *5*, 5879–5885, doi:10.1039/c4ra14956d.
98. Tsuchiya, K.; Ando, K.; Shimomura, T.; Ogino, K. Synthesis and Characterization of Poly(3-Hexylthiophene)-Block-Poly(Dimethylsiloxane) for Photovoltaic Application. *Polymer (Guildf)*. **2016**, *92*, 125–132, doi:10.1016/j.polymer.2016.03.092.
99. Hiorns, R.C.; Khoukh, A.; Gourdet, B.; Dagron-Lartigau, C. Extremely Regio-Regular Poly(3-Alkylthiophene)s from Simplified Chain-Growth Grignard Metathesis Polymerisations and the Modification of Their Chain-Ends. *Polym. Int.* **2006**, *55*, 608–620, doi:10.1002/pi.2013.
100. Kępska, K.; Jarosz, T.; Januskiewicz-Kaleniak, A.; Domagala, W.; Lapkowski, M.; Stolarczyk, A. Spectroelectrochemistry of Poly(3-Hexylthiophenes) in Solution. *Chem. Pap.* **2018**, *72*, 251–259, doi:10.1007/s11696-017-0277-6.
101. Iovu, M.C.; El, M.J.; Zhang, R.; Kowalewski, T.; McCullough, R.D. Conducting Block Copolymer Nanowires Containing Regioregular Poly(3-Hexylthiophene) and Polystyrene. *J. Macromol. Sci. Part A Pure Appl. Chem.* **2006**, *43*, 1991–2000, doi:10.1080/10601320600997906.
102. Iovu, M.C.; Craley, C.R.; Jeffries-EL, M.; Krankowski, A.B.; Zhang, R.; Kowalewski, T.; McCullough, R.D. Conducting Regioregular Polythiophene Block Copolymer Nanofibrils Synthesized by Reversible Addition Fragmentation Chain Transfer Polymerization (RAFT) and Nitroxide Mediated Polymerization (NMP). *Macromolecules* **2007**, *40*, 4733–4735, doi:10.1021/ma070406x.

103. Iovu, M.C.; Zhang, R.; Cooper, J.R.; Smilgies, D.M.; Javier, A.E.; Sheina, E.E.; Kowalewski, T.; Mccullough, R.D. Conducting Block Copolymers of Regioregular Poly(3-Hexylthiophene) and Poly(Methacrylates): Electronic Materials with Variable Conductivities and Degrees of Interfibrillar Order. *Macromol. Rapid Commun.* **2007**, *28*, 1816–1824, doi:10.1002/marc.200700401.
104. Dai, C.A.; Yen, W.C.; Lee, Y.H.; Ho, C.C.; Su, W.F. Facile Synthesis of Well-Defined Block Copolymers Containing Regioregular Poly(3-Hexyl Thiophene) via Anionic Macroinitiation Method and Their Self-Assembly Behavior. *J. Am. Chem. Soc.* **2007**, *129*, 11036–11038, doi:10.1021/ja0733991.
105. Craley, C.R.; Zhang, R.; Kowalewski, T.; Mccullough, R.D.; Stefan, M.C. Regioregular Poly(3-Hexylthiophene) in a Novel Conducting Amphiphilic Block Copolymer. *Macromol. Rapid Commun.* **2009**, *30*, 11–16, doi:10.1002/marc.200800487.
106. Higashihara, T.; Ueda, M. Synthesis and Characterization of a Novel Coil-Rod-Coil Triblock Copolymers Comprised of Regioregular Poly(3-Hexylthiophene) and Poly(Methyl Methacrylate) Segments. *React. Funct. Polym.* **2009**, *69*, 457–462, doi:10.1016/j.reactfunctpolym.2008.12.004.
107. Patra, S.K.; Ahmed, R.; Whittell, G.R.; Lunn, D.J.; Dunphy, E.L.; Winnik, M.A.; Manners, I. Cylindrical Micelles of Controlled Length with a  $\pi$ -Conjugated Polythiophene Core via Crystallization-Driven Self-Assembly. *J. Am. Chem. Soc.* **2011**, *133*, 8842–8845, doi:10.1021/ja202408w.
108. Radano, C.P.; Scherman, O.A.; Stingelin-stutzmann, N.; Mu, C.; Breiby, D.W.; Smith, P.; Janssen, A.J.; Meijer, E.W. Crystalline-Crystalline Block Copolymers of Regioregular Poly(3-Hexylthiophene) and Polyethylene by Ring-Opening Metathesis Polymerization. *J. Am. Chem. Soc.* **2005**, *127*, 12502–12503, doi:10.1021/ja054698y.
109. Alemseghed, M.G.; Gowrisanker, S.; Servello, J.; Stefan, M.C. Synthesis of Di-Block Copolymers Containing Regioregular Poly(3-Hexylthiophene) and Poly(Tetrahydrofuran) by a Combination of Grignard Metathesis and Cationic Polymerizations. *Macromol. Chem. Phys.* **2009**, *210*, 2007–2014, doi:10.1002/macp.200900262.
110. Alemseghed, M.G.; Servello, J.; Hundt, N.; Sista, P.; Biewer, C.; Stefan, M.C. Amphiphilic Block Copolymers Containing Regioregular Poly(3-Hexylthiophene) and Poly(2-Ethyl-2-Oxazoline). *Macromol. Chem. Phys.* **2010**, *211*, 1291–1297, doi:10.1002/macp.200900725.
111. Huang, K.; Fang, Y.; Hsu, J.; Kuo, C.; Chang, W.; Chen, W. Synthesis, Micellar Structures, and Multifunctional Sensory Properties of Poly(3-Hexylthiophene)-Block-Poly(2-(Dimethylamino)Ethyl Methacrylate) Rod-Coil Diblock Copolymers. *J. Polym. Sci. Part A Polym. Chem.* **2011**, *49*, 147–155, doi:10.1002/pola.24429.
112. Yang, H.; Xia, H.; Wang, G.; Peng, J.; Qiu, F. Insights into Poly(3-Hexylthiophene)-b-Poly(Ethylene Oxide) Block Copolymer: Synthesis and Solvent-Induced Structure Formation in Thin Films. *J. Polym. Sci. Part A Polym. Chem.* **2012**, *50*, 5060–5067, doi:10.1002/pola.26353.
113. Wu, Z.; Ono, R.J.; Chen, Z.; Bielawski, C.W. Synthesis of Poly(3-Alkylthiophene)-Block-Poly(Arylisocyanide): Two Sequential, Mechanistically Distinct Polymerizations Using a Single Catalyst. *J. Am. Chem. Soc.* **2010**, *132*, 14000–14001, doi:10.1021/ja106999q.
114. Zhang, Y.; Tajima, K.; Hashimoto, K. Nanostructure Formation in Poly(3-Hexylthiophene-Block-3-(2-Ethylhexyl)Thiophene)S. *Macromolecules* **2009**, *42*, 7008–7015, doi:10.1021/ma9013065.
115. Lee, E.; Hammer, B.; Kim, J.; Page, Z.; Emrick, T.; Ryan, C. Hierarchical Helical Assembly of Conjugated Poly(3-Hexylthiophene)-Block-Poly(3-Triethylene Glycol Thiophene) Diblock Copolymers. *J. Am. Chem. Soc.* **2011**, *133*, 10390–10393, doi:10.1021/ja2038547.
116. Pang, X.; Zhao, L.; Feng, C.; Lin, Z. Novel Amphiphilic Multiarm, Starlike Coil–Rod Diblock Copolymers via a Combination of Click Chemistry with Living Polymerization. *Macromolecules* **2011**, *44*, 7176–7183, doi:10.1021/ma201564t.
117. Pang, X.; Zhao, L.; Feng, C.; Wu, R.; Ma, H.; Lin, Z. Functional Copolymer Brushes

- Composed of a Hydrophobic Backbone and Densely Grafted Conjugated Side Chains via a Combination of Living Polymerization with Click Chemistry. *Polym. Chem.* **2013**, *4*, 2025–2032, doi:10.1039/c2py21124f.
118. Heinrich, C.D.; Thelakkat, M. Poly-(3-Hexylthiophene) Bottlebrush Copolymers with Tailored Side-Chain Lengths and High Charge Carrier Mobilities. *J. Mater. Chem. C* **2016**, *4*, 5370–5378, doi:10.1039/c6tc01029f.
  119. Ahn, S.K.; Pickel, D.L.; Kochemba, W.M.; Chen, J.; Uhrig, D.; Hinstrosa, J.P.; Carrillo, J.M.; Shao, M.; Do, C.; Messman, J.M.; et al. Poly(3-Hexylthiophene) Molecular Bottlebrushes via Ring-Opening Metathesis Polymerization: Macromolecular Architecture Enhanced Aggregation. *ACS Macro Lett.* **2013**, *2*, 761–765, doi:10.1021/mz4003563.
  120. Van As, D.; Subbiah, J.; Jones, D.J.; Wong, W.W.H. Controlled Synthesis of Well-Defined Semiconducting Brush Polymers. *Macromol. Chem. Phys.* **2016**, *217*, 403–413, doi:10.1002/macp.201500213.
  121. Obhi, N.K.; Jarrett-Wilkins, C.N.; Hicks, G.E.J.; Seferos, D.S. Self-Assembly of Poly(3-Hexylthiophene) Bottlebrush Polymers into End-On-End Linear Fiber Morphologies. *Macromolecules* **2020**, *53*, 8592–8599, doi:10.1021/acs.macromol.0c01641.
  122. Tran, H.M.; Nguyen, L.T.T.; Nguyen, T.H.; Nguyen, H.L.; Phan, N.T.S.; Zhang, G.; Yokozawa, T.; Tran, H. Le; Mai, P.T.; Nguyen, H.T. Efficient Synthesis of a Rod-Coil Conjugated Graft Copolymer by Combination of Thiol-Maleimide Chemistry and MOF-Catalyzed Photopolymerization. *Eur. Polym. J.* **2019**, *116*, 190–200, doi:10.1016/j.eurpolymj.2019.04.017.
  123. Wang, J.; Lu, C.; Mizobe, T.; Ueda, M.; Chen, W.C.; Higashihara, T. Synthesis and Characterization of All-Conjugated Graft Copolymers Comprised of n-Type or p-Type Backbones and Poly(3-Hexylthiophene) Side Chains. *Macromolecules* **2013**, *46*, 1783–1793, doi:10.1021/ma400043s.
  124. Steverlynck, J.; De Winter, J.; Gerbaux, P.; Lazzaroni, R.; Leclère, P.; Koeckelberghs, G. Influence of the Grafting Density on the Self-Assembly in Poly(Phenyleneethynylene)-g-Poly(3-Hexylthiophene) Graft Copolymers. *Macromolecules* **2015**, *48*, 8789–8796, doi:10.1021/acs.macromol.5b01830.
  125. Schiefer, D.; Hanselmann, R.; Sommer, M. All-Conjugated P3HT Donor PCDTBT Acceptor Graft Copolymers Synthesised: Via a Grafting through Approach. *Polym. Chem.* **2017**, *8*, 4368–4377, doi:10.1039/c7py00612h.
  126. Ahn, S.K.; Carrillo, J.M.Y.; Keum, J.K.; Chen, J.; Uhrig, D.; Lokitz, B.S.; Sumpter, B.G.; Michael Kilbey, S. Nanoporous Poly(3-Hexylthiophene) Thin Film Structures from Self-Organization of a Tunable Molecular Bottlebrush Scaffold. *Nanoscale* **2017**, *9*, 7071–7080, doi:10.1039/c7nr00015d.
  127. Jones, R.G.; Kahovec, J.; Stepto, R.; Wilks, E.S.; Hess, M.; Kitayama, T.; Metanowski, W.V. *Compendium of Polymer Terminology and Nomenclature*; The Royal Society of Chemistry: Cambridge, 2009; ISBN 9780854044917.
  128. Hanton, S.D. Mass Spectrometry of Polymers and Polymer Surfaces. *Chem. Rev.* **2001**, *101*, 527–569, doi:10.1021/cr9901081.
  129. Wong, M.; Hollinger, J.; Kozycz, L.M.; McCormick, T.M.; Lu, Y.; Burns, D.C.; Seferos, D.S. An Apparent Size-Exclusion Quantification Limit Reveals a Molecular Weight Limit in the Synthesis of Externally Initiated Polythiophenes. *ACS Macro Lett.* **2012**, *1*, 1266–1269, doi:10.1021/mz300333f.
  130. Dissanayake, D.S.; Sheina, E.; Biewer, M.C.; McCullough, R.D.; Stefan, M.C. Determination of Absolute Molecular Weight of Regioregular Poly(3-Hexylthiophene) by <sup>1</sup>H-NMR Analysis. *J. Polym. Sci. Part A Polym. Chem.* **2017**, *55*, 79–82, doi:10.1002/pola.28354.
  131. Holdcroft, S. Determination of Molecular Weights and Mark–Houwink Constants for Soluble Electronically Conducting Polymers. *J. Polym. Sci. Part B Polym. Phys.* **1991**, *29*, 1585–1588, doi:10.1002/polb.1991.090291303.



132. Yue, S.; Berry, G.C.; McCullough, R.D. Intermolecular Association and Supramolecular Organization in Dilute Solution. 1. Regioregular Poly(3-Dodecylthiophene). *Macromolecules* **1996**, *29*, 933–939, doi:10.1021/ma951008+.
133. Mao, H.; Xu, B.; Holdcroft, S. Structure-Property Relationships of Regioirregular Poly(3-Hexylthiophenes). *Macromolecules* **1993**, *26*, 1163–1169.
134. Barbarella, G.; Bongini, A.; Zambianchi, M. Regiochemistry and Conformation of Poly(3-Hexylthiophene) via the Synthesis and the Spectroscopic Characterization of the Model Configurational Triads. *Macromolecules* **1994**, *27*, 3039–3045, doi:10.1021/ma00089a022.
135. Mucci, A.; Schenetti, L. <sup>1</sup>H-<sup>13</sup>C NMR Inverse Detection of Poly(3-hexylthiophene): Characterization of the Structural Defects. *Macromol. Chem. Phys.* **1995**, *196*, 2687–2693, doi:10.1002/macp.1995.021960819.
136. Ferrari, M.; Mucci, A.; Schenetti, L. Complete Assignment of the Aliphatic Chains in Dimers, Trimers and Polymer of 3-Hexylthiophene through 2D-NMR Spectroscopy. *Magn. Reson. Chem.* **1995**, *33*, 657–663, doi:10.1002/mrc.1260330807.
137. Botta, C.; Stein, P.C.; Bolognesi, A.; Catellani, M.; Geng, Z. Spectroscopic Analysis of Structural Defects in Poly(3-Decylthiophene)s. Influence of the Polymerization Method. *J. Phys. Chem.* **1995**, *99*, 3331–3337, doi:10.1021/j100010a051.
138. Bras, J.; Pépin-Donat, B. <sup>1</sup>H and <sup>13</sup>C NMR Study of Regioregular Head-to-Tail Oligo(Octylthiophene)s and Poly(Octylthiophene). *Magn. Reson. Chem.* **2001**, *39*, 57–67, doi:10.1002/1097-458X(200102)39:2<57::AID-MRC799>3.0.CO;2-Q.
139. Senkovskyy, V.; Khanduyeva, N.; Komber, H.; Oertel, U.; Stamm, M.; Kuckling, D.; Kiriy, A. Conductive Polymer Brushes of Regioregular Head-to-Tail Poly(3-Alkylthiophenes) via Catalyst-Transfer Surface-Initiated Polycondensation. *J. Am. Chem. Soc.* **2007**, *129*, 6626–6632, doi:10.1021/ja0710306.
140. Kohn, P.; Huettner, S.; Komber, H.; Senkovskyy, V.; Tkachov, R.; Kiriy, A.; Friend, R.H.; Steiner, U.; Huck, W.T.S.; Sommer, J.U.; et al. On the Role of Single Regiodefects and Polydispersity in Regioregular Poly(3-Hexylthiophene): Defect Distribution, Synthesis of Defect-Free Chains, and a Simple Model for the Determination of Crystallinity. *J. Am. Chem. Soc.* **2012**, *134*, 4790–4805, doi:10.1021/ja210871j.
141. Davletbaev, R.S.; Zaripov, I.I.; Faizulina, Z.Z.; Davletbaeva, I.M.; Domrachova, D.S.; Gumerov, A.M. Synthesis and Characterization of Amphiphilic Branched Silica Derivatives Associated with Oligomeric Medium. *RSC Adv.* **2019**, *9*, 21233–21242, doi:10.1039/c9ra03683k.
142. Deriabin, K. V.; Dobrynin, M. V.; Islamova, R.M. A Metal-Free Radical Technique for Cross-Linking of Polymethylhydrosiloxane or Polymethylvinylsiloxane Using AIBN. *Dalt. Trans.* **2020**, *49*, 8855–8858, doi:10.1039/d0dt01061h.
143. Cancouët, P.; Daudet, E.; Héлары, G.; Moreau, M.; Sauvet, G. Functional Polysiloxanes. I. Microstructure of Poly(Hydrogenmethylsiloxane-Co-Dimethylsiloxane)s Obtained by Cationic Copolymerization. *J. Polym. Sci. Part A Polym. Chem.* **2000**, *38*, 826–836, doi:10.1002/(SICI)1099-0518(20000301)38:5<826::AID-POLA7>3.0.CO;2-9.
144. Saxena, A.; Markanday, M.; Sarkar, A.; Yadav, V.K.; Brar, A.S. A Systematic Approach to Decipher the Microstructure of Methyl Hydrosiloxane Copolymers and Its Impact on Their Reactivity Trends. *Macromolecules* **2011**, *44*, 6480–6487, doi:10.1021/ma201195c.
145. Skoog, D.A.; Holler, F.J.; Crouch, S.R. *Principles of Instrumental Analysis. Seventh Edition*; Skoog, D.A., Holler, F.J., Crouch, S.R., Eds.; 7th ed.; Cengage Learning: Boston, 2018; ISBN 978-1-305-57721-3.
146. Mazurkiewicz, R.; Salwińska, E. Spektroskopia w Podczerwieni. In *Metody spektroskopowe i ich zastosowanie do identyfikacji związków organicznych: praca zbiorowa*; Rajca, A., Zieliński, W., Eds.; Wydawnictwa Naukowo-Techniczne: Warszawa, 2000 ISBN 8320424798.
147. Hotta, S.; Rughooputh, S.D.D.V.; Heeger, A.J.; Wudl, F. Spectroscopic Studies of Soluble

- Poly(3-Alkylthienylenes). *Macromolecules* **1987**, *20*, 212–215, doi:10.1021/ma00167a038.
148. Wright, N.; Hunter, M.J. Organosilicon Polymers. III. Infrared Spectra of the Methylpolysiloxanes. *J. Am. Chem. Soc.* **1947**, *69*, 803–809, doi:10.1021/ja01196a018.
  149. Smith, A.L.; Anderson, D.R. Vibrational Spectra of Me<sub>2</sub>SiCl<sub>2</sub>, Me<sub>3</sub>SiCl, Me<sub>3</sub>SiOSiMe<sub>3</sub>, (Me<sub>2</sub>SiO)<sub>3</sub>, (Me<sub>2</sub>SiO)<sub>4</sub>, (Me<sub>2</sub>SiO)<sub>x</sub>, and Their Deuterated Analogs. *Appl. Spectrosc.* **1984**, *38*, 822–834, doi:10.1366/0003702844554549.
  150. Socrates, G. *Infrared and Raman Characteristic Group Frequencies. Tables and Charts*; Third Edit.; Chichester, 2001; ISBN 0 470 09307 2.
  151. Richards, R.E.; Thompsom, H.W. Infra-Red Spectra of Compounds of High Molecular Weight. Part IV. Silicones and Related Compounds. *J. Chem. Soc.* **1949**, 124–132, doi:10.1039/JR9490000124.
  152. Smith, A.L. Infrared Spectra-Structure Correlations for Organosilicon Compounds. *Spectrochim. Acta* **1960**, *16*, 87–105, doi:10.1016/0371-1951(60)80074-4.
  153. Bellamy, L.J. Organosilicon Compounds. In *The Infra-red Spectra of Complex Molecules*; Chapman and Hall: London, 1975; pp. 374–392 ISBN 978-94-011-6017-9.
  154. Smith, A.L.; McHard, J.A. Spectroscopic Techniques for Identification of Organosilicon Compounds. *Anal. Chem.* **1959**, *31*, 1174–1179, doi:10.1021/ac60151a029.
  155. Ehhalt, D.; Prather, M.; Dentener, F.; Derwent, R.; Dlugokencky, E.; Holland, E.; Isaksen, I.; Katima, J.; Kirchhoff, V.; Matson, P.; et al. Atmospheric Chemistry and Greenhouse Gases. In *Climate Change 2001: The Scientific Basis*; Houghton, J.T., Ding, Y., Griggs, D.J., Noguer, N., Linden, P.J. van der, Xiaosu, D., Maskell, K., Johnson, C.A., Eds.; CAMBRIDGE UNIVERSITY PRESS: New York, 2001; pp. 239–287 ISBN 0521-01495-6.
  156. *WHO Global Air Quality Guidelines. Particulate Matter (PM<sub>2.5</sub> and PM<sub>10</sub>), Ozone, Nitrogen Dioxide, Sulfur Dioxide and Carbon Monoxide*; World Health Organization: Geneva, 2021; ISBN 9789240034228.
  157. Chen, T.M.; Gokhale, J.; Shofer, S.; Kuschner, W.G. Outdoor Air Pollution: Nitrogen Dioxide, Sulfur Dioxide, and Carbon Monoxide Health Effects. *Am. J. Med. Sci.* **2007**, *333*, 249–256, doi:10.1097/MAJ.0b013e31803b900f.
  158. Hesterberg, T.W.; Bunn, W.B.; McClellan, R.O.; Hamade, A.K.; Long, C.M.; Valberg, P.A. Critical Review of the Human Data on Short-Term Nitrogen Dioxide (NO<sub>2</sub>) Exposures: Evidence for NO<sub>2</sub> No-Effect Levels. *Crit. Rev. Toxicol.* **2009**, *39*, 743–781, doi:10.3109/10408440903294945.
  159. Huangfu, P.; Atkinson, R. Long-Term Exposure to NO<sub>2</sub> and O<sub>3</sub> and All-Cause and Respiratory Mortality: A Systematic Review and Meta-Analysis. *Environ. Int.* **2020**, *144*, 105998, doi:10.1016/j.envint.2020.105998.
  160. Fine, G.F.; Cavanagh, L.M.; Afonja, A.; Binions, R. Metal Oxide Semi-Conductor Gas Sensors in Environmental Monitoring. *Sensors* **2010**, *10*, 5469–5502, doi:10.3390/s100605469.
  161. Li, Q.; Zeng, W.; Li, Y. Metal Oxide Gas Sensors for Detecting NO<sub>2</sub> in Industrial Exhaust Gas: Recent Developments. *Sensors Actuators B Chem.* **2022**, *359*, 131579, doi:10.1016/j.snb.2022.131579.
  162. Kim, B.J.; Song, I.G.; Kim, J.S. In<sub>2</sub>O<sub>3</sub>-Based Micro Gas Sensor for Detecting NO<sub>x</sub> Gases. *Electron. Mater. Lett.* **2014**, *10*, 509–513, doi:10.1007/s13391-013-3133-z.
  163. Wales, D.J.; Grand, J.; Ting, V.P.; Burke, R.D.; Edler, K.J.; Bowen, C.R.; Mintova, S.; Burrows, A.D. Gas Sensing Using Porous Materials for Automotive Applications. *Chem. Soc. Rev.* **2015**, *44*, 4290–4321, doi:10.1039/c5cs00040h.
  164. Cui, H.; Zheng, K.; Xie, Z.; Yu, J.; Zhu, X.; Ren, H.; Wang, Z.; Zhang, F.; Li, X.; Tao, L.Q.; et al. Tellurene Nanoflake-Based NO<sub>2</sub>sensors with Superior Sensitivity and a Sub-Parts-per-Billion Detection Limit. *ACS Appl. Mater. Interfaces* **2020**, *12*, 47704–47713, doi:10.1021/acsami.0c15964.
  165. Procek, M.; Stolarczyk, A.; Pustelny, T.; Maciak, E. A Study of a QCM Sensor Based on TiO<sub>2</sub>

- Nanostructures for the Detection of NO<sub>2</sub> and Explosives Vapours in Air. *Sensors* **2015**, *15*, 9563–9581, doi:10.3390/s150409563.
166. Lebel, E.D.; Finnegan, C.J.; Ouyang, Z.; Jackson, R.B. Methane and NO<sub>x</sub> Emissions from Natural Gas Stoves, Cooktops, and Ovens in Residential Homes. *Environ. Sci. Technol.* **2022**, *56*, 2529–2539, doi:10.1021/acs.est.1c04707.
  167. Nikolic, M.V.; Milovanovic, V.; Vasiljevic, Z.Z.; Stamenkovic, Z. Semiconductor Gas Sensors: Materials, Technology, Design, and Application. *Sensors (Switzerland)* **2020**, *20*, 1–31, doi:10.3390/s20226694.
  168. Zhang, Y.; Kim, J.J.; Chen, D.; Tuller, H.L.; Rutledge, G.C. Electrospun Polyaniline Fibers as Highly Sensitive Room Temperature Chemiresistive Sensors for Ammonia and Nitrogen Dioxide Gases. *Adv. Funct. Mater.* **2014**, *24*, 4005–4014, doi:10.1002/adfm.201400185.
  169. Navale, S.T.; Mane, A.T.; Khuspe, G.D.; Chougule, M.A.; Patil, V.B. Room Temperature NO<sub>2</sub> Sensing Properties of Polythiophene Films. *Synth. Met.* **2014**, *195*, 228–233, doi:10.1016/j.synthmet.2014.06.017.
  170. Navale, S.T.; Mane, A.T.; Chougule, M.A.; Sakhare, R.D.; Nalage, S.R.; Patil, V.B. Highly Selective and Sensitive Room Temperature NO<sub>2</sub> Gas Sensor Based on Polypyrrole Thin Films. *Synth. Met.* **2014**, *189*, 94–99, doi:10.1016/j.synthmet.2014.01.002.
  171. Bai, S.; Guo, J.; Sun, J.; Tang, P.; Chen, A.; Luo, R.; Li, D. Enhancement of NO<sub>2</sub>-Sensing Performance at Room Temperature by Graphene-Modified Polythiophene. *Ind. Eng. Chem. Res.* **2016**, *55*, 5788–5794, doi:10.1021/acs.iecr.6b00418.
  172. Han, S.; Yang, Z.; Li, Z.; Zhuang, X.; Akinwande, D.; Yu, J. Improved Room Temperature NO<sub>2</sub> Sensing Performance of Organic Field-Effect Transistor by Directly Blending a Hole-Transporting/Electron-Blocking Polymer into the Active Layer. *ACS Appl. Mater. Interfaces* **2018**, *10*, 38280–38286, doi:10.1021/acsami.8b07838.
  173. Yang, Z.; Han, S.; Liu, Y.; Zhuang, X.; Akinwande, D.; Yu, J. Investigation of the Atmosphere Influence on Device Characteristics and NO<sub>2</sub> Sensing Performance of Organic Field-Effect Transistors Consisting of Polymer Bulk Heterojunction. *Org. Electron.* **2018**, *62*, 114–120, doi:10.1016/j.orgel.2018.07.023.
  174. Kumar, C.; Rawat, G.; Kumar, H.; Kumar, Y.; Ratan, S.; Prakash, R.; Jit, S. Poly (3,3'''-Dialkylquaterthiophene) Based Flexible Nitrogen Dioxide Gas Sensor. *IEEE Sensors Lett.* **2018**, *2*, 10–13, doi:10.1109/LESENS.2018.2799851.
  175. Fan, H.; Li, H.; Han, J.; McKeever, N.; Yu, J.; Katz, H.E. A Humid-Air-Operable, NO<sub>2</sub>-Responsive Polymer Transistor Series Circuit with Improved Signal-to-Drift Ratio Based on Polymer Semiconductor Oxidation. *ACS Sensors* **2019**, *4*, 3240–3247, doi:10.1021/acssensors.9b01751.
  176. Yang, Z.; Zhuang, X.; Han, S.; Yu, J. Hole-Transporting Polymer Dilution Driven High Performance Organic Transistor-Based NO<sub>2</sub> Gas Sensor. *Mater. Lett.* **2019**, *236*, 285–288, doi:10.1016/j.matlet.2018.10.121.
  177. Hou, S.; Yu, J.; Zhuang, X.; Li, D.; Liu, Y.; Gao, Z.; Sun, T.; Wang, F.; Yu, X. Phase Separation of P3HT/PMMA Blend Film for Forming Semiconducting and Dielectric Layers in Organic Thin-Film Transistors for High-Sensitivity NO<sub>2</sub> Detection. *ACS Appl. Mater. Interfaces* **2019**, *11*, 44521–44527, doi:10.1021/acsami.9b15651.
  178. Mukhopadhyaya, T.; Wagner, J.S.; Fan, H.; Katz, H.E. Design and Synthesis of Air-Stable p-Channel-Conjugated Polymers for High Signal-to-Drift Nitrogen Dioxide and Ammonia Sensing. *ACS Appl. Mater. Interfaces* **2020**, *12*, 21974–21984, doi:10.1021/acsami.0c04810.
  179. Liang, J.; Song, Z.; Wang, S.; Zhao, X.; Tong, Y.; Ren, H.; Guo, S.; Tang, Q.; Liu, Y. Cobweb-like, Ultrathin Porous Polymer Films for Ultrasensitive NO<sub>2</sub> Detection. *ACS Appl. Mater. Interfaces* **2020**, *12*, 52992–53002, doi:10.1021/acsami.0c09821.
  180. Zhang, X.; Wang, B.; Huang, L.; Huang, W.; Wang, Z.; Zhu, W.; Chen, Y.; Mao, Y.L.; Facchetti, A.; Marks, T.J. Breath Figure-Derived Porous Semiconducting Films for Organic Electronics. *Sci. Adv.* **2020**, *6*, 1–9, doi:10.1126/sciadv.aaz1042.

181. Sahu, P.K.; Pandey, R.K.; Dwivedi, R.; Mishra, V.N.; Prakash, R. Polymer/Graphene Oxide Nanocomposite Thin Film for NO<sub>2</sub> Sensor: An in Situ Investigation of Electronic, Morphological, Structural, and Spectroscopic Properties. *Sci. Rep.* **2020**, *10*, 1–13, doi:10.1038/s41598-020-59726-5.
182. Yang, K.; Yuan, W.; Hua, Z.; Tang, Y.; Yin, F.; Xia, D. Triazine-Based Two-Dimensional Organic Polymer for Selective NO<sub>2</sub> Sensing with Excellent Performance. *ACS Appl. Mater. Interfaces* **2020**, *12*, 3919–3927, doi:10.1021/acsami.9b17450.
183. Zhao, S.; Hou, S.; Fan, H.; Wang, Z.; Yu, J. High Performance Nitrogen Dioxide Sensor Based on Organic Thin-Film Transistor Utilizing P3HT/OH-MWCNTs Blend Film. *Synth. Met.* **2020**, *269*, 116569, doi:10.1016/j.synthmet.2020.116569.
184. Guettiche, D.; Mekki, A.; Lilia, B.; Fatma-Zohra, T.; Boudjellal, A. *Flexible Chemiresistive Nitrogen Oxide Sensors Based on a Nanocomposite of Polypyrrole-Reduced Graphene Oxide-Functionalized Carboxybenzene Diazonium Salts*; 2021; Vol. 32; ISBN 0000000295796.
185. Gao, L.; Liu, C.; Peng, Y.; Deng, J.; Hou, S.; Cheng, Y.; Huang, W.; Yu, J. Ultrasensitive Flexible NO<sub>2</sub> Gas Sensors via Multilayer Porous Polymer Film. *Sensors Actuators B Chem.* **2022**, *368*, 132113, doi:10.1016/j.snb.2022.132113.
186. *Statistical Review of World Energy 2024*; 73 rd ed.; Energy Institute, 2024; ISBN 978-1-78725-408-4.
187. Sugie, A.; Nakano, K.; Tajima, K.; Osaka, I.; Yoshida, H. Dependence of Exciton Binding Energy on Bandgap of Organic Semiconductors. *J. Phys. Chem. Lett.* **2023**, *14*, 11412–11420, doi:10.1021/acs.jpcclett.3c02863.
188. Menke, S.M.; Ran, N.A.; Bazan, G.C.; Friend, R.H. Understanding Energy Loss in Organic Solar Cells: Toward a New Efficiency Regime. *Joule* **2018**, *2*, 25–35, doi:10.1016/j.joule.2017.09.020.
189. Hoppe, H.; Sariciftci, N.S. Organic Solar Cells: An Overview. *J. Mater. Res.* **2004**, *19*, 1924–1945, doi:10.1557/JMR.2004.0252.
190. Brabec, C.J.; Gowrisanker, S.; Halls, J.J.M.; Laird, D.; Jia, S.; Williams, S.P. Polymer-Fullerene Bulk-Heterojunction Solar Cells. *Adv. Mater.* **2010**, *22*, 3839–3856, doi:10.1002/adma.200903697.
191. Brabec, C.J.; Shaheen, S.E.; Winder, C.; Sariciftci, N.S.; Denk, P. Effect of LiF/Metal Electrodes on the Performance of Plastic Solar Cells. *Appl. Phys. Lett.* **2002**, *80*, 1288–1290, doi:10.1063/1.1446988.
192. Berger, P.R.; Kim, M. Polymer Solar Cells: P3HT:PCBM and Beyond. *J. Renew. Sustain. Energy* **2018**, *10*, 013508, doi:10.1063/1.5012992.
193. Gueymard, C.A.; Myers, D.; Emery, K. Proposed Reference Irradiance Spectra for Solar Energy Systems Testing. *Sol. Energy* **2002**, *73*, 443–467, doi:10.1016/S0038-092X(03)00005-7.
194. Cowan, S.R.; Roy, A.; Heeger, A.J. Recombination in Polymer-Fullerene Bulk Heterojunction Solar Cells. *Phys. Rev. B - Condens. Matter Mater. Phys.* **2010**, *82*, 245207, doi:10.1103/PhysRevB.82.245207.
195. Heeger, A.J. 25th Anniversary Article: Bulk Heterojunction Solar Cells: Understanding the Mechanism of Operation. *Adv. Mater.* **2014**, *26*, 10–28, doi:10.1002/adma.201304373.
196. Ma, W.; Yang, C.; Gong, X.; Lee, K.; Heeger, A.J. Thermally Stable, Efficient Polymer Solar Cells with Nanoscale Control of the Interpenetrating Network Morphology. *Adv. Funct. Mater.* **2005**, *15*, 1617–1622, doi:10.1002/adfm.200500211.
197. Moon, J.S.; Lee, J.K.; Cho, S.; Byun, J.; Heeger, A.J. “Columnlike” Structure of the Cross-Sectional Morphology of Bulk Heterojunction Materials. *Nano Lett.* **2009**, *9*, 230–234, doi:10.1021/nl802821h.
198. Padinger, F.; Rittberger, R.S.; Sariciftci, N.S. Effects of Postproduction Treatment on Plastic Solar Cells. *Adv. Funct. Mater.* **2003**, *13*, 85–88, doi:10.1002/adfm.200390011.
199. Fan, X.; Fang, G.J.; Qin, P.L.; Cheng, F.; Zhao, X.Z. Rapid Phase Segregation of

- P3HT:PCBM Composites by Thermal Annealing for High-Performance Bulk-Heterojunction Solar Cells. *Appl. Phys. A Mater. Sci. Process.* **2011**, *105*, 1003–1009, doi:10.1007/s00339-011-6533-7.
200. Gu, Z.; Kanto, T.; Tsuchiya, K.; Ogino, K. Synthesis of Poly(3-Hexylthiophene)-b-Poly(Ethylene Oxide) for Application to Photovoltaic Device. *J. Photopolym. Sci. Technol.* **2010**, *23*, 405–406, doi:10.2494/photopolymer.23.405.
  201. Gu, Z.; Kanto, T.; Tsuchiya, K.; Shimomura, T.; Ogino, K. Annealing Effect on Performance and Morphology of Photovoltaic Devices Based on Poly(3-Hexylthiophene)-b-Poly(Ethylene Oxide). *J. Polym. Sci. Part A Polym. Chem.* **2011**, *49*, 2645–2652, doi:10.1002/pola.24696.
  202. Chen, J.; Yu, X.; Hong, K.; Messman, J.M.; Pickel, D.L.; Xiao, K.; Dadmun, M.D.; Mays, J.W.; Rondinone, A.J.; Sumpter, B.G.; et al. Ternary Behavior and Systematic Nanoscale Manipulation of Domain Structures in P3HT/PCBM/P3HT-b-PEO Films. *J. Mater. Chem.* **2012**, *22*, 13013–13022, doi:10.1039/c2jm31124k.
  203. Yang, C.; Lee, J.K.; Heeger, A.J.; Wudl, F. Well-Defined Donor-Acceptor Rod-Coil Diblock Copolymers Based on P3HT Containing C60: The Morphology and Role as a Surfactant in Bulk-Heterojunction Solar Cells. *J. Mater. Chem.* **2009**, *19*, 5416–5423, doi:10.1039/b901732a.
  204. Sun, Z.; Xiao, K.; Keum, J.K.; Yu, X.; Hong, K.; Browning, J.; Ivanov, I.N.; Chen, J.; Alonzo, J.; Li, D.; et al. PS-b-P3HT Copolymers as P3HT/PCBM Interfacial Compatibilizers for High Efficiency Photovoltaics. *Adv. Mater.* **2011**, *23*, 5529–5535, doi:10.1002/adma.201103361.
  205. Gu, Z.; Tan, Y.; Tsuchiya, K.; Shimomura, T.; Ogino, K. Synthesis and Characterization of Poly(3-Hexylthiophene)-b-Polystyrene for Photovoltaic Application. *Polymers (Basel)*. **2011**, *3*, 558–570, doi:10.3390/polym3010558.
  206. Tsai, J.H.; Lai, Y.C.; Higashihara, T.; Lin, C.J.; Ueda, M.; Chen, W.C. Enhancement of P3HT/PCBM Photovoltaic Efficiency Using the Surfactant of Triblock Copolymer Containing Poly(3-Hexylthiophene) and Poly(4-Vinyltriphenylamine) Segments. *Macromolecules* **2010**, *43*, 6085–6091, doi:10.1021/ma1011182.
  207. Cheng, Y.J.; Hsieh, C.H.; Li, P.J.; Hsu, C.S. Morphological Stabilization by in Situ Polymerization of Fullerene Derivatives Leading to Efficient, Thermally Stable Organic Photovoltaics. *Adv. Funct. Mater.* **2011**, *21*, 1723–1732, doi:10.1002/adfm.201002502.
  208. Deribew, D.; Pavlopoulou, E.; Fleury, G.; Nicolet, C.; Renaud, C.; Mougner, S.J.; Vignau, L.; Cloutet, E.; Brochon, C.; Cousin, F.; et al. Crystallization-Driven Enhancement in Photovoltaic Performance through Block Copolymer Incorporation into P3HT:PCBM Blends. *Macromolecules* **2013**, *46*, 3015–3024, doi:10.1021/ma302128h.
  209. Yamakawa, S.; Tajima, K.; Hashimoto, K. Buffer Layer Formation in Organic Photovoltaic Cells by Self-Organization of Poly(Dimethylsiloxane)S. *Org. Electron.* **2009**, *10*, 511–514, doi:10.1016/j.orgel.2008.12.014.
  210. Wu, Q.; Bhattacharya, M.; Morgan, S.E. POSS-Enhanced Phase Separation in Air-Processed P3HT:PCBM Bulk Heterojunction Photovoltaic Systems. *ACS Appl. Mater. Interfaces* **2013**, *5*, 6136–6146, doi:10.1021/am4010489.
  211. Hwang, H.S.; Khang, D.Y. Charge-Carrier Selective Electrodes for Organic Bulk Heterojunction Solar Cell by Contact-Printed Siloxane Oligomers. *Thin Solid Films* **2015**, *589*, 125–132, doi:10.1016/j.tsf.2015.05.011.
  212. Senkovskyy, V.; Tkachov, R.; Beryozkina, T.; Komber, H.; Oertel, U.; Horecha, M.; Bocharova, V.; Stamm, M.; Gevorgyan, S.A.; Krebs, F.C.; et al. “Hairy” Poly(3-Hexylthiophene) Particles Prepared via Surface-Initiated Kumada Catalyst-Transfer Polycondensation. *J. Am. Chem. Soc.* **2009**, *131*, 16445–16453, doi:10.1021/ja904885w.
  213. Rathnayake, H.; Wright, N.; Patel, A.; Binion, J.; McNamara, L.E.; Scardino, D.J.; Hammer, N.I. Synthesis and Characterization of Poly(3-Hexylthiophene)-Functionalized Siloxane Nanoparticles. *Nanoscale* **2013**, *5*, 3212–3215, doi:10.1039/c3nr34249b.
  214. Sugimoto, R.; Takeda, S.; Gu, H.B.; Yoshino, K. Preparation of Soluble Polythiophene

- Derivatives Utilizing Transition Metal Halides as Catalysts and Their Property. *Chem. Express* **1986**, *1*, 635–638.
215. Niemi, V.M.; Knuuttila, P.; Österholm, J.-E.; Korvola, J. Polymerization of 3-Alkylthiophenes with FeCl<sub>3</sub>. *Polymer (Guildf)*. **1992**, *33*, 1559–1562, doi:10.1016/0032-3861(92)90138-M.
  216. Girolamo, J. De; Reiss, P.; Pron, A. Supramolecularly Assembled Hybrid Materials via Molecular Recognition between Diaminopyrimidine-Functionalized Poly (Hexylthiophene) and Thymine-Capped CdSe Nanocrystals Supp Info. *J. Phys. Chem. C* **2007**, *111*, 14681–14688, doi:10.1002/sml.
  217. Boudouris, B.W.; Frisbie, C.D.; Hillmyer, M.A. Nanoporous Poly(3-Alkylthiophene) Thin Films Generated from Block Copolymer Templates. *Macromolecules* **2008**, *41*, 67–75, doi:10.1021/ma071626d.
  218. Cheng, X.; Dong, X.; Huang, R.; Zeng, X.; Ungar, G.; Prehm, M.; Tschierske, C. Polygonal Cylinder Phases of 3-Alkyl-2,5-Diphenylthiophene-Based Bolaamphiphiles: Changing Symmetry by Retaining Net Topology. *Chem. Mater.* **2008**, *20*, 4729–4738, doi:10.1021/cm800509u.
  219. The National Institute of Advanced Industrial Science and Technology (AIST): Spectral Database for Organic Compounds (SDBS) 3-Hexylthiophene Available online: <https://sdb.sdb.aist.go.jp/sdb/cgi-bin/landingpage?sdbno=19017> (accessed on 2 April 2022).
  220. Leclerc, M.; Diaz, F.M.; Wegner, G. Structural Analysis of Poly(3-Alkylthiophene)S. *Makromol. Chemie* **1989**, *190*, 3105–3114, doi:10.1002/macp.1989.021901208.
  221. Mao, H.; Holdcroft, S. Grignard Synthesis of  $\pi$ -Conjugated Poly(3-Alkylthiophenes): Controlling Molecular Weights and the Nature of Terminal Units. *Macromolecules* **1992**, *25*, 554–558, doi:10.1021/ma00028a010.
  222. Verswyvel, M.; Monnaie, F.; Koeckelberghs, G. AB Block Copoly(3-Alkylthiophenes): Synthesis and Chiroptical Behavior. *Macromolecules* **2011**, *44*, 9489–9498, doi:10.1021/ma2021503.
  223. Xu, J.; Wang, J.; Mitchell, M.; Mukherjee, P.; Jeffries-El, M.; Petrich, J.W.; Lin, Z. Organic-Inorganic Nanocomposites via Directly Grafting Conjugated Polymers onto Quantum Dots. *J. Am. Chem. Soc.* **2007**, *129*, 12828–12833, doi:10.1021/ja074133x.
  224. Skibiński, A.; Rajca, A.; Bieg, T.; Salwińska, E.; Mazurkiewicz, R.; Zieliński, W.; Suwiński, J. *Metody Spektroskopowe i Spektrometria Mas w Zastosowaniu Do Identyfikacji Związków Organicznych: Praca Zbiorowa. T. 2, Tabele Korelacyjne*; Zieliński, W., Rajca, A., Eds.; Wydawnictwo Politechniki Śląskiej: Gliwice, 2018; ISBN 9788378805113.
  225. Kaplan, L. The Infrared Spectra of Tripropylsilane, Triphenylsilane and Triphenyldeuteriosilane. *J. Am. Chem. Soc.* **1954**, *76*, 5880–5882, doi:10.1021/ja01651a105.
  226. Li, J.; Peng, J.; Zhang, G.; Bai, Y.; Lai, G.; Li, X. Hydrosilylation Catalysed by a Rhodium Complex in a Supercritical CO<sub>2</sub>/Ionic Liquid System. *New J. Chem.* **2010**, *34*, 1330–1334, doi:10.1039/c0nj00012d.
  227. Safa, K.D.; Tofangdarzadeh, S.; Hassanpour, A. Facile Route to Synthesis of Functionalised Poly(Methylalkoxy)Siloxane under Mild and Aerobic Conditions in the Presence of Platinum Catalysts. *J. Organomet. Chem.* **2009**, *694*, 4107–4115, doi:10.1016/j.jorganchem.2009.08.018.
  228. Stiubianu, G.; Racles, C.; Cazacu, M.; Simionescu, B.C. Silicone-Modified Cellulose. Crosslinking of Cellulose Acetate with Poly[Dimethyl(Methyl-H)Siloxane] by Pt-Catalyzed Dehydrogenative Coupling. *J. Mater. Sci.* **2010**, *45*, 4141–4150, doi:10.1007/s10853-010-4503-7.
  229. Stein, J.; Lewis, L.N.; Gao, Y.; Scott, R.A. In Situ Determination of the Active Catalyst in Hydrosilylation Reactions Using Highly Reactive Pt(0) Catalyst Precursors. *J. Am. Chem. Soc.* **1999**, *121*, 3693–3703, doi:10.1021/ja9825377.
  230. Jarosz, T.; Kępska, K.; Ledwon, P.; Procek, M.; Domagała, W.; Stolarczyk, A. Poly(3-

- Hexylthiophene) Grafting and Molecular Dilution: Study of a Class of Conjugated Graft Copolymers Tomasz. *Polymers (Basel)*. **2019**, *11*, 205, doi:10.3390/polym11020205.
231. Grushevenko, E.A.; Borisov, I.L.; Volkov, A. V High-Selectivity Polysiloxane Membranes for Gases and Liquids Separation (Review). **2021**, *61*, 959–976, doi:10.1134/S0965544121090103.
  232. Maciak, E.; Procek, M.; Kępska, K.; Stolarczyk, A. Study of Optical and Electrical Properties of Thin Films of the Conducting Comb-like Graft Copolymer of Polymethylsiloxane with Poly(3-Hexylthiophene) and Poly(Ethylene) Glycol Side Chains for Low Temperature NO<sub>2</sub> Sensing. *Thin Solid Films* **2016**, *618*, 277–285, doi:10.1016/j.tsf.2016.08.031.
  233. Procek, M.; Kępska, K.; Stolarczyk, A. A Study on the Impact of Poly(3-Hexylthiophene) Chain Length and Other Applied Side-Chains on the NO<sub>2</sub> Sensing Properties of Conducting Graft Copolymers. *Sensors (Switzerland)* **2018**, *18*, 928, doi:10.3390/s18030928.
  234. Kaluzynski, P.; Kępska, K.; Maciuch, M.; Maciak, E.; Stolarczyk, A.; Procek, M.; Jarosz, T. Effect of Ultraviolet Activation on Sub-Ppm NO<sub>2</sub> Sensing Dynamics of Poly(3-Hexylthiophene)-Bearing Graft Copolymers. *Sensors* **2022**, *22*, 9824, doi:10.3390/s22249824.
  235. Molefe, F. V; Mothudi, B.M.; Dhlamini, M.S. The Effect of Deposition Method and Thickness Dependence on the Growth of P3HT for Organic Photovoltaic Devices. *Results Opt.* **2024**, *16*, 100684, doi:10.1016/j.rio.2024.100684.
  236. Li, D.; Shi, P.; Wang, J.; Li, J.; Su, R. High-Efficiency Absorption of High NO<sub>x</sub> Concentration in Water or PEG Using Capillary Pneumatic Nebulizer Packed with an Expanded Graphite Filter. *Chem. Eng. J.* **2014**, *237*, 8–15, doi:10.1016/j.cej.2013.09.069.
  237. Li, L.; Lu, G.; Yang, X. Improving Performance of Polymer Photovoltaic Devices Using an Annealing-Free Approach via Construction of Ordered Aggregates in Solution. *J. Mater. Chem.* **2008**, *18*, 1984–1990, doi:10.1039/b719945g.
  238. Kroon, R.; Lenes, M.; Hummelen, J.C.; Bloom, P.W.M.; de Boer, B. Small Bandgap Polymers for Organic Solar Cells (Polymer Material Development in the Last 5 Years). *Polym. Rev.* **2008**, *48*, 531–582, doi:10.1080/15583720802231833.